THE UNIVERSITY *of* EDINBURGH

This thesis has been submitted in fulfilment of the requirements for a postgraduate degree (e.g. PhD, MPhil, DClinPsychol) at the University of Edinburgh. Please note the following terms and conditions of use:

This work is protected by copyright and other intellectual property rights, which are retained by the thesis author, unless otherwise stated.
A copy can be downloaded for personal non-commercial research or study, without prior permission or charge.
This thesis cannot be reproduced or quoted extensively from without first obtaining permission in writing from the author.
The content must not be changed in any way or sold commercially in any format or medium without the formal permission of the author.
When referring to this work, full bibliographic details including the author, title, awarding institution and date of the thesis must be given.

Detection of Ionising Radiation using Single Photon Avalanche Diodes

Anthony Frederick Bulling

THE UNIVERSITY *of* EDINBURGH

A thesis submitted for the degree of Doctor of Philosophy

The University *of* Edinburgh

2019

To Anne and Silas.
With love to the moon and down again,
and around the stars and back again.

Abstract

Single photon avalanche diodes (SPADs) are highly sensitive solid-state photon detectors, and since their inception in 2003 into complementary metal oxide semiconductor (CMOS) technologies, have provided a platform of highly integrated and low-cost mass manufacture detectors, capable of rapid detection of single photons. The consequent commercial potential has led to the development and availability of a range of CMOS SPAD sensors and arrays.

As a consequence of their mature development in advanced processes, detection sensitivity and timing capabilities, CMOS SPADs have found their way into multiple applications, most notably biomedical fluorescence lifetime imaging microscopy (FLIM), Light Detection and Ranging (LiDAR), Time-of-Flight (ToF) imaging, Single Photon Counting (SPC), high speed imaging, biological particle tracking and more recently visible light communications. Although, all current applications are constrained to the visible and near infrared spectrums. The advances and broad applications of CMOS SPADs has led to increased development towards further miniaturisation, performance improvements and developing highly integrated intelligent sensors. Therefore, the investigation of the application of SPADs in the detection of ionising radiation has significant commercial potential as an alternative technology to current detectors.

The goal of this research is to explore the direct detection of ionising radiation with CMOS SPADs. The fundamental mechanism for detection is a depleted junction operated in Geiger mode, with an induced electric field that allows sensitive detection of generated electron-hole pairs as a result of incident radiation. Therefore, based on this principle it was hypothesised that SPADs can be applied beyond current photon specific detection applications into the detection of ionising radiation. Furthermore, high energy physics is transitioning towards CMOS processes with all the unprecedented advantages it provides. Therefore, it is believed that with SPAD advancement and maturity in CMOS technology, this parallel and continually developing technology may lend itself favourably towards progress and application in the detection of ionising radiation.

This work reports on a 3D-stacked backside illuminated (BSI) CMOS SPAD image sensor for the detection of accelerated electrons, pions and X-rays, utilising a scanning electron microscope, synchrotron particle accelerators and X-ray tube sources respectively. For accelerated electron detection, electron energies from 5 to 30 keV were detected, and statistical significance was found that both SPAD excess bias voltage and/or incident accelerated electron energy result in a distinct output. Furthermore, the SPAD image sensor was able to achieve time-resolved imaging of the electron beam raster scan pattern.

For X-ray detection, X-rays with peak photon energies from 30 to 160 keV were detectable using an X-ray tube, and it was found that an increase in either SPAD bias voltage, output beam voltage or beam intensity results in higher relative average counts per pixel, therefore demonstrating the potential application of SPAD image sensors in X-ray imaging. These results are the first demonstration and application of a CMOS SPAD in the detection of accelerated electrons and X-rays. Further investigation revealed that the attenuation of lower energy photons from an X-ray tube spectrum results in approximately 200 % increase in relative average counts.

Furthermore, The BSI CMOS SPAD image sensor was irradiated with a high energy pion beam at 120 GeV, using the Super Proton Synchrotron (SPS) at CERN, and high energy electrons at 2.5 GeV, using an electron accelerator at ELSA. For the pion irradiation, pions were conclusively detected, and it was found that an increase in SPAD bias voltage results in higher relative average counts per pixel. No conclusive detection of higher energy electrons was observed as a result of low beam intensity. After the pion irradiation, radiation damage to the SPAD image sensor was observed. These results are the first demonstration and application of a CMOS SPAD in the detection of high energy charged particles.

Declaration of Originality

I declare that this thesis has been composed solely by myself and that it has not been submitted, in whole or in part, in any previous application for a degree. Except where states otherwise by reference or acknowledgment, the work presented is entirely my own.

2. I confirm that this thesis presented for the degree of Doctor of Philosophy, has

i) been composed entirely by myself

ii) been solely the result of my own work

iii) not been submitted for any other degree or professional qualification

3. I declare that this thesis was composed by myself, that the work contained herein is my own except where explicitly stated otherwise in the text, and that this work has not been submitted for any other degree or processional qualification except as specified.

Anthony F. Bulling, Edinburgh, 2019

Acknowledgements

This PhD was written in four continents, in ten countries, across two oceans, it has been a true adventure. Edinburgh is a city of dreams and I have loved living in this wondrous city.

I had never imagined doing a PhD, however one man saw my potential and offered me the opportunity to do so. I am truly grateful and honoured to have met, been supervised, and mentored over the past four years by my supervisor Prof. Ian Underwood. Your constant guidance, support and trust has helped me develop my career as a researcher, engineer and individual. Your outlook, enthusiasm and experience have been invaluable in my development and I truly appreciate all I have learnt. Thank you for always lending an ear and trusting in me.

My time in Edinburgh is filled with wonderful memories filled with brilliant people I have met along the way, every one of them having a lasting impression upon me. There are many people I wish to acknowledge throughout my journey, and I would like to express my appreciation and gratitude to all my colleagues at the Institute for Integrated Micro and Nano Systems at the Scottish Microelectronics Centre for their invaluable expertise, dedication and time. They were the stepping stone I needed, and I am truly grateful for all their help and invaluable lessons.

Mom and Dad, thank you for absolutely everything. You are both incredible and I am so grateful for your love and wisdom. Thank you for being my rock and for always being there for me with unconditional love and support, and for believing in me. Without you I would not be the man I am today.

I wish to pay tribute to my colleagues Chandrasekaran Gunasekaran, Ricardo Guerrero, Hanning Mai, Tarek Al Abbas, Rui Song and Stephen Mahon. I thoroughly enjoyed discussing our work together and for making my time at the SMC so enjoyable. I wish to pay a special acknowledgement to Ricky, we started and finished together, and I am honoured to have worked with you and to call you my friend. Thank

you for always taking the time to listen and partake in my discussions, no matter the circumstances, your expertise and insights are fantastic.

In Edinburgh I found a new family, a family of friends whose relationships I will cherish for many years to come. Thank you, Chris, Elena, Chiara, Davide, Jinyu, Shuji, Ninni, James, Murve and Rohan for being such excellent people! A special mention must be given to James Maguire, thank you for all the extraordinary memories and for a friendship that is the finest single malt, sherry cask, aged to perfection.

With new life comes great responsibility, however it also comes with a life filled with unequivocal joy and a love I never thought possible. Silas my beautiful boy, I started this journey without you, but your support till the end has been amazing. Your constant smile and uncanny ability to lift my heart is enchanting. You are an absolute blessing and were a wonderful distraction from my writing.

To my incredible and beautiful wife Anne, the last four years with you have been the best of my life. From the moment I met you, you were brilliant and have been so ever since. I am immensely grateful for your unwavering love and tremendous support, and I look forward to our remarkable ongoing adventure together.

And finally, but not least, I am very grateful, and wish to acknowledge the Commonwealth Scholarship Commission and The University of Edinburgh for funding my PhD in the UK. Furthermore, I wish to acknowledge the Royal Society of Edinburgh and the David Mayes Travel Scholarship for funding my research at CERN.

Publications

[1] A. F. Bulling and I. Underwood, "Accelerated Electron Detection Using Single Photon Avalanche Diodes," 2018 IEEE SENSORS, New Delhi, 2018, pp. 1-4, doi: 10.1109/ICSENS.2018.8589781.

[2] A. F. Bulling and I. Underwood, "X-ray Detection using Single Photon Avalanche Diodes," 2019 IEEE SENSORS, Montreal, QC, Canada, 2019, pp. 1-4, doi: 10.1109/SENSORS43011.2019.8956558.

Acronyms

3D	Three-Dimensional
3D-IC	Vertically Integrated Circuit
APD	Avalanche Photodiode
BS	Backscattered
BSI	Back-Side Illuminated
BTBT	Band to Band Tunnelling
CCD	Charge Coupled Devices
CERN	The European Organization for Nuclear Research
CGS	Centimetre–Gram–Second
CMOS	Complementary Metal Oxide Silicon
CPGA	Ceramic Pin Grid Array
cps	Counts per Second (Hz)
CRT	Cathode Ray Tubes
CSDA	Continuous Slowing Down Approximation
DCR	Dark Count Rate
DNW	Deep n-type Well
DRAM	Dynamic Random-Access Memory
DST	Deep Submicron Technology
EM	Electron Microscope
FLIM	Fluorescence Lifetime Imaging Microscopy
FPGA	Field-Programmable Gate Array
FWHM	Full Width at Half Maximum
GM	Geiger Mode
HBM	High Bandwidth Memory
HBM	Hybrid Bond
HDCR	High Dark Count Rate
HEP	High Energy Physics

IC	Integrated Circuit
IO	Input/Output
LHC	Large Hadron Collider
LIDAR	Light Detection and Ranging
Linac	Linear Accelerator
MIP	Minimum Ionising Particles
NIEL	Non-Ionising Energy Loss
NIR	Near Infra-Red
NW	n-type Well
PCB	Printed Circuit Board
PDE	Photon Detection Efficiency
PDP	Photon Detection Probability
PMT	Photomultiplier Tubes
PS	Proton Synchrotron
Psub	p-type Substrate
PW	p-type Well
R&D	Research and Development
RTS	Random Telegraph Signal
SE	Standard Error of the Mean
SEM	Scanning Electron Microscope
SMC	Scottish Microelectronics Centre
SNR	Signal-to-Noise-Ratio
SPAD	Single Photon Avalanche Diode
SPC	Single Photon Counting
SPS	Super Proton Synchrotron
STEM	Scanning Transmission Electron Microscope
STI	Shallow Trench Isolation
TEM	Transmission Electron Microscope
TID	Total Ionising Dose
ToF	Time of Flight
WD	Working Distance

Contents

Figures

Tables

1. Introduction

This thesis explores the utilisation of complementary metal oxide silicon (CMOS) single photon avalanche diodes (SPADs) for the detection of incident ionising radiation. SPADs are highly sensitive single photon (visible spectrum) detectors with temporal resolution in picoseconds and quenching detection resolution in nanoseconds. Their inherent timing capabilities and single photon sensitivity allows SPADs to be utilized in high-speed imaging, single photon counting and time-resolved applications.

This work investigates the use of a 3D-stacked backside illuminated (BSI) CMOS SPAD image sensor for the detection of accelerated electrons, pions and X-rays, utilising a scanning electron microscope, synchrotron particle accelerators and X-ray tube sources respectively.

1.1 Motivation

SPAD technology has developed substantially over the past decades and has led to its inception in 2003 into CMOS technologies, which has provided a platform of highly integrated, miniaturised and low-cost mass manufacture avalanche detectors, capable of rapid detection [1], [2]. Furthermore, a consequence of their mature development in advanced processes, detection sensitivity, micron sized pixels and timing capabilities, CMOS SPADs have found their way into multiple applications. Most notable applications include, biomedical fluorescence lifetime imaging microscopy (FLIM), Light Detection and Ranging (LiDAR), Time-of-Flight (ToF) imaging, Single Photon Counting (SPC), high speed imaging, biological particle tracking and more recently visible light communications [3]–[10]. Although, all current applications are constrained to the visible and near infrared spectrums (NIR).

The advances and broad applications of CMOS SPADs has led to increased R&D and financial backing as a commercially viable technology. The motivation is towards further miniaturisation, performance improvements, 3D-stacking and developing highly integrated intelligent sensors with abounding integral capabilities.

Consequently, as SPADs operate similarly to silicon-based ionising radiation detectors, it is believed that with SPAD advancement and maturity over the past two decades in CMOS, this parallel and rapidly developing technology may lend itself favourably towards progress and application in the detection of ionising radiation. Limited not only in high energy particle physics, but every day commercial applications, such as X-ray imaging, beam therapy and electron microscopy, which would greatly reduce cost and help advance miniaturisation of current technology, improving both availability and mobility. Furthermore, the development of highly integrated ionising radiation detectors will allow for the miniaturisation and development of intelligent lab-on-chip applications, as well as facilitate the development of table-top particle accelerators for both research and potential medical therapy [11], [12]. Therefore, the investigation of the application of SPADs in the detection of ionising radiation has significant commercial potential as an alternative technology to current detectors.

1.2 Research Aims

The primary aim of this research is to investigate the direct detection of ionising radiation with CMOS SPADs. This includes both ionising photons and high energy charged particles. The starting point of this research is to identify a suitable CMOS SPAD for the detection of ionising radiation, that may have characteristic radiation hardness properties. Thereafter, the identification of suitable ionising radiation sources with emphasis on real world applications is required.

The subsequent aim is to demonstrate CMOS technology with integrated SPAD detectors and circuitry, as a viable alternative technology for ionising radiation detector applications, with all the associated benefits that assimilating both SPADs and CMOS, greatly reducing costs with rapid, high resolution detection and imaging. Target applications include, lab-on-chip applications, X-ray imaging, electron microscopy and table-top particle accelerators [11].

1.3 From Visible Light to Ionising Radiation

A SPAD is a reverse biased pn-junction fabricated on a semiconductor substrate, that employs avalanche breakdown to detect single photons. A SPAD is designed to be

reverse biased and function beyond its breakdown voltage, referred to as “Geiger” operation, wherein runaway avalanche multiplication and impact ionisation allow rapid detection of a single incident photon. SPADs operate solely in Geiger mode (GM), unlike avalanche photodiodes (APD), which allows for highly sensitive (large gain) single photon detection, with picosecond temporal resolutions. The fundamental mechanism for detection is the transfer of energy from an incident photon to an atomic electron, generating an electron-hole pair, which is accelerated under a large induced electric field, which causes impact ionisation and ultimately results in avalanche breakdown and a detected pulse.

Therefore, it is hypothesised that,

> *Ionising radiation incident upon a SPAD depletion region will produce electron-hole pairs and coupled with Geiger operation, the induced electric field and large inherent gain, will generate impact ionisation and subsequent avalanche breakdown. Therefore, resulting in the detection of incident ionising radiation using SPADs.*

However, one of the integral concerns with using SPADs for the detection of ionising radiation is the potential radiation damage to the SPAD detector.

1.4 Ionising Radiation

Ionising radiation is radiation that contains enough energy to ionise atoms. Ionising radiation propagating through matter interacts with the medium through energy transfer with atomic electrons and abides by the law of conservation of energy. Thereby, transferring enough energy to an atomic electron, which results in the release of that electron. Figure 1.1 provides a simplified illustration of the process of atom ionisation.

The minimum amount of energy to release an electron from an atom is the work function, whereas the energy required to release an electron from an atoms outermost valence band is the ionisation energy. The work function is the energy difference between the atoms Fermi level and electron emission (ionisation). For metals, the work function is equal to the ionisation energy, as there is an abundance of electrons, within

the valence band, with energy equal to the Fermi level. However, this is not the case for semiconductors, where the ionisation energy is larger than the work function. [13]

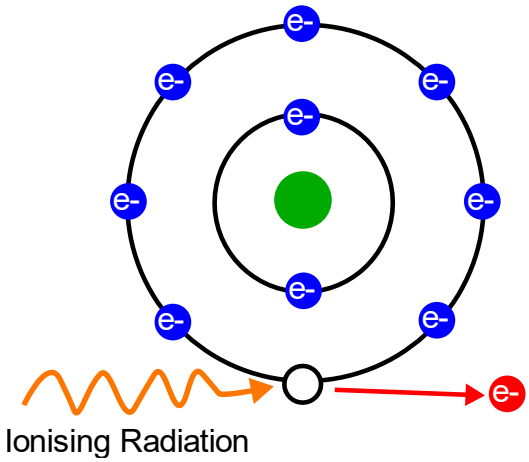

Figure 1.1. Illustration of ionisation process, where incident ionising radiation transfers enough energy to an atomic electron, resulting in its release, therefore ionising the atom.

There are two types of ionising radiation, ionising photons and high energy charged particles. Photons are electromagnetic radiation, and ionising photons are electromagnetic radiation on the higher energy end of the electromagnetic spectrum, which includes gamma- and X-rays. Ionising photons interact with matter predominantly through three processes, namely the emission of electrons through the photoelectric effect; Thomson and Compton scattering; and pair production. The photoelectric effect is when incident photons transfer enough energy to an atomic electron to overcome the atoms work function. Pair production is the creation of subatomic particles and their respective antiparticle, which predominantly occurs with higher energy photons (MeV range). [14]

High energy charged particles are accelerated charged particles, which interact with matter through coulomb interactions, where energy is transferred principally with atomic electrons, which in turn results in electron emission (ionisation). At high energies, radiative energy loss effects dominate, where charged particles lose energy via Bremsstrahlung producing radiative photon emission. The production of photons can generate subsidiary electrons, which in turn can generate further photons, resulting in a cascading effect known as electromagnetic cascade. [14]

1.5 Ionising Radiation Detectors

The detection of ionising radiation is achieved through a medium sensitive to ionising radiation, where the detection is contingent on the interaction between the medium and incident radiation, which generates some form of signal, e.g. light or current [15], [16]. There are three principal techniques for relating the generated signal to the incident radiation, namely counters, spectrometers and dosimeters [15]. Counters tally the number of total interactions that occur, spectrometers generate a signal which is proportional to the energy of the incident radiation and dosimeters measure the absorbed radiation dose [15].

For ionising radiation detectors, the principal mechanisms for detection is either ionisation or excitation. The most common ionising radiation detectors employed are, gas detectors, scintillation counters, semiconductor detectors, chemical detectors, calorimeters, photographic film and thermoluminescent dosimeters [15], [16]. An overview of each detector type, detection principles and typical applications are given in [15]. Furthermore, an overview of specific ionising radiation detectors and subdetectors used in high energy particle physics is given in [17].

This work mainly focuses on semiconductor detectors, specifically silicon-based detectors as a result of their inherent advantages for CMOS integration, high spatial resolution and timing capabilities. Additionally, silicon-based detectors are the detector of choice for the detection of charged particle and X-rays, particularly high energy physics (HEP) [18].

1.6 Silicon-Based Particle Detection

Silicon-based detectors for charged ionising radiation have already been developed for HEP in particle accelerator research, such as the state-of-the-art ATLAS hybrid inner pixel detector at CERN's Large Hadron Collider (LHC) [19]–[22]. The ATLAS and CMS detectors were used to detect a new elementary particle, which was proposed in the 1960s and was found to be consistent with the Higgs Boson in the Standard Model, and thus, the Higgs Boson was discovered [23], [24]. Figure 1.2 provides a computer generated image of the ATLAS inner detector showing the placement of hybrid pixel detectors and trackers [25].

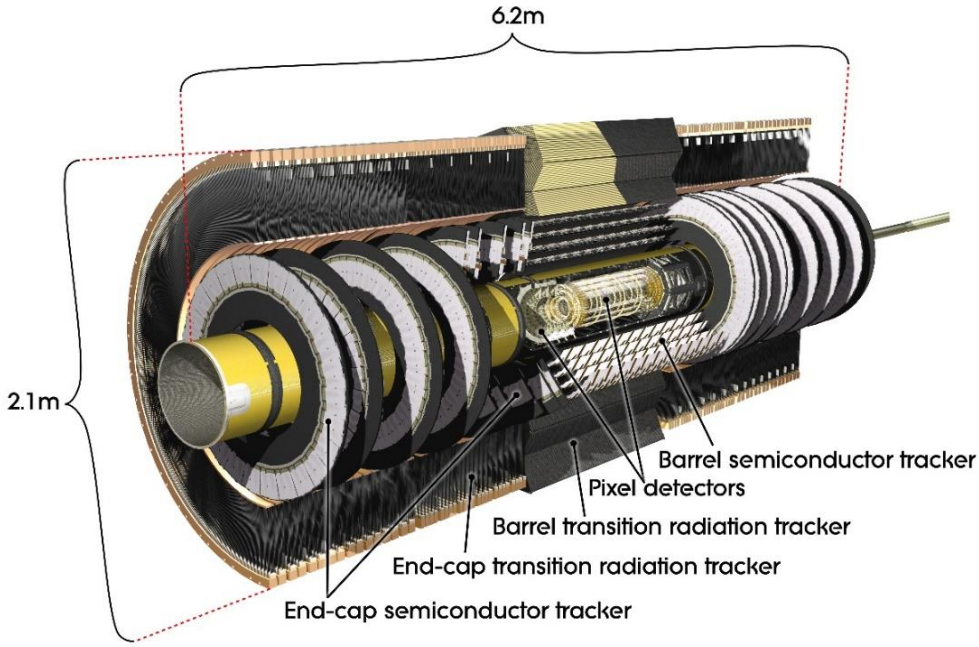

Figure 1.2. Computer generated image of ATLAS inner detector indicating placement of pixel detectors and trackers [25].

The pixel detector is a hybrid sensor fabricated in float-zone silicon and bump bonded to front-end integrated readout circuitry using a laboured process, which ultimately affects fabrication integrity, overall expenditure and expediency [26], [27]. At the heart of the detector is the sensor, which is simply a pixelated detector array of depleted solid-state bipolar diodes, in a high resistivity n-type bulk substrate, used to detect ionising radiation [22], [27]. A single pixel is made up of a highly doped p-region (p+) and a highly doped n-region (n+) on either side of the substrate and operated in reverse bias, depleting the entire active region, approximately 256 µm thickness, which creates a depleted ionisation chamber, with a pixel pitch of 55 µm [27], [28]. Figure 1.3 provides an illustrated cross-section and generic view of a hybrid pixel detector and illustrates how transient ionising radiation generates electron-hole pairs within the sensor tier, where the induced current is detected through charge collection on the electrode [29]–[31]. An extensive overview on hybrid pixel operating principles and design specifications are given in [17] and [27] respectively.

Hybrid pixel detectors work similarly to avalanche photo diodes (APD) and operate with limited gain and often at very low temperatures to reduce free charge carriers in the large depleted junction to ensure adequate signal-to-noise-ratio (SNR), without

breakdown [17]. A detailed explanation about the difference between APDs and SPADs is provided in section 2.1.1. A transient particle creates electron-hole pairs within the depleted junction, which generates a small current. Therefore, a low noise preamplifier with a high gain-bandwidth is required to ensure adequate detection, followed by a DC-coupled stage and differential discriminator with a pre-set range [22]. When an incident particle is detected within the discriminator threshold, the pixel and timing information allows for the calculation of the charge input to the preamplifier, proportional to the energy deposited by the incident ionising radiation [22].

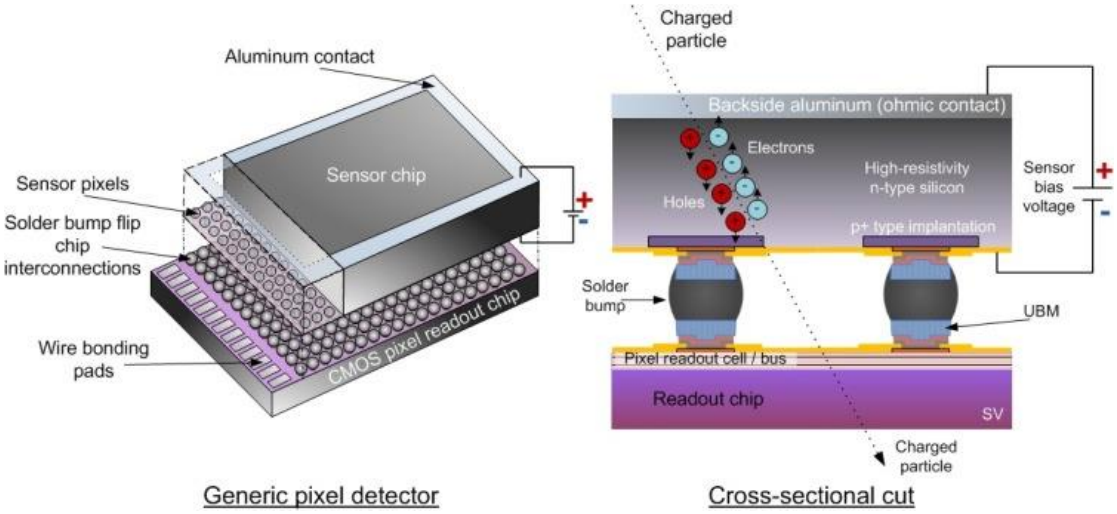

Figure 1.3. General operation, architecture and cross-section of a hybrid pixel detector, with charge carrier generation as a result of a transient charged particle [29].

The successful development of hybrid pixel detectors for the detection of ionising radiation in HEP has led to the commercialisation of hybrid detectors for SPC, medical imaging, space dosimetry and material analysis applications under the Medipix collaboration [21], [30], [32]. However, extensive R&D has been put towards the development of CMOS based monolithic sensors for the next generation of pixel detectors for the high-luminosity LHC upgrade due in 2024. CMOS development would allow all the associated benefits of combining both integrated circuitry and active pixel sensor within a single commercial process, greatly reducing production costs and integration complexity [26], [33]–[35]. The challenge in developing monolithic CMOS particle detectors that are additionally radiation hard, is ensuring a low capacitance and fully depleted sensor, capable of separating consecutive particle

collisions with a bunch spacing of 25 ns, while evading potential charge trapping [26]. The junction capacitance of a reverse biased pn-junction is calculated as follows,

$$C = A \cdot \frac{\varepsilon}{w_d} \tag{1.1}$$

where A is the cross-sectional area of the diode, ε the permittivity of the semiconductor and w_d the width of the depletion region. Therefore, for improved noise performance the capacitance is reduced by decreasing the cross-sectional area and increasing the depth of the depletion region.

1.7 Silicon Radiation Damage

There are two predominant areas of radiation damage namely surface and bulk damage. Ionising radiation loses energy primarily through ionisation, but a portion is lost through non-ionising energy loss (NIEL) [17], [36]. NIEL occurs primarily by coulomb interaction of incident ionising radiation with the atomic lattice, resulting in sputtering, the displacement of atoms from the original lattice site, which then migrate through the lattice structure creating a point defect and subsequent collection defects [17], [36]. Alternatively, depending on radiation type and energy, NIEL can also produce phonon excitation [37], [38]. An overview of NIEL is given in [17].

For surface damage, ionising radiation causes surface damage defects in primarily insulator materials such as silicon dioxide (SiO_2) by ionisation, where excited electrons diffuse and hole charge traps are produced [17]. An accumulation of charge traps generates a net positive charge in the oxide, and at an interface with silicon (Si), results in charge trapping affecting current-voltage characteristics and thus performance degradation [39]–[42].

Bulk damage in Si is caused by NIEL, and is the principal form of radiation damage that can result in operational failure of the device [17], [36]. The defects produced by NIEL cause lattice deformation and distortion of the operational properties of the initial device, resulting in increases in charge trapping and leakage currents [36], [43]. Furthermore, with lattice deformation, the effective doping concentration of the device is altered producing irregular junction performance, eventually resulting in failure of

Si pn-junctions [36], [43]. An extensive review of radiation damage in silicon devices and silicon pixel detectors is presented in [17] and [36].

The measure of absorbed ionising radiation dose is referred to as total ionising dose (TID), measured in the SI unit Gray (Gy) or centimetre–gram–second (CGS) unit Rad, and is the abortion of radiation energy in joules (J) in a unit mass (kg) of matter. Therefore, 1 Gy is equal to the absorption of 1 J of radiation energy in 1 kg of matter.

$$1\ \text{Gy} = \frac{1\ \text{J}}{1\ \text{kg}} = 100\ \text{rad} \tag{1.2}$$

1.8 Contributions to Knowledge

The primary contribution to knowledge of the research covered in this thesis is the following; a SPAD pn-junction reverse biased and operated in Geiger mode, can be used to detect ionising radiation, which includes both X-rays and high energy charged particles.

The specific types of ionising radiation detection covered in this thesis, including respective energy ranges where irradiation was detected, is as follows,

1. Accelerated electrons with kinetic energies in the range 5 to 30 keV were detected using a scanning electron microscope (SEM). The SPAD image sensor used, allowed for time-resolved imaging of the respective electron beam raster scan pattern across the sensor array. Furthermore, statistical significance was found that both SPAD excess bias voltage and/or incident accelerated electron energy result in distinct output detection.
2. Accelerated pions with kinetic energy of 120 GeV using the super proton synchrotron at CERN incident upon the SPAD image sensor were detectable, showing a definite increase in output counts per pixel during irradiation. Additionally, it was found that an increase in SPAD bias voltage results in higher relative average counts per pixel. The outcome confirms that a SPAD can be used to detect heavy charged particles in high energy physics environments.
3. X-rays with peak photon energies in the range 15 to 160 keV using tungsten target X-ray tubes were detectable. The results indicate no permanent radiation

damage to the SPAD image sensor after long periods of irradiation, a TID of 4.8 Mrad, and it was found that an increase in SPAD bias voltage results in higher relative average counts per pixel.

1.9 Thesis Outline

Chapter 2 presents a literature review of SPADs and their integration into CMOS, followed by a literature review on SPAD operating principles, structure and performance parameters. Thereafter, an overview of the 3D-Stacked back-side-illuminated (BSI) CMOS SPAD image sensor used throughout this thesis is presented, including operation, architecture, layout and performance.

Chapter 3 reports the application of a CMOS SPAD image sensor for the detection of accelerated electrons with a scanning electron microscope (SEM). The chapter begins with a literature review on electrons and their interaction and passage through matter, with emphasis on energy loss and total stopping power. An overview on electron acceleration and electron microscopy is also presented. Afterwards, the experimental method for electron detection is presented, followed by experimental results. Finally, a summary and conclusion are presented.

Chapter 4 is separated into two parts representing two separate experiments. The first experiment is the investigation of the detection of high energy pions, and the second the investigation of the detection of high energy electrons. The chapter commences with a literature review on the standard model of physics and passage of heavy charged particles in matter. Additionally, an overview on the respective particle accelerators used for the experiments is presented including an overview on the origin of pions. Thereafter, the experimental setups are presented followed by experimental results. And finally, a summary and conclusion are presented.

Chapter 5 reports the detection of X-rays, beginning with a literature review on X-ray interaction with matter, and the generation thereof using an X-ray tube. Thereafter, the experimental set-up is presented followed by experimental results and concluding remarks.

Chapter 6 is the final chapter of the thesis and presents a summary and concluding remarks of the thesis, followed by a view on future work of CMOS SPADs for the detection of ionising radiation.

2. CMOS Single Photon Avalanche Diodes

This Chapter presents a brief history of single photon avalanche diodes and their inception in CMOS technology. Thereafter, a literature review of SPADs is presented with emphasis on SPAD operating principles, structure and performance parameters.

Finally, an overview of the 3D-Stacked BSI CMOS SPAD image sensor used throughout this thesis is presented with emphasis of the image sensor operation, architecture, layout and performance.

2.1 Single Photon Avalanche Diodes

In the early 1950's avalanche breakdown of a reverse biased pn-junction was first observed, and subsequent research investigated the solid-state physics of this phenomenon including localised spots of electroluminescence [44], [45]. Thereafter, avalanche breakdown was linked to the effect, avalanche multiplication, where the minority carriers in a depleted pn-junction at high electric fields are accelerated across the junction, generating additional electron-hole pairs, effectively multiplying the number of charge carriers [45]–[49].

In the 1960's at Shockley Semiconductor laboratories in California, research on the physics of avalanche multiplication inadvertently led to the development of the precursor to SPADs, as single photons were detected [50], [51]. To attain single photon detection using a reverse biased pn-junction, a guard ring, known as the Goetzberger diffused guard ring structure [51], was employed to prevent premature edge breakdown, to permit a bias voltage higher than the pn-junctions' planar breakdown voltage [51], [52]. Thereafter, R. H. Haitz, provided a better understanding of the fundamentals of avalanche pn-junctions, including elucidations on junction noise and afterpulsing [53], as well as the development of the first Geiger detectors for low light applications [54]. Further research investigated the application of avalanche pn-junctions for photodetectors, the predecessors to APD [55], [56].

In 1981 researchers from Politecnico di Milano proposed the application of solid-state avalanche pn-junctions as a replacement for photomultiplier tubes (PMTs) for picosecond single photon counting (SPC), and were the first to introduce the

designation “Single Photon Avalanche Diode” [57]. Thereafter in 1983, demonstrating picosecond SPC using SPADs, with the measurement of low-light fluorescence lifetimes [58]. Subsequent decades of research and development followed, resulting in enhanced and varied SPAD structures [8], [59]–[63]. A review of this SPAD technology and development can be found in [64] and [65].

During the 1950’s and 60’s semiconductor technology and silicon processing was only beginning, and so the development of pn-junctions and ultimately avalanche detectors in standard processes was not viable, as junction manufacturing resulted in many defects and low product yields [1], [2]. However, over the coming decades CMOS technology developed for reliable commercial development and up until 2003, SPAD devices were only realised in fully customisable processes, which allowed manufacturers the freedom of SPAD parameter and structure optimisation, but with the disadvantage of only discrete devices [1], [2]. This changed in 2003, when the first CMOS SPAD was realised in a 0.8 µm high-voltage CMOS process [66], [67], and paved the way for the current era of highly integrated circuitry and SPADs in CMOS [68]. For an extensive explanation of SPAD operation, physics, historical development and CMOS integration, the reader is redirected to the following references [68] and [2].

2.1.1 SPAD Operation

Avalanche breakdown is the phenomenon that APD exploit for photon detection. A pn-junction or diode is reverse biased, depleting the junction of majority carriers, known as the depletion region, resulting in an electric field across the junction. When an electron in the conduction band enters the junction as a minority carrier, the electric field accelerates the electron across, if the electric field is large enough the accelerated electron acquires enough energy to cause impact ionisation, in which the accelerating electron collides with another electron in the valence band, generating a secondary electron-hole pair [52], [69], [70]. The secondary electron and initial accelerated electron may cause further impact ionisation known as avalanche multiplication [2], [47], [52], and if the conditions are favourable may cause runaway avalanche multiplication, a continuous avalanche breakdown, known as Geiger breakdown, which requires a quench and recharge circuit to recover.

For a reverse biased pn-junction there are three modes of operation illustrated in Figure 2.1, namely integration, avalanche and Geiger. Photodiodes operate in the integration or linear region, APD operate in the avalanche region with limited gain 10 - 100, below the junction breakdown voltage (V_{BD}) and SPADs operate in the Geiger region, above V_{BD}.

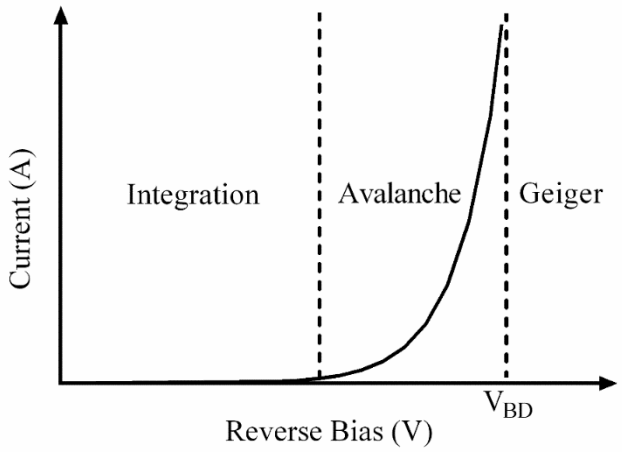

Figure 2.1. IV curve for reverse biased pn-junction, indication modes of operation: integration, avalanche and Geiger.

In the integration region, incident photons generate a linearly conforming current as a result of electron-hole pair generation, proportional to the light intensity. In the avalanche region, avalanche multiplication is larger as a result of impact ionisation, resulting in a larger gain, which amplifies the current, thus increasing sensitivity to incident photon detection. However, suffering from inherent noise generated by avalanche multiplication. Therefore, APDs need to limit operational gain to ensure adequate SNR, without breakdown [1], [56]. APDs are capable of single photon detection, but with the limited gain and subsequently small current generated by an arriving photon, a low noise preamplifier with a high gain-bandwidth is required to ensure adequate detection [1].

SPADs on the other hand operate in the Geiger region, where the pn-junction is biased beyond V_{BD}, allowing quasi-stable operational bias for a limited period beyond breakdown. Stability is maintained until a minority carrier enters the depletion region, by an arriving photon, and causes runaway avalanche breakdown as a result of considerable impact ionisation and avalanche multiplication. This distinction is

important to consider, because unlike APD's which are unsustainable, when light irradiation is removed, SPADs require an avalanche quench and recharge once breakdown occurs, to allow for additional detection.

Quenching of the SPAD stops runaway avalanching and is achieved using complimentary quenching circuitry to force the bias voltage across the SPAD to below V_{BD}, ceasing current flow, followed by a recharge, which returns the bias condition above V_{BD} to the initial state of Geiger operation. Figure 2.2 (a) provides a simple illustration of a passively (resistive) quenched SPAD detector with the output tied to an output inverter. For APDs avalanche multiplication results in a proportional increase in junction current, which is amplified for detection, however for SPADs, runaway breakdown results in a large pulse of current through the junction as shown in Figure 2.2 (b); this rapid pulse of current allows for picosecond detection of a single photon. However, an inherent disadvantage of this configuration is the resulting detector dead time, the time it takes for the SPAD to quench and recharge over the inverter transient threshold voltage (V_T), and thus the 'dead' or inactive time between the detection of single photons. [2], [71]

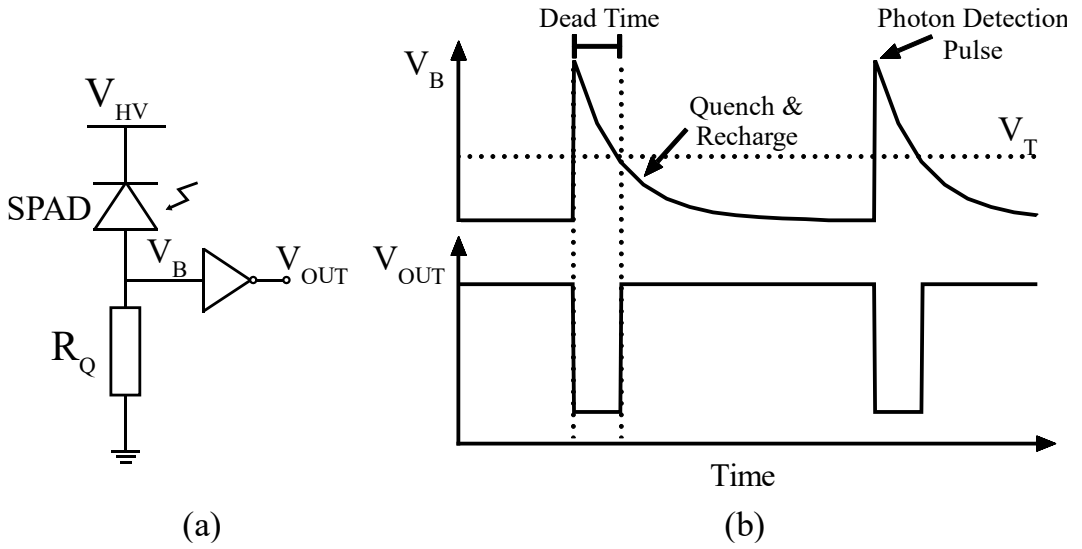

Figure 2.2. (a) Simplified SPAD circuit with passive quenching resistor R_Q, with (b) SPAD output waveforms indicating photon arrival pulse, deadtime, quench and recharge and correlating output detection signal.

A detailed explanation and overview of SPAD quenching circuits and their progress can be found in [26] and [32]. For quenching circuitry there are two types, passive and

active, which are both integrable in CMOS [73]–[75]. Passive quenching is realised through a resistor, which reduces the voltage across the SPAD to below V_{BD} while conducting, effectively halting avalanche [2], [71]. Active quenching provides more control over SPAD performance, and achieves the same result as passive quenching, however substantially quicker, by employing complex transistor circuitry to detect avalanche breakdown and actively turn the SPAD off (quenching), thereafter actively driving the SPAD back on (recharge), to reduce dead time [71], [75]. Though, active quenching is also used to reduce SPAD afterpulsing, by introducing a SPAD off-delay (controlled increase in dead time) to ensure the release of any unwanted trapped charges [76], effectively reducing noise. Furthermore, SPADs developed in CMOS processes utilising passive quenching, implement a transistor for resistance instead of a dedicated resistor, which reduces required design area [67], [77].

2.1.2 SPAD Structures

As discussed briefly in the preceding section, in order to successfully design and produce a SPAD, achieving Geiger-mode operation, a reverse biased pn-junction requires a guard ring to prevent premature avalanche breakdown on the periphery of the junction. The guard ring ensures the depletion layer formed is uniformly distributed along the entire junction interface, allowing bias beyond the planar junction breakdown voltage. The implementation of a physical guard ring is illustrated in Figure 2.3 and stems from its first proposal by Goetzberger et al. in 1963 [51], highlighting the shift in breakdown region with and without a guard ring structure. Furthermore, the implementation of a guard ring reduces surface noise effects as a result of lattice imperfections, with a shift in the resulting breakdown area [1].

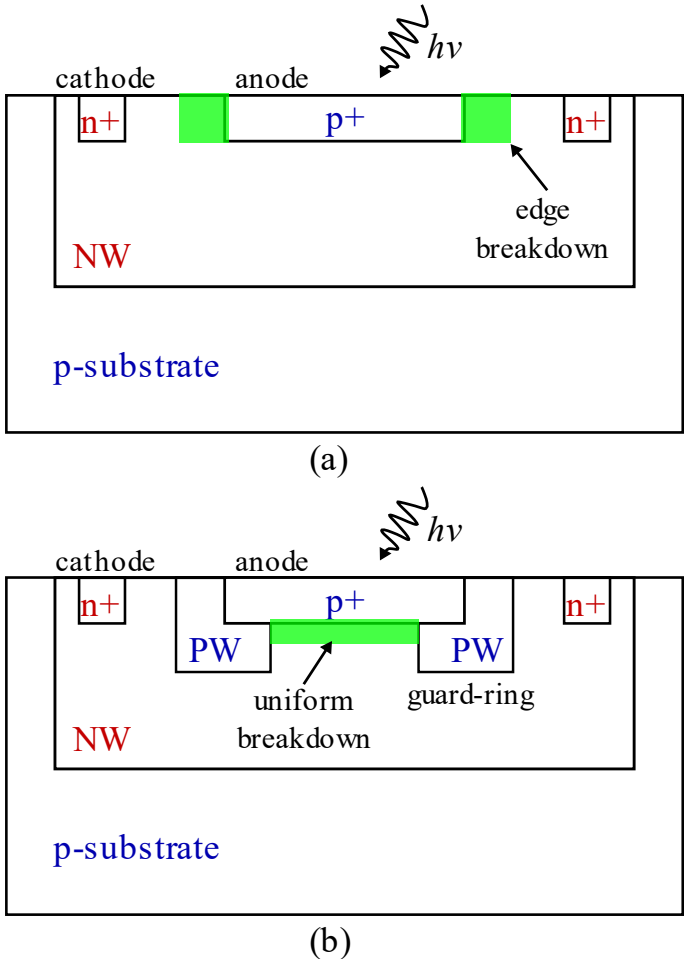

Figure 2.3. p+ to NW SPAD junction, showing resulting change in depletion region, (a) without and (b) with an integrated guard ring.

Numerous guard ring structures have been proposed and implemented in both custom and CMOS processes [8], [56], [60]–[63], [78]–[80]. The guard ring implemented in Figure 2.3 (b) illustrates the most commonly designed CMOS SPAD and guard ring structure, first demonstrated by Rochas in 2003 in a high voltage 0.8 µm CMOS process [67]. The junction periphery is surrounded by a lower doped p-well (PW) guard ring, to prevent edge breakdown, as the pn-junction comprising the higher doped p+ and n-well (NW) under reverse bias has a lower breakdown voltage, due to increased doping concentration [81]. Comparable forms of this guard ring structure have been successfully implemented in several other advanced CMOS processes including 180 and 130 nm processes [82]–[88].

For the revolutionary Rochas diffused guard-ring, there is an inherent design limitation, when designing in CMOS processes below 130 nm. As the CMOS process

feature size decreases, doping concentrations increase to ensure nominal junction operation, which causes lower junction breakdown voltages and higher SPAD noise as a result of band-to-band tunnelling [89]–[92]. Furthermore, a reduction in feature size restricts the scalability of the SPAD to ensure a sufficiently sized implanted guard ring, to prevent guard ring depletion region mergence [1].

Solutions have been proposed and implemented, such as shallow trench isolation (STI) available in limited processes [80], [93], able to isolate large electric fields while requiring less area to ensure a sufficient guard ring [79], but at the cost of increased noise due to injection defects at the junction interface [94]. An alternative method is the implementation of a virtual guard ring using a deep n-well (DNW) implant and the precise spacing of implant areas, that results in a naturally low doped area between the anode and cathode, forming a natural guard ring [95]. Similarly, a retrograde DNW can be used to develop a p-type epitaxy between the NWs of the SPAD creating an implicit guard ring, realised in both 130 and 150 nm processes respectively [89], [96].

However, such structures still exhibit high noise as a result of high doping concentrations of the diffusion implants within the inherent shallow junctions [1]. In 2009 a PW to retrograde DNW SPAD structure, based on the previous virtual guard ring structure, was developed in a 130 nm process [97], [98], producing a deeper depletion junction with an undoped epitaxy guard ring structure between the PW and NW, illustrated in Figure 2.4. The SPAD structure results in reduced noise and higher breakdown voltage [98]. The PW to retrograde DNW was then demonstrated in a 90 nm process [99] and subsequently industrialised in both a 130 nm process [100] and 40 nm deep submicron technology (DST) process [101].

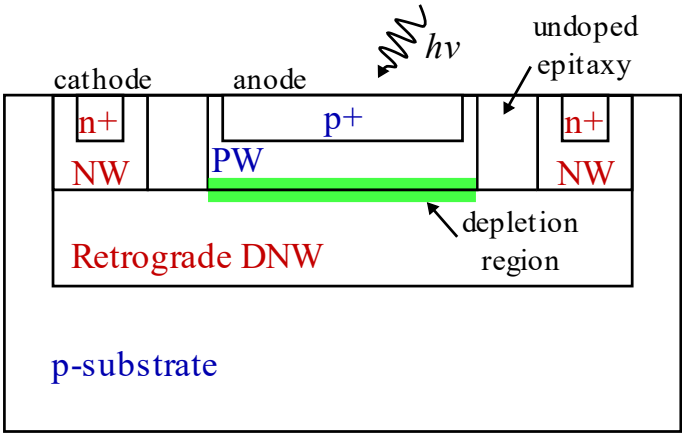

Figure 2.4. PW to retrograde DNW SPAD junction, with undoped epitaxy virtual guard ring structure.

SPADs developed with virtual guard rings allow for improved scalability and implementation of high performance SPADs in advanced processes with lower noise levels. This progress has led to the development of SPADs in multiple different CMOS processes including, but not limited to, 130 to 40 nm with varying capabilities, applications and distinct virtual guard ring structures [62]-[76]. For an extensive review on varying SPAD structures and advances, the reader is redirected to [1].

SPAD miniaturisation and use of either physical or virtual guard rings does not imply optimal performance, instead it provides the designer with a variety of options that lends itself to a specific application. Furthermore, the technology is continually developing and benefits from the development of already established and advancing commercial processes.

2.1.3 Performance Parameters

SPADs are quantified on certain performance parameters namely detection probability, dark count rate (DCR) and timing resolution. Furthermore, secondary performance parameters namely afterpulsing and crosstalk.

SPAD efficacy is measured by and referred to as photon detection probability (PDP) and is the probability of a SPAD to detect an incident photon. The PDP is a weighted probability and is the product of both SPAD quantum efficiency and avalanche breakdown probability. The internal and external quantum efficiencies of the CMOS SPAD structure determine the overall quantum efficiency. Avalanche breakdown probability is the probability a generated minority carrier within the multiplication

region causes runaway avalanche breakdown, which is directly dependent on the applied electric field [116]. Furthermore, photon detection efficiency (PDE) is the PDP proportional to the SPAD fill factor, therefore the ratio of SPAD count rate vs the number of incident photons over the total area of the SPAD [117].

If avalanche is triggered by a carrier not generated by an arriving photon, this is a spurious detection, and is referred to as a dark count and is a measure of specious counts associated with SPADs. There are three main contributors to DCR that generate carriers, namely thermal generation; Shockley-Read-Hall trap-assisted generation [118], [119], and band-to-band tunnelling [90], [120]. Furthermore, certain SPADs suffer from unwanted DCR instability known as random telegraph signal (RTS) noise, where the SPAD DCR fluctuates between different states during operation [121]–[123]. RTS noise has been attributed to charge trapping at metastable locations within the SPAD device as a result of impurities and lattice defects [122].

SPAD timing resolution or jitter is measured in picoseconds and is the statistical variation in SPAD output pulse rate once an incident photon is detected. Therefore, jitter is the variation in the time it takes a photo-generated carrier to generate an output pulse. Moreover, jitter is influenced by the origin of the photo-generated carrier and its diffusion tail, as there is an inherent delay for the carrier to reach the SPAD multiplication region if the carrier originates outside the depleted region [124]. SPAD jitter is measured using a pulsed laser and is commonly reported in full width at half maximum (FWHM). Theoretical analysis and Monte Carlo simulation of avalanche breakdown and jitter are presented in [125] and [126] respectively.

Afterpulsing is a contributing factor to DCR due to secondary spurious counts after an initial photon detection and augments total photon counts, which affects PDE [127]. When a photon is detected and the SPAD avalanches, lattice defects and impurities allow for carriers to be trapped within the SPAD junction [127]. Thereafter, when the subsequent carrier is released, there is a possibility the free carrier causes an after-pulse and is thus a false photon detection.

SPAD array crosstalk is spurious avalanche breakdown in an adjacent SPAD to a SPAD which avalanches as a result of an incident detected photon and limits SPAD

dynamic range. Crosstalk is caused either electrically or optically. Electrical crosstalk is the result of coupling capacitances between SPAD anodes and cathodes, resulting in free carrier diffusion into a neighbouring SPAD depletion region [128], [129]. Optical crosstalk is the result of hot-carrier electroluminescence during SPAD avalanche, which produces a population of energetic (hot) carriers that generate secondary photons, and electromagnetic cascading affect [130]–[135]. Such photons may indirectly or directly cause avalanching in an adjacent SPAD junction [129].

2.2 Backside Illuminated CMOS SPAD

The SPAD image sensor used for this research, hereinafter referred to as MINI3D, is a 120 x 128-pixel CMOS miniature time-resolved SPAD array, and the first presented 3D-stacked backside illuminated (BSI) silicon sensor capable of both time-resolved imaging and single photon counting (SPC) [1], [7]. 3D-stacking technology is driven by the demand for increased transistor density and is a key technology in dynamic random access memory (DRAM) fabrication and high bandwidth memory interface (HBM) technology to improve both bus speeds with shorter bus paths, and reduce overall power consumption by reducing RC parasitics [136], [137]. An extensive overview on SPAD architectures and 3D-stacking technologies is given in [1].

2.2.1 MINI3D 3D-Stacked BSI CMOS SPAD Image Sensor

The MINI3D image sensor pixel comprises of two tiers, connected with a wafer to wafer hybrid bonding connection [1], [138]. The SPAD image sensors are implemented on the top tier, within an imaging 65 nm CMOS process, without active circuitry, for optimised fill factor of 45 % and pixel pitch of 7.83 µm [1]. The bottom tier houses all the necessary integrated circuitry and is implemented within a complimentary 40 nm process [1]. Figure 2.5 shows an illustration of the cross section of the MINI3D 3D stacked image sensor layout, presenting both tiers, connected via a vertical stack of metal layers [1]. The stacked wafers are bonded at both the hybrid bond (HB) Cu-to-Cu and oxide interfaces using a dual damascene integration [1]. Each pixel has a dedicated 12-bit ripple counter providing a binning capacity for 4096 photon counts [1]. The MINI3D SPAD image sensor structure resembles a hybrid pixel detector and is therefore expected to have improved radiation hardness capabilities.

The top tier is inverted allowing incident photons to enter the backside of the die, and thus the device is referred to as a BSI SPAD image sensor, where the incident material is silicon. The backside of the die has been wafer thinned and the thickness is undisclosed to author. The SPAD junction is a PW to shared retrograde DNW as illustrated in Figure 2.4 with an isolated substrate and NMOS quench transistor. [1]

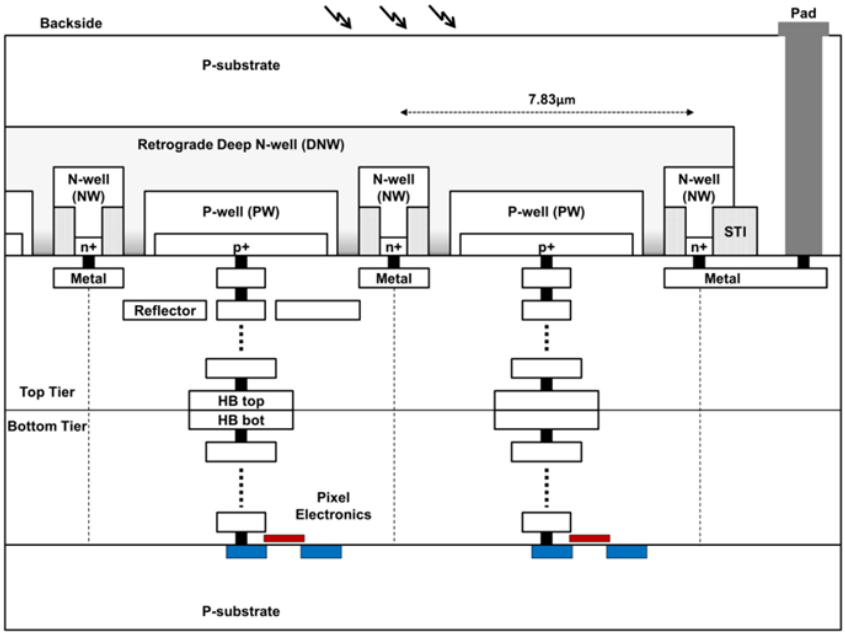

Figure 2.5. Illustrated cross section of the MINI3D BSI 3D-stacked pixel layout showing with a 1-to-1 hybrid bond connection between top and bottom tiers [1].

Figure 2.6 shows a block diagram of the image sensor system architecture and pixel array together with a micrograph of the top tier backside with periphery aluminium pads. Each trial area is 1.2 × 1.2 mm^2 and the die area is approximately 2.4 × 2.4 mm^2. The operational static controls are performed through column buffers, where gating signals and dynamic controls are operated by the clock trees located below the array. The bottom serial readout is split between two input/output (IO) pads with a maximum frame rate of 500 Hz. The main trial in Figure 2.6 is the only operational image sensor on the die with a 128 × 120-pixel array. Each pixel has an effective 12-bit counter, which is split into two 6-bit counters and can operate linearly, allowing time-resolved measurements for time-of-flight (ToF) and fluorescence lifetime imaging (FLIM). [1]

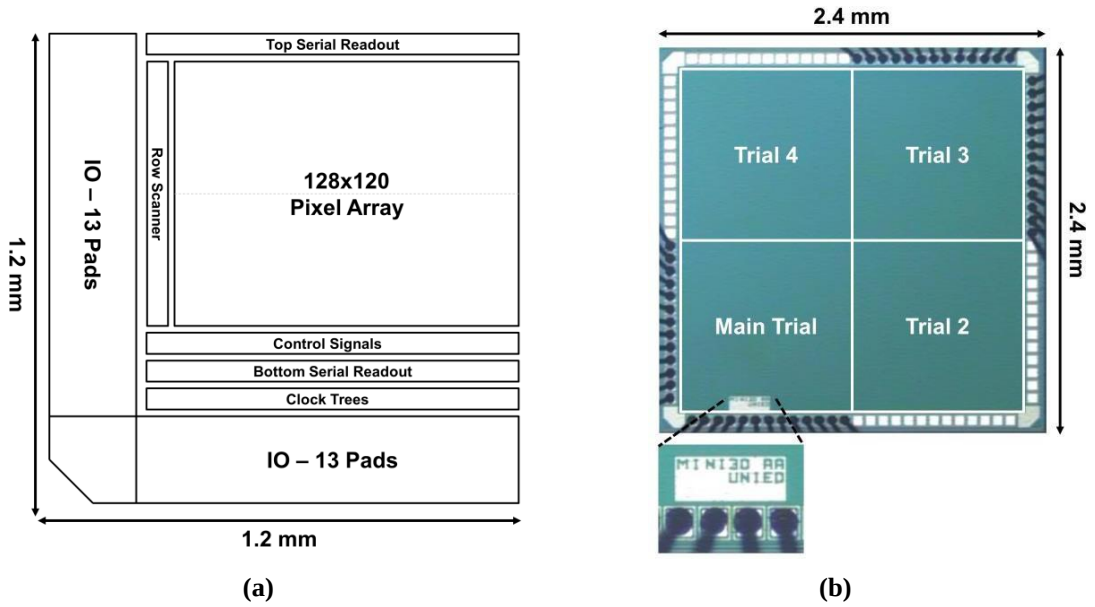

Figure 2.6. (a) MINI3D SPAD image sensor block diagram of the image sensor system architecture and pixel array. (b) Micrograph of the die backside top tier. [1]

Figure 2.7 (a) shows the SPAD DCR as a function of breakdown voltage in counts per one millisecond and (b) shows the distribution of the breakdown voltage across the SPAD array with a mean breakdown voltage of 11.7 V and standard deviation of 30 mV. Figure 2.8 shows the median DCR for the SPAD image sensor as a function of excess bias voltage, where the curve is exponential in nature, which indicates that tunnelling is the dominant contributor to DCR. Figure 2.9 shows the cumulative DCR for the SPAD array at varying excess bias voltages, which shows that approximately 80 % of pixels exhibit a uniform DCR distribution, whereas the remaining 20 % exhibit a high non-uniform DCR distribution, which skews the DCR distribution of the array. Furthermore, the jitter of the device was measured using two lasers with 0.44 µm and 0.77 µm wavelengths respectively and a maximum jitter of approximately 230 ps was measured, with an impulse response function peak of 17 ns. [1]

An extensive overview of the MINI3D SPAD architecture, circuitry, performance characterisation and comparison to other sensors is provided in [1]. For external operation and interface with a computer, all operational, control and supply signals are externally generated and connected using a field-programmable gate array (FPGA).

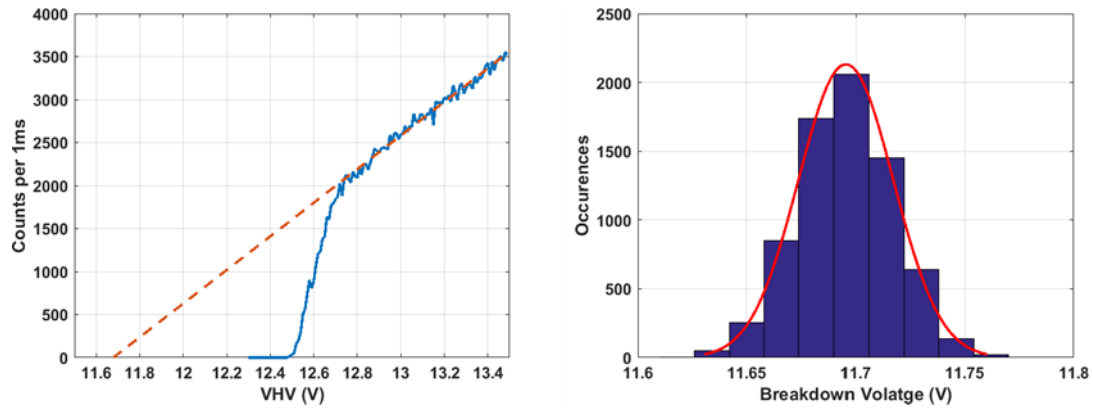

Figure 2.7. (a) SPAD output counts per 1 ms frame exposure time as a function of breakdown voltage. (b) Breakdown voltage distribution across array with calculated mean of 11.7 V and standard deviation of 30 mV. [1]

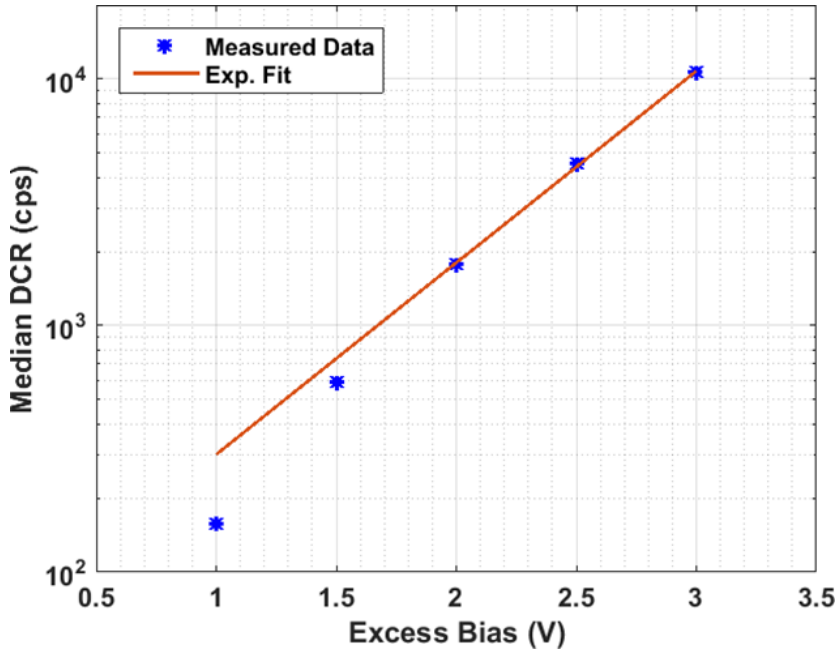

Figure 2.8. MINI3D SPAD image sensor median DCR as a function of excess bias voltage at room temperature [1].

The pursuit of 3D-stacked CMOS SPAD technology is seen as a key process in realising miniature CMOS SPADs with highly integrated circuitry capability, that would otherwise be unachievable in monolithic CMOS technology [1]. 3D-stacking permits high pixel array fill factors that are scalable, while optimising pixel driver circuitry without compromise, by separating the sensor and IC tiers to deliver optimal performance and capability [1].

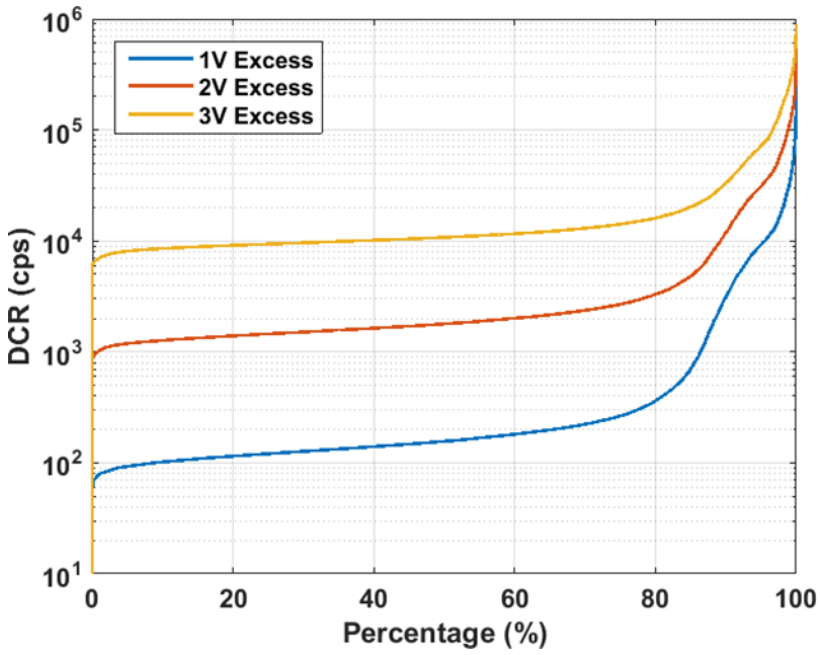

Figure 2.9. MINI3D SPAD image sensor cumulative DCR as a function of excess bias voltage at room temperature [1].

2.3 Summary and Conclusion

The chapter begins with a brief history on the development of SPADs and their integration into CMOS technology. Thereafter a literature review on SPAD operating principles is presented, with emphasise on Geiger operation and how runaway avalanche quenching is achieved. A literature review on various SPAD guard ring structures is presented followed by an overview of primary and secondary SPAD performance parameters.

Section 2.2 provides an overview of the MINI3D 3D-stacked BSI CMOS SPAD image sensor that was used for the research reported in this thesis, including SPAD operation, architecture, layout and performance. The SPAD is BSI and therefore the medium for incident ionising radiation will be silicon. The 3D-stacked SPAD image sensor structure resembles a hybrid pixel detector and was therefore selected due to its potential improved radiation hardness capabilities.

The pursuit of CMOS 3D-stacked technology for SPADs is an interesting development, when compared to Hybrid pixel detectors. Both 3D-stacked CMOS SPADs and hybrid detectors are fabricated to separate IC and pixel sensor tiers to achieve optimal performance of each respective tier. However, hybrid pixel detectors

are not wholly developed in a dedicated CMOS process unlike 3D-stacked CMOS SPAD technology. Furthermore, the HEP community is transitioning ionising radiation pixel detectors to planar monolithic CMOS with all the associated benefits that CMOS provides. Therefore, 3D-stacking CMOS technology may be a complimentary technology to hybrid pixel detectors.

The following chapter reports on the application of the MINI3D CMOS SPAD image sensor for the detection of accelerated electrons with a SEM.

3. Accelerated Electron Detection using SPADs

An electron is a negatively charged particle, discovered in 1897 by Sir Joseph John Thomson, and was the first subatomic particle to ever be discovered [139]. The discovery of the electron transformed our understanding of the atom and the known universe. We know that electrons bond to atomic nuclei through the electromagnetic force, but are not restricted to bound to atoms, they can be emitted through thermionic emission, where electrons, acquire enough energy to overcome the material's work function [140], [141]. Such electrons are commonly used in cathode ray tubes (CRT), scanning electron microscopes (SEM), transmission electron microscopes (TEM) and high energy particle accelerators.

This chapter reports the application of CMOS SPADs for the detection of direct accelerated electrons within a vacuum, within a SEM. The chapter first provides a literature review of the collision effects of accelerated electrons with incident atoms, then moves on to a brief overview of a SEM. Thereafter, results of electron detection are presented and analysed, followed by conclusions regarding the suitability of CMOS SPADs for the detection of accelerated electrons.

3.1 Passage of Electrons Through Matter

3.1.1 The Atom

To understand the passage of an accelerated electrons through matter, it is important to understand the environment of which matter is made, atoms. The radii of atoms are approximately between 0.05 and 0.25 nm or 0.5 to 2.5 Å, whereas, the charge radius of a proton is approximately 0.85 fm. Therefore, for particles passing through matter it is important to consider incident cross-sections. For example, the spherical silicon atom with atomic number (Z) of 14, has an approximate radius of 0.12 nm and a geometrical cross-section of 4.524×10^{-20} m^2, whereas, the silicon nucleus has a radius of 3.6 fm and a geometrical cross-section of 4.072×10^{-29} m^2. Therefore, the geometrical probability of an incident particle colliding with the nucleus is approximately nine orders magnitude lower than interacting with the surrounding electrons. [14], [18], [142], [143]

3.1.2 The Electron

Within the standard model of particle physics an electron is classified as a lepton, with an electric charge of negative one. Electrons at rest have an electric field about them and are bound to the nuclei by coulomb forces. Coulomb interactions result in the exchange of energy with other atomic electrons, which result in either excitation or ionisation. For particle trajectory the overall elastic scattering of the particle is subject to the mass and charge of the particle, which adheres to the principle of conservation of energy. Therefore, for heavy charged particles (protons, alpha particles, heavier ions etc.) the interaction with atomic electrons, results in minimal scattering and the overall trajectory is not significantly affected. However, as the charge to mass ratio of an electron (e/m) is large, accelerated electrons emit electromagnetic radiation and experience large accelerations under induced electric fields, thus experiencing significant scattering and dramatically different trajectories. [1], [5], [141], [142] When an electron traverses matter and strikes an atom, the electron may elastically scatter, without the loss of energy, or interact with the atom and lose energy via collisional or radiative energy loss. Collisional energy loss involves inelastic scattering, where an atomic electron gains energy from the incident accelerated electron and is either raised to an excited state (excitation) or is removed from the atom (ionisation). Radiative energy loss known as Bremsstrahlung, is when the electron loses energy by emitting a photon while scattering from the atom. Elastic scattering affects the overall trajectory and mean free path of the electron; whereas collisional and radiative energy loss, cause the electron to come to eventual rest, related to the total stopping power.[14], [18], [142], [143]

3.1.3 Energy Loss and Total Stopping Power

For accelerated electrons passing through and interacting within a given medium the rate of energy loss is expressed by the total stopping power and is defined as follows

$$-\left(\frac{dE}{dx}\right)_{total} = \left(-\frac{dE}{dx}\right)_{collisional} + \left(-\frac{dE}{dx}\right)_{radiative} \tag{3.1}$$

where E, and x are the kinetic energy of the charged electron, and the length traversed within the given medium respectively. Furthermore, the total stopping power is the

sum of both the collisional and radiative stopping powers. In particle physics it is common to express total stopping power in units of MeV·cm^2/g as a function of βγ, the relative energy of the particle. β is the relativistic speed of the particle and γ is the Lorentz factor, expressed in equations 3.2 and 3.3 respectively. [14], [18], [143]–[146]

$$\beta = {}^{v}/_{c} \tag{3.2}$$

$$\gamma = \frac{1}{\sqrt{1-\beta^2}} \tag{3.3}$$

where v is the velocity of the particle and c the speed of light. For accelerated electrons with kinetic energy E, passing through an incident material with an atomic number Z, the collisional stopping power formula for electrons is used and expressed in equation 3.4. [146]

$$\left(-\frac{dE}{dx}\right)_{collisional} = \frac{K}{2}\cdot\frac{Z}{A}\cdot\frac{1}{\beta^2}\left[\begin{array}{l} ln\frac{m_e c^2\beta^2\gamma^2 W_{max}}{I^2} + (1-\beta^2) - \\ \frac{2\gamma-1}{\gamma^2}ln\,2 + \frac{1}{8}\left(\frac{\gamma-1}{\gamma}\right)^2 - \delta(\beta\gamma) \end{array}\right] \tag{3.4}$$

where W_{max} is the maximum energy transfer in a single collision [146], and is expressed as follows,

$$W_{max} = \frac{m_e c^2(\gamma-1)}{2} \tag{3.5}$$

A summary and description of constants and variables used in equations 3.4 and 3.5 are provided in [147].

Table 3.1. Summary of Variables used for Electron Stopping Power.

Symbol	Definition	Value and/or units
e	elementary charge	$1.602\ 176 \times 10^{-19}$ C
ε_0	permittivity of free space	$8.854\ 219 \times 10^{-12}$ F/m
m_e	electron mass	9.1094×10^{-31} kg 0.510 999 MeV/c^2
c	speed of light	299 792 458 m/s
r_e	classical electron radius	2.817 940 fm
N_A	Avogadro's number	$6.022\ 140\ 857 \times 10^{23}$ mol^{-1}
K	$= 4\pi N_A r_e^2 m_e c^2$ $(-dE/-dx)$ coefficient	0.307075 MeV mol^{-1} cm^2
ρ	mass density of stopping medium [a]	g cm^{-3}
W_{max}	maximum energy transfer to an electron	MeV
Z	atomic number of stopping medium [a]	
A	atomic mass of stopping medium [a]	g mol^{-1}
I	mean excitation energy of stopping medium [a]	MeV
$\frac{\delta(\beta\gamma)}{2}$	density-effect correction for ionisation energy loss at very high energies	$\rightarrow \ln(\hbar\omega_p/I) + \ln(\beta\gamma) - 1/2$
$\hbar\omega_p$	plasma energy of stopping medium [a]	eV

[a]Atomic and nuclear properties available in [145]

Other authors also express stopping power in units of MeV/cm, known as the linear stopping power, expressed as *(-dE/dx)×ρ*, where ρ is the density of the stopping medium in units of g/cm^3. Figure 3.1 shows the contribution of the collisional and radiative stopping powers towards the total stopping power for silicon in MeV·cm^2/g, for electron energies in the range, 0.01 < E < 1000 MeV [145]. From Figure 3.1 the collisional energy loss is the most significant component towards total stopping power, for lower energy electrons. This indicates that for electron energies below 10 MeV, the energy loss is predominately ionisation, whereas above the critical energy (silicon, E_C = 40.19 MeV for e^-), high energy electrons lose energy in matter primarily by radiative energy loss, Bremsstrahlung [145], [146], [148], [149]. The radiative energy loss of electrons can be expressed by the product of the electron kinetic energy E, and the inverse radiation length X_0, in units of g·cm^{-2} as follows

$$\left(-\frac{dE}{dx}\right)_{radiative} = \frac{E}{X_0} \tag{3.6}$$

$$\frac{1}{X_0} = 4\alpha r_e^2 \cdot \frac{N_A}{A} \cdot \left[Z^2\left(L_{rad} - f(Z)\right) + ZL'_{rad}\right] \tag{3.7}$$

$$L_{rad} = ln\left(184.15 \cdot Z^{-\frac{1}{3}}\right) \tag{3.8}$$

$$L'_{rad} = ln\left(1194 \cdot Z^{-\frac{2}{3}}\right) \tag{3.9}$$

where α is the fine structure constant, 1/137.036, Z the atomic number of stopping medium and $f(Z)$ an infinite sum function, which can be represented by equation 3.10 for $Z < 92$.

$$f(Z) = a^2\left[\frac{1}{(1+a^2)} + 0.20206 - 0.0369a^2 + 0.0083a^4 - 0.002a^6\right] \tag{3.10}$$

where $a = \alpha Z$.

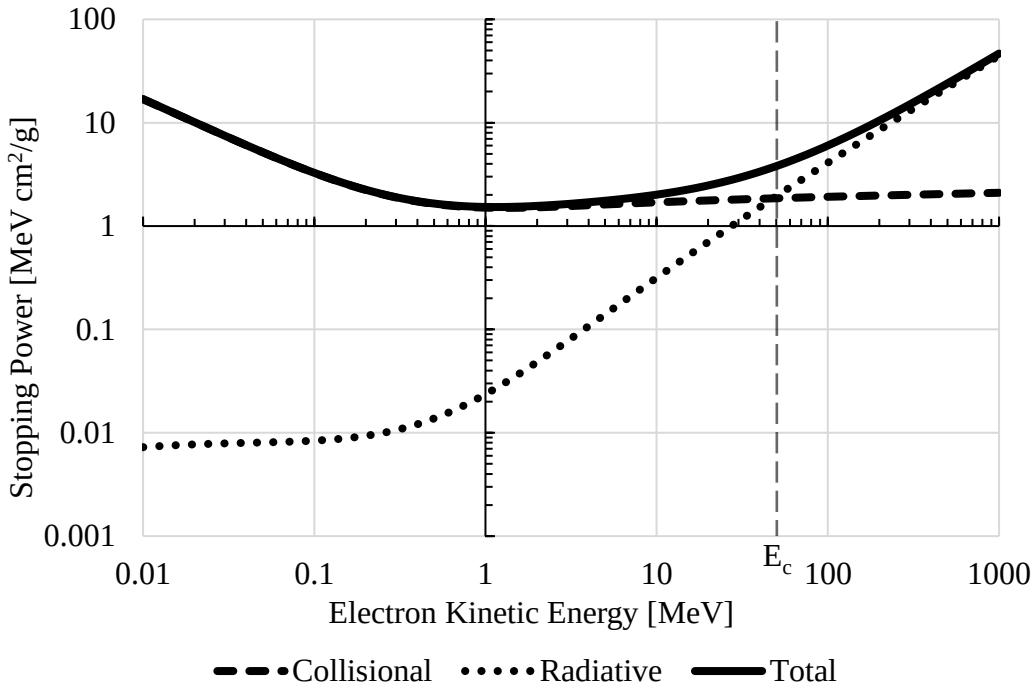

Figure 3.1. Total stopping power as a function of electron kinetic energy for silicon. Plot data from National Institute of Standards and Technology public database [145], [148].

Figure 3.2 shows the total stopping power as a function of energy for several elements and common process materials used in CMOS. Furthermore, Table 3.2 shows the approximate densities of these elements and mediums respectively, allowing the calculation of the approximate linear stopping length in cm, as a function of kinetic energy, shown in Figure 3.3.

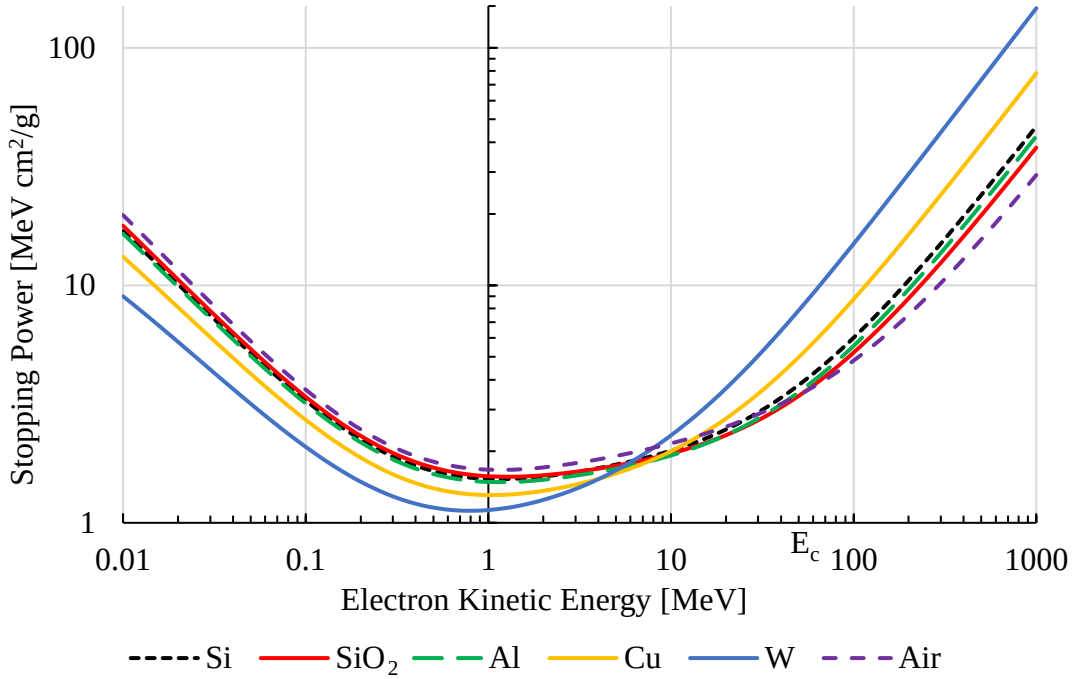

Figure 3.2. Total stopping as a function of electron kinetic energy for several stopping mediums [148].

From Figure 3.2 it can be seen that, as the atomic mass increases the collisional energy losses decrease, whereas the radiative energy losses increase about the critical energy point. From Figure 3.3 and Table 3.2 the density of the stopping medium is an important parameter in determining the linear stopping length of an incident electron, which is discernible that with increased density there will be increased collisional and radiative losses. Furthermore, both silicon and aluminium have similar atomic numbers and respective densities, which result in comparable total stopping power and linear stopping lengths.

Table 3.2. Mass densities for elements and stopping mediums.

Medium	Symbol	Density ρ (g cm^{-3}) [a]
Silicon	Si	2.329
Aluminium	Al	2.699
Copper	Cu	8.960
Tungsten	W	19.30
Silicon dioxide	SiO_2	2.200
Air (dry, 1 atmosphere) at 20 °C		1.205×10^{-3}

[a]Atomic and nuclear properties available at [145]

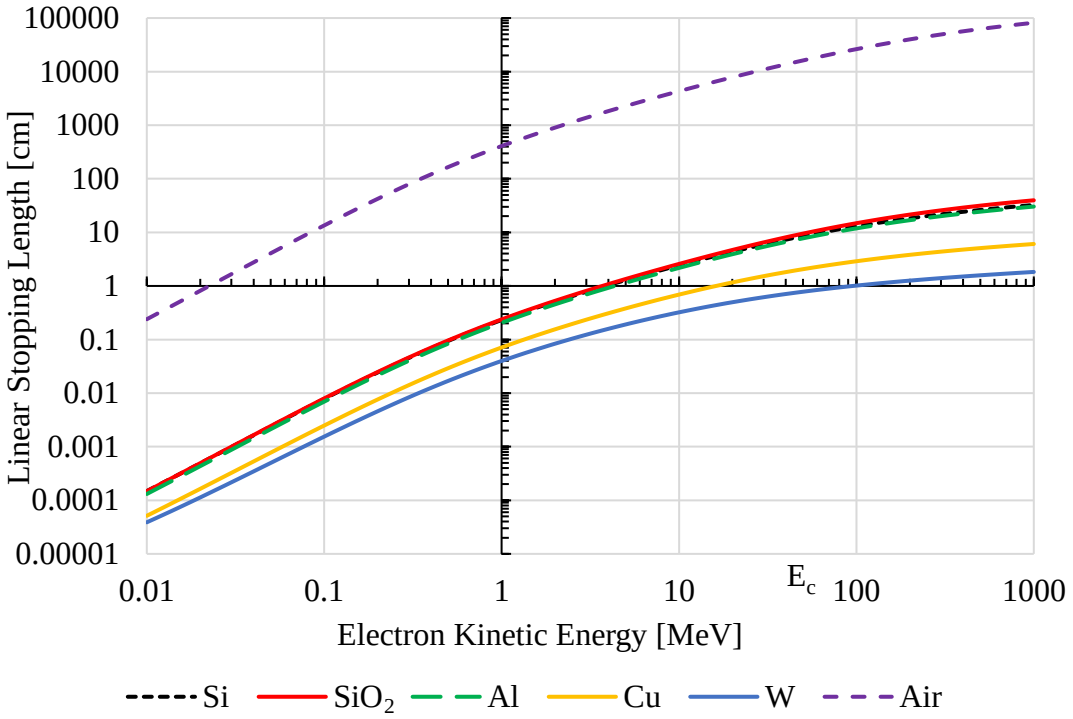

Figure 3.3. Linear stopping length as a function of electron kinetic energy for several stopping mediums [148].

3.2 Electron Acceleration

3.2.1 Electron Beam

As discussed in the beginning of this chapter, electrons can be discharged from an atom through thermal electron emission, in which the electrons acquire the minimum required energy to overcome the material's work function [140], [141]. This is achieved by heating up a filament, for example tungsten (within a vacuum). The vacuum allows for the formation of an electron cloud or free electrons around the heated cathode within a Wehnelt cylinder. Electrons are charged particles and can therefore be manipulated using electromagnetic fields. If a voltage is applied across the cathode and a suitably placed anode, an electric field is formed, accelerating the free electrons toward the positively charged anode, providing the electrons with increased kinetic energy. Therefore, an applied voltage (accelerating voltage) across the cathode and anode can be used to create an accelerated beam of electrons as shown in Figure 3.4, which provides a rudimentary operation of an electron gun in a vacuum chamber. Furthermore, the advantage of using a vacuum reduces both inelastic and elastic scattering of electrons.

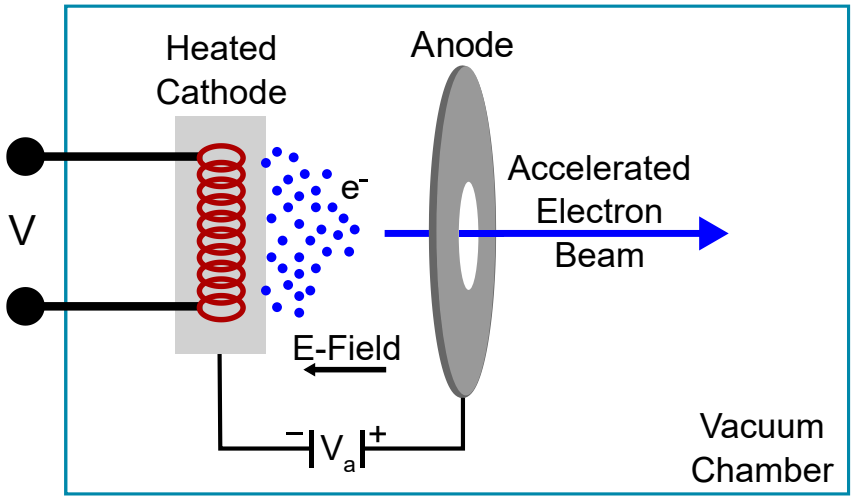

Figure 3.4. Simplified schematic of an Electron beam operation, in which the heated filament (cathode) creates a cloud of free electrons, which are focussed and accelerated towards the anode. The electron kinetic energy is a function of the applied voltage Va.

The velocity of the accelerated electrons can be calculated from the kinetic energy of the electron as a function of the applied voltage V_a using equation 3.13.

$$E = V_a \cdot e = mc^2 = (m_{rel} - m_e) \cdot c^2 \tag{3.11}$$

where E is the electron kinetic energy, e the electron charge, m_{rel} the electron relativistic mass, m_e the electron rest mass, c the speed of light. Using equations 3.2 and 3.3,

$$m_{rel} = \gamma \cdot m_e = \frac{m_e}{\sqrt{1 - \frac{v^2}{c^2}}} \tag{3.12}$$

where γ the Lorenz factor therefore,

$$v = c \cdot \sqrt{1 - \frac{1}{\left(1 + \frac{V_a \cdot e}{m_e \cdot c^2}\right)^2}} \tag{3.13}$$

Figure 3.5 shows the relativistic velocity of an electron as a function of the applied voltage, and that the velocity of the accelerated electron converges towards the speed of light. Furthermore, if the applied voltage is known, equation 3.13 can be used to calculate β in equation 3.2.

The development of electron beams led to the application thereof in many branches of technology and sciences including biological sciences, medicine, engineering and physics [141], [150]–[152]. Most notably in the commercial sector with the development of cathode ray tubes, used in e.g. televisions, monitors and oscilloscopes [141], [150]–[152]. Furthermore, electron guns are used in electron welding, electron microscopy, particle accelerators, etc. [141], [150]–[152].

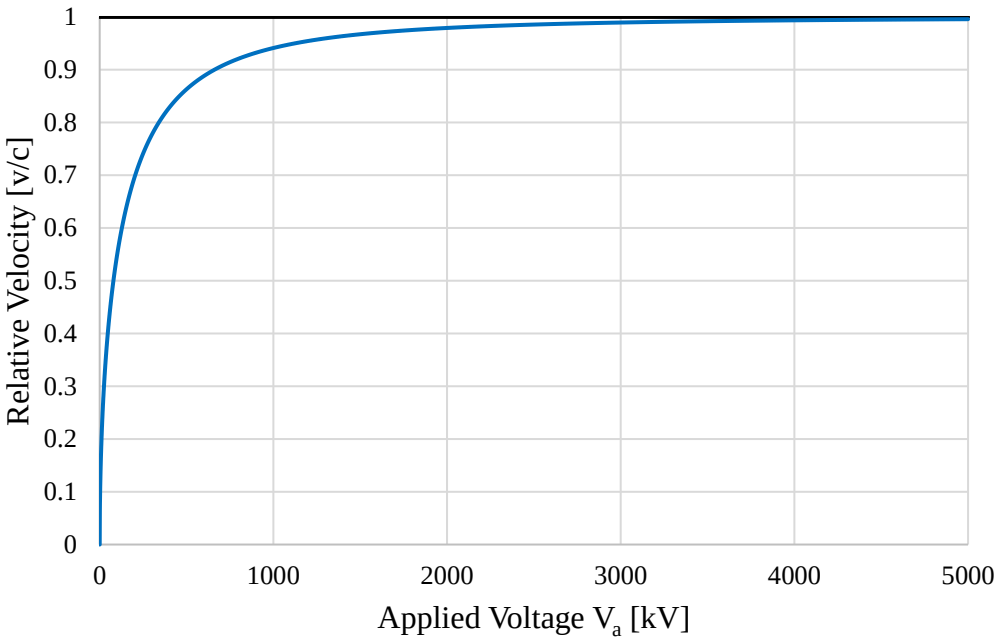

Figure 3.5. Relative accelerated electron velocity as a function of applied voltage.

3.2.2 Electron Microscopy

The development of the electron microscope (EM) began with the limitations of image resolution when using visible-light microscopes, limited by the wavelength of visible light. When it was discovered that electrons showed wave-like properties and could be accelerated within a vacuum, it was thereafter suggested to use electrons for microscopy, as the wavelength is smaller than that of visible light and would result in improved image minimum-resolvable distances (resolution) [141], [153]. The wavelength of electrons is inversely proportional to the kinetic energy of the electron expressed in equation 3.14, considering the relativistic effects.

$$\lambda = \frac{h}{\left[2m_e E\left(1 + \frac{E}{2m_e c^2}\right)\right]^{1/2}} \tag{3.14}$$

where h is Planck's constant = 6.626 ×10^{-34} J·s, E the electron kinetic energy, m_e the electron mass and c the speed of light. For example, if the kinetic energy of an electron is 10 keV the wavelength of the electron equals approximately 12.2 pm, which is smaller than the size of an atom. However, such resolutions are not yet achievable in an EM as a result of the electron lens imperfections, such as spherical and chromatic aberrations, and astigmatism [141]. Practically, transmission electron microscopes (TEMs) and scanning electron microscopes (SEMs) have minimum resolution diameters of approximately 0.2 to 30 nm [141].

3.2.3 Electron Beam Damage

Incident ionising radiation damage is covered in section 1.7. However, A brief overview of incident high-energy electron beam damage is presented. Incident high-energy electrons on a sample cause inelastic scattering, which are exploited and provide useful information, e.g. the detection of secondary electron emissions for SEM imaging. However, the electron beam also results in an undesirable side-effect in the form of radiation damage of the atomic lattice. The magnitude of radiation damage is dependent on the electron kinetic energy and TID. There are three primary forms of radiation damage as a result of incident high-energy electrons, namely radiolysis, sputtering and heating. Radiolysis is the physical breaking of chemical bonds as a result of inelastic scattering effects; sputtering is the atomic lattice displacement of atoms and potential discharge of an atom; and atomic lattice heating is the result of phonon generation, collective excitation or vibration of atoms. Phonon generation as a result of an incident high-energy electron beam causes the medium to heat up and induces phonon scattering. [141]

3.3 Experimental Method

3.3.1 Scanning Electron Microscope

For the investigation of the detection of accelerated electrons using CMOS SPADs, it was decided to use an electron beam found within an EM, as the electron beam is

focusable, and the electron beam kinetic energy is comparatively low, keV range. An electron beam with kinetic energies in the keV range was favoured, to minimize potential radiation damage to the SPAD. The two most common electron microscope types are TEMs and SEMs, and a combination of the two are known as a scanning transmission electron microscope (STEM). TEMs are often used for 2D imaging, as the image is viewed in transmission, whereas SEMs provide a raster-scanned 3D image of the sample surface topography, as the electrons interact with the atoms in the sample surface and resulting radiative electrons are detected. [141]

Figure 3.6 provides a simplified illustration of the interaction of an incident electron beam on a sample surface showing the elastic backscattered (BS) electrons, inelastic secondary electrons as a result of charge generation and recombination, and radiative Bremsstrahlung photons and characteristic X-rays. Characteristic X-rays emission is the result of outer-shell electrons filling lower-shell electron vacancies as a result of lower-shell electron emission due to inelastic scattering. TEMs have accelerating electron energies up to 300 keV, while SEMs limit the range up to 30 keV to prevent sample surface damage, particularly for biological samples. [141]

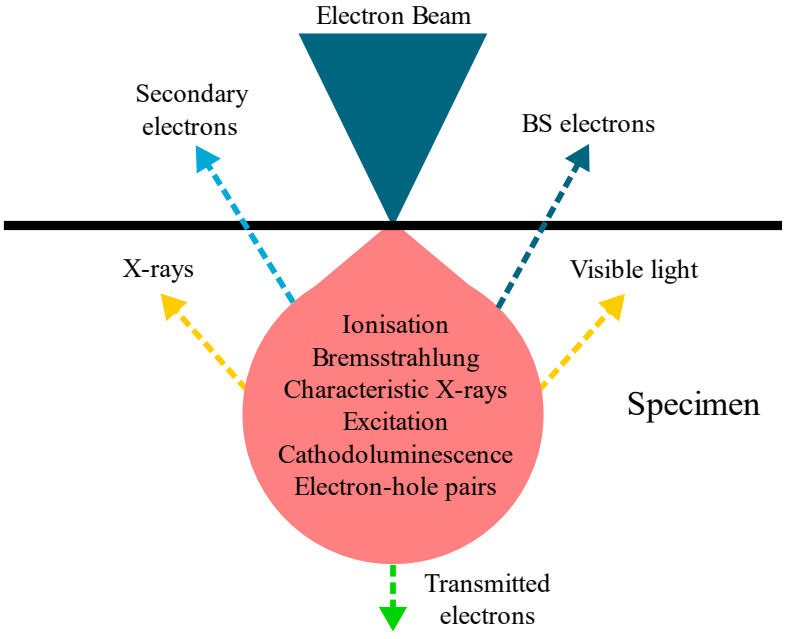

Figure 3.6. Schematic illustration of the interaction of incident accelerated electrons on a sample surface for electron microscopy.

For the experiment and with the unknown radiation hardness of the MINI3D SPAD image sensor it was decided to use a SEM as the primary electron source. The electron microscope chosen was the Tescan Vega 3, a tungsten heated filament SEM, intended for both high- and low-vacuum microscopy with an electron beam energy range from 200 eV to 30 keV. The SEM is configured with an XM (extra-large) chamber with a 5-axis fully motorised x, y, z, rotation and tilting stage, with inner dimensions 13 × 13 × 10 cm^3. The best achievable resolution is 3 nm at an electron beam energy of 30 keV in high-vacuum mode with pressure < 9 mPa. An image of the Tescan Vega 3 SEM used is shown in Figure 3.7.

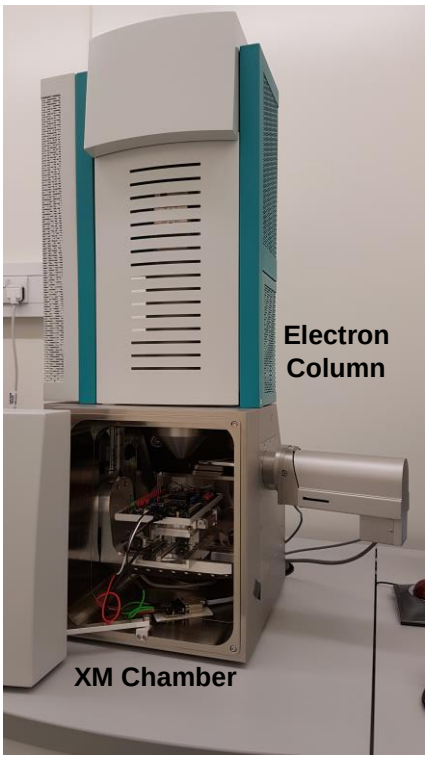

Figure 3.7. Tescan Vega 3 SEM showing electron beam column, XM chamber and SPAD image sensor with operational circuitry.

Before testing could begin an electric feedthrough was installed on the SEM and provided a 15-way D-Sub connector interface, as shown in Figure 3.8. The MINI3D SPAD image sensor FPGA and breakout board were placed inside the SEM vacuum chamber, where the SPAD image sensor interfaces using an FPGA, which requires a USB 3.0 and DC power connection. Therefore, two complimentary PCB circuits were manufactured to interface a computer to the FPGA via the D-Sub connectors to enable

data collection. The PCB layouts are shown in Figure 3.9 with the pin D-Sub connector on the left and socket D-Sub connector on the right.

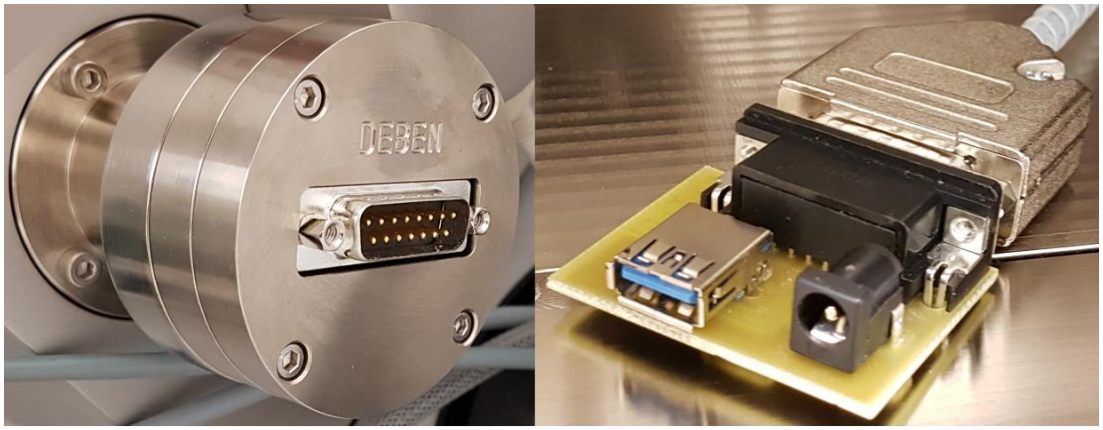

Figure 3.8. (a) External 15-way pin D-sub connector. (b) Internal 15-way socket D-sub connector.

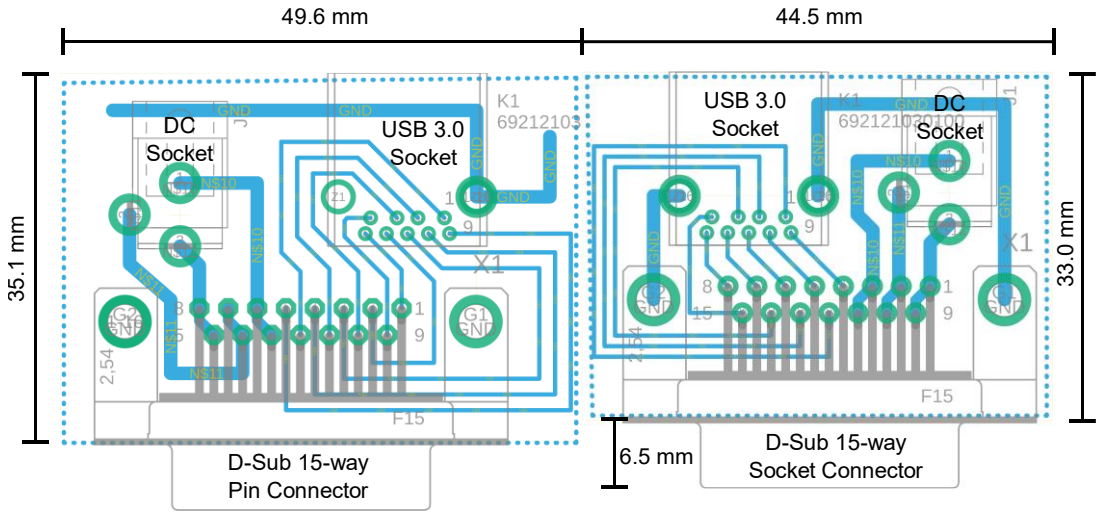

Figure 3.9. 15-way D-Sub connector PCB layouts for pin and socket connector, with USB 3.0 socket connector and DC power socket.

3.3.2 SPAD Image Sensor

From section 2.2 the MINI3D SPAD image sensor was used for the following experiments. The SPAD is a 3D-stacked BSI sensor designed for SPC and time resolved imaging and comprises a 128 × 120 pixel array with a pixel pitch of 7.83 µm and fill factor of 45 %. Each pixel has a dedicated 12-bit ripple counter providing a binning capacity for 4096 photon counts [1]. With BSI the incident material for the accelerated electrons is silicon, furthermore, the top tier of the SPAD image sensor was wafer etched to reduce the amount of bulk silicon required for incident photons to

reach the depletion region, however, the finished thickness of the top tier wafer is undisclosed to the author. [7]

For the detection of accelerated electrons, the operation of the detector depends on the interaction and transfer of energy to the electrons within the depletion region of the SPAD pixel. Therefore, an investigation of accelerated electron energy loss and total stopping power is given in section 3.1.3 and the linear stopping lengths for several materials including silicon is shown in Figure 3.3. Therefore, as the SEM is limited to maximum electron kinetic energy of 30 keV, Table 3.3 provides the approximate linear stopping lengths in silicon for accelerated electrons with kinetic energies from 10 to 30 keV, using the continuous slowing down approximation (CSDA) data in [148] and known density of silicon in Table 3.2. From the table the maximum linear stopping length is approximately 9.91 µm in silicon at an electron kinetic energy of 30 keV.

Table 3.3. Approximate Linear Stopping Lengths for Accelerated Electrons Incident upon Silicon.

Kinetic Energy (keV)	Total Stopping Power ($MeV \cdot cm^2/g$)	CSDA Range (g/cm^2)	Approximate Linear Stopping Length (µm)
10	16.90	3.461×10^{-4}	1.486
15	12.52	6.946×10^{-4}	2.982
20	10.11	1.142×10^{-3}	4.903
25	8.564	1.682×10^{-3}	7.222
30	7.487	2.308×10^{-3}	9.910

3.4 Experimental Results

For the operation of the SPAD image sensor, four distinct operational bias voltages were selected, namely 12.5, 13, 14 and 15 V. For image capture, 400 frames were collected for each electron irradiation, with a constant exposure time of 1 ms. The electron beam within the SEM is raster scanned, with an adjustable scanning speed in steps from 20 ns to 10 ms per pixel with image size of 1024 × 768 pixels. For all the experimentation the scanning speed was set to 3.2 µs/pixel. Figure 3.10 shows a SEM image of the SPAD image sensor die at 5 keV mounted within the 68-pin ceramic pin grid array (CPGA) package. The SEM used is placed in a class 10 clean room at the Scottish Microelectronics Centre (SMC) at The University of Edinburgh, King's

Buildings. The cleanroom has a controlled temperature of 21 (± 1) °C and a relative humidity of 40 (± 5) % [154].

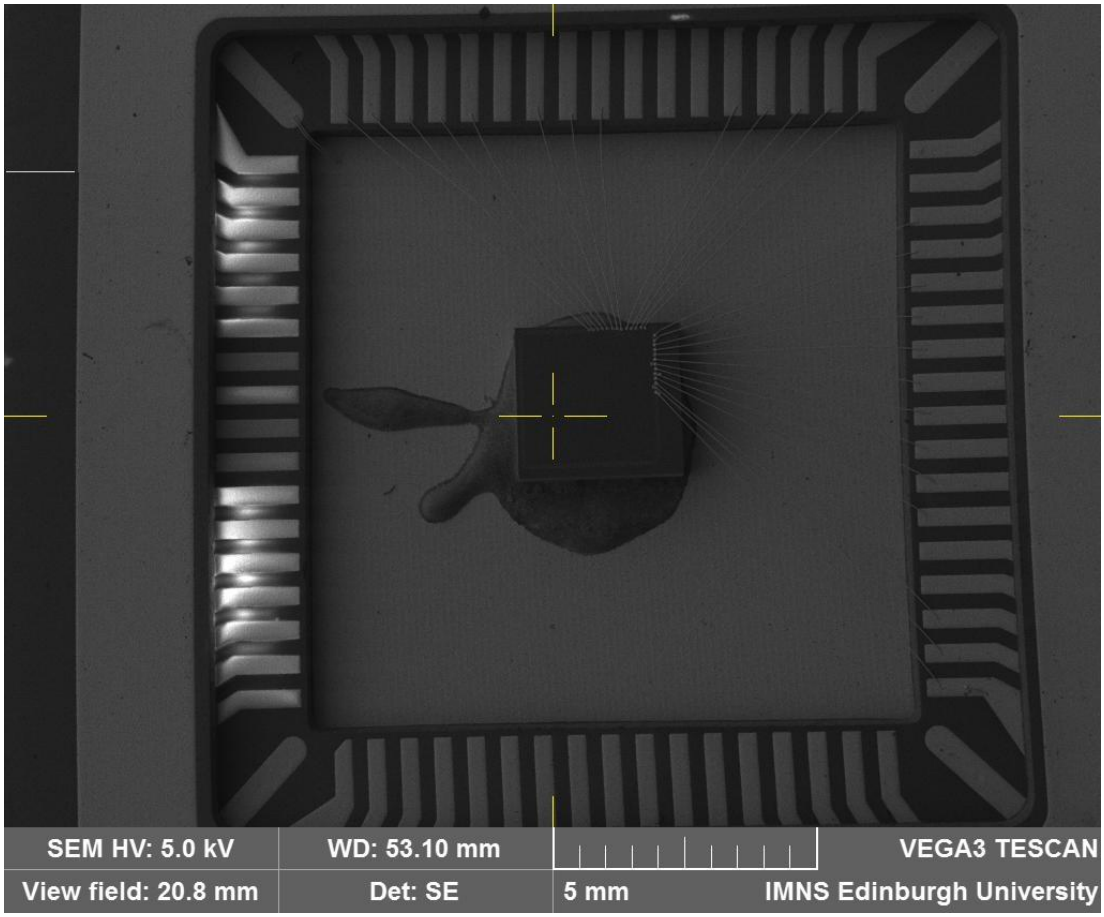

Figure 3.10. SEM image of MINI3D CMOS SPAD image sensor, with die mounted in a 68-pin CPGA package with gold wire bonds.

3.4.1 Time-Resolved Imaging of Accelerated Electron Beam

The first experiment was time-resolved imaging of the accelerated electron beam over the entire SPAD image sensor, with a field of view larger than the image sensor itself. The image sensor was irradiated with a range of electron kinetic energies from 5 to 30 keV (5 keV increments) with both a constant field of view and working distance (WD). Figure 3.11 shows a SEM image of the SPAD image sensor die at 20 keV at a WD of 58.58 mm and field of view of 1.85 mm, and 4:3 aspect ratio.

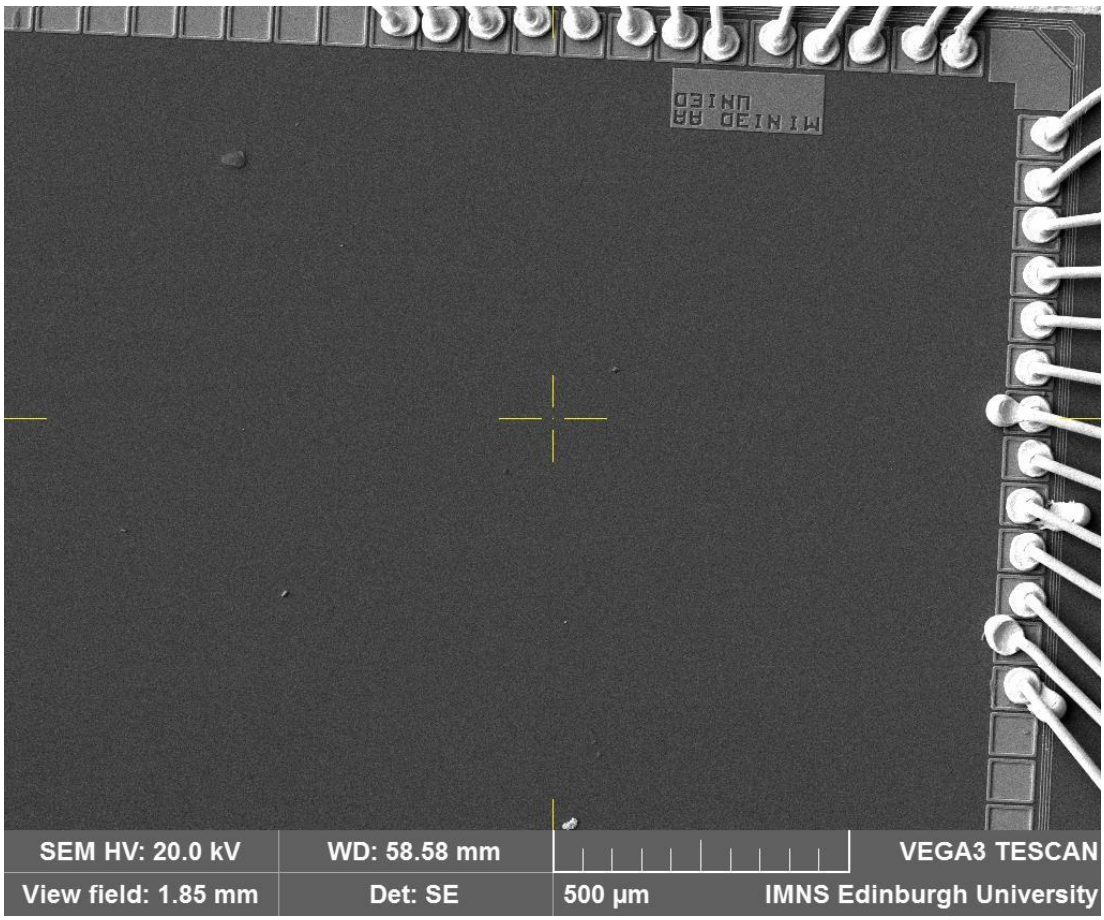

Figure 3.11. SEM image of MINI3D CMOS SPAD image sensor at electron kinetic energy of 5 keV.

The experiment provides time resolved imaging, frame by frame imaging to track the raster scanned electron beam when incident over the image sensor. Before and after irradiation a control measurement is taken, 1000 frames each, for comparison and used to identify high dark count rate (HDCR) pixels. Figure 3.12 shows the average DCR across the MINI3D SPAD image sensor 128 × 120 pixel array, for each select bias voltage, where the HDCR pixels can be identified. Furthermore, it is observed that with increasing bias voltage there is increase in HDCR as expected [7]. The measured average DCR is approximately 0.285, 3.377, 9.956 and 29.16 counts/pixel (kHz) at 12.5, 13, 14 and 15 V respectively, over 1000 frames.

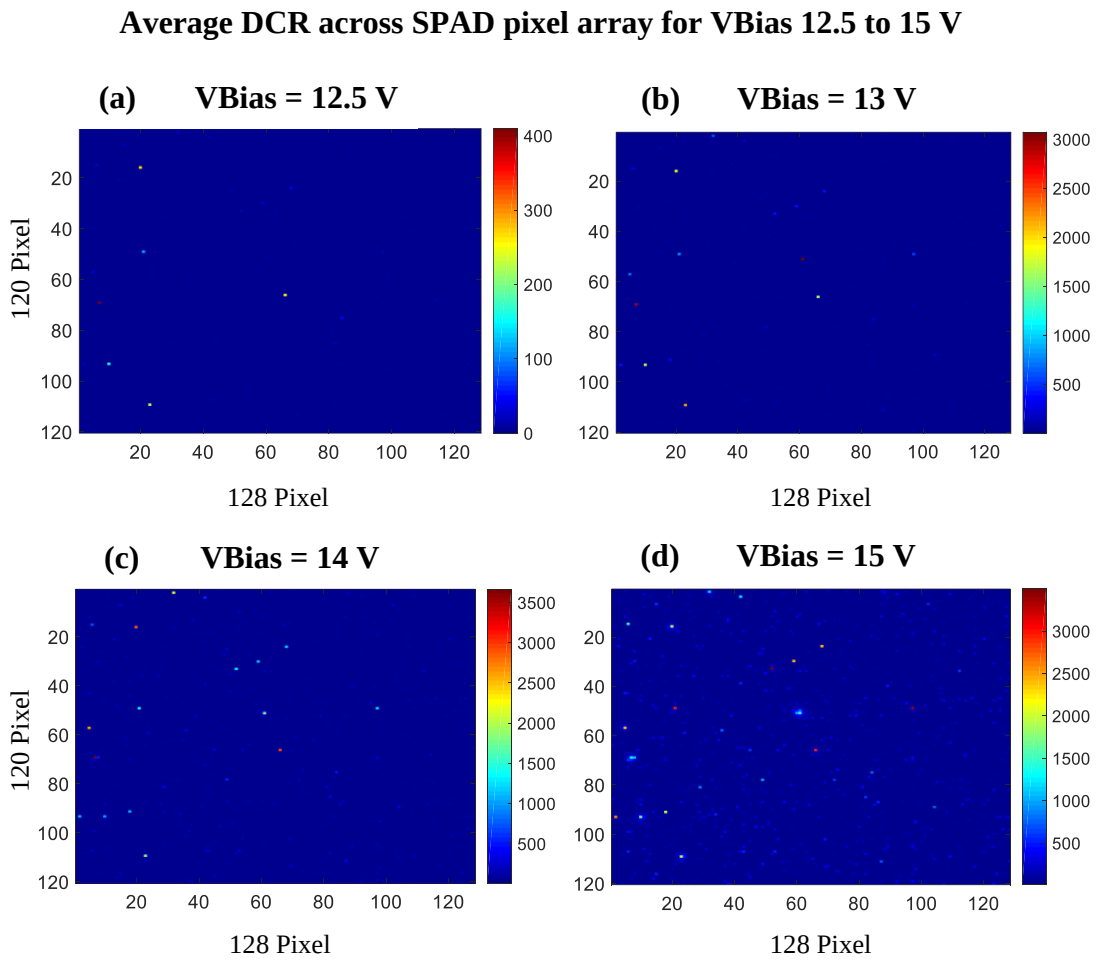

Figure 3.12. Average DCR across the MINI3D CMOS SPAD image sensor, 128 × 120 pixel array, for selected excess bias voltages namely, (a) 12.5 V, (b) 13 V, (c) 14 V and (d) 15 V over 1000 frames at a set exposure time of 1 ms per frame.

With a known pixel pitch of 7.83 µm, field of view of 1.85 mm and raster scan speed of 3.2 µs/image-pixel it is determined that with a set exposure time of 1 ms, the raster scan should irradiate a width of approximately 565 µm or 72 pixels across. For each irradiation 400 frames were taken at each selected bias voltage at varying electron kinetic energies from 5 to 30 keV, at 5 keV increments. Therefore, a total of 24 data sets were collected. Figure 3.13 shows a select frame for each irradiation with electron kinetic energies from 15 to 30 keV at SPAD bias voltage of 12.5 V. Each frame shows the detection of the incident accelerated electron beam, confirming the detection of accelerated electrons with kinetic energies from, but not limited to, 15 to 30 keV. Furthermore, time-resolved imaging of the electron beam and the frames show the raster scan pattern of the SEM, with an approximate irradiation exposure length of 70

pixels as calculated. However, no discernible detection was found at 5 and 10 keV with SPAD bias of 12.5 V. Figure 3.14 to Figure 3.16 show the select frames for each irradiation at varying electron kinetic energies from 15 to 30 keV for SPAD bias voltage of 13 V, 14 V and 15 V respectively.

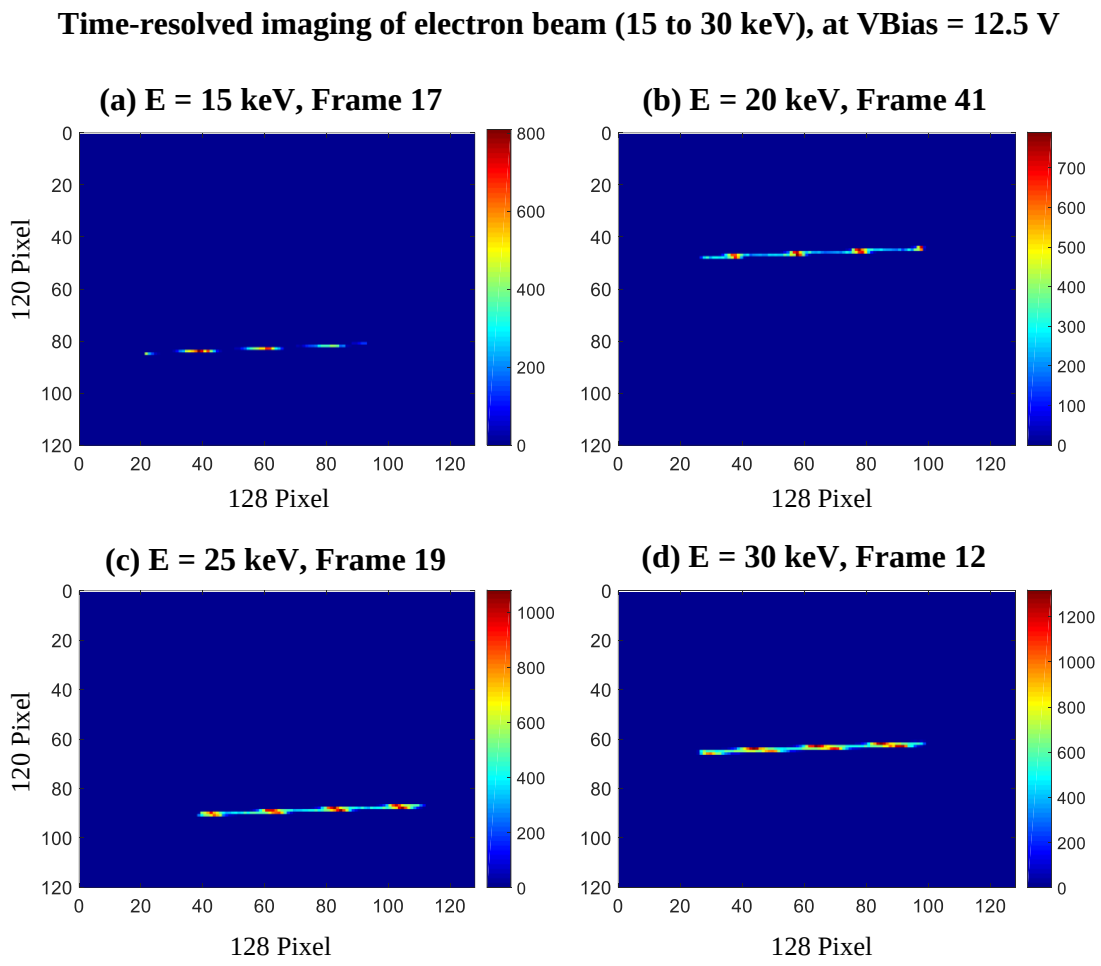

Figure 3.13.Time-resolved imaging of the SEM raster scan electron beam incident across the MINI3D SPAD image sensor array measured in counts, at SPAD bias voltage of 12.5 V. Electron beam kinetic energy (a) 15 keV, (b) 20 keV, (c) 25 keV and (d) 30 keV respectively. Frame exposure time 1 ms.

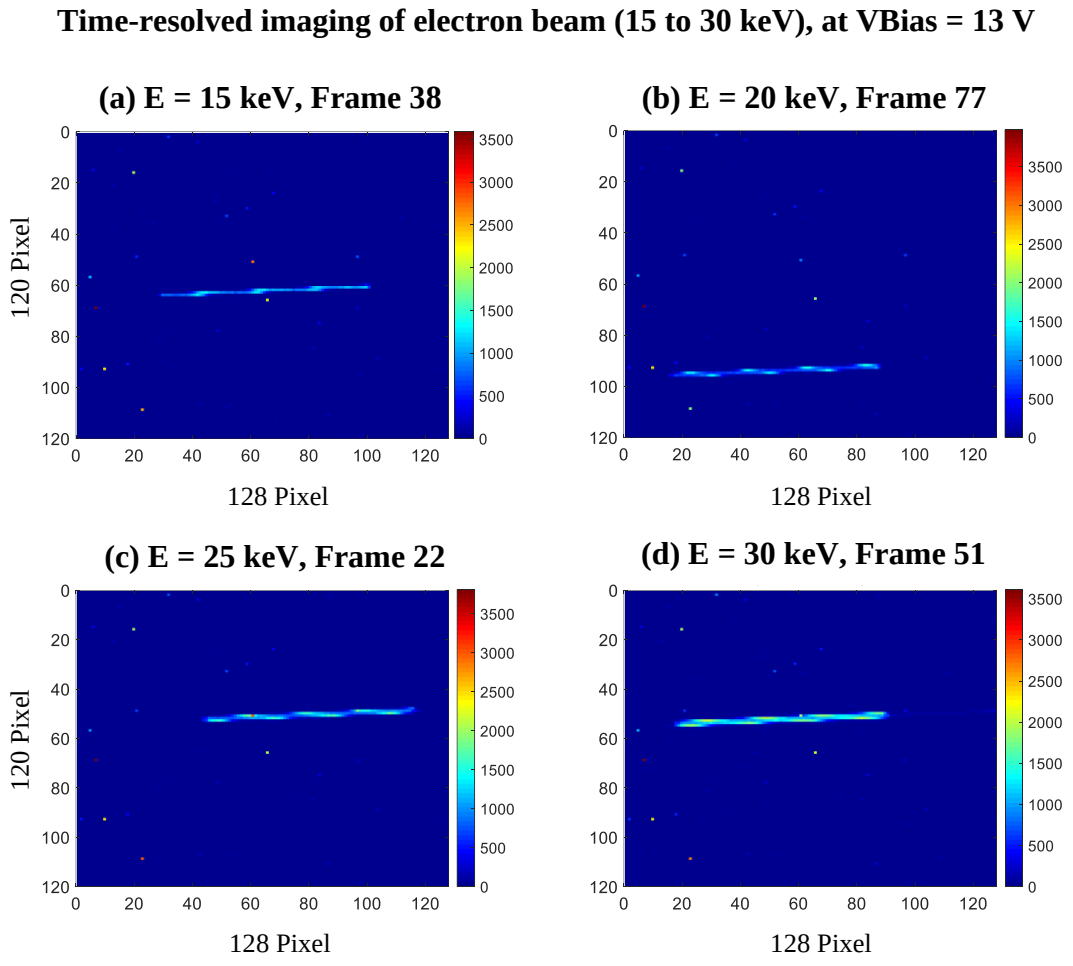

Figure 3.14. Time-resolved imaging of the SEM raster scan electron beam incident across the MINI3D SPAD image sensor array measured in counts, at SPAD bias voltage of 13 V. Electron beam kinetic energy (a) 15 keV, (b) 20 keV, (c) 25 keV and (d) 30 keV respectively. 1 ms frame exposure.

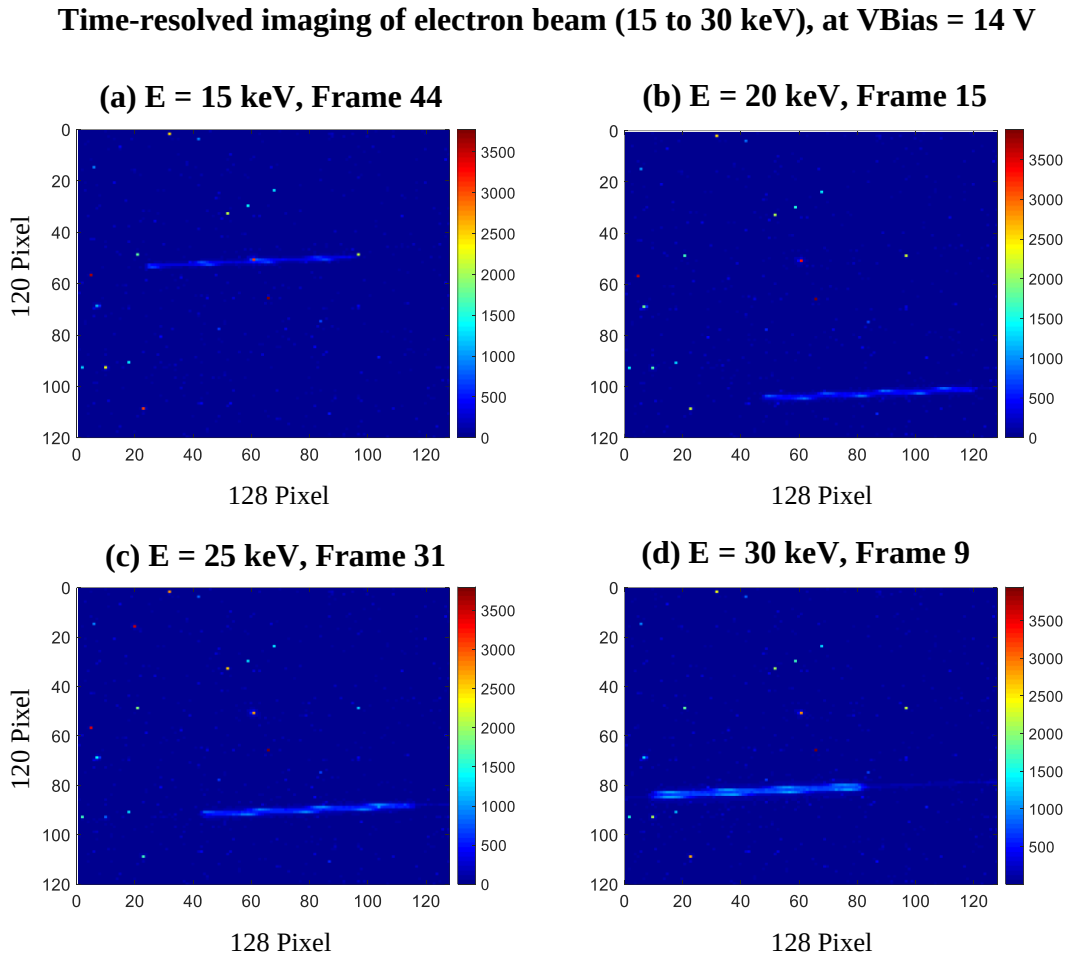

Figure 3.15. Time-resolved imaging of the SEM raster scan electron beam incident across the MINI3D SPAD image sensor array measured in counts, at SPAD bias voltage of 14 V. Electron beam kinetic energy (a) 15 keV, (b) 20 keV, (c) 25 keV and (d) 30 keV respectively. 1 ms frame exposure.

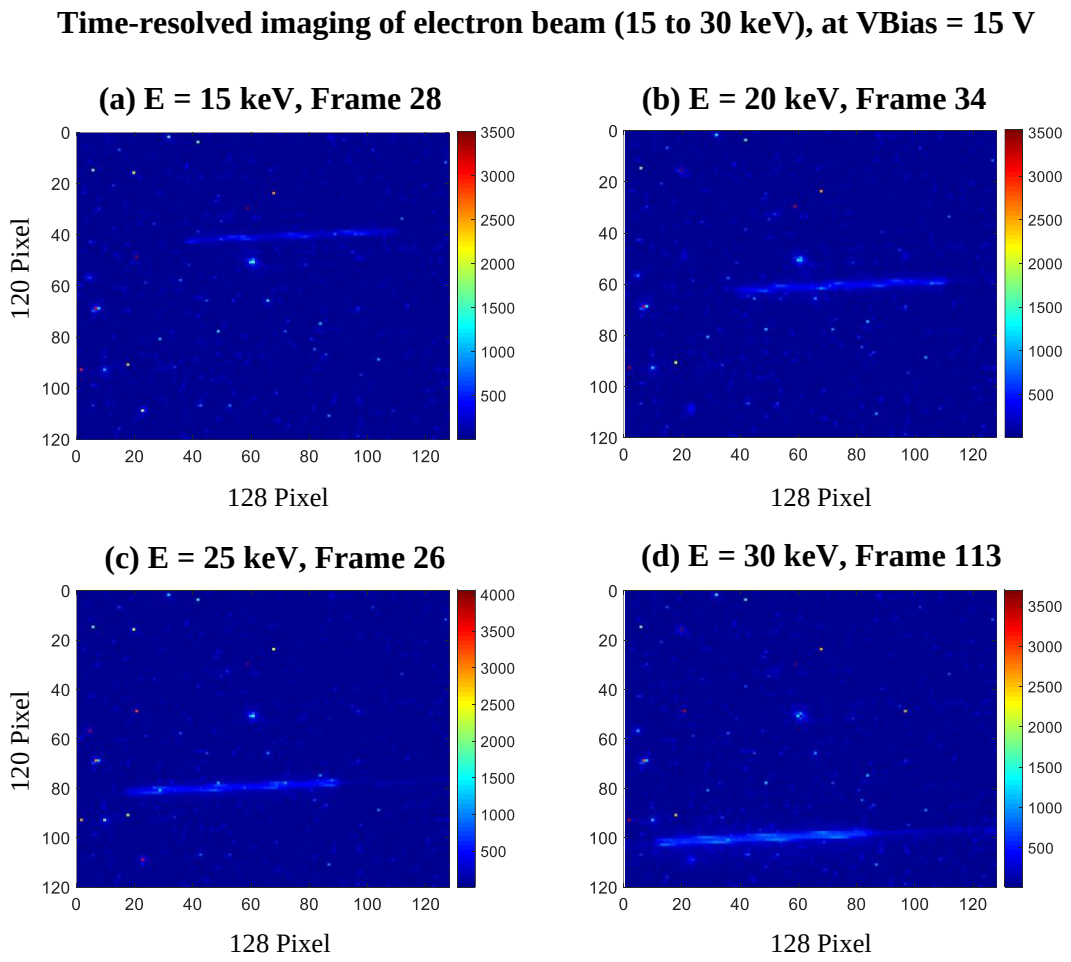

Figure 3.16. Time-resolved imaging of the SEM raster scan electron beam incident across the MINI3D SPAD image sensor array measured in counts, at SPAD bias voltage of 15 V. Electron beam kinetic energy (a) 15 keV, (b) 20 keV, (c) 25 keV and (d) 30 keV respectively. 1 ms frame exposure.

For all time-resolved electron irradiations, electrons were only detected with electron kinetic energies from 15 to 30 keV for all SPAD bias voltages, except at 10 keV with SPAD bias voltage of 15 V, shown in Figure 3.17, where the SEM raster scan electron beam can partially be seen. Furthermore, with comparison of Figure 3.13 with Figure 3.16 it is observed that an increase in electron kinetic energy, results in an increase in surrounding pixel activity because of increased radiative processes.

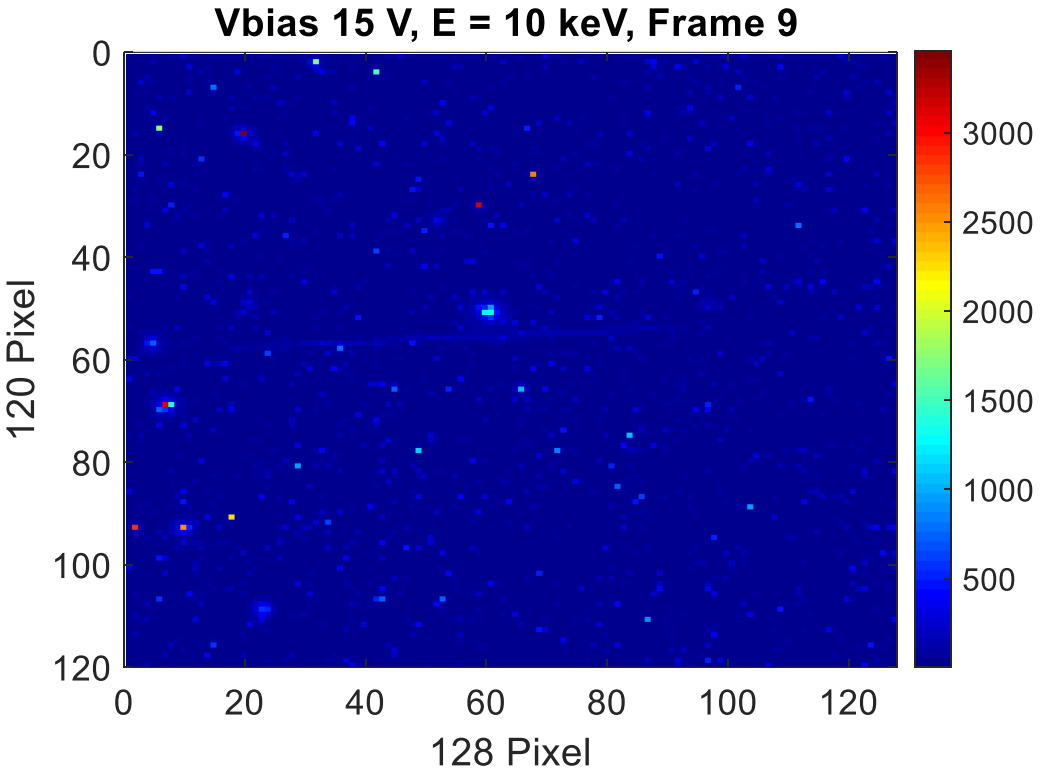

Figure 3.17. Time-resolved image of SEM raster scan electron beam incident across the MINI3D SPAD image sensor array measured in counts, at SPAD bias voltage of 15 V with electron beam kinetic energy of 10 keV. Frame exposure time of 1 ms used.

Figure 3.18 shows the distribution of average DCR per pixel across the SPAD image sensor over 1000 frames at SPAD bias of 15 V, which shows a positive skew as a result of HDCR pixels. Figure 7.1 in the appendix presents a sample of individual pixel DCR distributions from the SPAD image sensor, at SPAD bias voltage of 15 V, which shows that the DCR for each pixel is normally distributed. The calculated mean from Figure 3.12 at SPAD bias voltage of 15 V is 29.16 counts/pixel, however, if you look at the average DCR distribution per pixel in Figure 3.18 the HDCR pixels positively skew the distribution. Therefore, with the control data sets taken before irradiation, the standard deviation and mean for each pixel is calculated, to allow identification and removal of HDCR pixels.

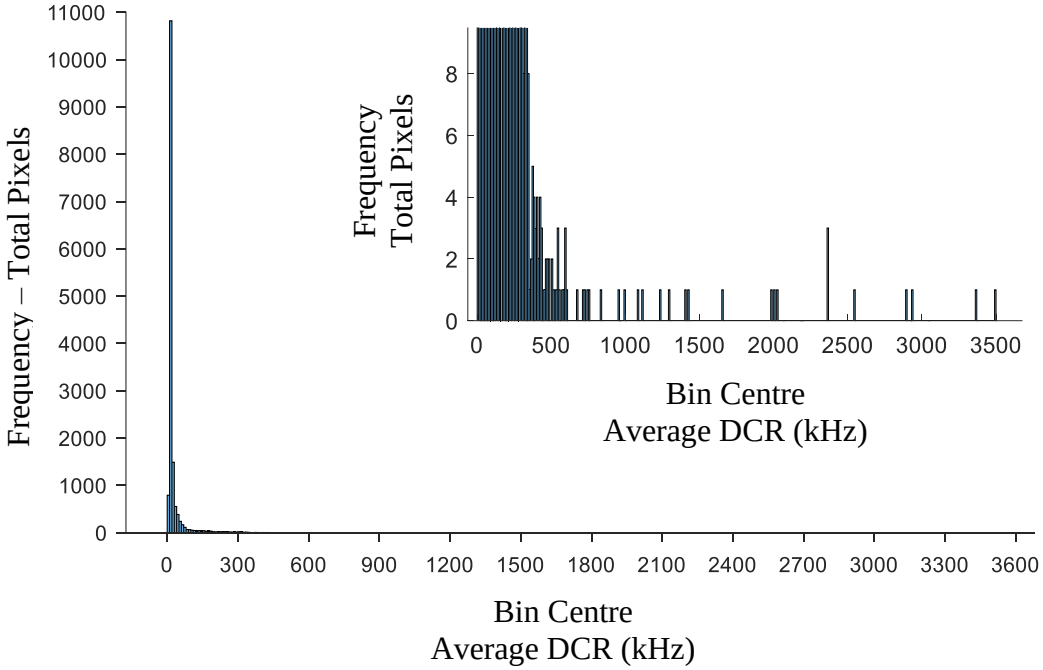

Figure 3.18. Histogram distribution of the average DCR for each pixel across the SPAD image sensor vs the frequency of total pixels, at SPAD bias voltage of 15 V.

With the mean and standard deviation of each pixel calculated, the mean and standard deviation of the sample means can be calculated. Thereafter, each pixel mean is compared to the mean of the sample mean and if the pixel mean does not lie within 2 standard deviations, a confidence interval of 95 %, the pixel is flagged as a HDCR pixel. This allows for the filtering of HDCR pixels and will remove spurious counts during analysis of detected accelerated electrons.

Table 3.4 provides the mean ($\bar{x}$) of the sample means and standard deviation ($\sigma_{\bar{x}}$) of the sample means before and after filtering HDCR pixels for comparison, including total HDCR pixels filtered respectively. Figure 3.19 shows the new distribution of average DCR per pixel across the SPAD image sensor with removed HDCR pixels at SPAD bias voltage of 15 V with reduced bin sizes. From

Table 3.4 the removal of the identified HDCR pixels greatly reduces the $\bar{x}$ and $\sigma_{\bar{x}}$ and the distribution in Figure 3.19 is more normally distributed.

Table 3.4. Mean of the Sample Means ($\bar{x}$) and Standard Deviation of the Sample Means ($\sigma_{\bar{x}}$) before and after filtering HDCR pixels, at SPAD bias voltage of 12.5, 13, 14 and 15 V.

Statistical function (cps or Hz)	SPAD bias voltage			
	12.5 V	13 V	14 V	15 V
$\bar{x}$	284.7	3377.3	9956.1	29156.8
$\bar{x}$ after HDCR pixels removed	162.7	2069.6	6939.7	21186.1
$\sigma_{\bar{x}}$	5160.9	47991.7	66227.6	89287.2
$\sigma_{\bar{x}}$ after HDCR pixels removed	628.5	6702.6	15009.1	24302.3
Total HDCR pixels	28	27	103	282
% of HDCR pixels	0.182 %	0.176 %	0.671 %	1.836 %

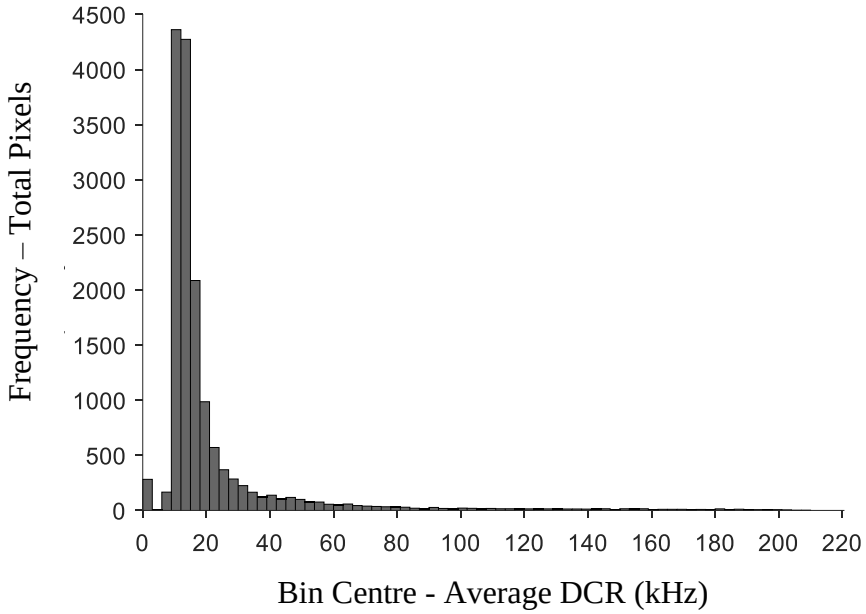

Figure 3.19. Sample distribution of the mean DCR for each pixel across the SPAD image sensor vs the frequency of total pixels after HDCR pixels filtered. SPAD bias voltage of 15 V.

For improved analysis and detection integrity during electron beam irradiation a confidence interval of 4σ was selected, using the known normal distribution DCR for each pixel and their calculated mean and standard deviation. Therefore, during electron

beam irradiation for each frame, the pixel count is compared with the pixels' control distribution, and if the count value is larger than 4σ for that respective pixel according DCR $\bar{x}$ and $\sigma_{\bar{x}}$, the value is retained, else rejected to improve signal contrast. With the process of HDCR filtering and 4σ confidence interval processing, the frame in Figure 3.17 was processed and the subsequent result is shown in Figure 3.20. With comparison to Figure 3.17, there is a clear improvement in frame image integrity with a maximum pixel count of 162.5 when compared to 3457 previously, this clearly shows the detection of the SEM raster scan electron beam at kinetic energy of 10 keV.

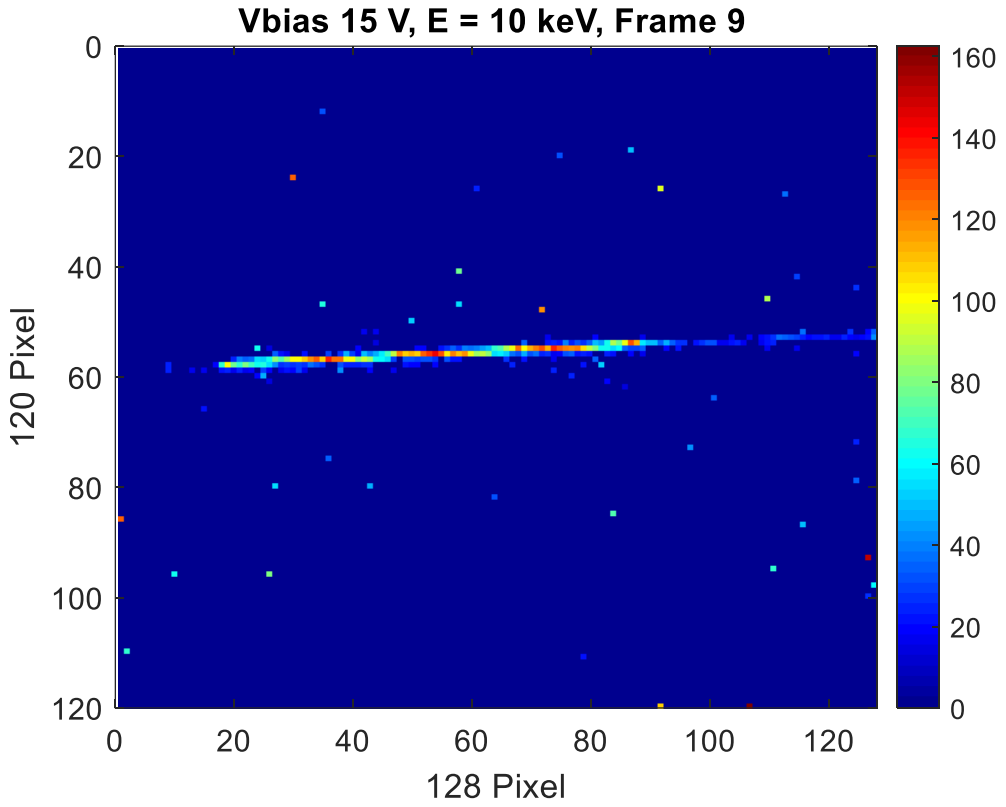

Figure 3.20. Processed time-resolved image of SEM raster scan electron beam incident across the MINI3D SPAD image sensor array measured in counts, at SPAD bias voltage of 15 V with electron beam kinetic energy of 10 keV. Frame exposure time of 1 ms used.

Figure 3.21 provides a 3D rendering for comparison of the frame before and after processing to emphasise the improvement in the detection of accelerated electrons. The following process was repeated for all SPAD bias voltages for electron kinetic energies of 5 and 10 keV to discern if detection is possible. Time-resolved images at varying SPAD bias voltages for each SEM electron beam irradiation after processing is shown in Figure 3.22.

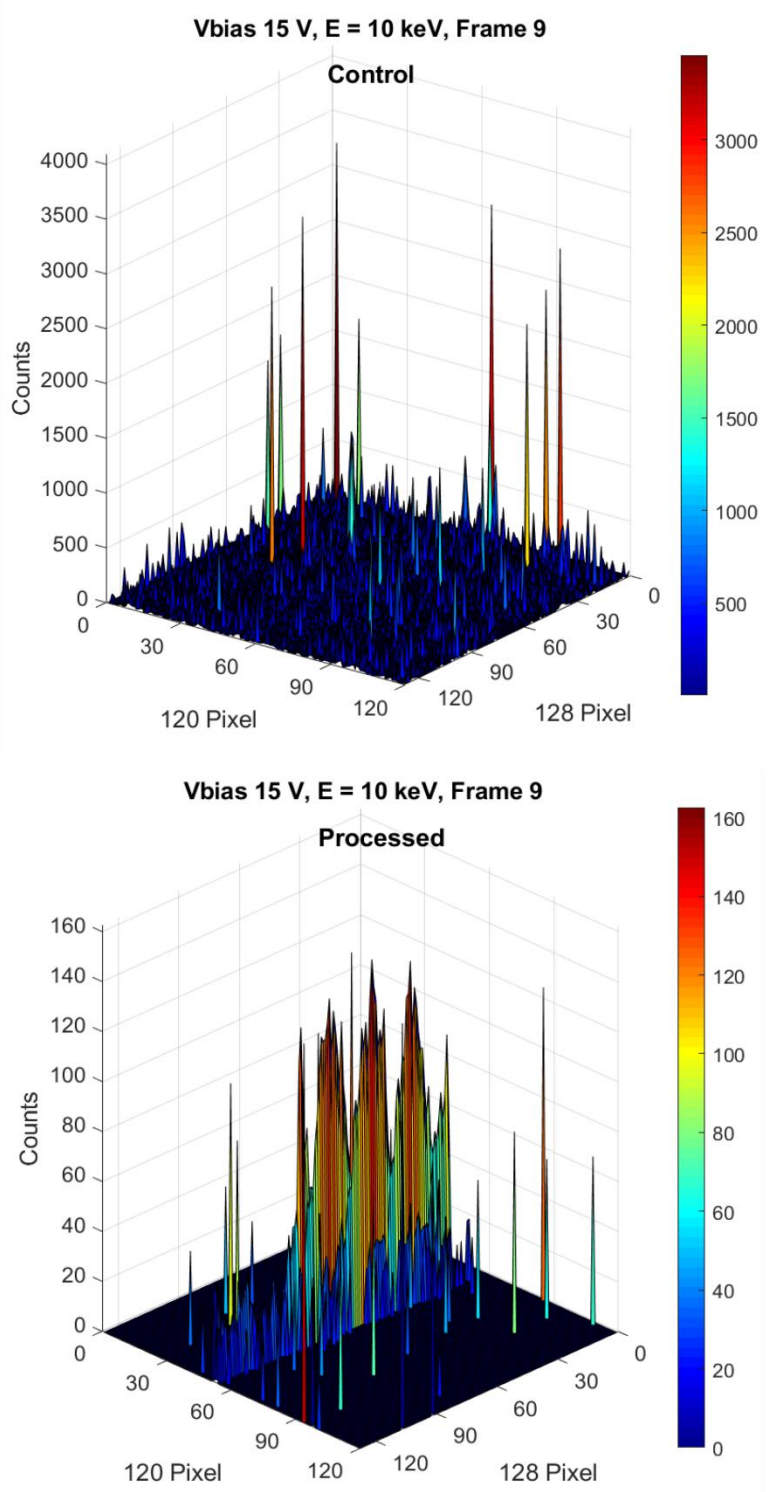

Figure 3.21. 3D comparison of time-resolved image before and after HDCR pixels filtering and 4σ confidence interval processing. At SPAD bias voltage of 15 V and SEM raster scan electron beam energy of 10 keV. Frame exposure time of 1 ms.

After processing, accelerated electron energies at 5 keV were only detectable at a SPAD bias voltage of 13 V shown in Figure 3.22 (a), whereas, accelerated electron energies at 10 keV were detectable at SPAD bias voltages 13 to 15 V. For accelerated electron energies of 5 and 10 keV, no discernible detection was found at SPAD bias voltage of 12.5 V.

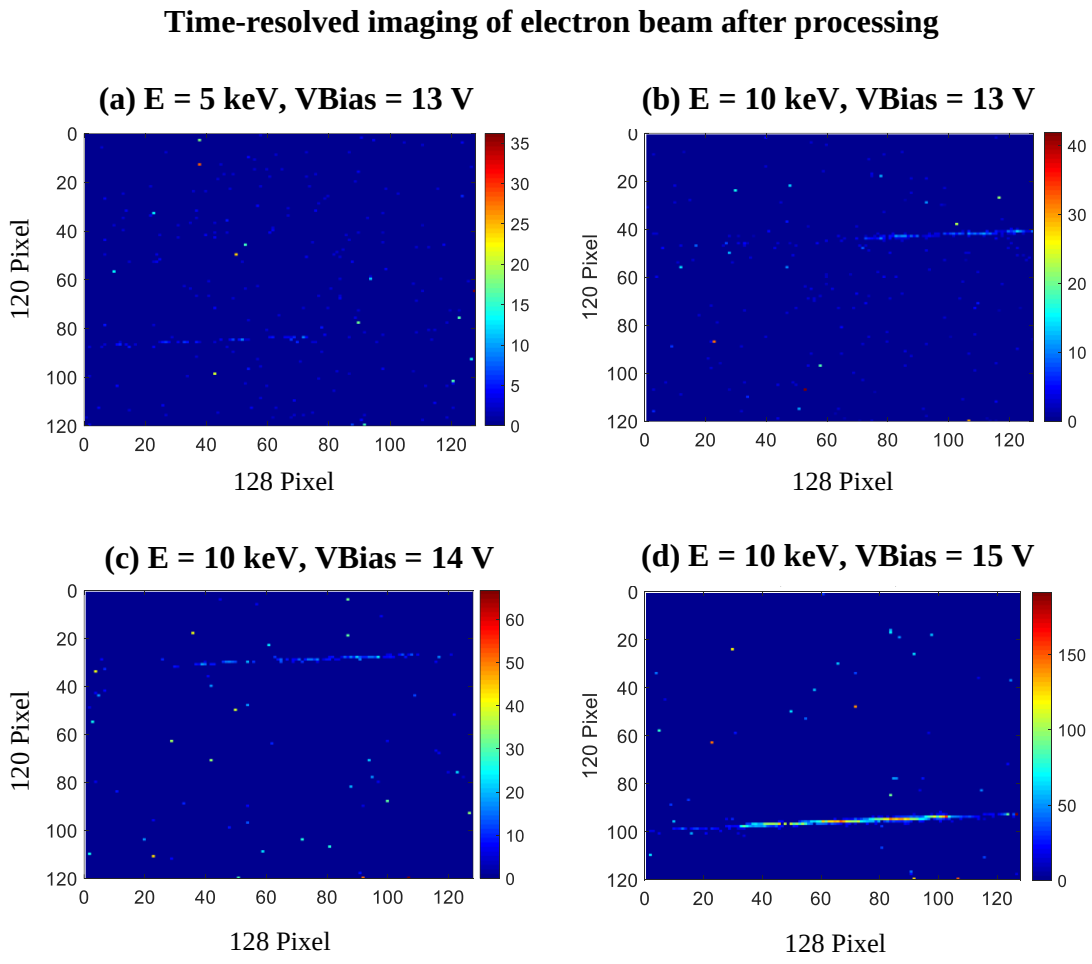

Figure 3.22. Time-resolved imaging of the SEM raster scan electron beam incident across the MINI3D SPAD image sensor array measured in counts after HDCR pixels filtering and 4σ confidence interval processing. At SPAD bias voltage and electron beam kinetic energy (a) Vbias 13 V and E = 5 keV, (b) Vbias 13 V and E = 10 keV, (c) Vbias 14 V and E = 10 keV and (d) Vbias 14 V and E = 10 keV respectively. 1 ms frame exposure.

3.4.2 SPAD Fixed Area Accelerated Electron Irradiation

The following experiment investigates the relationship of SPAD bias voltage and electron kinetic energy on the SPAD output counts per pixel. Therefore, a fixed area on the SPAD image sensor was continuously irradiated to calculate the average counts

per irradiated pixel as a function of both SPAD bias voltage and electron kinetic energy. Figure 3.23 shows the specified area size irradiated, 233.36 × 233.36 μm^2 (~30 × 30 pixels), with all the same beam parameters in the previous experiment namely, WD 58.58 mm, field of view 1.85 mm, scanning speed of 3.2 μs/pixel. The irradiation square was moved for each subsequent increase in electron kinetic energy to minimise any damage or temporary change in DCR for irradiated pixels, that would skew the results.

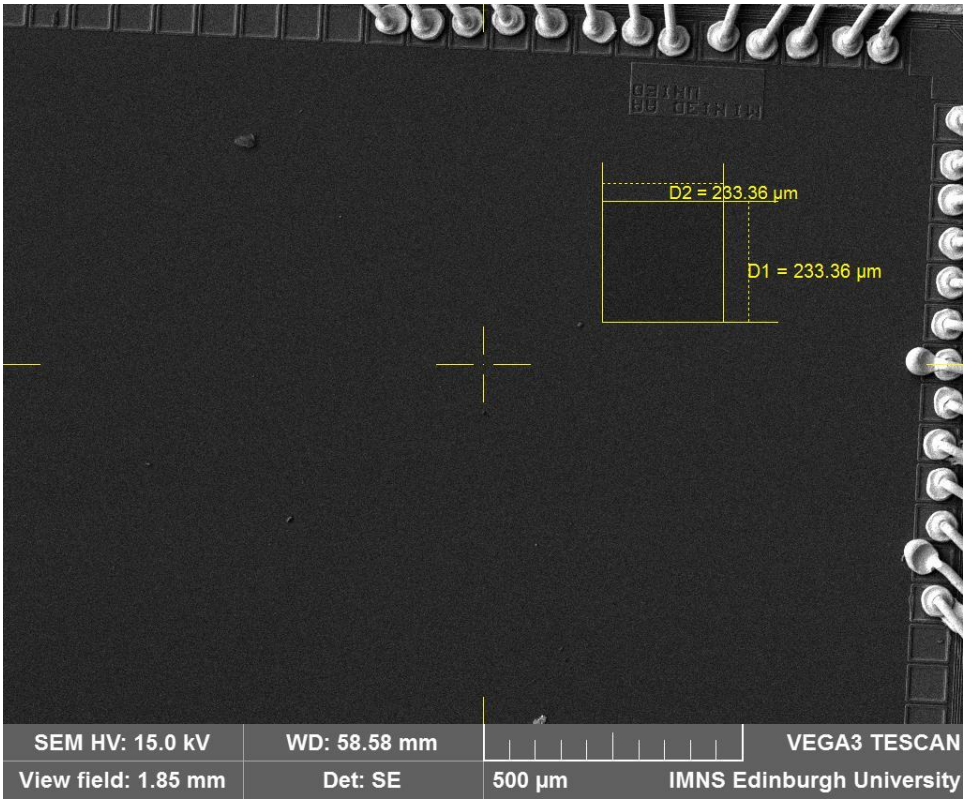

Figure 3.23. SEM image of MINI3D SPAD image sensor at electron kinetic energy of 15 keV, showing fixed area of accelerated electron beam irradiation.

For the following irradiation experiments the image sensor exposure time was kept at 1 ms, and for each irradiation 400 frames were taken at each selected SPAD bias voltage with varying electron kinetic energies from 5 to 30 keV, at 5 keV increments. Therefore, a total of 24 data sets were collected, and for each irradiation HDCR pixel were filtered and 4σ confidence interval processing was used. Figure 3.24 to 3.29 show a select frame (frame 200 was selected for all irradiations) for each SPAD bias voltage of 12.5 V to 15 V at electron kinetic energies 5, 10, 15, 20, 25 and 30 keV respectively during electron beam irradiation.

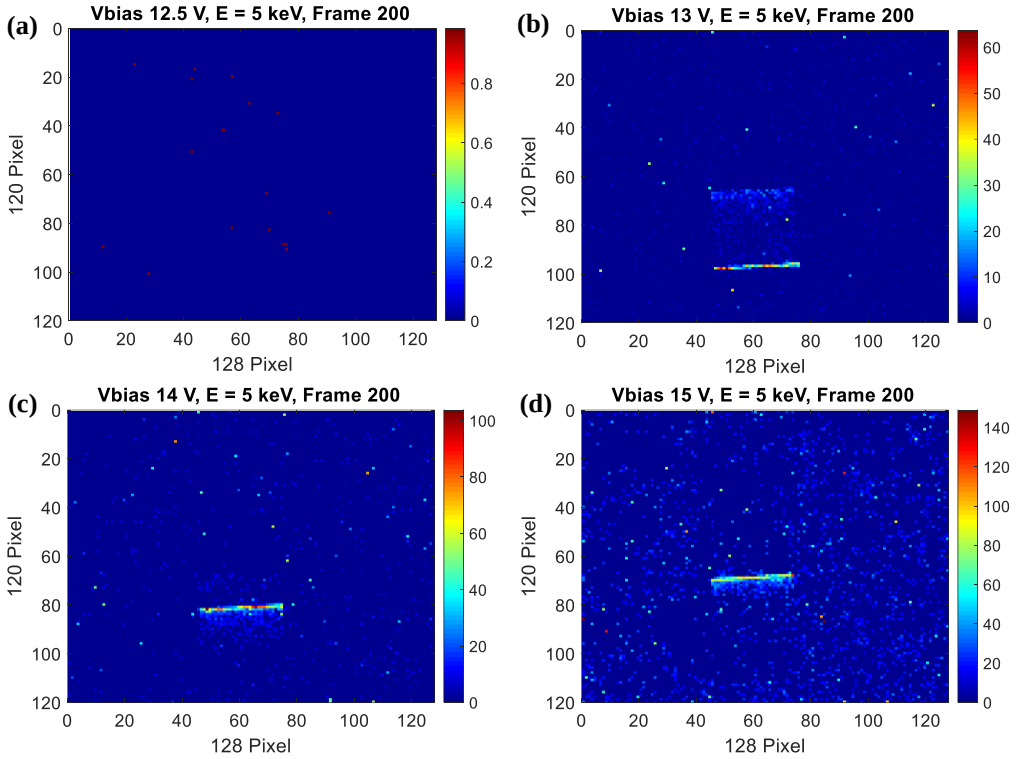

Figure 3.24. Frame 200 of 400 for SPAD bias voltages (a) 12.5 V, (b) 13 V, (c) 14 V and (d) 15 V for fixed electron beam raster scan irradiation area, 233.36 × 233.36 μm^2 (~30 × 30 pixels), at a fixed electron kinetic energy of 5 keV.

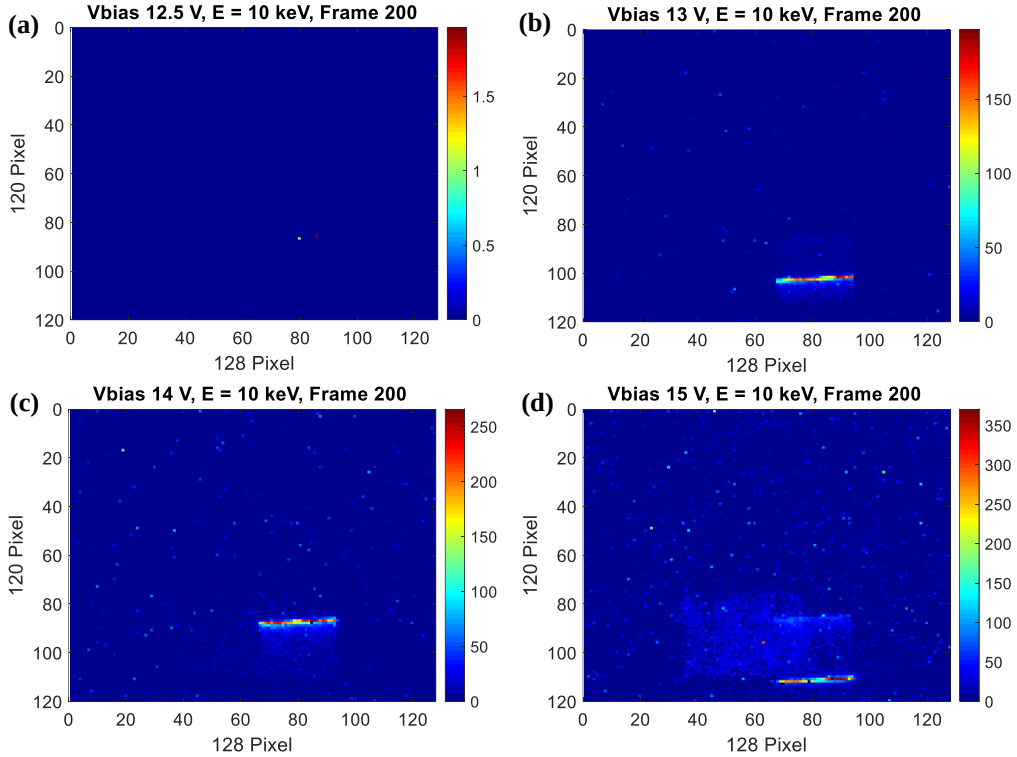

Figure 3.25. Frame 200 of 400 for SPAD bias voltages (a) 12.5 V, (b) 13 V, (c) 14 V and (d) 15 V for fixed electron beam raster scan irradiation area, 233.36 × 233.36 μm^2 (~30 × 30 pixels), at a fixed electron kinetic energy of 10 keV.

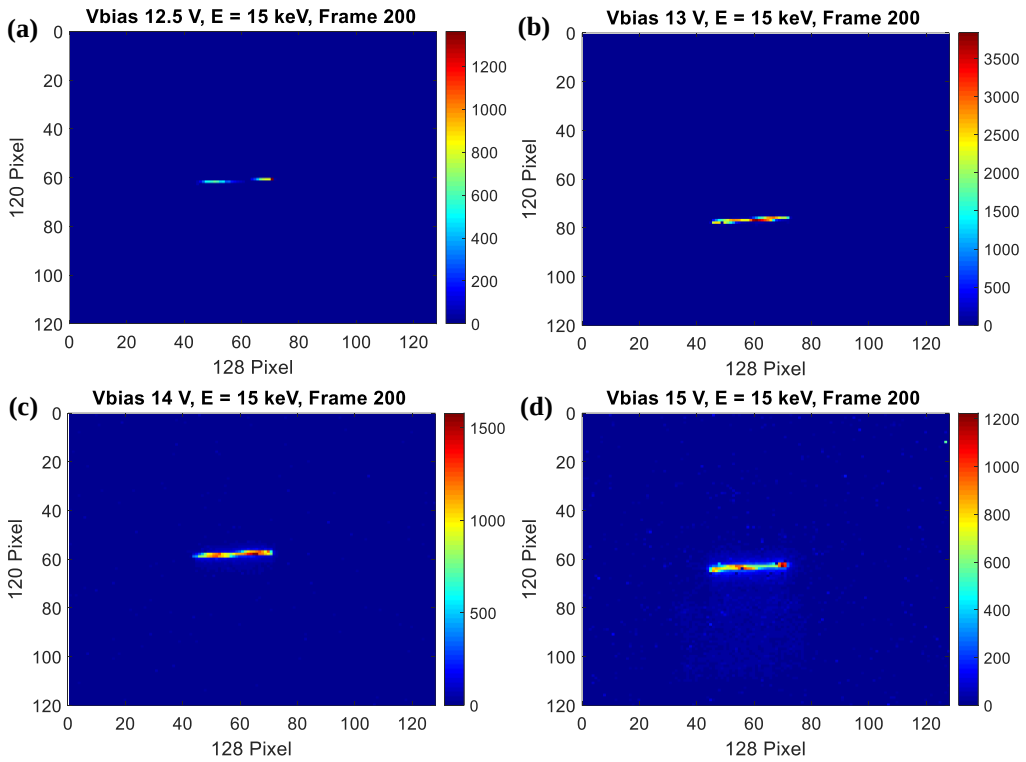

Figure 3.26. Frame 200 of 400 for SPAD bias voltages (a) 12.5 V, (b) 13 V, (c) 14 V and (d) 15 V for fixed electron beam raster scan irradiation area, 233.36 × 233.36 μm^2 (~30 × 30 pixels), at a fixed electron kinetic energy of 15 keV.

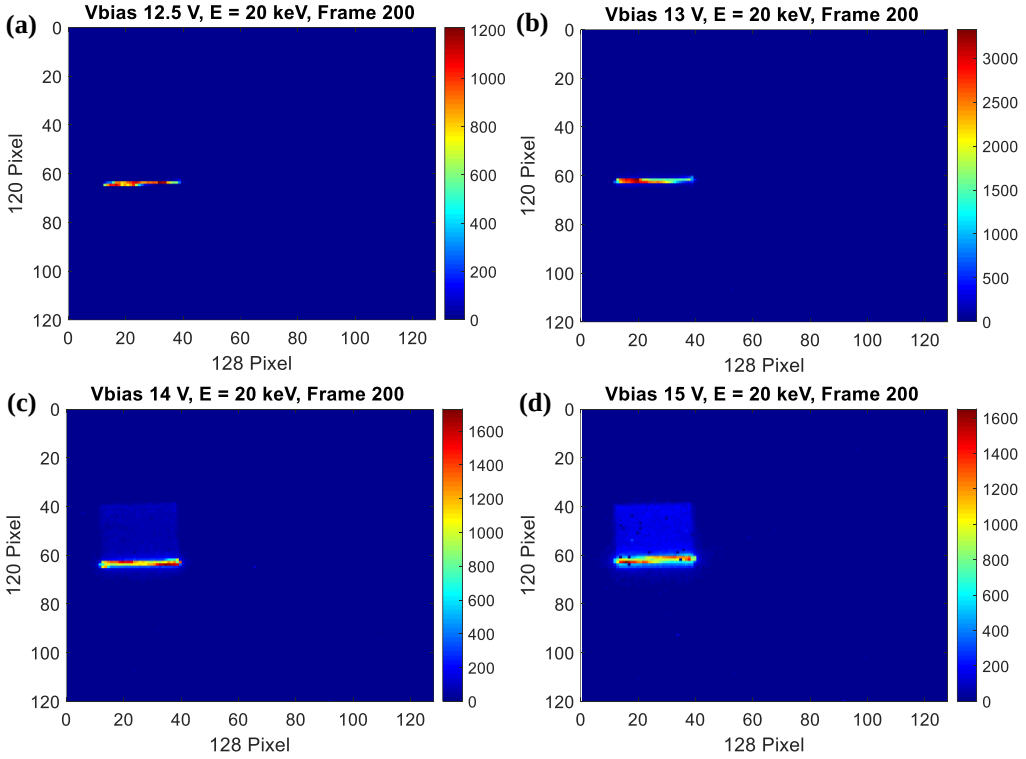

Figure 3.27. Frame 200 of 400 for SPAD bias voltages (a) 12.5 V, (b) 13 V, (c) 14 V and (d) 15 V for fixed electron beam raster scan irradiation area, 233.36 × 233.36 μm^2 (~30 × 30 pixels), at a fixed electron kinetic energy of 20 keV.

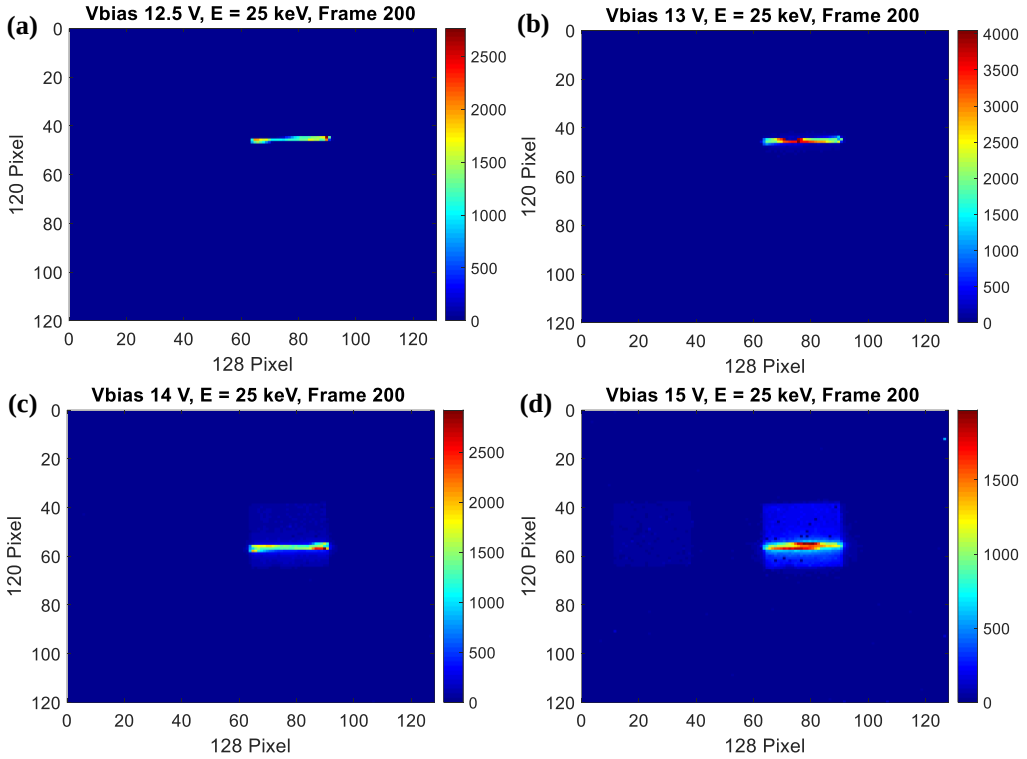

Figure 3.28. Frame 200 of 400 for SPAD bias voltages (a) 12.5 V, (b) 13 V, (c) 14 V and (d) 15 V for fixed electron beam raster scan irradiation area, 233.36 × 233.36 μm^2 (~30 × 30 pixels), at a fixed electron kinetic energy of 25 keV.

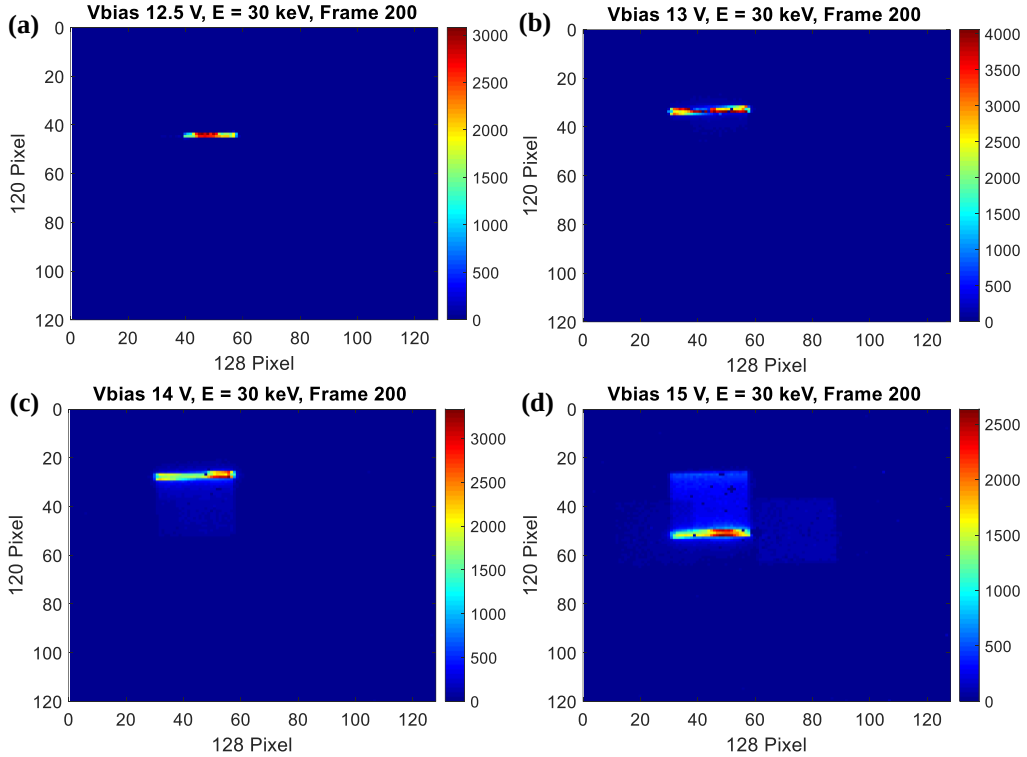

Figure 3.29. Frame 200 of 400 for SPAD bias voltages (a) 12.5 V, (b) 13 V, (c) 14 V and (d) 15 V for fixed electron beam raster scan irradiation area, 233.36 × 233.36 μm^2 (~30 × 30 pixels), at a fixed electron kinetic energy of 30 keV.

From Figure 3.24 to Figure 3.29, it is evident that the raster scan accelerated electron beam is detected, and that a SPAD bias voltage of 13 V results in the highest count sensitivity when compared to bias voltages of 12.5, 14 and 15 V respectively. At a SPAD bias voltage of 12.5 V, electrons are only detected at kinetic energies 15 keV and above. Furthermore, it can be seen in the selected frames that at a SPAD bias voltage of 14 and 15 V for all electron kinetic energies 20 to 30 keV, the previous set of irradiation experiments, result in temporary pixel hysteresis, where the average pixel counts in the previously irradiated area are evidently higher when compared to surrounding non-irradiated pixels. The hysteresis was temporary, a control data set taken approximately 9 min later, after the final irradiation at 30 keV, showed no hysteresis, and no permanent damage was observed.

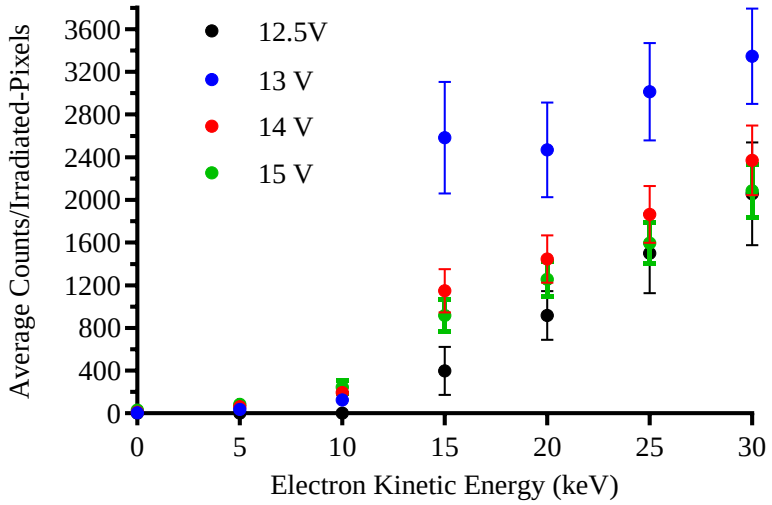

Figure 3.30. Average counts/pixel and standard deviation, for 32 irradiated pixels/frame for 400 frames, as a function of electron kinetic energy, at SPAD bias voltages 12.5 V to 15 V.

For this experiment, the constant raster irradiation and fixed area allows for analysis of the irradiated pixels, approximately 30 pixels irradiated per frame over 400 frames. Figure 3.30 shows the relationship of average counts/irradiated-pixel for each SPAD bias voltages from 12.5 V to 15 V, as a function of electron kinetic energies from 5 to 30 keV, including standard deviation and Table 3.5 provides the respective statistical data. From Figure 3.30 it is evident that an increase in incident electron kinetic energies results in increased average counts, however, the standard deviations overlap in the graph, which means a statistical analysis is required to determine the significance of both SPAD bias voltage and electron kinetic energy on average counts.

Table 3.5. Statistical data in counts for SPAD fixed area accelerated electron irradiation over 400 frames, for varying SPAD bias voltages and varying incident electron kinetic energies.

Spad Bias Voltage	12.5 V						13 V					
Electron Kinetic Energy	5 keV	10 keV	15 keV	20 keV	25 keV	30 keV	5 keV	10 keV	15 keV	20 keV	25 keV	30 keV
Number of values	0	0	4637	6000	5995	5050	5989	6000	6000	6000	6000	5056
						Units in counts						
Minimum	0	0	55.973	509.928	156.993	257.971	8.638	42.678	1309.66	1221.706	1604.651	1417.359
25% Percentile	0	0	214.9885	744.9907	1276.978	1734.72	28.699	92.66475	2209.149	2179.676	2752.757	3009.671
Median	0	0	373.993	868.9725	1482.985	2040.815	36.725	122.739	2465.419	2426.58	2997.737	3418.133
75% Percentile	0	0	541.399	1055.854	1706.985	2355.97	45.568	148.7388	2847.389	2712.602	3265.519	3715.666
Maximum	0	0	1682.972	2627.983	3705.974	3995.974	106.487	319.758	4093.45	4082.587	4094.765	4094.496
Mean	0	0	397.395	918.1276	1499.478	2055.381	37.38044	123.7076	2581.398	2469.5	3014.391	3347.858
Std. Deviation	0	0	224.009	228.133	372.5448	483.1509	12.07517	37.07467	524.8436	444.6627	457.1828	447.2146
Std. Error of Mean	0.0000	0.0000	3.2896	2.9452	4.8115	6.7989	0.1560	0.4786	6.7757	5.7406	5.9022	6.2894
Lower 95% CI of mean	0	0	390.9457	912.3539	1490.045	2042.053	37.16426	122.7694	2568.115	2458.246	3002.821	3335.528
Upper 95% CI of mean	0	0	403.8442	923.9012	1508.91	2068.71	37.59661	124.6459	2594.681	2480.753	3025.961	3360.188
Sum	0	0	1842720	5508766	8989369	10379680	224077	742245.9	15488390	14817000	18086350	16926770

Spad Bias Voltage	14 V						15 V					
Electron Kinetic Energy	5 keV	10 keV	15 keV	20 keV	25 keV	30 keV	5 keV	10 keV	15 keV	20 keV	25 keV	30 keV
Number of values	5984	6000	6000	6000	6000	6000	5805	6000	6000	6000	6000	6000
						Units in counts						
Minimum	16.476	80.74	618.773	881.431	997.214	1234.745	37.167	104.804	510.984	694.831	866.703	1257.231
25% Percentile	49.088	151.6348	1000.576	1282.247	1678.457	2159.648	67.4255	196.6755	811.5662	1137.661	1457.495	1907.177
Median	60.552	193.1455	1127.516	1406.257	1810.636	2305.774	80.767	245.3525	895.3225	1229.172	1560.531	2045.792
75% Percentile	72.509	227.0645	1265.075	1572.465	2002.354	2535.581	94.9575	285.619	1002.237	1352.971	1706.244	2224.889
Maximum	189.19	957.551	2455.798	2668.399	3135.878	3756.693	367.55	531.226	1766.754	2192.497	2987.725	3111.422
Mean	61.43168	193.5339	1149.312	1446.276	1863.488	2371.705	82.57477	245.7594	915.2263	1257.093	1592.969	2085.695
Std. Deviation	17.55368	51.9434	205.4298	221.8314	264.8742	327.7741	20.1047	60.10943	149.093	167.5098	195.0892	247.4599
Std. Error of Mean	0.2269	0.6706	2.6521	2.8638	3.4195	4.2315	0.2639	0.7760	1.9248	2.1625	2.5186	3.1947
Lower 95% CI of mean	61.11737	192.2193	1144.113	1440.662	1856.785	2363.41	82.21206	244.2382	911.453	1252.854	1588.032	2079.432
Upper 95% CI of mean	61.74599	194.8485	1154.511	1451.891	1870.192	2380	82.93748	247.2807	918.9995	1261.332	1597.906	2091.958
Sum	368098.65	1161203	6895873	8677659	11180930	14230230	487397.55	1474557	5491358	7542558	9557815	12514170

To calculate statistical significance between groups the statistical hypothesis student t-test is used [155]–[157], and its result will allow for determining whether the difference in group average counts is statistically significant or not. Therefore, from the results obtained during the fixed area electron irradiation tests, it is hypothesised that an increase in accelerated electron kinetic energy or SPAD bias voltage results in a greater than 2σ significant difference in SPAD pixel average counts. The null hypothesis ($H_{\emptyset}$) for the independent t-test is that an increase in accelerated electron kinetic energy or SPAD bias voltage does not result in a greater than 2σ significant difference in SPAD pixel average counts (μ_x), therefore, for $H_{\emptyset}$, $\mu_1 = \mu_2$. For an independent t-test the following parameters must be true, that the data is normally distributed, randomly sampled and the sample size is suitable. Furthermore, it must be determined if the data is paired or unpaired; if the variance of the data sets are the same; and whether the sample sizes are the same.

From Table 3.5 it is shown that approximately 6000 data points were collected for each irradiation across ~900 pixels. Therefore, there are multiple data readings for multiple pixels, which may not be evenly distributed for each irradiation experiment, as the irradiation data readings from the SPAD image sensor are influenced by many variables, e.g. raster scan pattern, scanning speeds, FPGA read-out speeds and total frames taken for each irradiation experiment. Therefore, a sample of independent irradiated pixels is required, and as each irradiation area was changed for varying electron kinetic energies, the data samples are deemed to be unpaired. Furthermore, for the same reasons mentioned for uneven pixel reading distributions, not all 900 pixels may have irradiation measurements, therefore the sample size for each irradiation is assumed uneven.

From the approximate 6000 data points for each irradiation, a single measurement is taken at random for each irradiated pixel, confirmed using the HDCR pixel filtering and 4σ confidence interval processing. Thereafter, the sample statistical data is calculated and is shown in Table 3.6, where the standard deviations and sample sizes compared are dissimilar, and the standard error of the mean (SE) is calculated using equation 3.15 as follows

$$\sigma_M = \frac{\sigma}{\sqrt{n}} \tag{3.15}$$

where σ_M is the SE, σ the sample standard deviation and n the sample size.

Table 3.6. Statistical data for samples of independent irradiated pixels measured in counts for SPAD fixed area accelerated electron irradiation, for varying SPAD bias voltages and varying incident electron kinetic energies.

Spad Bias Voltage	12.5 V						13 V					
Electron Kinetic Energy	5 keV	10 keV	15 keV	20 keV	25 keV	30 keV	5 keV	10 keV	15 keV	20 keV	25 keV	30 keV
Number of values	0	0	732	736	785	521	882	741	733	745	760	645
						Units in counts						
Minimum	0.000	0.000	59.972	509.928	156.993	257.971	9.745	50.700	1326.649	1221.706	1626.780	1841.639
25% Percentile	0.000	0.000	226.229	725.939	874.984	1740.493	29.594	93.719	2228.172	2167.644	2747.684	3003.149
Median	0.000	0.000	389.868	842.494	1239.987	2019.413	37.746	124.720	2469.660	2389.022	2965.124	3412.244
75% Percentile	0.000	0.000	574.985	1034.966	1582.609	2282.336	45.487	150.493	2816.526	2644.300	3249.636	3702.927
Maximum	0.000	0.000	1638.964	2250.953	3371.988	3510.216	99.487	290.581	4055.652	3888.747	4090.500	4089.710
Mean	0.000	0.000	411.149	899.209	1220.742	1978.931	37.875	124.951	2587.210	2407.698	2986.748	3335.443
Std. Deviation	0.000	0.000	228.127	223.806	500.262	557.408	11.400	38.383	515.513	421.909	466.755	447.999
Std. Error of Mean	0.000	0.000	8.432	8.250	17.855	24.420	0.384	1.410	19.041	15.458	16.931	17.640
Lower 95% CI of mean	0.000	0.000	394.595	883.013	1185.693	1930.957	37.121	122.182	2549.829	2377.353	2953.510	3300.805
Upper 95% CI of mean	0.000	0.000	427.702	915.404	1255.792	2026.905	38.628	127.719	2624.592	2438.044	3019.985	3370.082
Sum	0	0	300960.8	661817.5	958282.8	1031023	33405.5	92588.31	1896425	1793735	2269928	2151361

Spad Bias Voltage	14 V						15 V					
Electron Kinetic Energy	5 keV	10 keV	15 keV	20 keV	25 keV	30 keV	5 keV	10 keV	15 keV	20 keV	25 keV	30 keV
Number of values	875	724	746	744	754	748	863	731	737	722	725	703
						Units in counts						
Minimum	19.024	82.482	626.871	886.422	1016.804	1236.555	38.496	112.804	510.984	694.831	950.740	1294.217
25% Percentile	50.640	147.548	1003.678	1263.501	1666.127	2147.722	68.371	190.721	797.966	1134.766	1431.147	1873.343
Median	61.946	192.203	1129.583	1378.483	1779.021	2268.522	82.278	238.747	878.128	1228.323	1544.558	1998.080
75% Percentile	73.534	226.191	1271.251	1558.317	1957.454	2470.800	97.465	278.075	978.850	1340.831	1704.083	2166.852
Maximum	119.088	459.671	1917.884	2668.399	3101.802	3360.880	174.801	423.807	1511.169	1795.827	2987.725	2884.599
Mean	62.763	191.037	1152.500	1433.810	1836.711	2326.818	84.255	239.711	896.042	1246.544	1581.277	2026.776
Std. Deviation	15.861	52.410	203.090	232.666	264.791	297.558	19.352	57.065	150.340	157.900	209.177	247.130
Std. Error of Mean	0.536	1.948	7.436	8.530	9.643	10.880	0.659	2.111	5.538	5.876	7.769	9.321
Lower 95% CI of mean	61.710	187.213	1137.902	1417.064	1817.781	2305.459	82.962	235.568	885.170	1235.007	1566.025	2008.476
Upper 95% CI of mean	63.815	194.861	1167.097	1450.555	1855.642	2348.177	85.548	243.855	906.913	1258.082	1596.528	2045.075
Sum	54917.2	138310.6	859764.9	1066755	1384880	1740460	72712.23	175228.8	660382.6	900005.1	1146426	1424823

For each sample their respective distributions are plotted in Figure 3.31, where it is shown that the sample distributions are considered normally distributed. Therefore, it is concluded that for each sample the data is unpaired, normally distributed and the variance and sample sizes are dissimilar. As the variance and sample sizes are dissimilar a Welch t-test is required [158], [159].

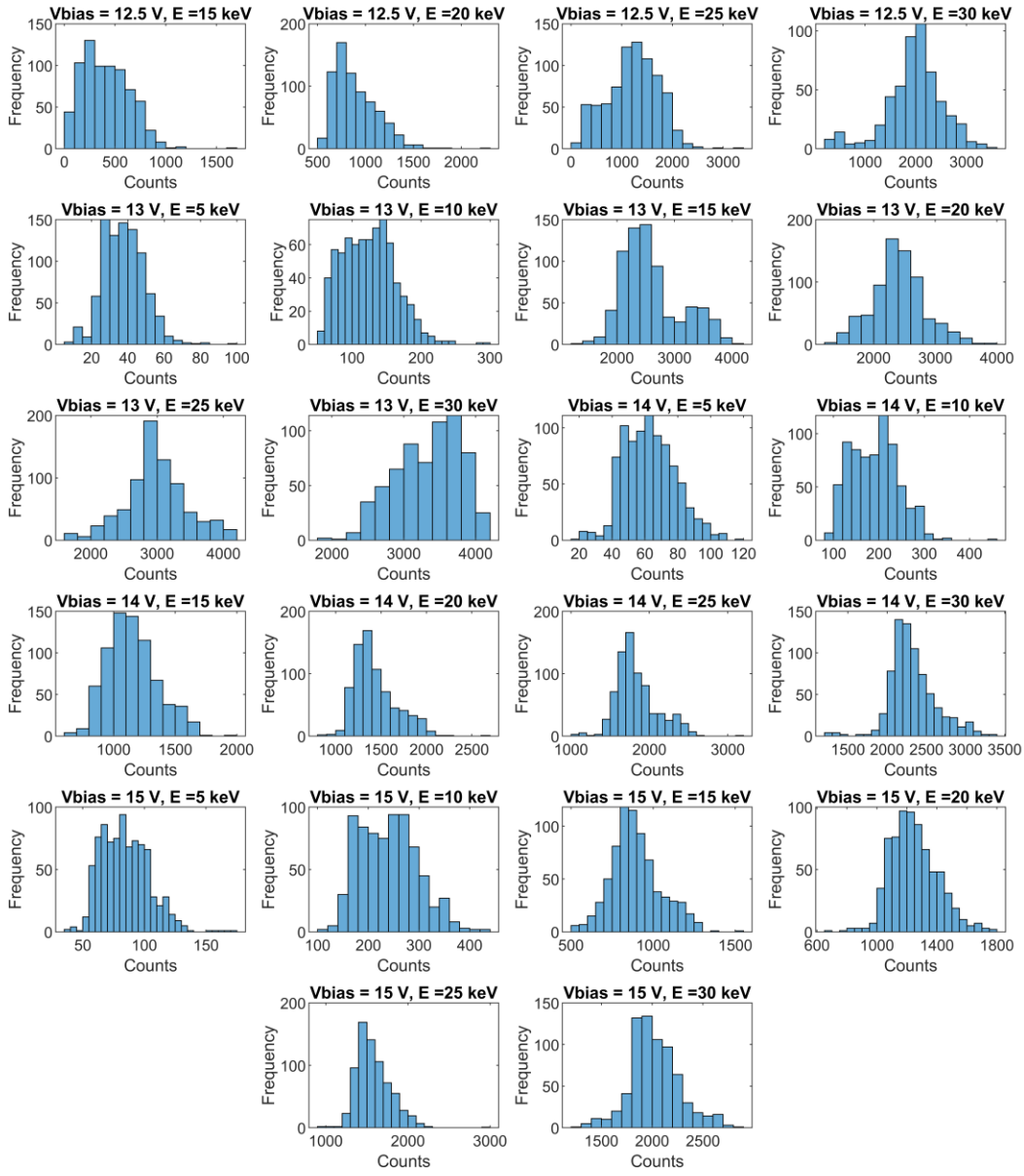

Figure 3.31. Sample distribution for the single electron irradiated pixel samples for SPAD bias voltages from 12 to 15 V and electron kinetic energies from 5 to 30 keV respectively.

Figure 3.32 and Figure 3.33 show the average counts and SE bar graphs for each data set grouped by SPAD bias voltage and electron kinetic energy respectively. It is

evident from the graphs that for each SPAD bias voltage, as the electron kinetic energy increases the average counts increase, except for SPAD bias voltage of 13 V at electron kinetic energy of 20 keV, where the average counts is lower than at 15 keV.

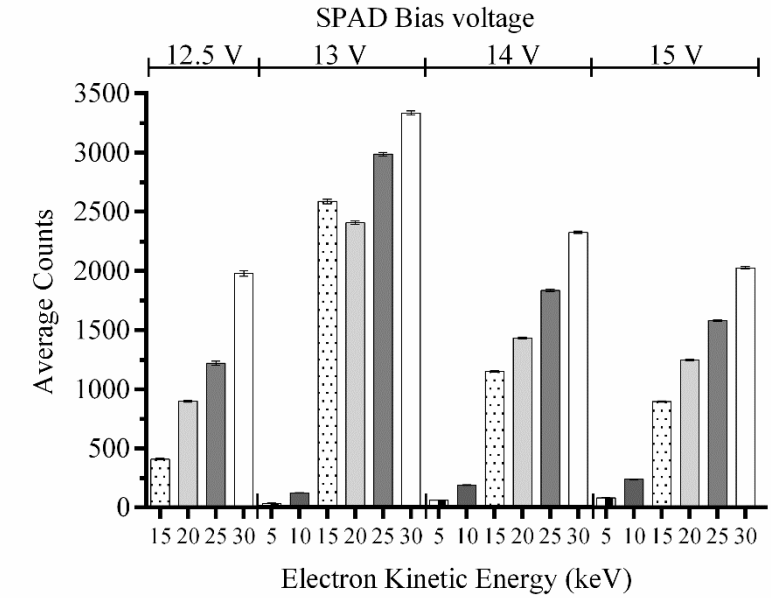

Figure 3.32. Average counts and standard error of the mean bar graph for each data sample, grouped by SPAD bias voltages from 12.5 to 15 V as a function of electron kinetic energy.

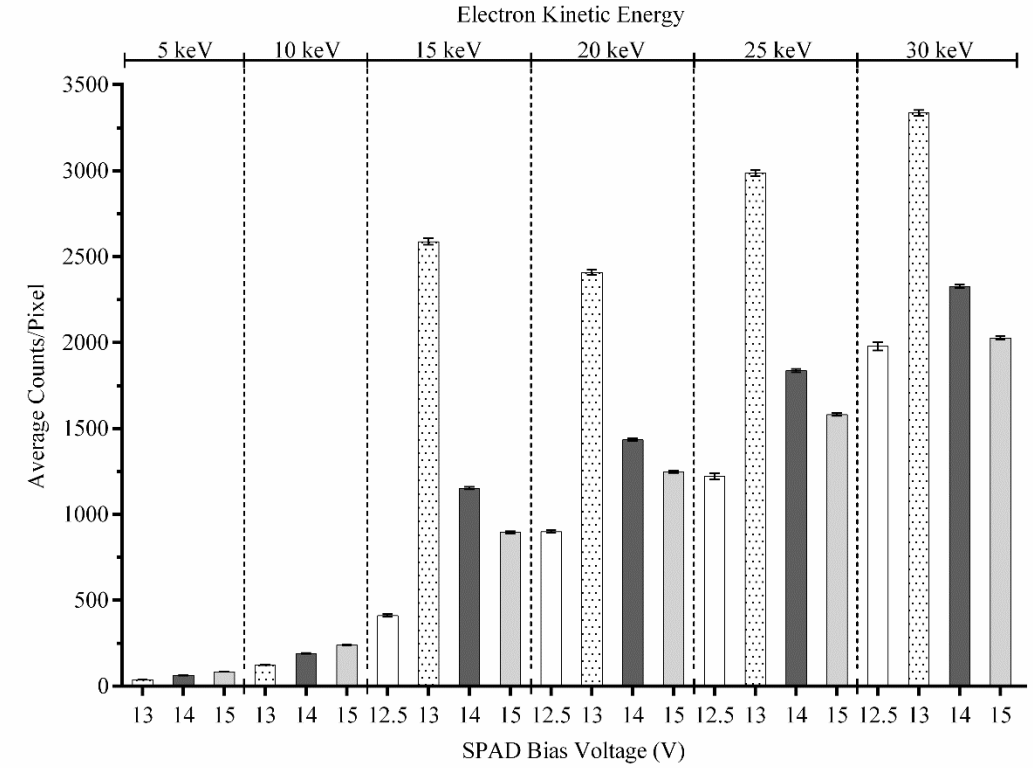

Figure 3.33. Average counts and standard error of the mean bar graph for each data sample, grouped by electron kinetic energies from 5 to 30 keV as a function of SPAD bias voltage.

The Welch t-tests were calculated for each relationship to calculate significance and the results are provided in Table 3.7 for changes in electron kinetic energy at each respective SPAD bias voltage, and in Table 3.8 for changes in SPAD bias voltage at each respective electron kinetic energy.

For all significance tests the null hypothesis can be rejected, with a significance > 99.99 %, except for t-test 27 in Table 3.8, which compares the average counts for SPAD bias voltage of 12.5 V and 15 V with incident electron energy of 30 keV. The t-test accepts the null hypothesis that the means are not significantly different for a confidence level of 95 % but is rejected if the confidence level is set to 93.24 %. With the results in Table 3.7 and Table 3.8 and Figure 3.32 and Figure 3.33, it can be concluded that there is a significant difference in average counts/pixel as a function of both SPAD bias voltages at 12.5, 13, 14 and 15 V, and incident accelerated electron energies from 5 to 30 keV in 5 keV increments.

For incident electron energies from 15 to 30 keV, a SPAD bias voltage of 13 V results in the highest average counts/pixel. For detection at 5 and 10 keV, a SPAD bias voltage of 15 V results in the highest average counts/pixel. Therefore, an increase in SPAD bias voltage does not result in an increase in average counts/pixel. Overall, the average counts/pixel increase with increasing incident electron kinetic energy at SPAD bias voltages of 12 V, 14 V and 15 V respectively. However, there is an exception, at SPAD bias voltage of 13 V, where it is shown that incident electron kinetic energy of 20 keV results in a lower average counts/pixel when compared to electron kinetic energy of 15 keV.

In Figure 3.30 there is a significant increase in average counts between 10 and 15 keV, where it is theorised that at 15 keV the approximate linear stopping length of the electron beam is directly incident upon the SPAD depletion region. Therefore, it can be calculated that the depth of the SPAD depletion region is approximately 3 μm below the silicon surface.

Table 3.7. T-test results for significant difference in SPAD average counts as a function of increasing electron kinetic energy.

t-test Analysis	SPAD Bias Voltage																			
	12.5 V			13 V						14 V					15 V					
t-test	1	2	3	4	5	6	7	8	9	10	11	12	13	14	15	16	17	18	19
Data Set A	15 keV	20 keV	25 keV	5 keV	10 keV	10 keV	15 keV	20 keV	25 keV	5 keV	10 keV	15 keV	20 keV	25 keV	5 keV	10 keV	15 keV	20 keV	25 keV
Data Set B	20 keV	25 keV	30 keV	10 keV	15 keV	20 keV	20 keV	25 keV	30 keV	10 keV	15 keV	20 keV	25 keV	30 keV	10 keV	15 keV	20 keV	25 keV	30 keV
A Sample Size	732	736	785	882	741	741	745	745	760	875	724	746	744	754	863	731	737	722	725
B Sample Size	736	785	521	741	733	745	745	760	645	724	746	744	754	748	731	737	722	725	703
Unpaired two-tailed t-tests with Welch's correction																			
P value	< 0.0001	< 0.0001	< 0.0001	< 0.0001	< 0.0001	< 0.0001	< 0.0001	< 0.0001	< 0.0001	< 0.0001	< 0.0001	< 0.0001	< 0.0001	< 0.0001	< 0.0001	< 0.0001	< 0.0001	< 0.0001	< 0.0001
Significantly different (P < 0.05)	Yes	Yes	Yes	Yes	Yes	Yes	Yes	Yes	Yes	Yes	Yes	Yes	Yes	Yes	Yes	Yes	Yes	Yes	Yes
Welch-corrected t, df	t=41.37 df=1465	t=16.35 df=1101	t=25.06 df=1029	t=59.59 df=849.8	t=129.0 df=740.0	t=147.1 df=756.4	t=7.319 df=1412	t=25.26 df=1493	t=14.26 df=1382	t=63.49 df=832.8	t=125.1 df=846.6	t=24.86 df=1460	t=31.29 df=1476	t=33.71 df=1477	t=70.31 df=872.1	t=110.7 df=945.2	t=43.41 df=1450	t=34.36 df=1347	t=36.72 df=1373
Mean ± SEM Data Set A	411.1 ± 8.432	899.2 ± 8.250	1221 ± 17.86	37.87 ± 0.3838	125.0 ± 1.410	125.0 ± 1.410	2587 ± 19.04	2408 ± 15.46	2987 ± 16.93	62.76 ± 0.5362	191.0 ± 1.948	1152 ± 7.436	1434 ± 8.530	1837 ± 9.643	84.26 ± 0.6587	239.7 ± 2.111	896.0 ± 5.538	1247 ± 5.876	1581 ± 7.769
Mean ± SEM Data Set B	899.2 ± 8.250	1221 ± 17.86	1979 ± 24.42	125.0 ± 1.410	2587 ± 19.04	2408 ± 15.46	2408 ± 15.46	2987 ± 16.93	3335 ± 17.64	191.0 ± 1.948	1152 ± 7.436	1434 ± 8.530	1837 ± 9.643	2327 ± 10.88	239.7 ± 2.111	896.0 ± 5.538	1247 ± 5.876	1581 ± 7.769	2027 ± 9.321
Difference between means	488.1 ± 11.80	321.5 ± 19.67	758.2 ± 30.25	87.08 ± 1.461	2462 ± 19.09	2283 ± 15.52	-179.5 ± 24.53	579.0 ± 22.93	348.7 ± 24.45	128.3 ± 2.020	961.5 ± 7.687	281.3 ± 11.32	402.9 ± 12.87	490.1 ± 14.54	155.5 ± 2.211	656.3 ± 5.926	350.5 ± 8.075	334.7 ± 9.741	445.5 ± 12.13
95% confidence interval	464.9 to 511.2	282.9 to 360.1	698.8 to 817.5	84.21 to 89.94	2425 to 2500	2252 to 2313	-227.6 to -131.4	534.1 to 624.0	300.7 to 396.7	124.3 to 132.2	946.4 to 976.6	259.1 to 303.5	377.6 to 428.2	461.6 to 518.6	151.1 to 159.8	644.7 to 668.0	334.7 to 366.3	315.6 to 353.8	421.7 to 469.3

Table 3.8. T-test results for significant difference in SPAD average counts as a function of increasing SPAD bias voltage.

t-test Analysis	Electron Kinetic Energy														
	5 keV			10 keV			15 keV						20 keV		
t-test	1	2	3	4	5	6	7	8	9	10	11	12	13	14	15
Data Set A	13 V	13 V	14 V	13 V	13 V	14 V	12.5 V	12.5 V	12.5 V	13 V	13 V	14 V	12.5 V	12.5 V	12.5 V
Data Set B	14 V	15 V	15 V	14 V	15 V	15 V	13 V	14 V	15 V	14 V	15 V	15 V	13 V	14 V	15 V
A Sample Size	882	882	875	741	741	724	732	732	732	733	733	746	736	736	736
B Sample Size	875	863	863	724	731	731	733	746	737	746	737	737	745	744	722
Unpaired two-tailed t-tests with Welch's correction															
P value	< 0.0001	< 0.0001	< 0.0001	< 0.0001	< 0.0001	< 0.0001	< 0.0001	< 0.0001	< 0.0001	< 0.0001	< 0.0001	< 0.0001	< 0.0001	< 0.0001	< 0.0001
Significantly different (P < 0.05)	Yes	Yes	Yes	Yes	Yes	Yes	Yes	Yes	Yes	Yes	Yes	Yes	Yes	Yes	Yes
Welch-corrected t, df	t=37.74 df=1586	t=60.83 df=1390	t=25.30 df=1663	t=27.48 df=1324	t=45.21 df=1276	t=16.95 df=1445	t=104.5 df=1008	t=65.94 df=1450	t=48.07 df=1264	t=70.19 df=950.6	t=85.28 df=855.0	t=27.66 df=1373	t=86.10 df=1135	t=45.05 df=1477	t=34.29 df=1323
Mean ± SEM Data Set A	37.87 ± 0.3838	37.87 ± 0.3838	62.76 ± 0.5362	125.0 ± 1.410	125.0 ± 1.410	191.0 ± 1.948	411.1 ± 8.432	411.1 ± 8.432	411.1 ± 8.432	2587 ± 19.04	2587 ± 19.04	1152 ± 7.436	899.2 ± 8.250	899.2 ± 8.250	899.2 ± 8.250
Mean ± SEM Data Set B	62.76 ± 0.5362	84.26 ± 0.6587	84.26 ± 0.6587	191.0 ± 1.948	239.7 ± 2.111	239.7 ± 2.111	2587 ± 19.04	1152 ± 7.436	896.0 ± 5.538	1152 ± 7.436	896.0 ± 5.538	896.0 ± 5.538	2408 ± 15.46	1434 ± 8.530	1247 ± 5.876
Difference between means	24.89 ± 0.6594	46.38 ± 0.7624	21.49 ± 0.8494	66.09 ± 2.405	114.8 ± 2.538	48.67 ± 2.872	2176 ± 20.82	741.4 ± 11.24	484.9 ± 10.09	-1435 ± 20.44	-1691 ± 19.83	-256.5 ± 9.271	1508 ± 17.52	534.6 ± 11.87	347.3 ± 10.13
95% confidence interval	23.59 to 26.18	44.88 to 47.88	19.83 to 23.16	61.37 to 70.80	109.8 to 119.7	43.04 to 54.31	2135 to 2217	719.3 to 763.4	465.1 to 504.7	-1475 to -1395	-1730 to -1652	-274.6 to -238.3	1474 to 1543	511.3 to 557.9	327.5 to 367.2

t-test Analysis	Electron Kinetic Energy														
	20 keV			25 keV						30 keV					
t-test	16	17	18	19	20	21	22	23	24	25	26	27	28	29	30
Data Set A	13 V	13 V	14 V	12.5 V	12.5 V	12.5 V	13 V	13 V	14 V	12.5 V	12.5 V	12.5 V	13 V	13 V	14 V
Data Set B	14 V	15 V	15 V	13 V	14 V	15 V	14 V	15 V	15 V	13 V	14 V	15 V	14 V	15 V	15 V
A Sample Size	745	745	744	785	785	785	760	760	754	521	521	521	645	645	748
B Sample Size	744	722	722	760	754	725	754	725	725	645	748	703	748	703	703
Unpaired two-tailed t-tests with Welch's correction															
P value	< 0.0001	< 0.0001	< 0.0001	< 0.0001	< 0.0001	< 0.0001	< 0.0001	< 0.0001	< 0.0001	< 0.0001	< 0.0001	0.0676	< 0.0001	< 0.0001	< 0.0001
Significantly different (P < 0.05)	Yes	Yes	Yes	Yes	Yes	Yes	Yes	Yes	Yes	Yes	Yes	NO	Yes	Yes	Yes
Welch-corrected t, df	t=55.16 df=1159	t=70.22 df=954.0	t=18.08 df=1311	t=71.77 df=1541	t=30.35 df=1202	t=18.52 df=1068	t=59.02 df=1204	t=75.45 df=1063	t=20.63 df=1424	t=45.03 df=987.2	t=13.01 df=727.0	t=1.830 df=672.0	t=48.67 df=1091	t=65.59 df=983.5	t=20.94 df=1428
Mean ± SEM Data Set A	2408 ± 15.46	2408 ± 15.46	1434 ± 8.530	1221 ± 17.86	1221 ± 17.86	1221 ± 17.86	2987 ± 16.93	2987 ± 16.93	1837 ± 9.643	1979 ± 24.42	1979 ± 24.42	1979 ± 24.42	3335 ± 17.64	3335 ± 17.64	2327 ± 10.88
Mean ± SEM Data Set B	1434 ± 8.530	1247 ± 5.876	1247 ± 5.876	2987 ± 16.93	1837 ± 9.643	1581 ± 7.769	1837 ± 9.643	1581 ± 7.769	1581 ± 7.769	3335 ± 17.64	2327 ± 10.88	2027 ± 9.321	2327 ± 10.88	2027 ± 9.321	2027 ± 9.321
Difference between means	-973.9 ± 17.65	-1161 ± 16.54	-187.3 ± 10.36	1766 ± 24.61	616.0 ± 20.29	360.5 ± 19.47	-1150 ± 19.48	-1405 ± 18.63	-255.4 ± 12.38	1357 ± 30.13	347.9 ± 26.73	47.84 ± 26.14	-1009 ± 20.73	-1309 ± 19.95	-300.0 ± 14.33
95% confidence interval	-1009 to -939.2	-1194 to -1129	-207.6 to -166.9	1718 to 1814	576.2 to 655.8	322.3 to 398.7	-1188 to -1112	-1442 to -1369	-279.7 to -231.1	1297 to 1416	295.4 to 400.4	-3.478 to 99.17	-1049 to -968.0	-1348 to -1270	-328.1 to -271.9

3.5 Summary and Conclusion

The chapter investigates the detection of accelerated electrons using a SEM. First a literature review on the passage of electrons through matter is presented, where electron energy loss and total stopping powers are discussed and the calculation of the approximate attenuation lengths for accelerated electrons traversing silicon is calculated. Additionally, an overview on electron acceleration and its application in

electron microscopy is presented. For accelerated electrons with kinetic energies in the keV range, collisional energy loss dominates as a result of inelastic scattering. It was decided to use a SEM as the primary electron beam source as the electron kinetic energy is limited to 30 keV, to limit the radiation damage to the MINI3D CMOS SPAD image sensor, as its radiation hardness capabilities are unknown

The SPAD image sensor is placed within the vacuum chamber of an SEM and irradiated with the electron beam at incremental kinetic energies from 5 to 30 keV. The SEM beam follows a raster scan pattern, and the first experiment confirms the detection of incident accelerated electrons, therefore confirming the initial hypothesis of this thesis. Furthermore, the results present the first time-resolved imaging of an electron beam raster scanning pattern using a SPAD.

Further experimentation was conducted, and a technique for the removal of HDCR pixels is presented. The results confirm that incident accelerated electrons with energies in the range 5 to 30 keV are detectable using a CMOS SPAD. Furthermore, statistical analysis shows that a change in SPAD excess bias voltage and/or change in electron kinetic energy results in a statistically significant output in average counts/pixel but does not show linear regression. For all significance tests the null hypothesis can be rejected, with a significance > 99.99 %, except for t-test 27 in Table 3.8Table 3.8, where a confidence level of 93.24 % is accepted. The analytical results are shown in Figure 3.32 and Figure 3.33, where it is revealed that a SPAD bias voltage of 13 V, compared to 12.5, 14 and 15 V, results in the largest average counts per pixel during irradiation. An investigation into the non-linear regression is required.

During accelerated electron irradiation it was observed that previously irradiated pixels display hysteresis, especially after higher electron kinetic energy exposure, with previously irradiated pixels exhibiting increased DCR. The effect is not permanent and after a period of non-exposure the DCR returns to normal. A control data set taken approximately 9 minutes after the final irradiation at 30 keV, showed no hysteresis. Therefore, it is hypothesised that the cause for the pixel hysteresis or “after-glow” is primarily the result of phonon generation. However, long term exposure may lead to permanent radiation damage, as discussed in section 3.2.3. Future work should

investigate the radiation tolerance of the SPAD image sensors to incident high energy electrons, and the use of thermal annealing to reduce long term radiation damage.

Figure 3.30 presents the average counts per pixel for each operating bias voltage as a function of incident electron kinetic energy, where it is observed that there is a surge in counts between 10 and 15 keV. It was concluded that the difference in counts is a result of the incident electrons reaching the depletion area of the SPAD, as the approximate linear stopping length of electrons increases with increasing kinetic energy. It was calculated that the depth of the SPAD depletion region is approximately 3 µm below the silicon surface. Therefore, this technique could be used to determine the depth of a SPAD's depletion region.

With the discovery that SPADs can detect ionising radiation, it was decided to investigate the detection of higher energy electrons as well as heavy charged particles. The following chapter reports on the application of the MINI3D CMOS SPAD image sensor for the detection of higher energy electrons and pions using particle accelerators.

4. Detection of Pions and High Energy Electrons using SPADs

With the capability of SPADs to detect photons within the visible spectrum and low energy electrons up to 30 keV [160], as reported in chapter 3, the next step was to investigate if other forms of ionising radiation detection could be detected, for example heavy charged particles, higher energy electrons and higher energy photons (X-rays). Chapter 5 reports on the application of the MINI3D CMOS SPAD image sensor for the detection of X-rays.

This chapter reports on the application of CMOS SPADs for detection of pions and higher energy electrons using particle accelerators. The chapter first provides a brief summary on the standard model of particle physics, followed by a literature review on the passage of electrically charged particles through matter at intermediate relative energies. Thereafter, an overview of particle accelerators used for the experiments is given, followed by a brief overview on pions. Finally, results of pion and higher energy electron detection are presented and analysed, and a conclusion regarding CMOS SPADs for the detection of high energy particles is provided.

4.1 The Standard Model of Particle Physics

The standard model of particle physics provides a consistent quantum theory on the fundamental structure of all matter, defines three of the known four fundamental forces or interactions, and categorises all known elementary particles. The three forces defined by the standard model are the electromagnetic, weak and strong forces. The fourth known force outside of the standard model is gravity. The standard model of elementary particles is often represented as illustrated in Figure 4.1, which shows the principle building blocks of all known matter in the universe. Although, the standard model is highly successful in its theoretical predictions and experimental findings, the theory is not complete and leaves many questions unanswered.

There are two types of elementary particles: fermions and bosons. Bosons are force carriers and are mediators of the known forces, holding matter together. Photons are the force carriers of the electromagnetic force, $W^{\pm}$ and Z bosons mediate the weak force and gluons mediate the strong force. The latest addition to the standard model was the

discovery of the Higgs boson in 2012, by the ATLAS and CMS experiments at CERN using the Large Hadron Collider (LHC) reported in [24] and [23] respectively. The Higgs boson is a scalar boson and is the elementary particle associated with the Higgs field. The interaction of elementary particles with the Higgs field provides them with mass.

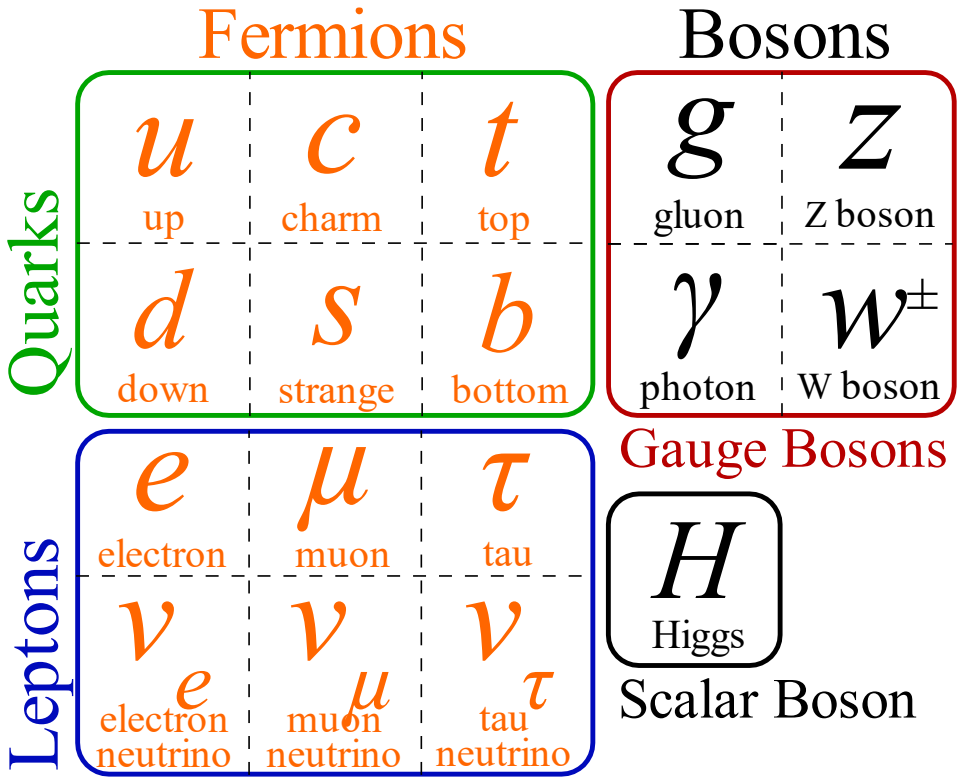

Figure 4.1. Standard model of Particle Physics with all known elementary particles.

Fermions on the other hand are elementary particles that interact with the known forces and are generally associated with matter. There are two types of fermions, quarks and leptons, of which there are three generations. Quarks are the fundamental constituents of matter, and when combined by the strong force, form composite particles known as hadrons, the most notable of which are protons and neutrons. Leptons are elementary particles that do not interact with the strong force and there are two types, charged and neutral. Charged leptons can combine with composite particles to form atoms, the most notable charged lepton is the electron. Charged leptons and quarks interact with the electromagnetic force, whereas neutral leptons, known as neutrinos, do not participate in the strong and electromagnetic forces, only the weak force. Figure 4.2 provides a more comprehensive illustration of the standard model of particle physics with the

emphasis on the relation between fermions and bosons with the known forces including elementary particle charge, spin and mass [161].

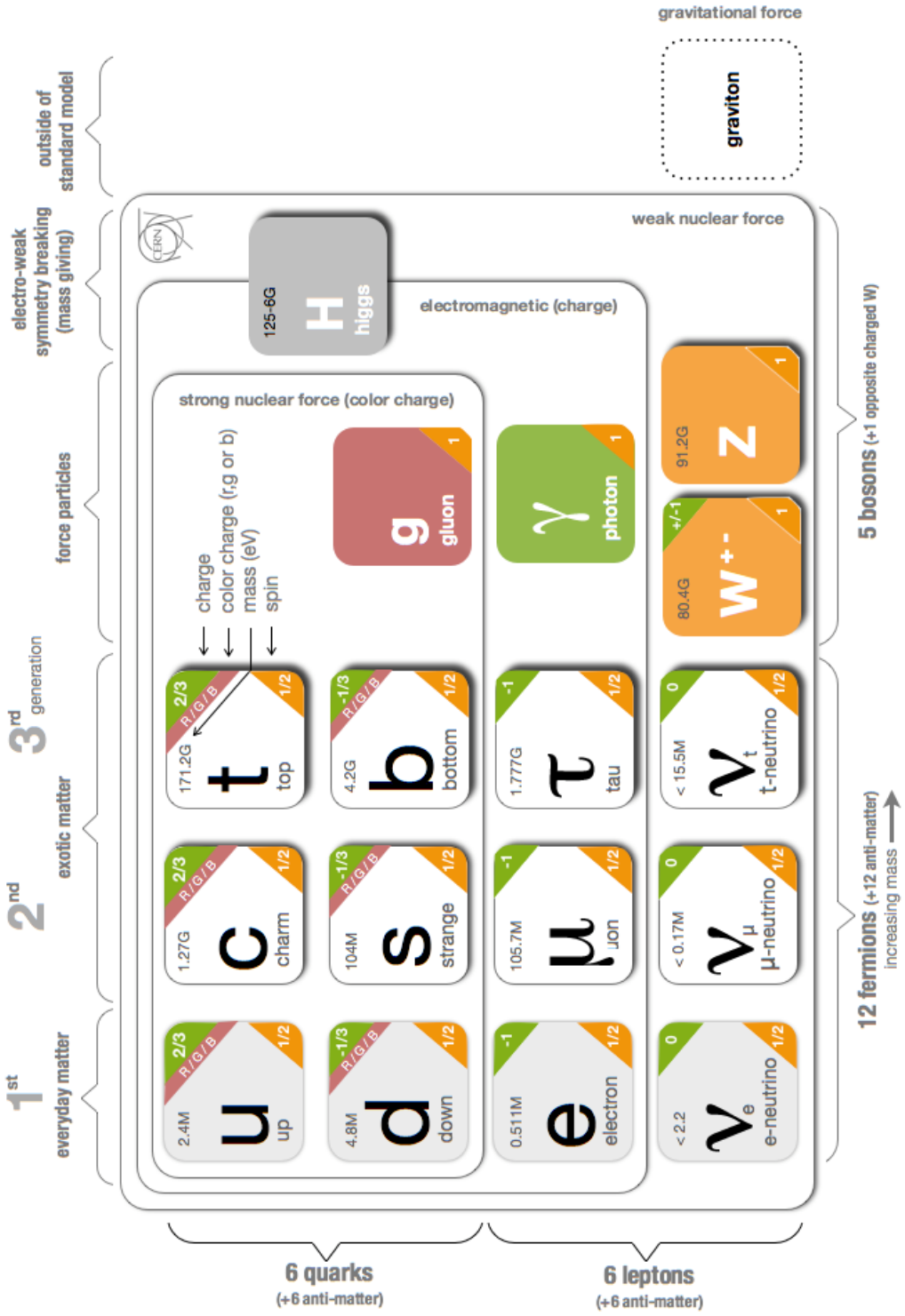

Figure 4.2. The Standard Model of elementary particles and their interaction with the known forces, including elementary particle charge, spin and mass [161].

4.2 Passage of Heavy Charged Particles in Matter

The discovery of alpha (α) radiation and its passage through matter by Rutherford for examining atomic structure, including the formation of quantum mechanical principles, led to the development of the Bethe-Bloch formula, which provided an expression for the mean energy loss of the interaction of charged particles traversing matter [14], [146]. Unlike electrons discussed in Section 3.1, heavy charged particles like protons have a significantly larger mass, hence when traversing matter, the interaction of heavy charged particles (protons, alpha particles, heavier ions) with atomic electrons, the trajectory is negligibly affected, thus reducing elastic scattering as briefly discussed in Section 3.1.2. Therefore, the predictability and derivation of particle path is easier to determine.

4.2.1 Mass Stopping Power of Heavy Particles

Accelerated particles passing through matter interact with the medium through energy transfer. The energy loss is predominately through ionisation or excitation of atomic electrons. Energy loss through nuclear reactions do occur, however such interactions are rare.

For accelerated charged particles with relative energies in the range of $0.1 < \beta\gamma < 1000$ passing through a stopping medium, the Bethe-Bloch equation for mediums with intermediate atomic numbers, provides the mass stopping power or energy loss over traversed length, and is expressed as follows in units of MeV·cm^2/g [14], [146].

$$\left(-\frac{dE}{dx}\right) = Kz^2 \cdot \frac{Z}{A} \cdot \frac{1}{\beta^2}\left[\frac{1}{2} ln \frac{2m_e c^2 \beta^2 \gamma^2 W_{max}}{I^2} - \beta^2 - \frac{\delta(\beta\gamma)}{2}\right] \qquad (4.1)$$

where E is the energy of the accelerated charged particle, and x the length traversed within the given stopping medium. W_{max} is the maximum energy transfer in a single collision and is expressed as follows

$$W_{max} = \frac{2m_e c^2 \beta^2 \gamma^2}{1 + 2\gamma m_e/M + (m_e/M)^2} \qquad (4.2)$$

where a summary of constants and variables used in equations 4.1 and 4.2 are provided in Table 4.1.

Table 4.1. Summary of Variables for Mass Stopping Power.

Symbol	Definition	Value and/or units
e	elementary charge	1.6022×10^{-19} C
ε_0	permittivity of free space	8.8542×10^{-12} F/m
m_e	electron mass	0.510999 MeV/c^2
c	speed of light	299 792 458 m/s
r_e	classical electron radius	2.81794 fm
N_A	Avogadro's number	6.02214×10^{23} mol^{-1}
K	$= 4\pi N_A r_e^2 m_e c^2$ $(-dE/-dx)$ coefficient	0.307075 MeV mol^{-1} cm^2
β	relativistic speed of incident particle	Equation 313.2
γ	Lorentz factor	Equation 3.3
ρ	mass density of stopping medium	g cm^{-3}*
W_{max}	maximum energy transfer to an electron	MeV
M	incident particle mass	MeV/c^2
z	incident particle charge number	*
Z	atomic number of stopping medium	*
A	atomic mass of stopping medium	g mol^{-1}*
I	mean excitation energy of stopping medium	eV*
$\frac{\delta(\beta\gamma)}{2}$	density-effect correction for ionisation energy loss at very high energies $\rightarrow \ln(\hbar\omega_p/I) + \ln(\beta\gamma) - 1/2$	
$\hbar\omega_p$	plasma energy of stopping medium	eV*

*Atomic and nuclear properties available at [145]

As discussed in section 3.1.3, the linear stopping power in units MeV/cm, is derived as *(-dE/dx)*×ρ, where ρ is the density of the stopping medium in units of g/cm^3. Figure 4.3 provides the mass stopping power for accelerated charged particles incident upon different stopping mediums, as a function of intermediate relative energies $\beta\gamma$. The mass stopping power is proportional to $1/\beta^2$ at low energies and *ln*(γ) at high energies. From the figure the minimum mass stopping power, known as minimum ionisation loss, is at $\beta\gamma \approx 5$, and accelerated charged particles with the same relative energy are denoted as minimum ionising particles (MIP). Figure 4.4 provides the total stopping power of positive muons (μ^+) in copper as a function of $\beta\gamma$ = 0.001 to 10^6 [146]. The figure provides a comparative example of a charged particles total mass stopping power, as a function of relative energy $\beta\gamma$ across nine orders of energy

magnitude. Furthermore, for $\beta\gamma > 1000$, radiative energy losses dominate. The data values for $\beta\gamma < 0.1$ are given in [162] and for $\beta\gamma > 0.1$ are given in [144].

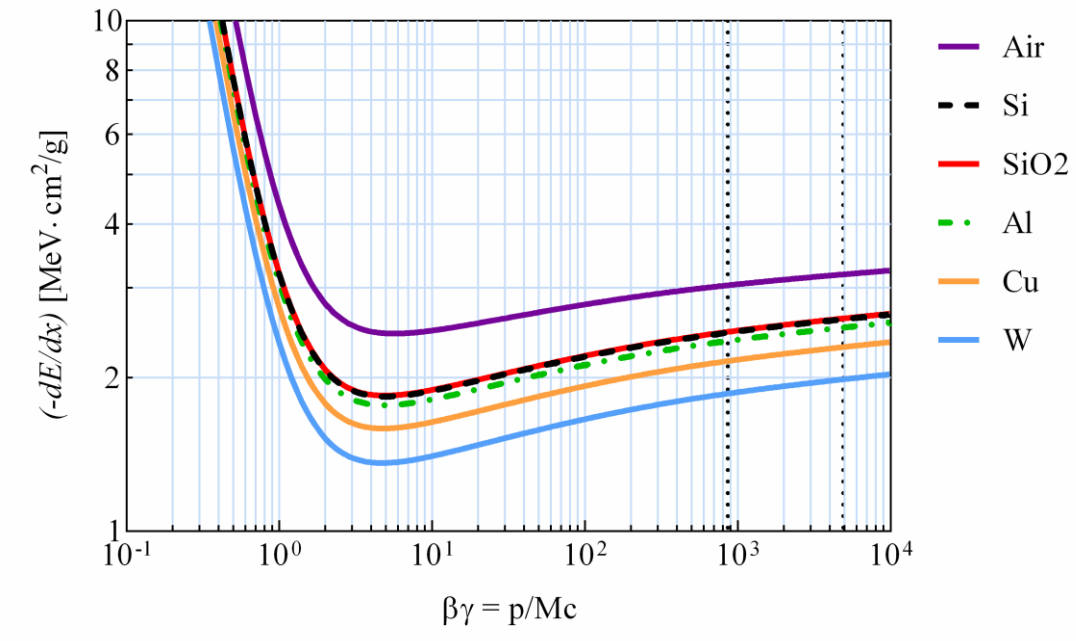

Figure 4.3. Mass stopping power for several media, common in CMOS, as a function of $\beta\gamma$ for incident accelerated charged particles. Atomic and nuclear properties available at [145].

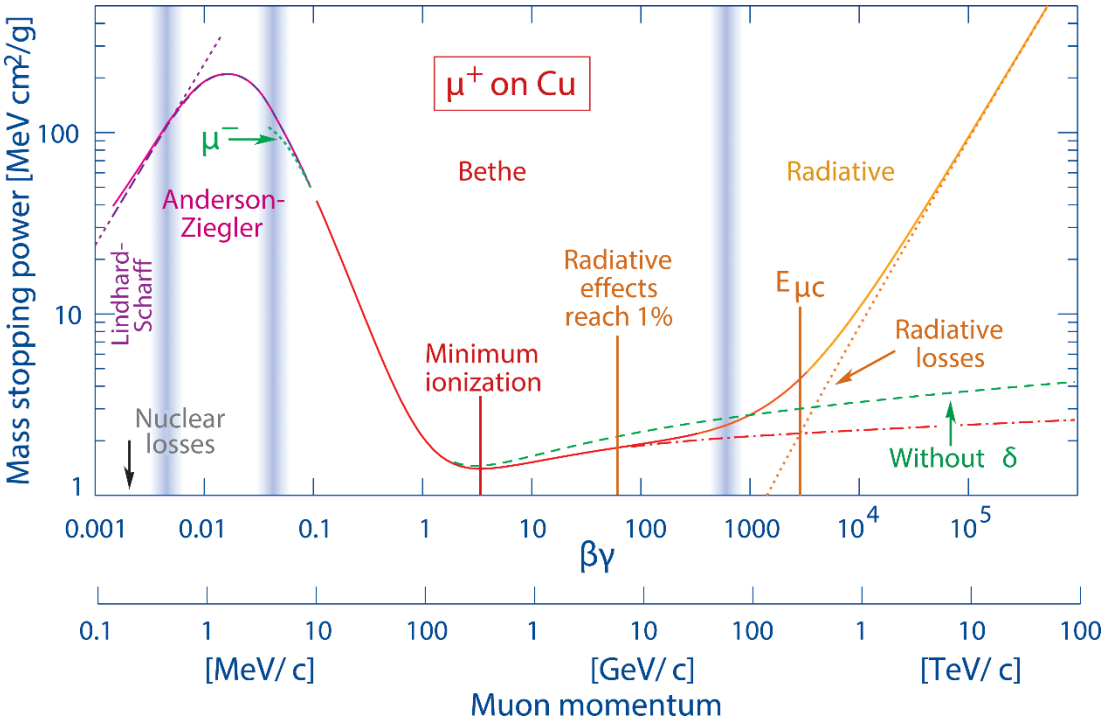

Figure 4.4. Mass stopping power of positive muons (μ^+) in copper as a function of $\beta\gamma = 10^{-4}$ to 10^6 [146].

4.3 Particle Accelerators

Particle accelerators use electromagnetic fields to accelerate charged particles to high energies and focus the beam of particles. Particle accelerators are used in multiple areas including particle physics research, ion implantation for semiconductor device fabrication and radiotherapy [152], [163]–[165]. An extensive review on particle accelerators is provided in [166].

The world's highest energy particle accelerator is the LHC, completed in 2008, and is based at the European Organisation for Nuclear Research (CERN) in Geneva, Switzerland [164], [167]. The LHC is a hadron collider with a maximum design beam energy of 14 TeV and overall circumference of 27 km. In order to achieve proton collisions, several stages of acceleration and particle delivery are required. Figure 4.5 provides a schematic of the CERN accelerator complex [168].

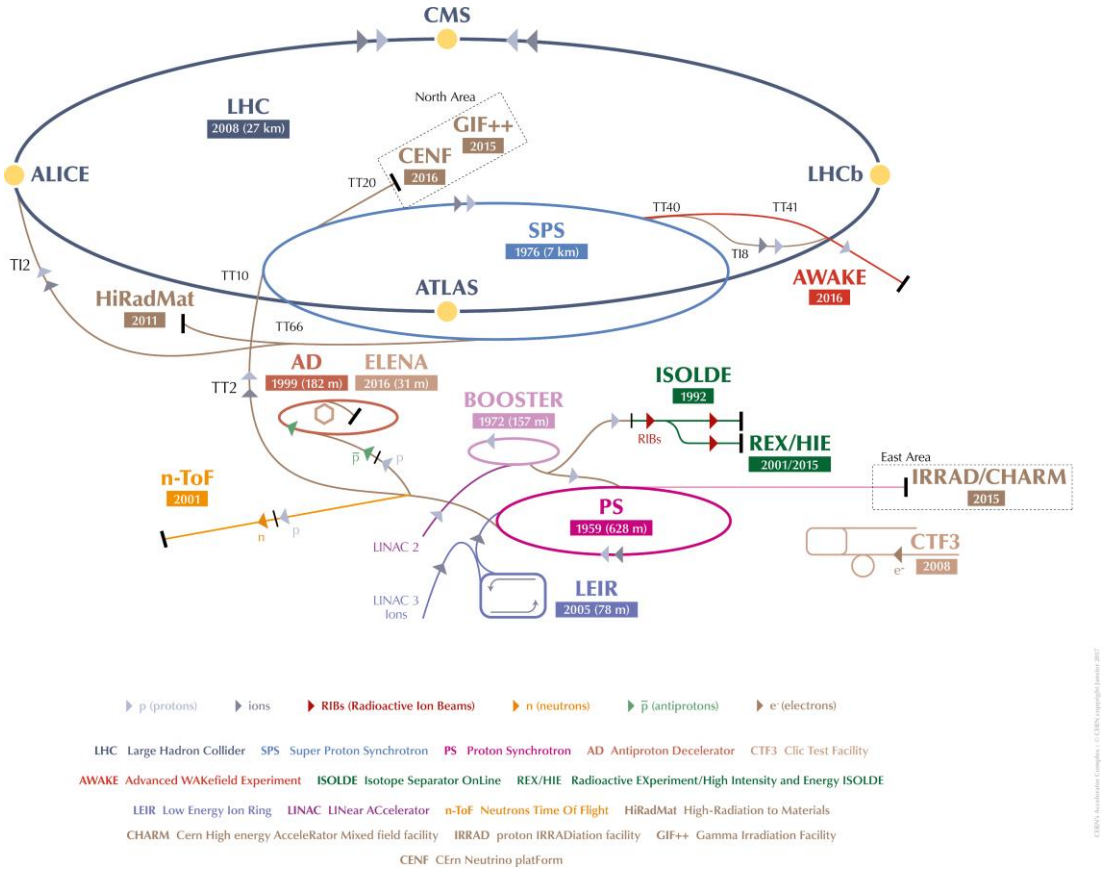

Figure 4.5. Schematic of the complete accelerator complex at CERN [168].

For proton-proton collisions, the journey begins with hydrogen, which is ionised by an electric field to strip off electrons and produce bare protons [169]. The protons are separated into bunches and accelerated up to 50 MeV in the linear accelerator 2 (Linac 2) and delivered to the Proton Synchrotron Booster accelerator. The Booster accelerates the protons to 1.4 GeV and injects the protons into the Proton Synchrotron (PS) [170], which further accelerates the protons to 26 GeV [171]. In addition to protons the PS also accelerates a range of other particles e.g. electrons and helium nuclei [171]. The accelerated particles from the PS are injected into the Super Proton Synchrotron (SPS), which are accelerated up to 450 GeV and finally injected into the LHC for final acceleration and ensuing collision, which create rare processes, allowing scientists to investigate particle properties and provide an improved understanding of matter [172].

4.3.1 The Super Proton Synchrotron and Pion Generation

For the investigation of heavy charged particle detection using CMOS SPADs, the first experiment involved the SPS at CERN and the production of hadrons with the collision of accelerated particles and fixed targets [173]. The hadrons are produced by colliding protons at 400 GeV from the SPS into a fixed beryllium target plate [174], the hadron properties are measured using detectors and then redirected towards north area, where the specific hadrons are separated into multiple beam lines using a wobbling station, allowing researchers to conduct measurements on select hadron beams and trial new detector technology [173]. The heavy charged particle beam line available for detector testing at CERN was the pion beam line.

A pion (π) as stated is a hadron, or more specifically is categorised as a meson, as mesons are composite particles made of one quark and one antiquark, bound together by the strong force. There are three pion compositions namely positive (π^+), negative (π^-) and neutral (π^0), of which the combinations of up, anti-down, anti-up and down quarks determine the charge of the pion, illustrated in Figure 4.6. The pion is the lightest of mesons and are unstable composite particles and therefore decay. Charged pions have a mean lifetime of 26.033 (± 0.005) ns, whereas the neutral pions have a mean lifetime of 85.2 (± 1.8) as. The masses of charged and neutral pions are

139.57061 (± 0.00024) MeV/c^2 and 134.9770 (± 0.0005) MeV/c^2 respectively, which is approximately 270 times larger than the mass of an electron. [146], [175]

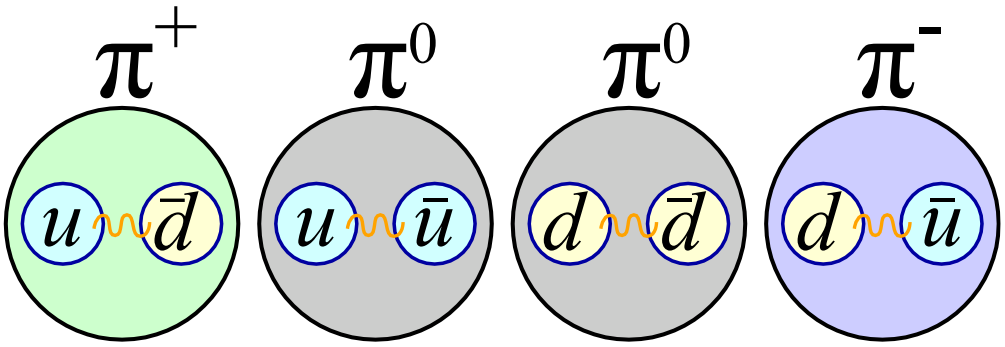

Figure 4.6. All pion compositions, π^+, π^- and π^0. The pions comprise of one up or down quark and one anti-up or anti-down quark, which determines the overall charge of the pion.

4.3.2 Electron Accelerator ELSA

Chapter 3 reported the detection of lower energy electrons in the range 5 to 30 keV with CMOS SPADs and SEM. Therefore, the second experiment was the investigation of higher energy electron detection using CMOS SPADs. This was achieved using the ELSA electron stretcher-ring accelerator in Bonn, Germany.

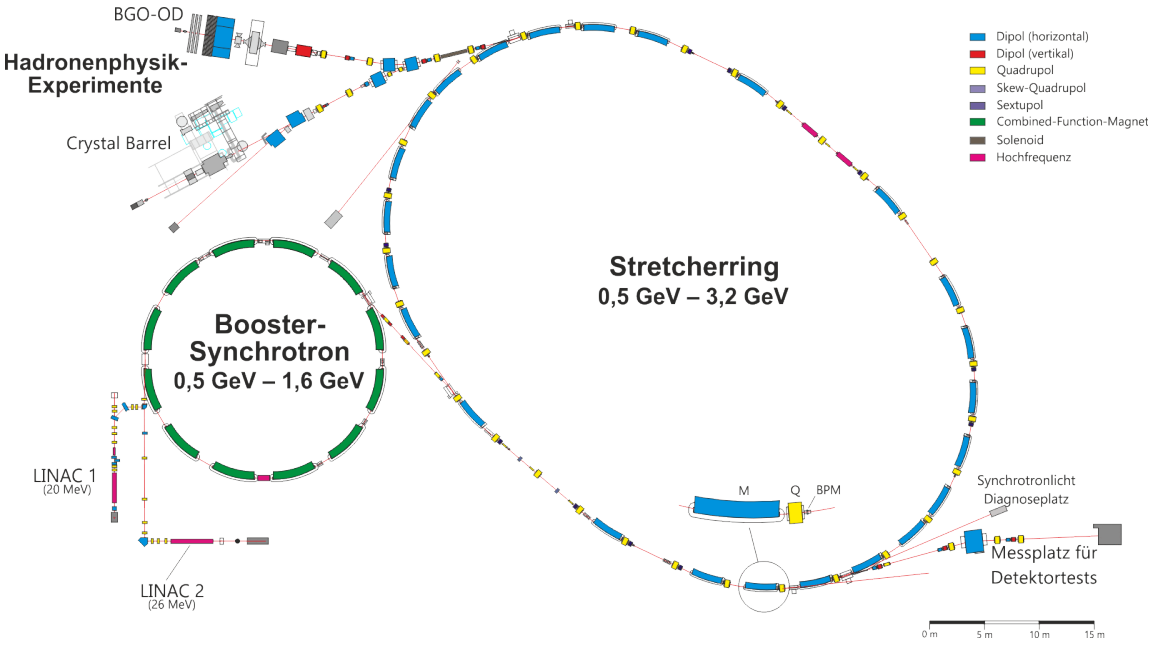

Figure 4.7. Schematic of ELSA electron stretcher-ring accelerator complex [176].

Similar to the accelerator complex at CERN, electron acceleration is initially achieved with a linear accelerator which injects accelerated electrons into the booster

synchrotron at a maximum of 26 MeV. Thereafter the booster increases the electron energy to a maximum of 1.6 GeV and injects the electrons into the stretcher ring accelerator, which accelerates the electrons to a maximum of 3.2 GeV. Finally, the accelerated electrons in the range 0.5 to 3.2 GeV are delivered to the measurement and test areas. Figure 4.7 provides a schematic of the accelerator complex at ELSA. [176]

4.4 Experimental Setup

For both experiments the MINI3D BSI CMOS SPAD image sensor was used [1]. However, one of the limitations of the back-end read-out hardware was the delay in data output via the FPGA and computer, as the firmware of the FPGA is fixed to 200 MHz. Initially the delay between frame capture for a 1 ms frame exposure time was measured to be approximately 500 ms, but after a software update the frame capture delay was reduced and measured to be approximately 71 ms. If the frame exposure time is increased, this results in both increased DCR and increased data collection, which results in reduced SNR and a proportional delay, therefore a 1 ms frame exposure time was selected. In the accelerated electron detection experiments reported in chapter 3 the results were taken with the updated FPGA software.

The delay in subsequent frame captures poses an efficiency problem, unlike the SEM used in chapter 3 where the electron beam is assumed constant, particle accelerators deliver particles in spills, where each spill is made up of particle bunches with a predefined frequency and intensity. Therefore, for a 1 ms frame exposure time and subsequent 71 ms delay, the total time detection efficiency is approximately 1.4 %.

4.4.1 Pion Experiment Parameters

For the detection of high energy pions, the H6 beam line at CERN's North Area was used, Figure 4.8 provides an image of the test area and Figure 4.9 provides a diagram of the north area including targets and respective beam lines. The primary 400 GeV proton beam from the SPS is directed onto a fixed beryllium target generating a secondary beam which is a mixture of hadrons and electrons, where an incident lead absorber is used to remove electrons.[177]

The pion beam delivered to line H6 is based on priorities of other projects that were being conducted at the time, including programs of all facilities served by the SPS and

LHC. All of which, result in variability of the beam line spill cycle, spot size, intensity and beam energy. Nevertheless, during most pion irradiations the average spill cycle was approximately 5 seconds, the spot size resolution 5 × 5 mm^2, intensity approximately 10^7 particles per spill, and beam energy = 120 GeV. [177], [178]

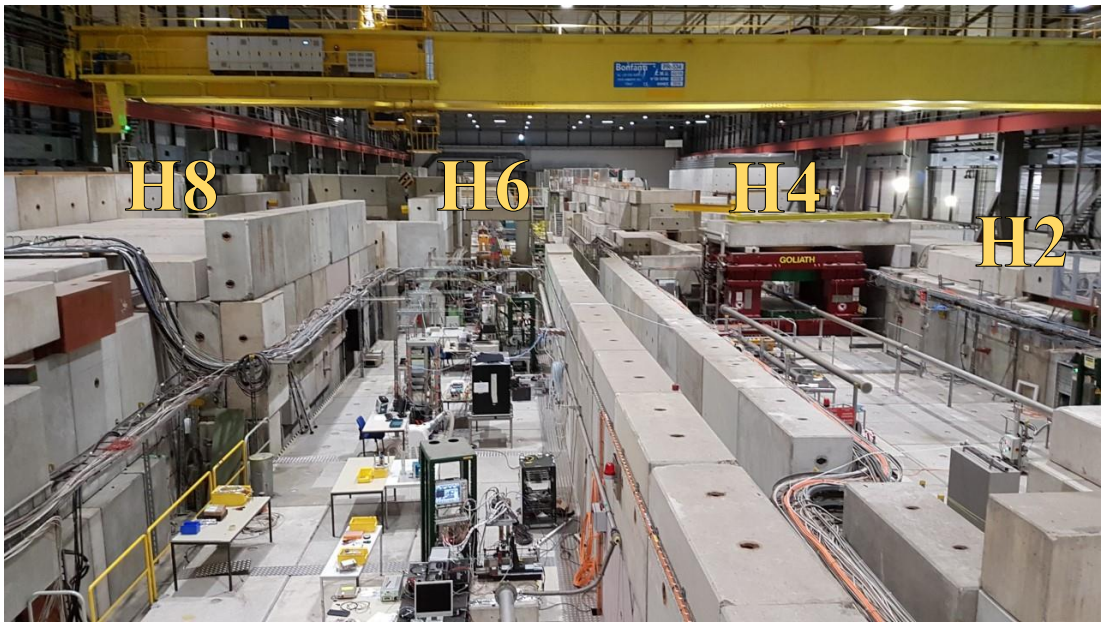

Figure 4.8. Image of North Area testing area, with beam lines labelled. The respective beam line used was H6.

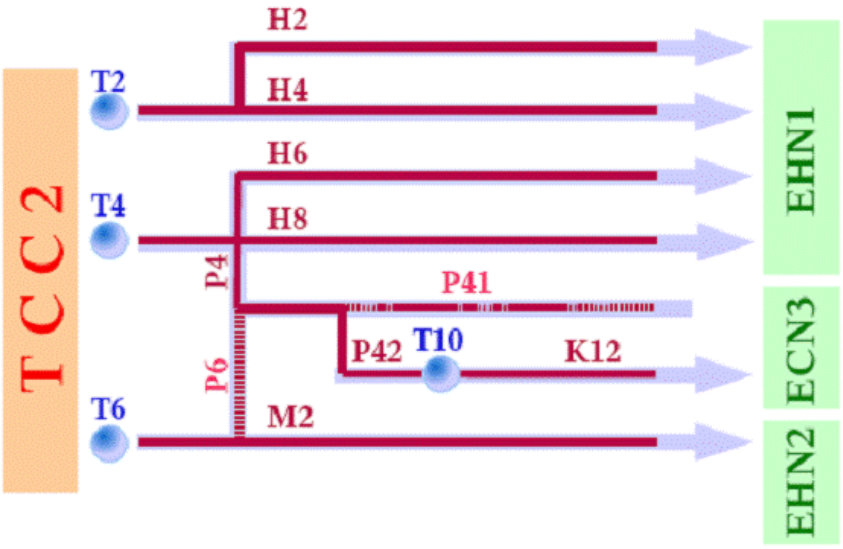

Figure 4.9. Schematic of the North Area SPS targets and respective beam lines [177]. The pion beam line used was H6.

With a known time detection efficiency of 1.4 %, the SPAD will be active to detect approximately 140 000 pions/spill. Additionally, the spill is assumed to have an even distribution of pions, therefore with a spill cycle of approximately 5 seconds and SPAD exposure time of 1 ms the SPAD image sensor will be able to capture approximately 69 frames/spill, and 2000 pions/frame, however, the beam spot size has not been considered. The spot size has an approximate rms area of 25 mm^2 [178], and the SPAD image sensor an active pixel area of 0.94 mm^2 [1], therefore the image sensor only covers 3.76 % of the beam area and thus the SPAD image sensor is exposed to an approximate total of 75 pions/frame (75 kHz) across 15360 pixels. Under optimal beam conditions, with a beam intensity of 10^8 particles per spill, spot size area of 12.6 mm^2 and minimum spill time of 4.8 s, the beam exposure increases to approximately 1554 pions/frame (≈1.55 MHz).

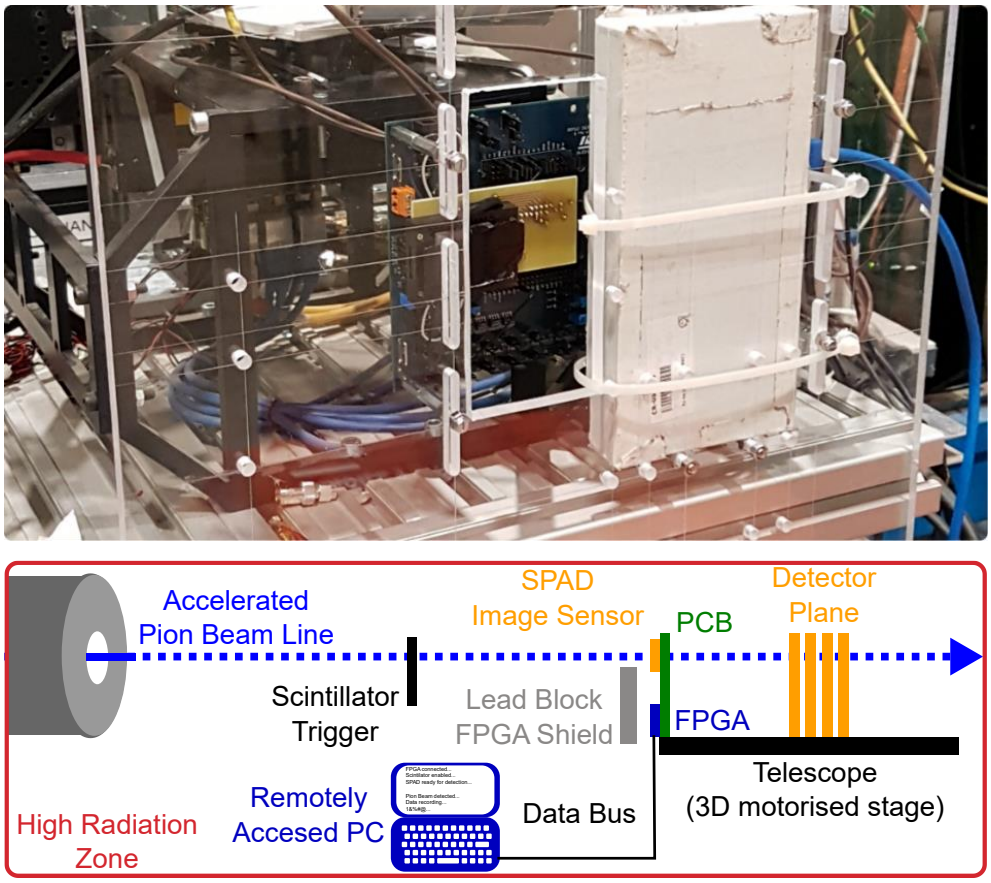

Figure 4.10. MINI3D BSI CMOS SPAD image sensor mounted to telescope for pion beam irradiation, including schematic diagram of the experimental setup.

The SPAD image sensor and PCB with FPGA was fixed to the Malta plane detector telescope [35]. The SPAD image sensors location was aligned to a Malta detector plane

and along with the 3D motor stage on the telescope, tolerance 1 mm, the SPAD array was positioned within the beam line. A scintillation counter was used to trigger data capture during spill cycle and subsequently pause data capture to ensure continuous pion detection per frame. Figure 4.10 provides an image of the SPAD image sensor within the beam line attached to the Malta plane telescope, with a lead block to reduce potential radiation damage to the FPGA, including a schematic diagram of the experimental setup [35].

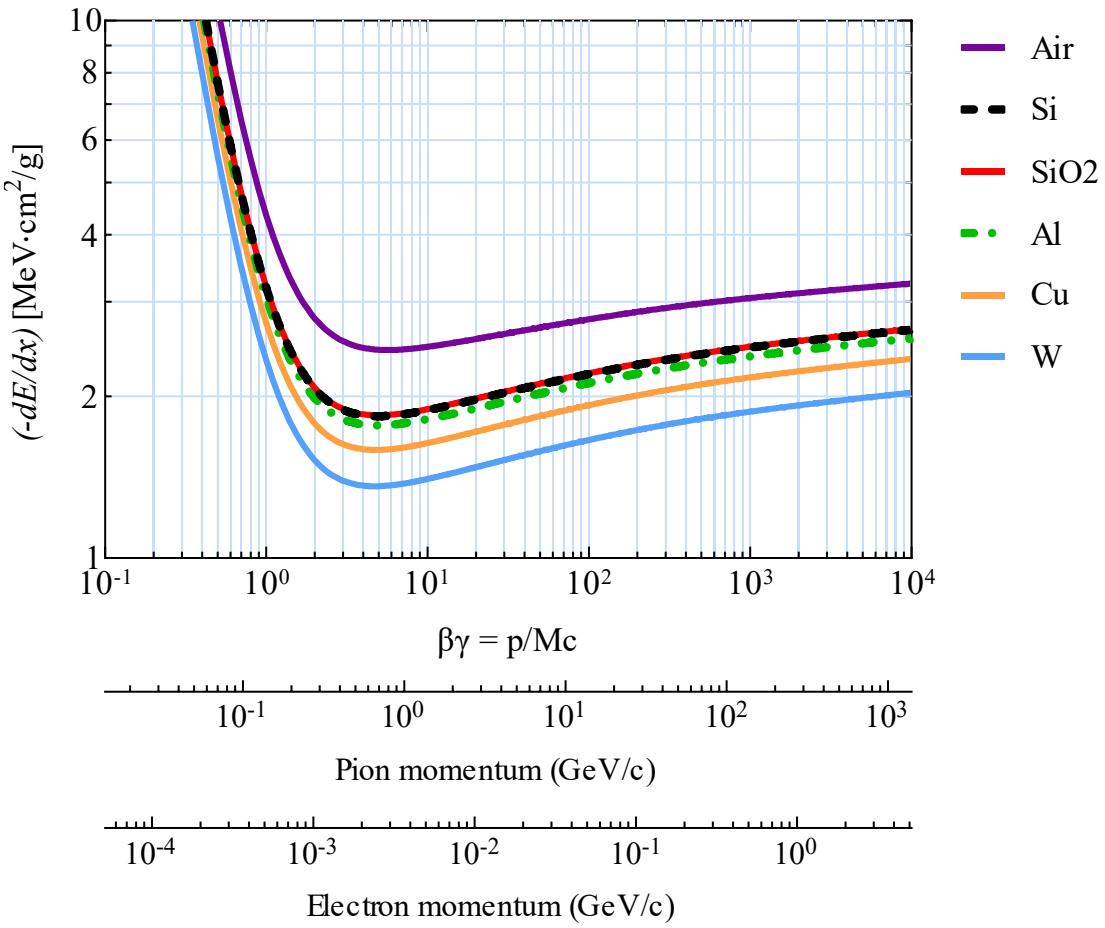

Figure 4.11. Mass stopping power for several mediums, common in CMOS, as a function of βγ for incident accelerated pions and electrons. Atomic and nuclear properties available at [125].

With a known pion beam momentum of 120 GeV/c, the mass stopping power for several stopping mediums as a function of both pion and electron momentum is interpolated onto Figure 4.3, and shown in Figure 4.11. Furthermore, Figure 4.12, provides the linear stopping power for the same stopping mediums with known densities [145], as a function of both pion and electron momentum. The SPAD image sensor is BSI and the incident stopping medium is silicon, therefore with pion beam

energy of 120 GeV, equation 4.1 and the known density of silicon in Table 3.2 the projected linear stopping length is roughly 210 m. From Figure 4.12 the MIP energy for a pion is approximately 680 MeV, and comparison with a 120 GeV pion beam, the mass stopping power is approximately three times larger.

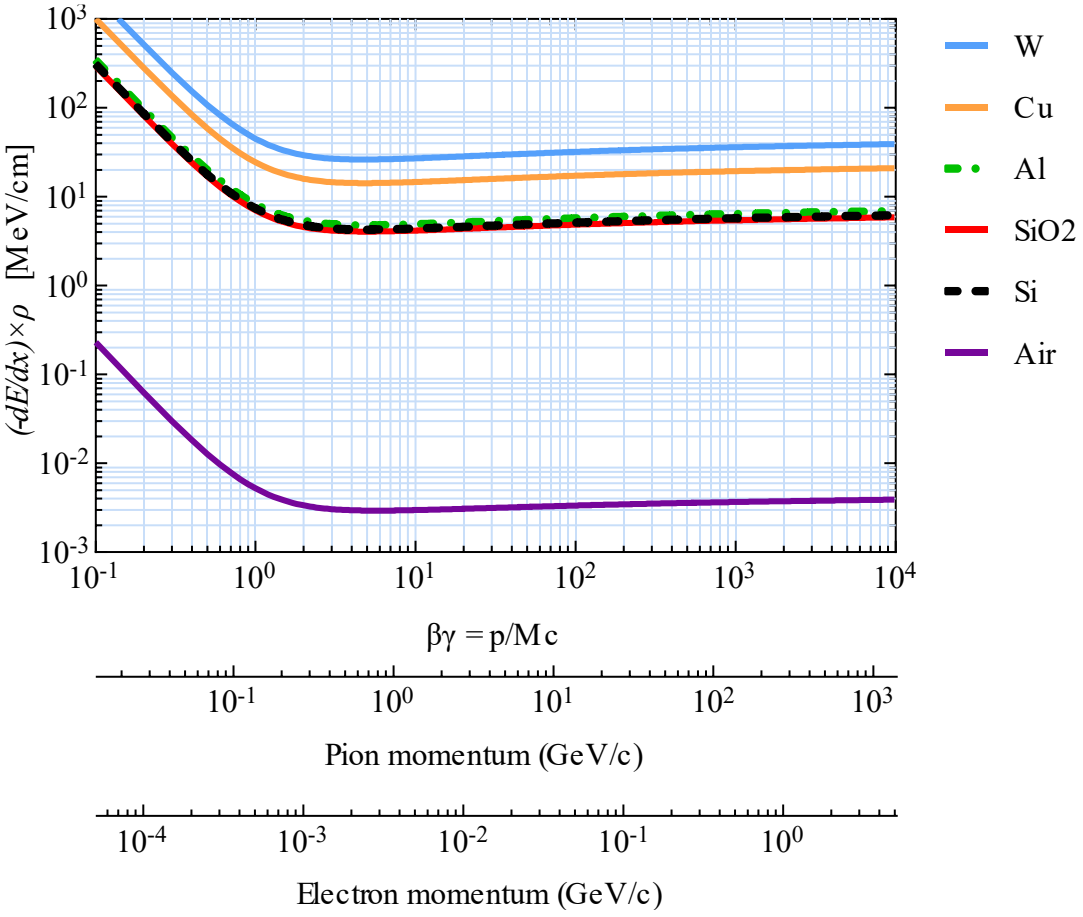

Figure 4.12. Linear stopping power for several mediums, common in CMOS, as a function of βγ for incident accelerated pions and electrons. Atomic and nuclear properties available at [125].

4.4.2 High Energy Electron Experiment Parameters

For the detection of high energy electrons, the ELSA electron stretcher-ring accelerator was utilised with an accelerated electron energy of 2.5 GeV. A 48-hour session of measurements was scheduled, but due to beam technical difficulties and other beam priorities approximately only 15 hours were available. During beam operation the external beam intensity was at its lowest at approximately 1 pA [176], which translates to 6.25 MHz, therefore 6.25 million electrons/second. As a result of the beam technical difficulties the beam spot size was limited to 100 mm^2. The SPAD image sensor

mounting procedure was similar to that of the pion experiment, with mounting to a telescope with a 3D motorised stage, and an FE-I4B 2 × 2 cm^2 pixel detector plane for alignment of SPAD image sensor [179].

Following the same calculation for the pion experiment in section 4.4.1 the expected exposure intensity per frame is approximately 59 electrons (59 kHz) with a frame exposure time of 1 ms. Furthermore, with the known electron energy of 2.5 GeV, equation 4.1 and the known density of silicon in Table 3.2 the projected linear stopping length of the accelerated electrons in silicon is approximately 1388 m.

4.5 Experimental Results

For probable detection it is important to determine the average DCR noise floor of the SPAD image sensor including respective standard deviation for each pixel. The expected exposure intensity for both the pion and high energy electron experiments across the entire CMOS SPAD array of 15360 pixels is low, equating to approximately 4.88 and 3.84 Hz respectively, which equates to 0.0488 pions/pixel and 0.0384 electrons/pixel per frame. For example, in

Table 3.4 the measured average DCR for the MINI3D CMOS SPAD image sensor used at SPAD bias voltage of 13 V, after filtering HDCR pixels, is approximately 2070 Hz. The total dark counts across the entire image sensor is approximately 32 MHz. Therefore, as the DCR of the MINI3D SPAD image sensor is significantly larger than the predicted detections/frame as a result of relative low intensities for both the pion and high energy electron beams, the detection is not discernible over the inherent DCR of the SPAD. Therefore, a significant data sample size is required to reduce the standard error of the mean, as the sample means will cluster closer to the true population mean allowing potential identification of the incident particles.

4.5.1 Pion Experiment

For the pion experiment, there were a total of four irradiation sets of measurements taken, named E1, E2, E3 and E4 respectively. The total number of experiments was limited by beam availability and approved access. For each irradiation exposure a control set of data was taken before irradiation, and HDCR pixels filtered. A total of

43500 frames of control data was taken at each SPAD bias voltage. For each irradiation the experimental procedure was as follows:

1. Beam access granted, access to beam line area H6 for set-up.
2. SPAD image sensor hardware installed and mounted to telescope.
3. Remote access confirmed and initialisation of SPAD image sensor.
4. Control data set initiated for SPAD bias voltage of 12.5 V for predetermined number of frames, then SPAD bias voltage changed from 12.5 V to 13 V to 14 V to 15 V in turn, and respective control data sets taken.
5. SPAD image sensor is reset and predetermined frames per irradiation cycle is set.
6. SPAD frame capture initiated for each pion beam spill and paused after each spill. Run and pause was triggered using a scintillator.
7. Once predefined number of frames captured, the SPAD bias voltage is changed from 12.5 V to 13 V to 14 V to 15 V in turn until current cycle complete, then a new cycle of measurements is taken and so forth, until beam run has ended.
8. After irradiation, a control data set is taken. The SPAD image sensor is then powered off and hardware removed until beam access is granted once more.

Table 4.2 provides an overview of each experiment with total frames taken before, during and after irradiation including respective start and end dates (dd/mm in 2018).

Table 4.2. Pion beam experiments total frames taken before, during and after irradiation, with respective start and end dates.

	Experiment 1			Experiment 2		
	Control Before	Irradiation	Control After	Control Before	Irradiation	Control After
Frames	1500	52500	13000	20000	21500	10000
Date (start-end)	24/10	24/10 – 26/10	26/10	01/11	01/11 – 02/11	02/11

	Experiment 3			Experiment 4		
	Control Before	Irradiation	Control After	Control Before	Irradiation	Control After
Frames	10000	237000	10000	12000	102000	10000
Date (start-end)	02/11	02/11 – 07/11	07/11	09/11	09/11 – 12/11	12/11

To adequately analyse the data and to determine the DCR noise floor of the SPAD image sensor, at each respective bias voltage, the average DCR for each experiment control frame was calculated and plotted in Figure 4.13. From the figure it is evident that the DCR of the SPAD array is not consistent and varies with each control set taken. However, what is consistent is the DCR pattern for each bias voltage. Certain environmental factors like temperature and surrounding ambient light were not controllable.

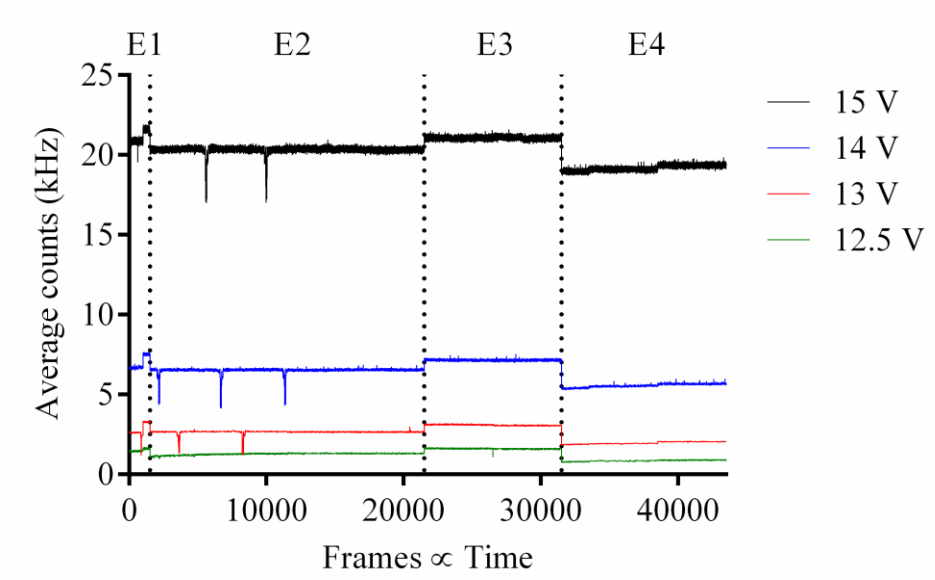

Figure 4.13. MINI3D DCR (kHz) per frame for each control data set taken before irradiation for each experiment, 1 to 4.

As the control DCR vary between experiments and the low expected total incident exposure intensity of the pion beam, the calculated DCR noise floor for each experiment must be calculated using the respective control data set taken before each experiment for each respective bias voltage. Therefore, a total of four DCR are calculated for each experiment, with the calculated mean and standard deviation for each pixel.

Using the cumulative DCR noise floors for each experiment and each respective bias voltage, a cumulative HDCR list of pixels for the MINI3D SPAD image sensor used was acquired and a total of 2892 pixels were flagged as HDCR pixels and removed for any data analysis. This equates to approximately 18.8 % of all pixels, which is below the expected 20 % as indicated in Figure 2.9 [1]. A heatmap of flagged HDCR is shown

in Figure 4.14, with HDCR pixels indicated in black. For each frame taken during each experimental irradiation, all HDCR are removed from analysis, and the average counts per pixel (kHz) for each frame is calculated.

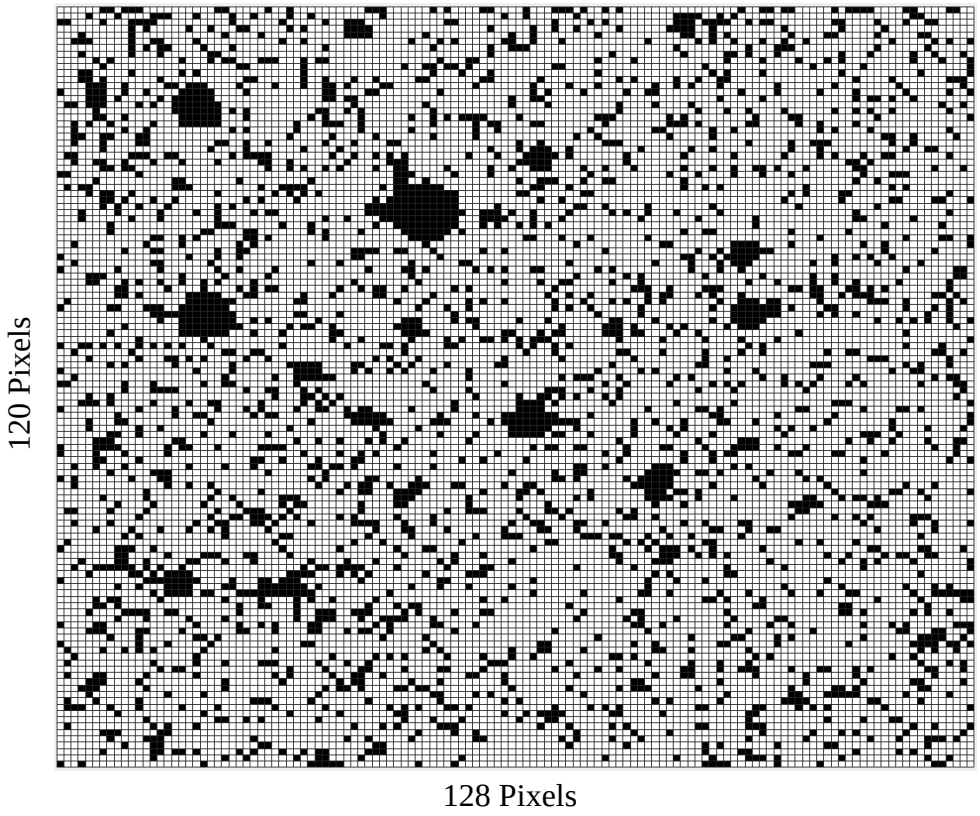

Figure 4.14. HDCR pixel heatmap for MINI3D CMOS SPAD image sensor used for pion beam experiment. HDCR pixels indicated in black.

For experiment 1, the average counts/pixel vs frame for before, during and after irradiation (separated by vertical dotted lines) is combined for each SPAD bias voltage and shown in Figure 4.15. From the figure during pion beam irradiation the average counts per pixel increases for all bias voltages, though fluctuating and with a gradual increase in base average counts. It is also observed that once irradiation is ended the average counts at each bias voltage remains high with reduced variation. The analysis is repeated for experiments 2 through to 4 and shown in Figure 4.16 to Figure 4.18 respectively. For experiment 2 and 3, it is evident that the DCR returns to its original state, therefore indicating that the large increase in DCR after irradiation is impermanent. However, for experiment 4 the variation of the DCR for all bias voltages

is significantly larger, indicating potential radiation damage to the SPAD image sensor after irradiation.

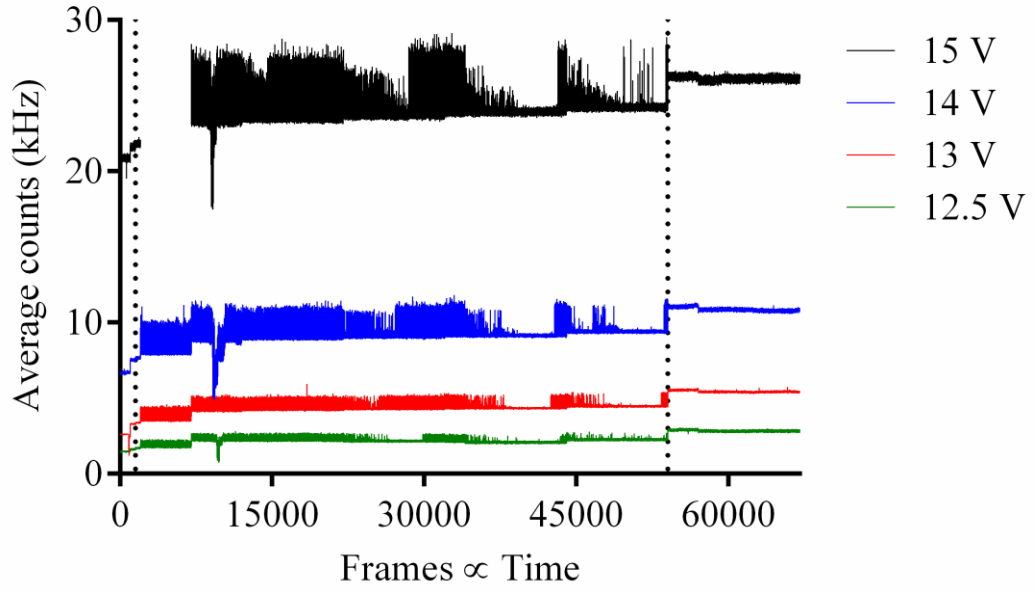

Figure 4.15. Pion experiment 1, average counts per pixel vs frame for before, during and after pion beam irradiation for each respective SPAD bias voltage with 120 GeV pion beam. Before, during and after irradiation separated by vertical dotted lines.

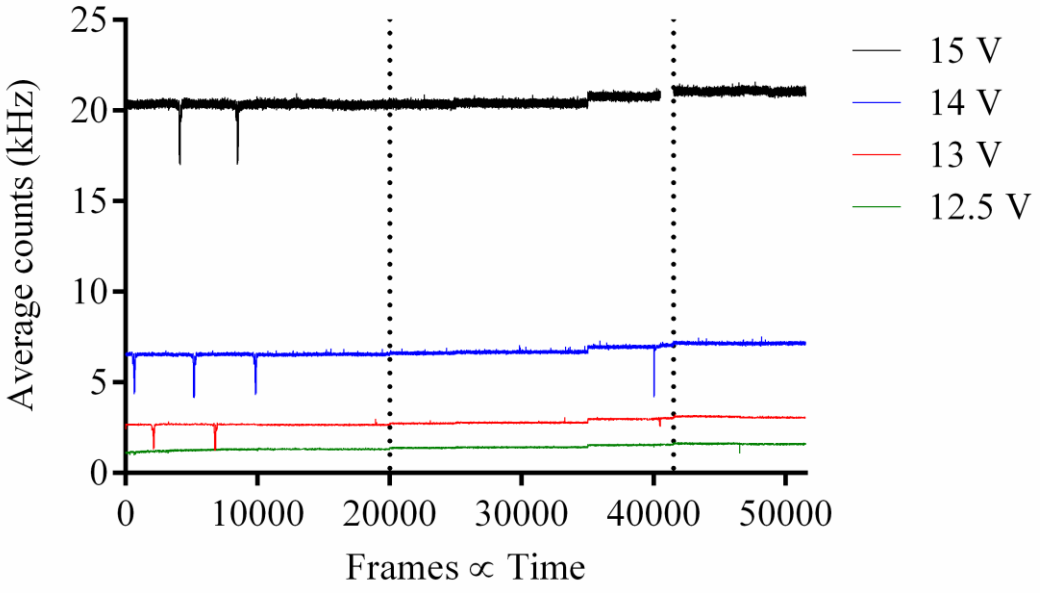

Figure 4.16. Pion experiment 2, average counts per pixel vs frame for before, during and after pion beam irradiation for each respective SPAD bias voltage with 120 GeV pion beam. Before, during and after irradiation separated by vertical dotted lines.

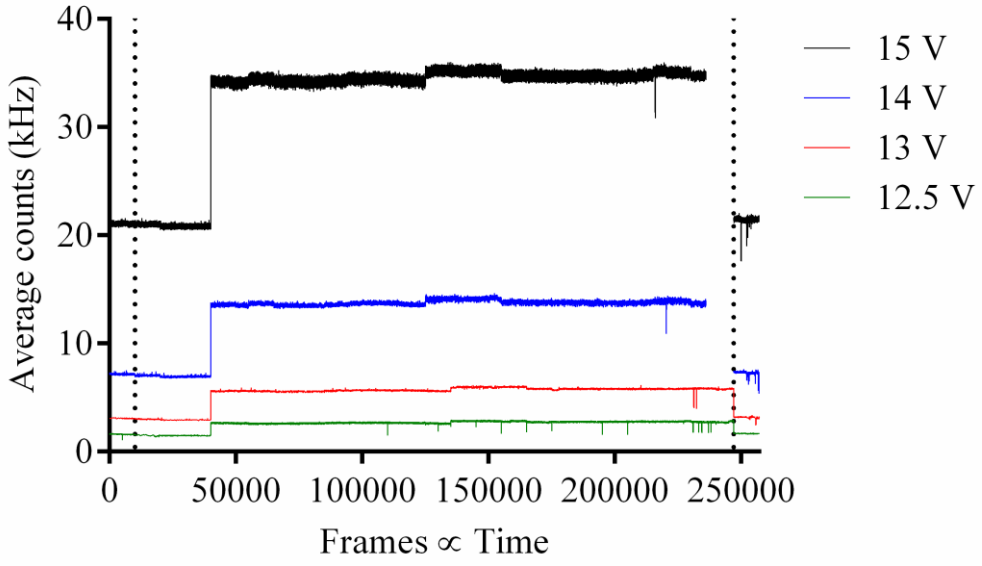

Figure 4.17. Pion experiment 3, average counts per pixel vs frame for before, during and after pion beam irradiation for each respective SPAD bias voltage with 120 GeV pion beam. Before, during and after irradiation separated by vertical dotted lines.

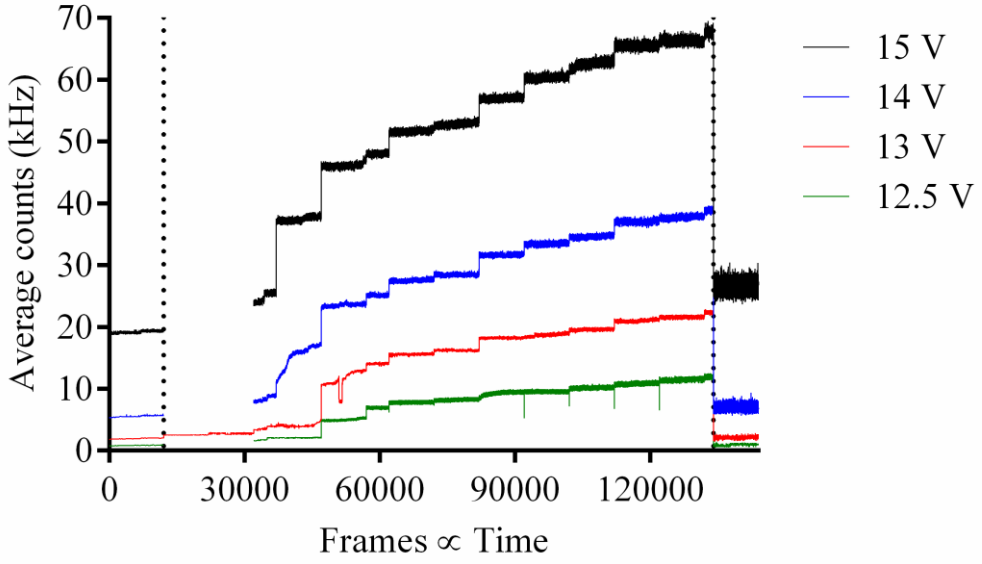

Figure 4.18. Pion experiment 4, average counts per pixel vs frame for before and during pion beam irradiation for each respective SPAD bias voltage with 120 GeV pion beam. Before and during irradiation separated by a vertical dotted line.

For pion experiment 2, the average counts per pixel vs frames is shown in Figure 4.16, where there is no apparent increase or change in average counts before, during or after irradiation, except for a gradual increase in base average counts. Hence, as experiment 2 was conducted 6 days after experiment 1 and beam parameters may have

changed e.g. beam spot size, it was assumed the image sensor was misaligned and not directly within the pion beam. Therefore, for experiment 3 the 3D motorised stage on the telescope was used to move the SPAD image sensor in increments of 1mm until a change in average counts was observed. As can be seen in Figure 4.17 at frame 40001, there is a distinct increase in average counts across all bias voltages after the image sensor position was changed during irradiation to within the beam line.

For experiment 3 during irradiation, the average counts have a minor increase in variation when compared to average counts before irradiation, however this does not resemble the response measured in experiment 1 in Figure 4.15, which shows a much larger variation during irradiation. Additionally, comparison of average counts for experiments 1 and 3 after irradiation, it is shown that for experiment 3 the average counts decreases significantly when the pion beam is off but after experiment 1 the same behaviour is not observed.

For pion beam experiment 4, the average counts vs frame for before, during and after irradiation are shown in Figure 4.18. Initially the image sensor required the motorised stage to align the sensor within the pion beam, indicated by the constant recorded operation for SPAD bias voltage of 13 V, until a significant change was observed. During irradiation, the average counts increase, however the increase in average counts is not consistent, but incrementally increases for each consecutive cycle until the beam has ended. This was a pre-set by the main user of the beam. Furthermore, unlike experiment 1, both experiment 3 and 4 have slight increases in average count variation during irradiation when compared to average counts before irradiation. However, for experiment 4 the average count variation after irradiation is significantly larger when compared to before irradiation and permanent, indicating radiation damage to the SPAD image sensor.

With the average DCR calculated for every pixel at each respective bias voltage, for each experiment, the total number of pions detected for every frame during irradiation was calculated. Figure 4.19, Figure 4.20 and Figure 4.21 show the distribution of 120 GeV pion counts detected/pixel during irradiation and Table 7.1, Table 7.2 and Table 7.3 provide the complete statistical results for experiments 1, 3 and 4 respectively.

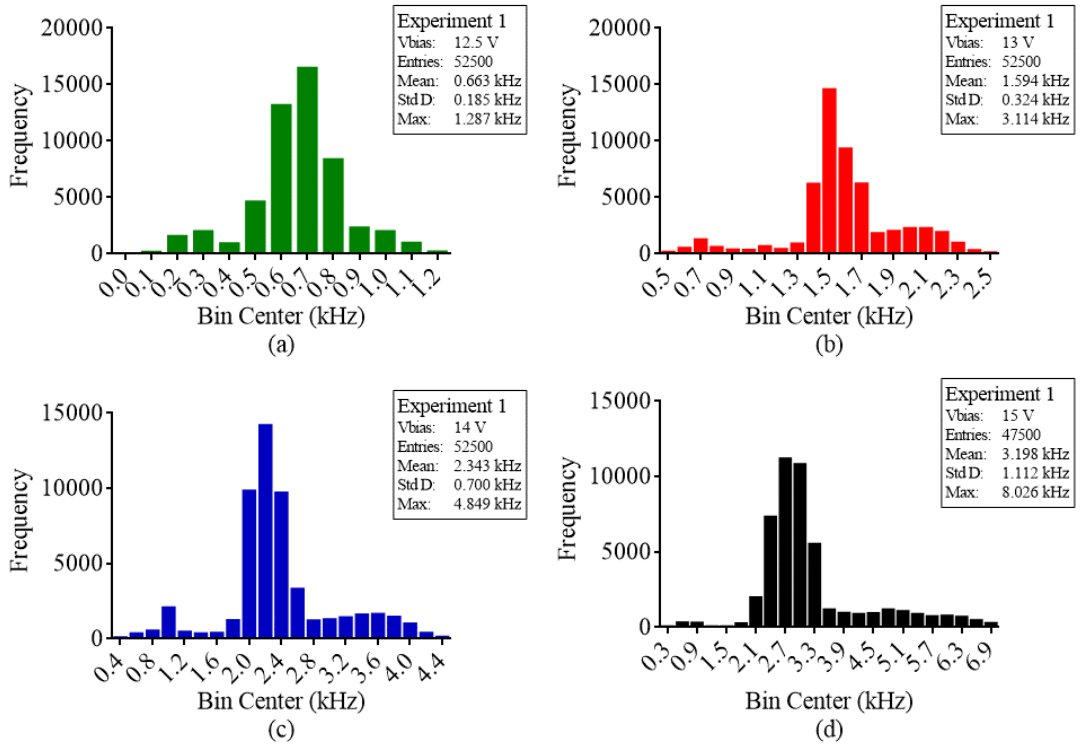

Figure 4.19. Pion beam experiment 1, frame distribution of average counts per pixel (kHz) during pion beam irradiation for SPAD bias voltage (a) 12.5 V, (b) 13 V, (c) 14 V and (d) 15 V.

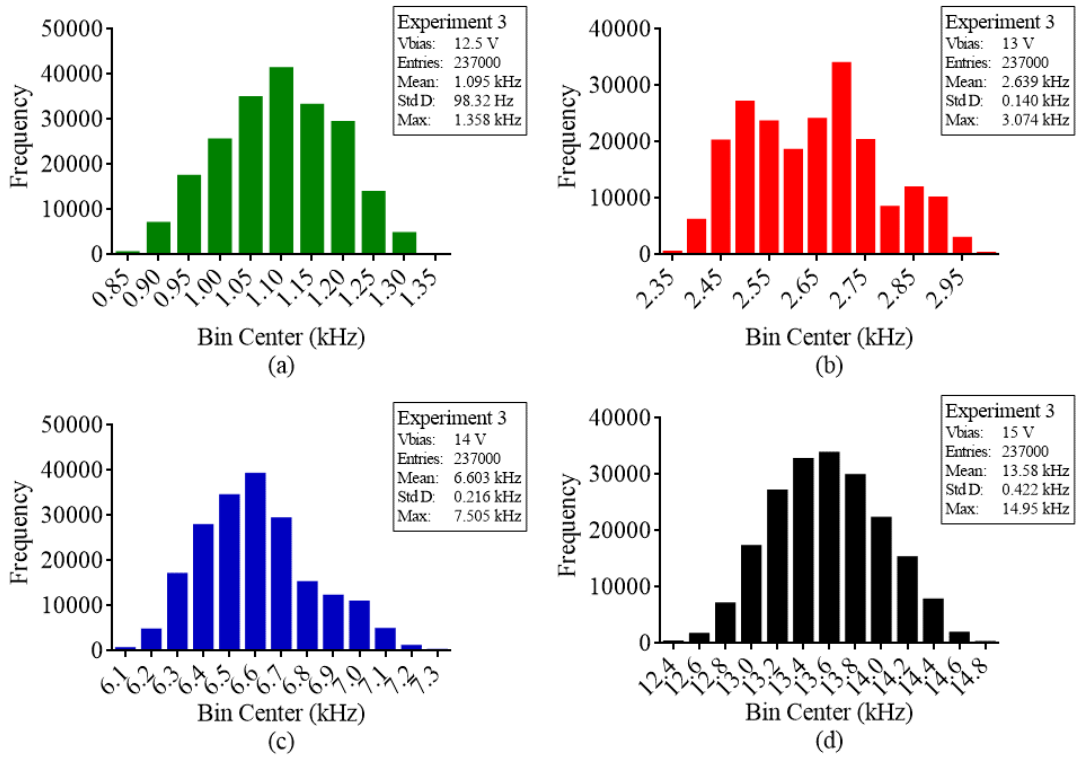

Figure 4.20. Pion beam experiment 3, frame distribution of average counts per pixel (kHz) during pion beam irradiation for SPAD bias voltage (a) 12.5 V, (b) 13 V, (c) 14 V and (d) 15 V.

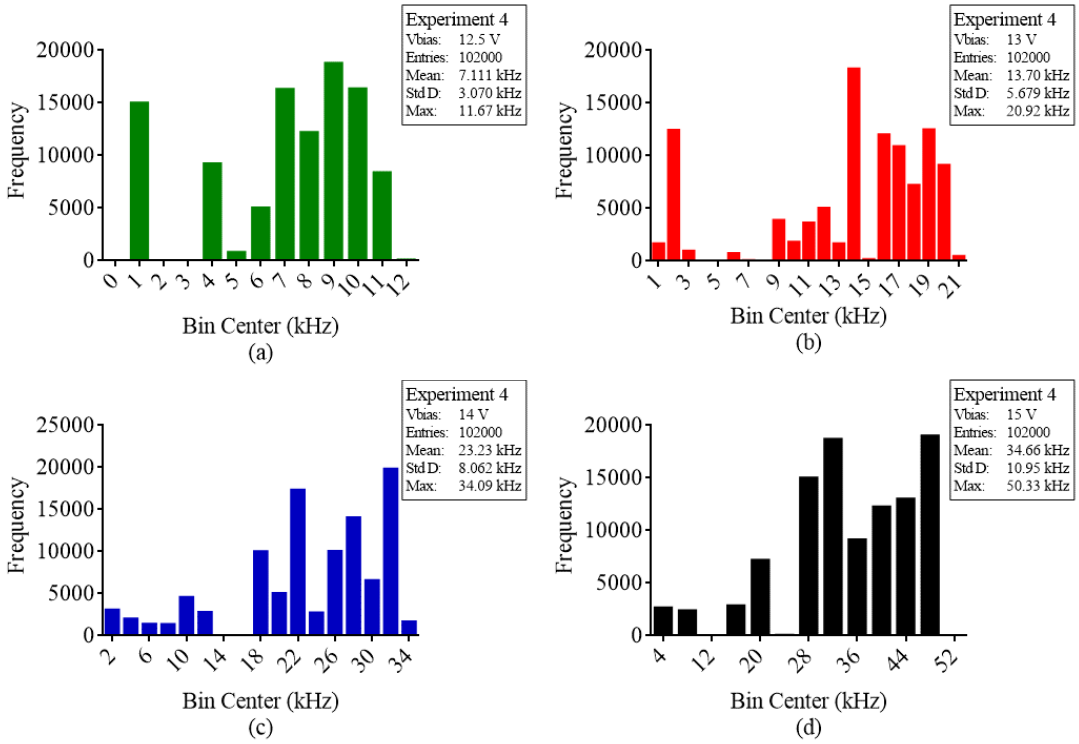

Figure 4.21. Pion beam experiment 4, frame distribution of average counts per pixel (kHz) during pion beam irradiation for SPAD bias voltage (a) 12.5 V, (b) 13 V, (c) 14 V and (d) 15 V.

Table 4.3. Average ($\bar{x}$) pion counts/frame and standard deviation (σ) vs SPAD bias voltage for pion experiments.

	Average Pion Counts/Frame[a] and Standard Deviation (MHz)					
SPAD Bias Voltage	Experiment 1		Experiment 3		Experiment 4	
	$\bar{x}$	σ	$\bar{x}$	σ	$\bar{x}$	σ
12.5 V	8.3	2.3	13.7	1.2	88.7	38.3
13 V	19.9	4.0	32.9	1.7	170.8	70.8
14 V	29.2	8.7	82.3	2.7	289.7	100.5
15 V	39.9	13.9	169.4	5.3	432.1	136.5

[a]12468 measured pixels

With Figure 4.19 to Figure 4.21 and Table 7.1 to Table 7.3, it is evident that the measured pion counts/frame are significantly higher than the calculated value of 75 kHz and optimal value of 1.554 MHz. Furthermore, with increased bias voltage there is a distinct increase in counts. Table 4.3 provides the average pion counts/frame ($\bar{x}$) and standard deviation (σ) for each pion experiment vs SPAD bias voltage and plotted in Figure 4.22. From the figure it is evident that the increase in average counts is linear for an increase in SPAD bias voltage. The standard deviation for experiment 4 is

significantly larger as a result of the gradual increase in pion beam intensity during irradiation.

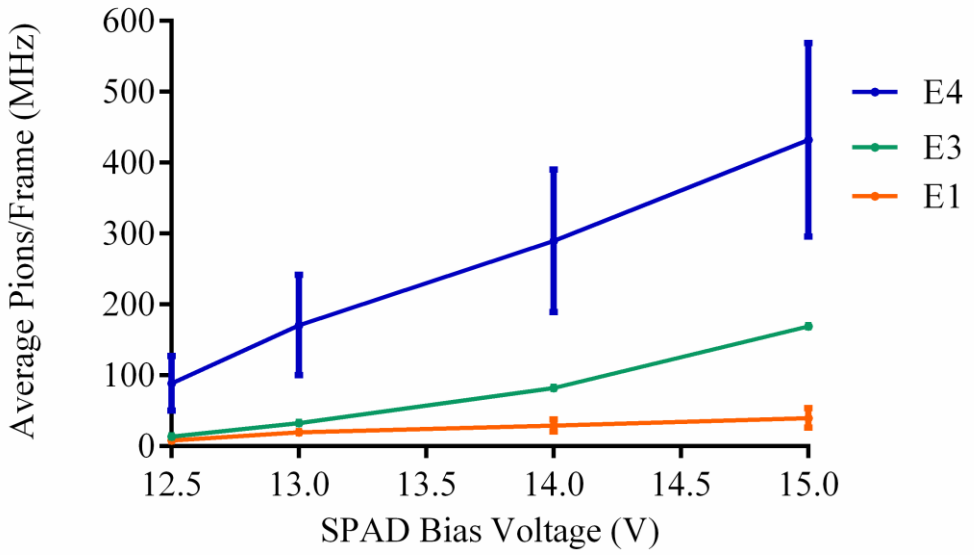

Figure 4.22. Average pion counts/frame including standard deviation as a function of SPAD bias voltage for each respective pion experiment.

4.5.2 High Energy Electron Experiment

For the high energy electron experiment only one set of irradiation measurements was taken. For the experiment a control set of data was taken before irradiation, and HDCR pixels filtered. A total of 5000 frames of control data was taken at each SPAD bias voltage, except at 12.5 V. Based on the results in the pion experiment, and the limited beam time, it was decided to remove measurements at 12.5 V. The experimental procedure was the same as in the pion experiment, once a predefined number of frames captured, the SPAD bias voltage was changed from 13 V to 14 V to 15 V in turn until cycle complete, followed by a new cycle of measurements and so forth, until beam run had ended. Thereafter, a control set of data of 10000 frames was taken. A total of 26000 frames were taken at 14 V and 15 V, whereas 65000 frames were taken at 13 V.

With the DCR calculated for each respective bias voltage, a HDCR list of pixels for the MINI3D SPAD image sensor used was acquired. A total of 2221 pixels were flagged as HDCR pixels and removed from data analysis, which equates to approximately 14.5 % of all pixels. A heatmap of the flagged HDCR SPAD image sensor array is shown in Figure 4.23, with HDCR pixels indicated in black.

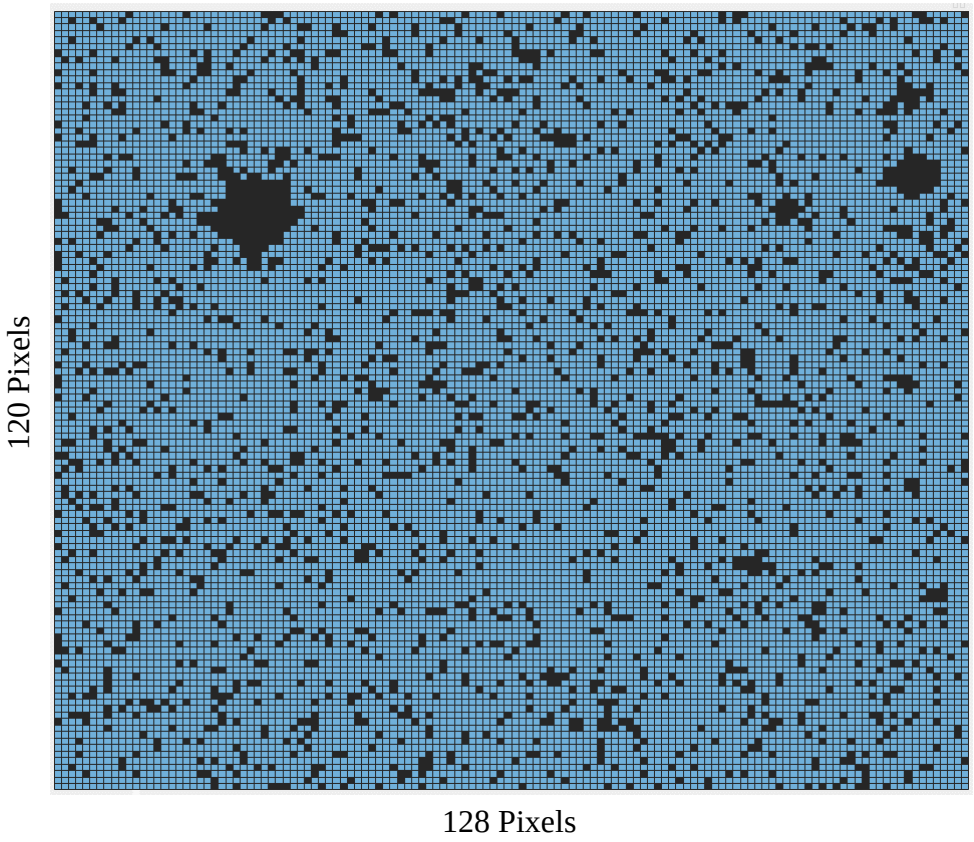

Figure 4.23. HDCR pixel heatmap for MINI3D CMOS SPAD image sensor used for high energy electron beam experiment. HDCR pixels indicated in black.

For the high energy electron detection experiment, the average counts/pixel vs frame for before, during and after irradiation (separated by vertical dotted lines) is combined for each SPAD bias voltage and shown in Figure 4.24. During initial irradiation no discernible detection was measured, therefore, a position sweep test was directed using the 3D-motorised stage on the telescope to attempt positioning of the SPAD image sensor within the beam line. However, during the sweep test at 13 V SPAD bias, no apparent detection was observed. Table 4.4 provides a summary of the statistical results for the high energy electron beam experiment. From Figure 4.24 and Table 4.4 with each successive measurement the mean gradually increases, however, the average counts/pixel during irradiation measurements lie within 2σ of the controls, therefore, no distinct detection of accelerated electrons at 2.5 GeV. Certain environmental factors like temperature and surrounding ambient light were not controllable.

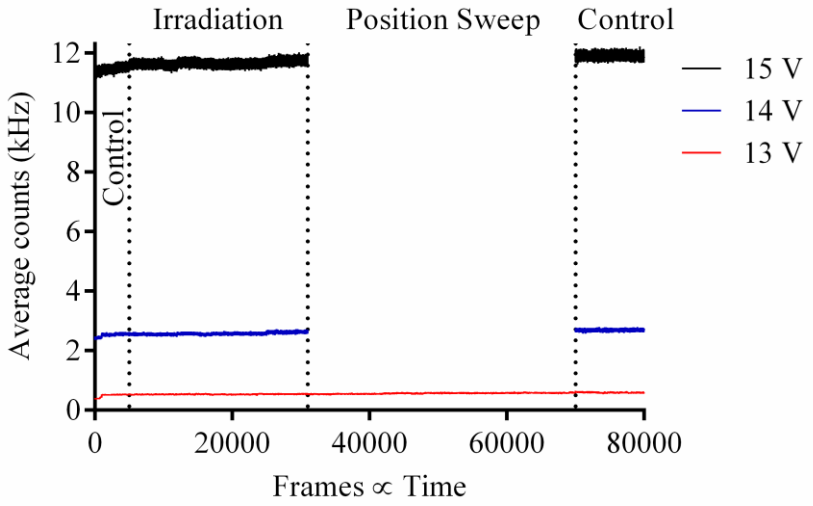

Figure 4.24. High energy electron detection experiment, average counts per pixel vs frame for before, during and after electron beam irradiation for each respective SPAD bias voltage with 2.5 GeV electron beam. Before, during and after irradiation separated by vertical dotted lines.

Table 4.4. Summary of results for high energy electron detection experiment.

SPAD Bias Voltage	Control Before			Irradiation		
	Frame	$\bar{x}$ (Hz)	σ (Hz)	Frame	$\bar{x}$ (Hz)	σ (Hz)
13 V	5000	497.0	50.7	26000	535.3	11.6
14 V	5000	2522.0	54.1	26000	2573.2	39.7
15 V	5000	11460.9	106.8	26000	11653.3	100.1

SPAD Bias Voltage	Position Sweep			Control After		
	Frame	$\bar{x}$ (Hz)	σ (Hz)	Frame	$\bar{x}$ (Hz)	σ (Hz)
13 V	39000.0	566.3	19.7	10000	592.9	15.6
14 V				10000	2689.4	32.7
15 V				10000	11907.8	94.9

4.6 Summary and Conclusion

Successful pion irradiation of the MINI3D SPAD image sensor was achieved. The results presented confirm the detection of high energy pions at 120 GeV using the MINI3D BSI 3D-stacked CMOS SPAD image sensor with the SPS accelerator at CERN. With a mass approximately 270 times larger than that of an electron, it can be concluded that accelerated heavy charged particles are detectable using CMOS SPADs.

For the pion detection experiments, the measured average counts per frame are significantly larger than the calculated range of 75 kHz to 1. 55 MHz, with a minimum measured average counts/frame of 8.3 MHz at a SPAD bias voltage of 12.5 V and a maximum of 432.1 MHz at 15 V during pion irradiation. Furthermore, there is a positive linear correlation between the average counts and increasing SPAD bias voltage.

The increase in counts may be attributed to increased impact ionisation, electromagnetic cascade, afterpulsing and crosstalk. Additionally, electron-hole pair generation in the silicon bulk may occur, causing secondary free carriers to drift into the depletion region resulting in additional spurious counts. Regardless, the exact intensity and total number of incident pions per frame is unknown, therefore further investigation is required to investigate the particle detection efficiency of the device, including other types of heavy charged particles. After pion irradiation, the SPAD image sensor DCR was permanently altered as a result of ionising radiation damage.

For the high energy electron detection experiment, only one set of irradiation measurements was taken, and the results are inconclusive. It was disclosed after the irradiation that the electron beam intensity was below 6.25 MHz and was measured to be approximately 50 kHz with a minimum intensity of 12 kHz, as a result of beam faults and technical difficulties. This equates to approximately 470 Hz or 0.47 electrons/frame. Therefore, coupled with the measured DCR, the probability of detection is unfeasible, and further experimentation is required.

The following chapter reports on the application of the MINI3D CMOS SPAD image sensor for the detection of higher energy photons (X-rays) using tungsten target X-ray tubes.

5. X-Ray Detection using SPADs

With the known capability of SPADs to detect photons within the visible spectrum [71], accelerated electrons in the keV range [160], and high energy pions, the present chapter reports on the application of the MINI3D CMOS SPAD image sensor for the detection of higher energy photons, X-rays.

The chapter first provides an overview of X-rays followed by the production of X-rays and its respective spectrum. Thereafter, the set-up for each experiment is given, followed by experimental results. And finally, a summary and conclusion of the results is provided.

5.1 Shift in the Electromagnetic Spectrum

X-rays were discovered in 1895 by Wilhelm Röntgen at the Julius-Maximilians University of Würzburg in Bavaria, and united with the discovery of the electron, helped develop the modern theory of atomic physics, resulting in significant progresses and development in various areas of research, particularly medical research and diagnostics, e.g. X-ray imaging, the discovery of the molecular structure of DNA and development of computer assisted tomography [180]–[184]. For an extensive overview and history on X-rays and the ensuing years of research and discovery that followed, the reader is redirected to [180].

X-rays are electromagnetic radiation and have the same characteristics as photons within the visible spectrum, however with much shorter wavelengths. The wavelengths of X-rays range from approximately 80 nm to 0.01 nm [180]. Electromagnetic radiation with short wavelengths are comparable to the size of atoms, 0.1 to 0.5 nm, therefore the photon behaves more like a particle than a wave, with the particle behaviour dominating with individual atomic structure interactions [14], [180], [185]. The electromagnetic radiation energy in eV is related to the frequency or wavelength of the photon and is calculated as follows,

$$E = hv \tag{5.1}$$

where h is Planck's constant = 6.626 $\times 10^{-34}$ J·s and v the electromagnetic radiation frequency. The frequency of a photon is calculated as follows,

$$v = c/\lambda \tag{5.2}$$

where c is the speed of light and λ the wavelength. With equations 5.1 and 5.2, the electromagnetic radiation can be expressed as a wavelength, frequency or energy. An illustrated electromagnetic spectrum and tabulated conversion table between wavelength, frequency and energy is shown in Figure 5.1 [186]. With the known wavelength of X-rays, the calculated energy range is approximately 15 eV to 124 keV.

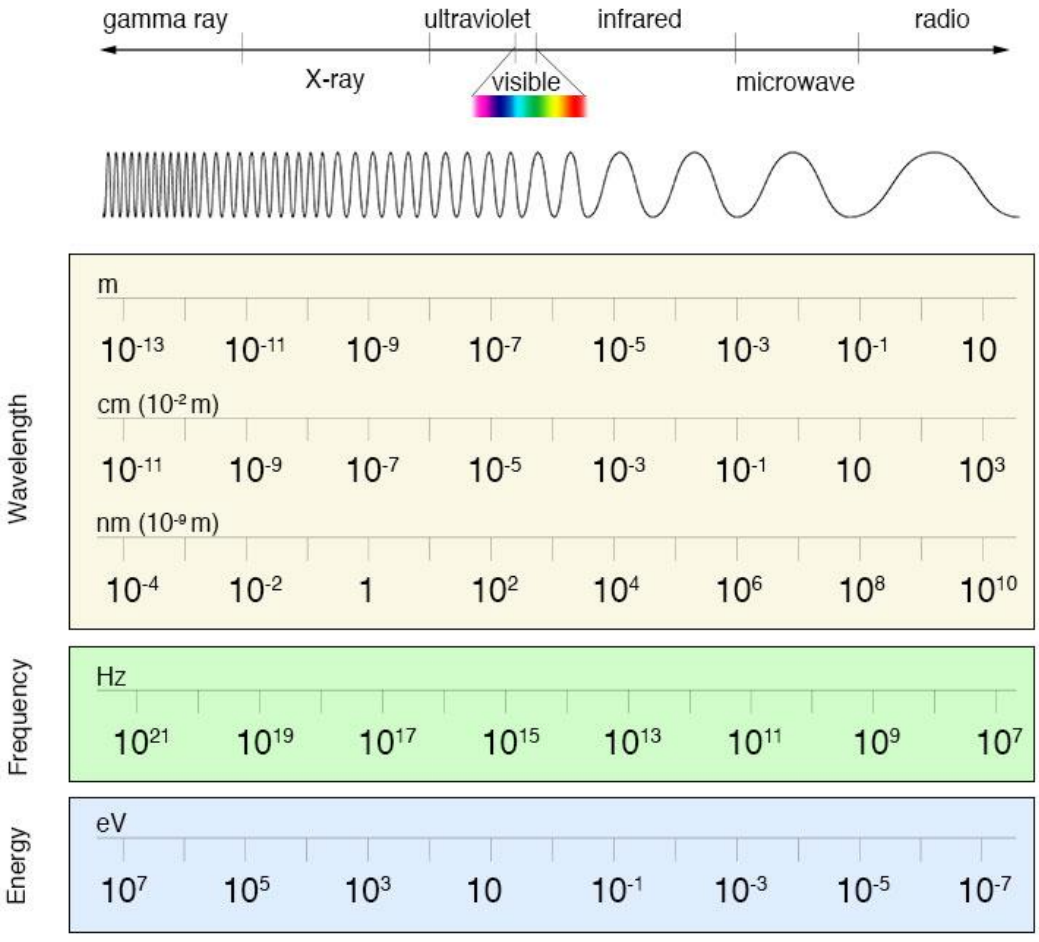

Figure 5.1. Electromagnetic spectrum, with conversion table between wavelength frequency and energy [186].

An incident photon interacts with matter primarily in one of four processes, namely:

1. Elastic or coherent Rayleigh scattering, where the incident photon loses no energy and the atom gains no energy, but the photon is scattered in an alternative direction and the atom remains in its original state.
2. Inelastic scattering also known as incoherent or Compton scattering, is where the incident photon transfers energy to an atomic electron, resulting in removal of the electron from the atom (ionisation) and a subsequent secondary photon is emitted with lower energy.
3. Photoelectric absorption is when a photon is completely absorbed, losing all its energy to an atomic electron, which is then ejected from the atom (ionisation). The vacancy in the shell is filled by a higher energy outer electron resulting in either the emission of a photon (fluorescence) or removal of another outer electron (Auger electron).
4. Pair production is when a photon is eliminated, and an electron-positron pair is generated. This photon interaction predominantly occurs for photon interactions with energies in the MeV range.

An extensive explanation of photoelectric absorption, coherent Rayleigh scattering, Compton scattering, pair production and photon cross-sections is given in [14]. Moreover, there are other possible processes for which photons interact with atomic electrons and nuclei, however the probability of such processes occurring are considered negligible. An overview of these additional interaction processes are also provided in [14].

5.2 X-Ray Tubes

5.2.1 Fundamental principles

For X-ray generation the most common source used is an X-ray tube. In an X-ray tube an electron beam is used, as in a SEM, where the electrons produced through thermionic emission are accelerated towards a fixed target, where the accelerated electrons interact with the target material atoms and lose energy through multiple processes [180]. An overview of these processes are already covered in sections 3.2 and 3.3 and illustrated in Figure 3.6. Nevertheless, the electron interactions of interest

for X-ray generations are radiative energy loss, as a result of inelastic scattering of electrons, which accounts for approximately 1 % of all accelerated electron energy loss [14], [180]. The two predominant forms of radiative energy loss resulting in electromagnetic radiation emission are Bremsstrahlung and characteristic X-ray production. Figure 5.2 provides an illustration of electromagnetic radiation emission in an X-ray tube as a result of accelerated electrons incident upon a fixed tungsten (W) target. In section 3.2 an overview on electron accelerations is given, where the applied voltage V_a, determines the kinetic energy of the accelerated electrons.

Illustrated in Figure 5.2 there is a filter placed within the path of the generated X-rays, this is done to selectively attenuate certain wavelengths for monochromatic X-rays and filter lower energy photons. For medical imaging, lower energy photons do not contribute to X-ray imaging as the photons do not pass through the patient soft tissue and are thus absorbed, therefore filtering is required to minimise radiation exposure to the patient. [180]

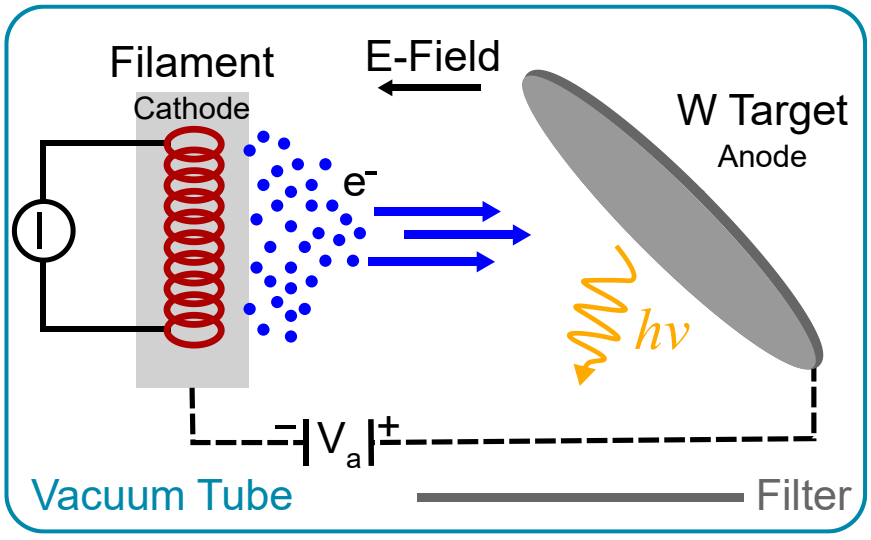

Figure 5.2. Illustration of X-ray tube operation with the generation of X-rays as a result of radiative energy loss of incident accelerated electrons upon a fixed tungsten (W) target within a vacuum tube.

5.2.2 X-ray Mass Attenuation Coefficient

The X-ray mass attenuation coefficient, μ/ρ in cm^2/g is used to calculate the penetration depth of photons in matter [187]. The mass attenuation coefficients for atomic numbers Z = 1 to 92 have already been calculated and are available in [187]. The mass attenuation coefficient is calculated as follows,

$$\mu/\rho = \frac{\ln(I_o/I)}{x} \tag{5.3}$$

where I_o is the incident intensity for a narrow beam of monochromatic photons, I the emerging intensity and x the mass thickness in g/cm^2. The mass thickness is the product of the incident material density ρ, and its thickness t. With I_o, t and μ/ρ known, the emerging photon intensity I can be calculated using equation 5.3.

5.2.3 Continuous X-Ray Spectrum

Bremsstrahlung which means breaking radiation, occurs as a result of coulomb interactions between the accelerated electron and atomic nucleus resulting in inelastic scattering and deceleration of the transient electron. This radiative energy loss results in electromagnetic radiation emission. Figure 5.3 provides an illustration of Bremsstrahlung production. [180]

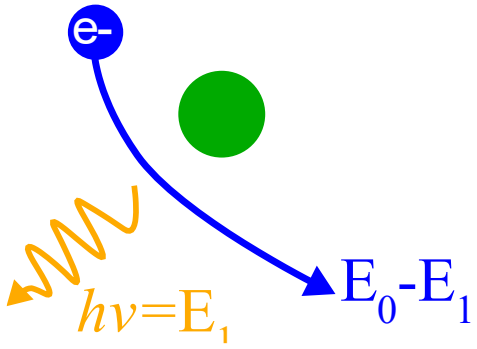

Figure 5.3. Bremsstrahlung radiation as a result of coulomb interactions between transient electron and atomic nucleus, resulting in electromagnetic radiation emission.

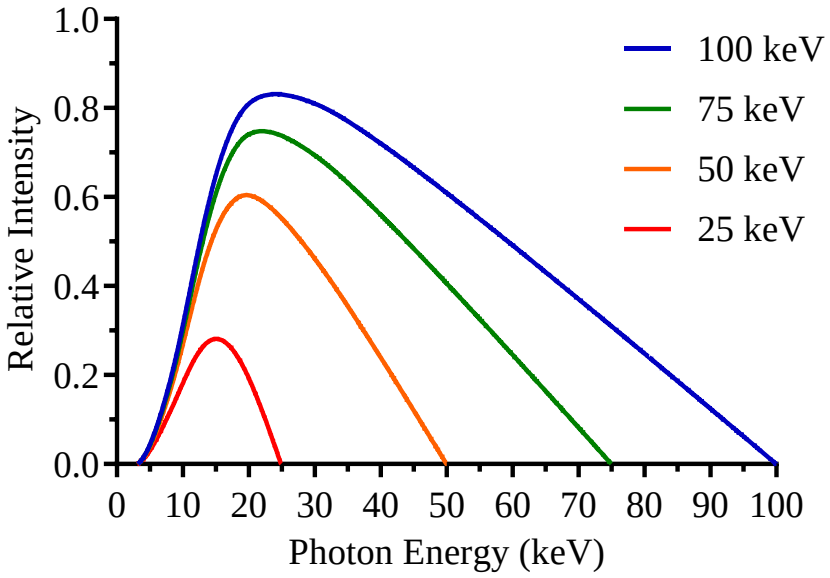

Figure 5.4. Example of continuous X-ray spectrum, showing relative intensity as a function of photon energy (keV) with increasing applied voltage V_a.

Bremsstrahlung for a given target is a continuous process for the incident electron as it experiences continuous inelastic scattering as a result of multiple coulomb interactions, resulting in steady loss of energy. This gradual loss of energy results in a continuous spectrum of generated photons. The shape of the continuous spectrum including intensity and maximum photon energy is dependent on the applied voltage V_a. Figure 5.4 illustrates a typical continuous spectrum with increasing V_a, for relative intensity vs photon energy in keV, with a 10 keV filter.

5.2.4 Characteristic X-ray Spectrum

The second predominant form of radiative energy loss resulting in electromagnetic radiation emission is the production of characteristic X-rays. Characteristic X-rays are a consequence of electron emission (ionisation) of an inner-shell electron, followed by electron relaxation, in which an outer-shell electron fills the lower-shell electron vacancy to restore atom stability. The electron shell transition results in the emission of an X-ray, with an energy which is distinct of the ionisation energy difference between electron shells. Figure 5.5 illustrates the process of characteristic X-ray emission in four stages. [180], [188]

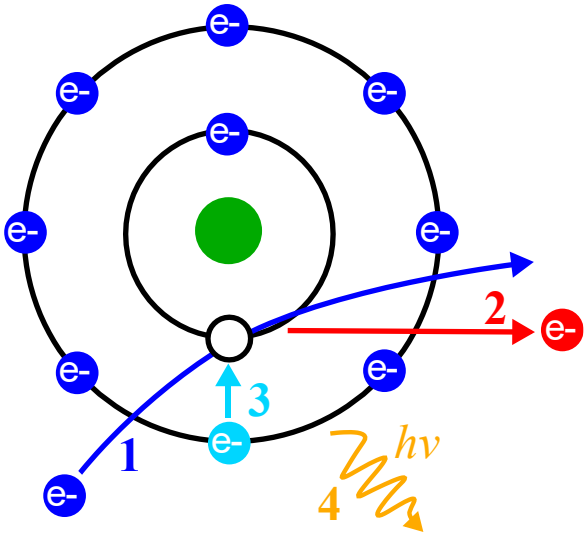

Figure 5.5. Illustration of characteristic X-ray emission process. Firstly, an incident accelerated electron transfers energy to an inner-shell electron. Second, the electron is emitted causing the atom to be ionised. Subsequently, an outer-shell electron transitions to the vacancy in the inner-shell to restore stability, and finally resulting in characteristic X-ray emission.

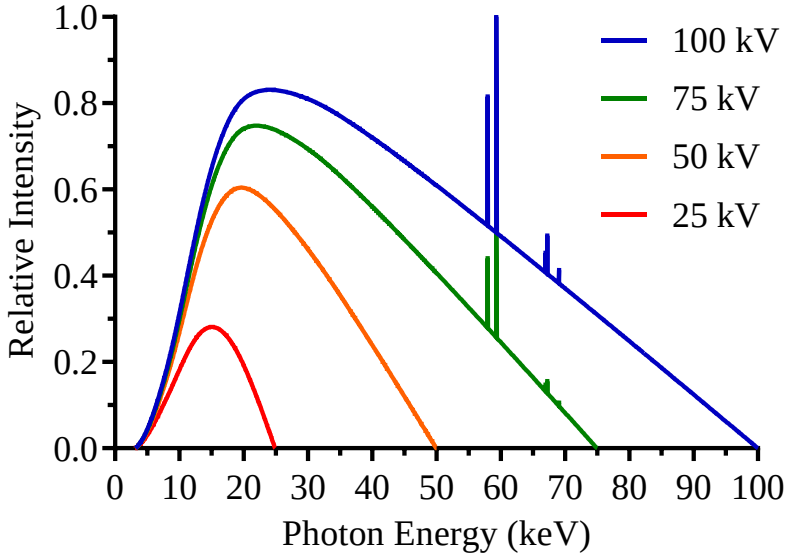

Figure 5.6. Example X-ray spectrum with superimposed continuous spectrum and characteristic X-ray peaks, showing relative intensity as a function of photon energy (keV) with increasing applied voltage V_a.

For every element each subshell has a discrete ionisation energy, therefore the difference between ionisation energies is characteristic of that element, a technique used in X-ray spectroscopy to determine the elemental properties of a sample [185], [189], [190]. Figure 5.6 shows an example X-ray spectrum with characteristic peaks

superimposed on the continuous spectrum. A concise document on element X-ray properties, including binding and emission energies, fluorescence yield, mass absorption coefficients etc. is available in [191].

5.3 Experimental Setup

For the investigation of X-ray detection using the MINI3D CMOS SPAD image sensor, two separate X-ray experiments were conducted using two different X-ray sources. The need for a second source was a result of the initial X-ray source requiring maintenance due to operational failure of the stage. However, both sources generate X-rays using a tungsten target with a maximum achievable photon peak energy of 160 and 100 keV respectively. The two experiments are referred to as experiment A and B respectively. The dominant process for photon energy loss is photoelectric absorption for photon energies $E \lesssim 100$ keV, and Compton scattering for photon energies $E \lesssim 1$ MeV, for elements where the atomic number, $Z \lesssim 30$.

5.3.1 X-ray Experiment A

For experiment A, the standard Precision X-ray IR-160 biological irradiator was used. The cabinet X-ray irradiator has a large, shielded cabinet with a motorised stage (1 cm tolerance), and cabinet port to feed electrical cables within. For all experiments, the SPAD was placed as close as possible to the source, approximately 10 cm away and the FPGA was shielded using lead blocks. The maximum output voltage of the X-ray tube is 160 kV at a current of 18.75 mA, with a maximum achievable current of 25 mA at output voltages up to 120 kV. The X-ray tube has an inherent beryllium filter with thickness of 800 µm, and in addition, an aluminium filter slide with thickness of 100 µm was used for all measurements. [192]

The mass attenuation coefficients and densities for beryllium and aluminium are given in [187] and [145] respectively. With the known filter properties and thicknesses, the relative intensity X-ray spectrums for tungsten for increasing output voltage, are determined and shown in Figure 5.7, with characteristic peaks labelled at 57.98 keV, 59.32 keV and 67.24 keV respectively. Table 5.1 provides the photon energies of principal K-, L- and M-shell emission lines for tungsten (W) with relative shell

intensities. From the figure, photons energies $\lesssim$ 10keV are filtered from the spectrum as a result of the beryllium and aluminium filters.

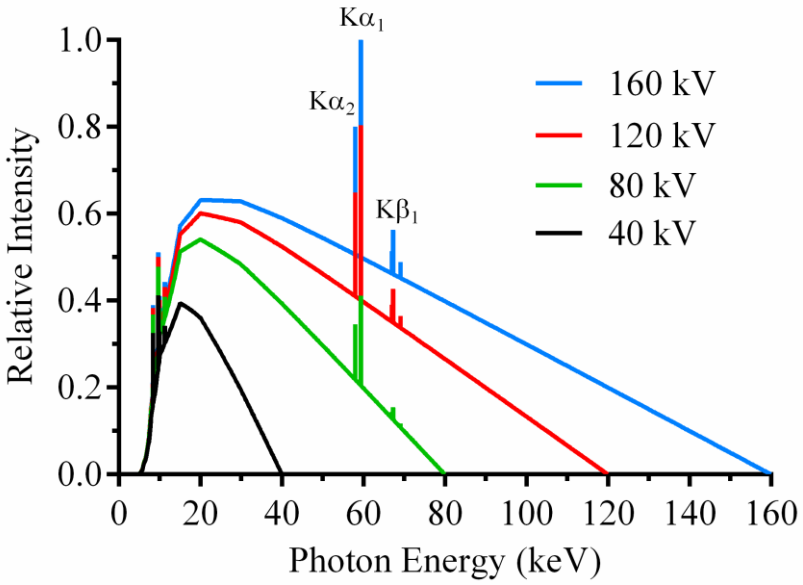

Figure 5.7. Tungsten X-ray spectrum with relative intensity as a function of photon energy (keV), with increasing output voltage.

Table 5.1. Photon energies in eV, of principal K-, L- and M-shell emission lines for tungsten (W) with relative shell intensity.

$K\alpha_1$	$K\alpha_2$	$K\beta_1$	$K\beta_2$	$L\alpha_1$
59 318.24	57 981.7	67 244.3	69 067.0	8 397.6
100	58	22	8	100

$L\alpha_2$	$L\beta_1$	$L\beta_2$	$L\gamma_1$	$M\alpha_1$
8 335.2	9 672.35	9 961.5	11 285.9	1 775.4
11	67	21	13	100

The X-rays emitted from the X-ray tube will be incident upon silicon, Z = 14, before reaching the SPAD depletion region. With the mass attenuation coefficients for silicon in [187], and known density of silicon in Table 3.2, the approximate attenuation length as a function of photon energies is calculated for 10 to 160 keV and shown in Table 5.2. It is evident that all photons with energies E $\geq$ 10 keV, will propagate through the SPAD depletion region.

Table 5.2. Approximate Photon Attenuation Lengths in Silicon [187].

Kinetic Energy (keV)	Attenuation Coefficient μ/ρ (cm^2/g)	Approximate Attenuation length (mm)[a]
10	33.89	0.127
15	10.34	0.415
20	4.464	0.962
30	1.436	2.99
40	0.7012	6.12
50	0.4385	9.79
60	0.3207	13.39
70	0.2638	16.27
80	0.2228	19.27
90	0.2011	21.35
100	0.1835	23.40
120	0.1650	26.03
140	0.1508	28.48
160	0.1407	30.51

[a]Silicon density, 2.329 $g \cdot cm^{-3}$

5.3.2 X-ray Experiment B

For experiment B, the GLADD lab-based X-ray tube was used at Glasgow University [193], equipped with a tungsten target for X-ray emission, 150 µm thick aluminium filter and large shielded cabinet. The X-ray setup has a motorised stage to align any sample within the beam path. Alignment is also optimised with a cross laser pointer, shown in Figure 5.8, which allows for optimal positioning of the SPAD image sensor in the X-ray beam. The X-ray source has an output voltage range of 20 to 100 kV with an electron beam current range of 3 to 17 mA, but the maximum beam current for an output voltage of 100 kV is 9 mA.

Furthermore, as in experiment A, the SPAD image sensor was placed approximately 10 cm from the X-ray source, and Figure 5.9 provides a dose rate map of the incoming X-ray beam at 10 cm from the source, with an output voltage of 100 kV, measured using a pin diode. From Figure 5.9 the approximate maximum dose rate at 100 kV is 1.3 Mrad/h, with a nominal dose rate of 1.2 Mrad/h. Figure 5.10 shows the measured relative intensity X-ray spectrum for output voltages of 100 kV, with distinct characteristic peaks. Both the measurements and data required to develop Figure 5.9

and Figure 5.10 were provided by Dr. Dima Maneuski from the University of Glasgow [194].

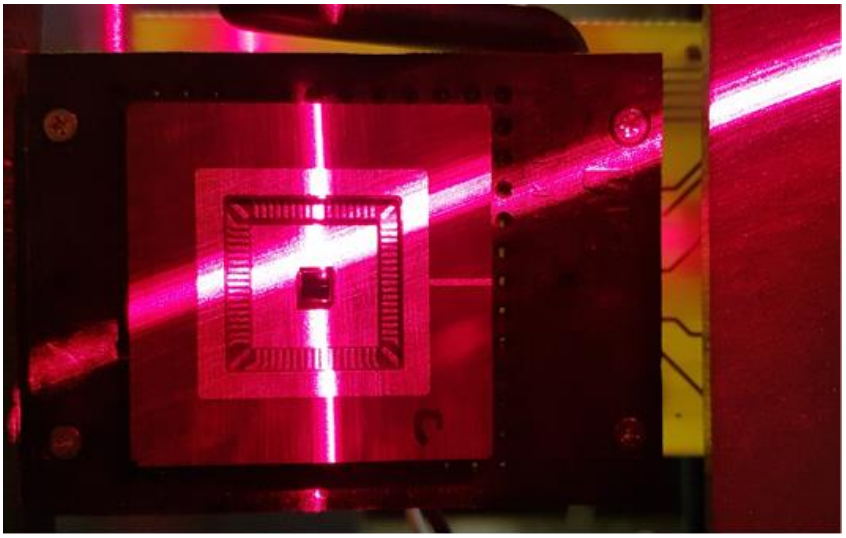

Figure 5.8. MINI3D CMOS SPAD image sensor alignment and positioning using a cross laser pointer, within the GLADD X-ray tube chamber for X-ray experiment B.

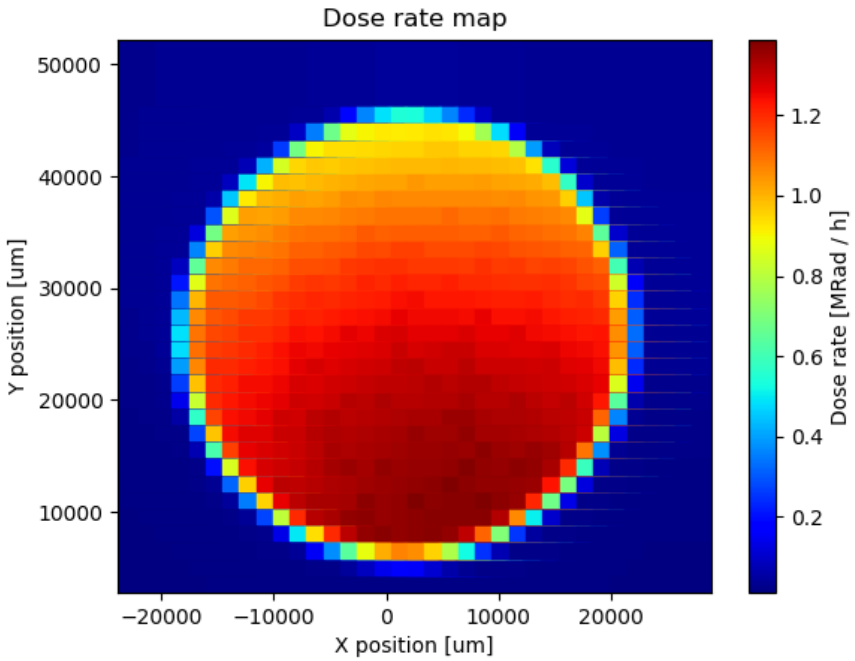

Figure 5.9. Dose rate map of X-ray emission, measured in Mrad/h, at a distance of 10 cm from the GLADD X-ray source at 100 kV output voltage, with 150 µm Al filter.

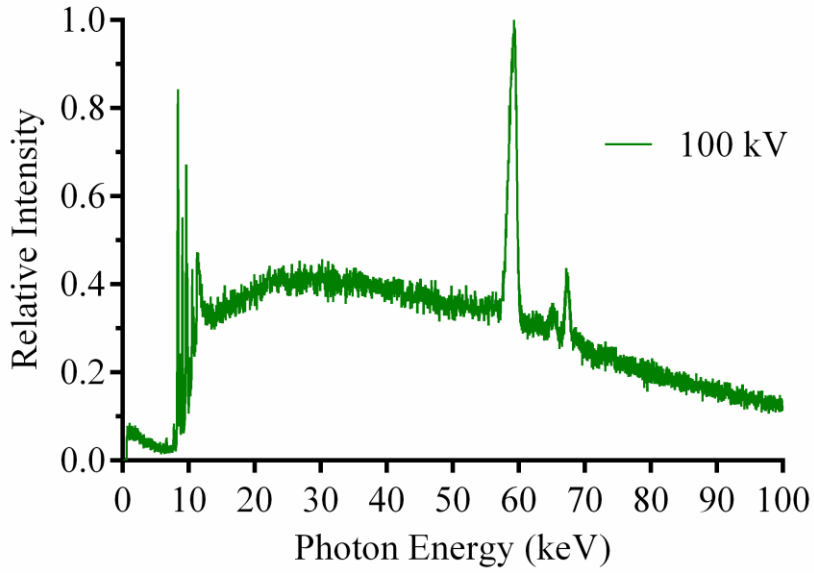

Figure 5.10. Measured X-ray spectrum for GLADD X-ray source at 100 kV output voltage, with tungsten target and fixed 150 µm Al filter.

5.4 Experimental Results

5.4.1 X-ray Experiment A

As mentioned *supra*, the results obtained were limited as a result of required maintenance and stage replacement in the X-ray chamber due to operational failure. For irradiation the four regularly used SPAD bias voltages were selected, namely 12.5, 13, 14 and 15 V for comparison, and for all experiments the frame exposure time was set to 1 ms. For each SPAD bias voltage a control set of data of 10000 frames was taken before irradiation and HDCR pixels identified.

The first experiment was to investigate if X-rays could be detected. The SPAD image sensor was irradiated with X-rays with varying peak photon energies from 15 to 120 keV, with a fixed beam current of 25 mA. For each irradiation 400 frames were taken. An increase in X-ray source output voltage above 120 keV results in a decrease in available beam current, therefore omitted from the initial experiment. Figure 5.11 and Figure 5.12 show the measured average counts/pixel including standard deviation at each respective bias voltage as a function of X-ray peak photon energy. From the figures it is evident that exposure to X-rays results in an increase in average accounts, which confirms X-ray detection. It is observed at 80 keV there is a distinct drop in

average counts/pixel measured, discussed further in section 5.4.3. The statistical data for Figure 5.11 and Figure 5.12 is summarised in Table 7.4.

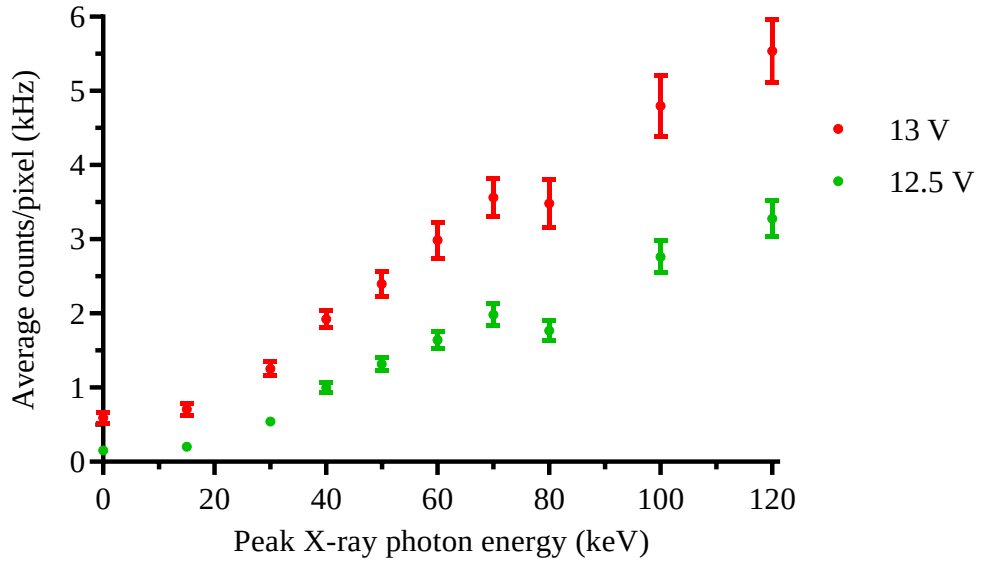

Figure 5.11. Average counts/pixel and standard deviation at SPAD bias voltage of 12.5 and 13 V as a function of peak X-ray photon energies from 0 to 120 keV.

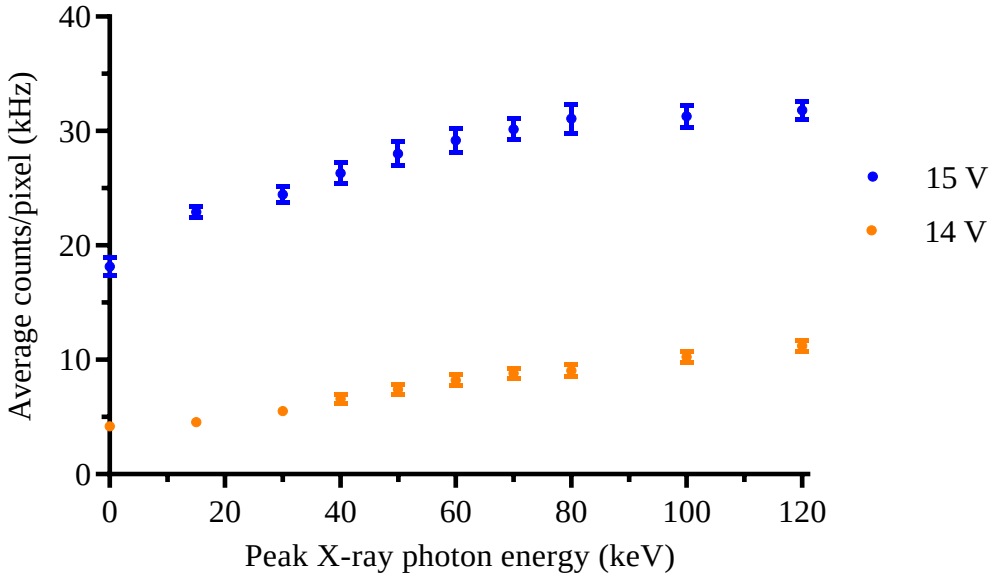

Figure 5.12. Average counts/pixel and standard deviation at SPAD bias voltage of 14 and 15 V as a function of peak X-ray photon energies from 0 to 120 keV.

Figure 5.13 shows the relative increase in average counts/pixel at each SPAD bias voltage as a function of increasing peak photon energy. It is observed that an increase in SPAD bias voltage, results in higher average counts/pixel, however the standard

deviation also increases as expected, which affects the discernible detection of X-rays at lower peak photon energies, in this case 15 keV.

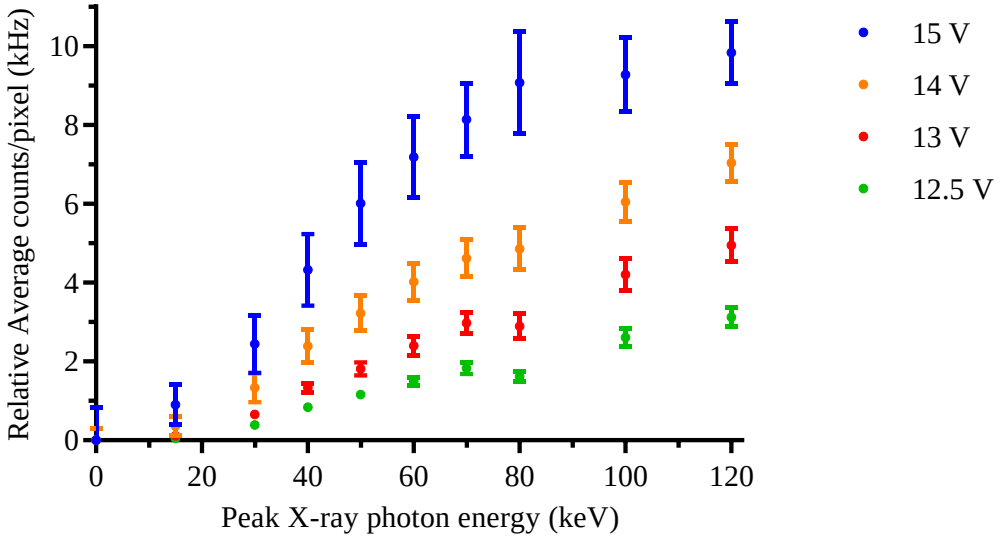

Figure 5.13. Relative average counts/pixel including standard deviation for SPAD bias voltages 12.5 to 15 V, as a function of peak X-ray photon energy from 0 to 120 keV.

The following experiment investigates the average counts/pixel for each respective bias voltage, 12.5 to 15 V, for X-ray peak photon energies of 15 and 30 keV for comparison. During irradiation 400 frames are captured and the X-ray source is switched on for approximately 15 seconds to observe the frame-by-frame response and transition during irradiation. Figure 5.14 to Figure 5.17 show the normalised average counts/pixel for each respective bias voltage over 400 frames. For SPAD bias voltage of 12.5 V the detection of X-rays at 15 keV is evident with a clear increase in average counts during irradiation, however when compared to 13 V and above, the inherent DCR deviation and RTS noise is too large to conclusively discern detection. Therefore, at a SPAD bias voltage of 12.5 V, X-rays with peak photon energy of 15 keV is detectable. Figure 5.18 to Figure 5.21 show the normalised average counts/pixel for each respective bias voltage over 400 frames for peak photon energies from 30 to 120 keV, where it is evident that a SPAD bias voltage of 12.5 V provides the best SNR for X-ray detection. Two additional irradiation measurements were taken at X-ray source output voltages of 140 and 160 kV, and the results are shown in Figure 7.2 and Figure 7.3 respectively.

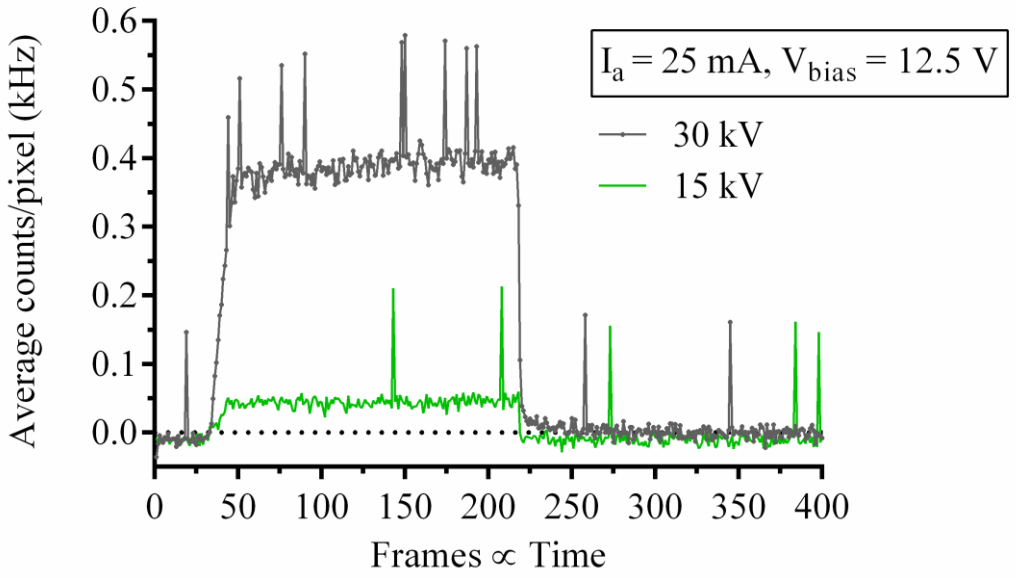

Figure 5.14. Normalised average counts/pixel at 12.5 V SPAD bias voltage over 400 frames for peak photon energies of 15 and 30 keV. During each irradiation the X-ray tube is turned on for approximately 15 seconds.

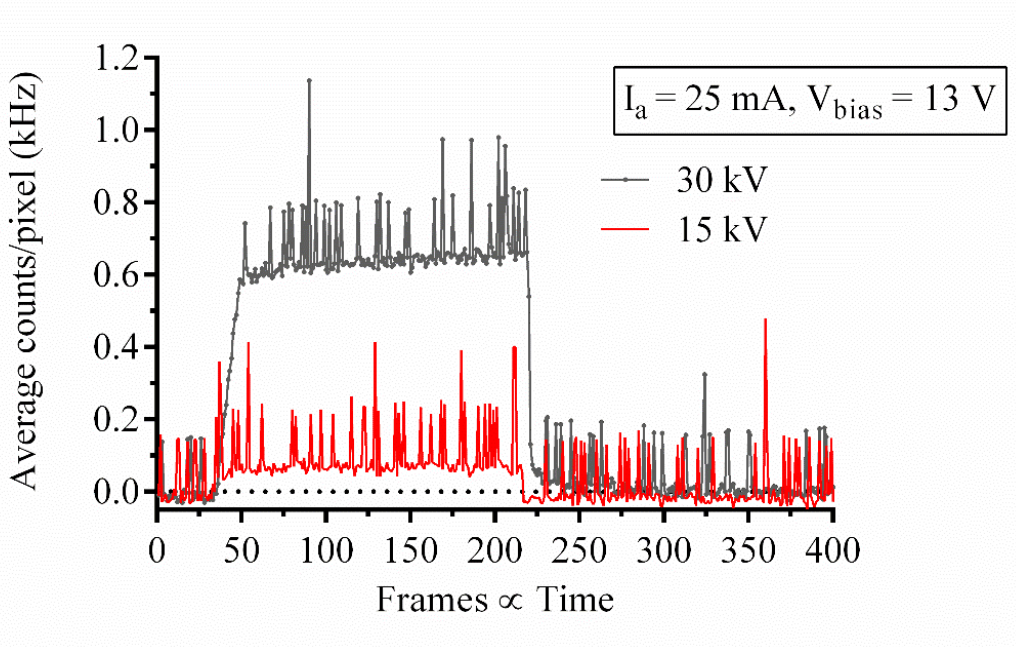

Figure 5.15. Normalised average counts/pixel at 13 V SPAD bias voltage over 400 frames for X-ray irradiation at peak photon energies of 15 and 30 keV. During each irradiation the X-ray tube is turned on for approximately 15 seconds.

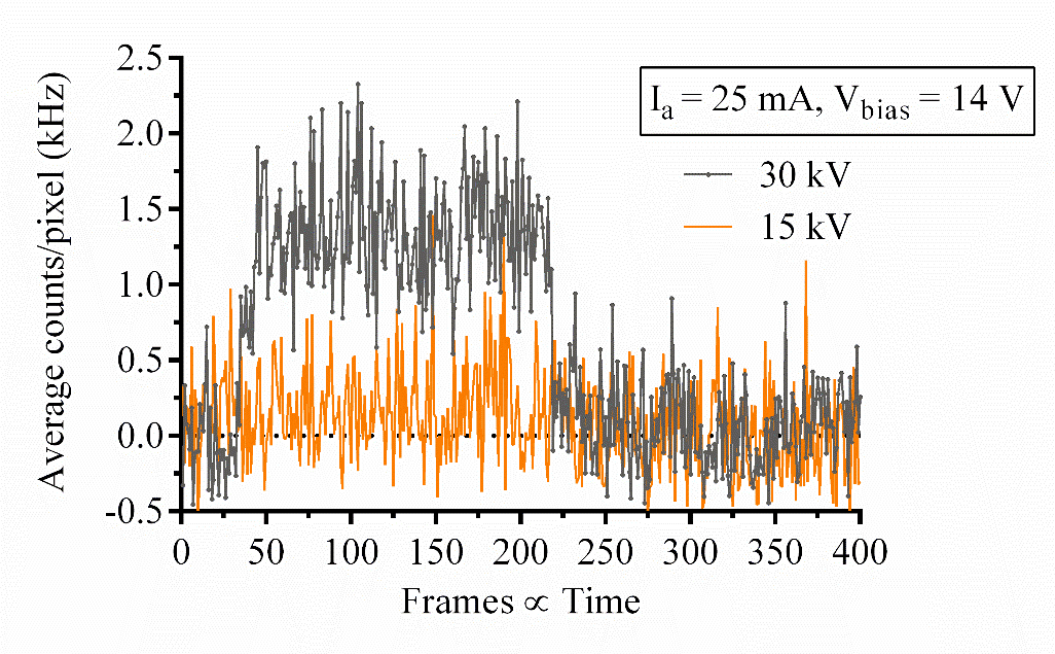

Figure 5.16. Normalised average counts/pixel at 14 V SPAD bias voltage over 400 frames for X-ray irradiation at peak photon energies of 15 and 30 keV. During each irradiation the X-ray tube is turned on for approximately 15 seconds.

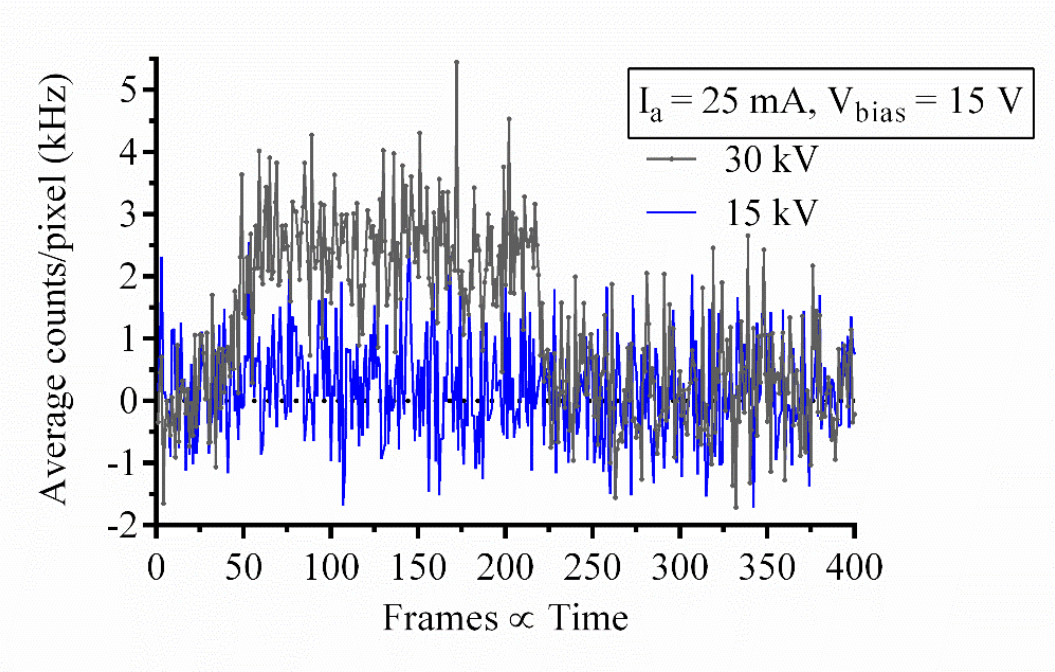

Figure 5.17. Normalised average counts/pixel at 15 V SPAD bias voltage over 400 frames for X-ray irradiation at peak photon energies of 15 and 30 keV. During each irradiation the X-ray tube is turned on for approximately 15 seconds.

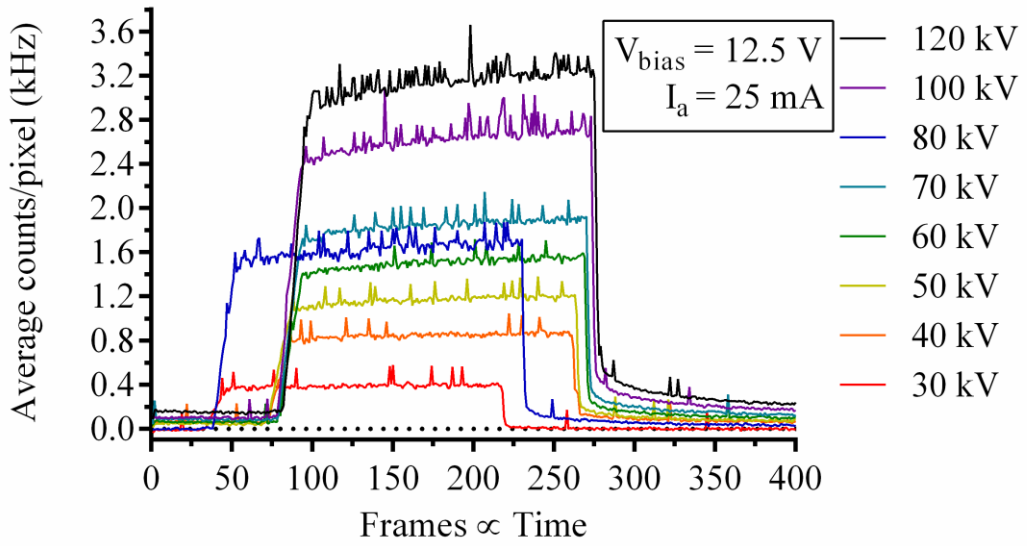

Figure 5.18. Normalised average counts/pixel at 12.5 V SPAD bias voltage over 400 frames for X-ray irradiation at peak photon energies from 30 and 120 keV. During each irradiation the X-ray tube is turned on for approximately 15 seconds.

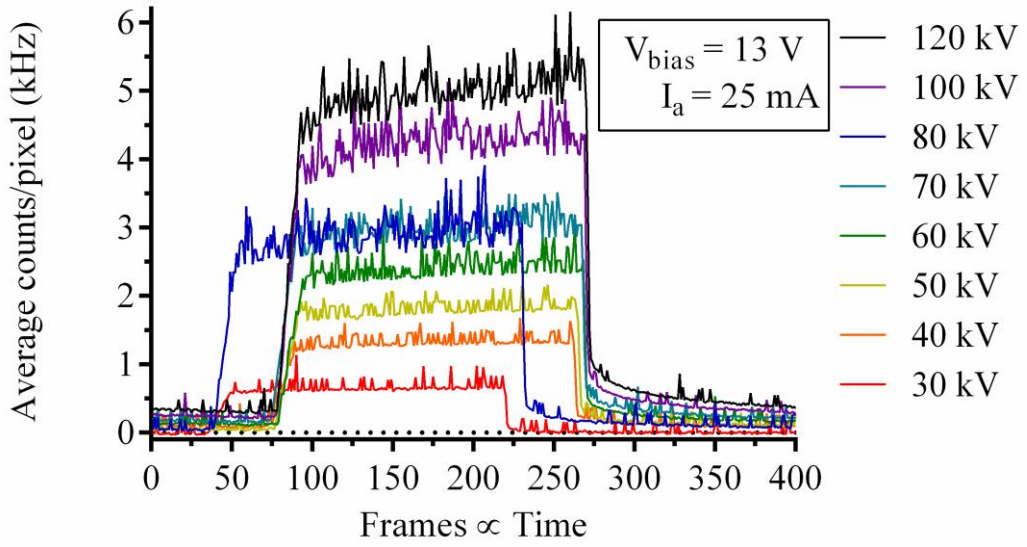

Figure 5.19. Normalised average counts/pixel at 13 V SPAD bias voltage over 400 frames for X-ray irradiation at peak photon energies from 30 and 120 keV. During each irradiation the X-ray tube is turned on for approximately 15 seconds.

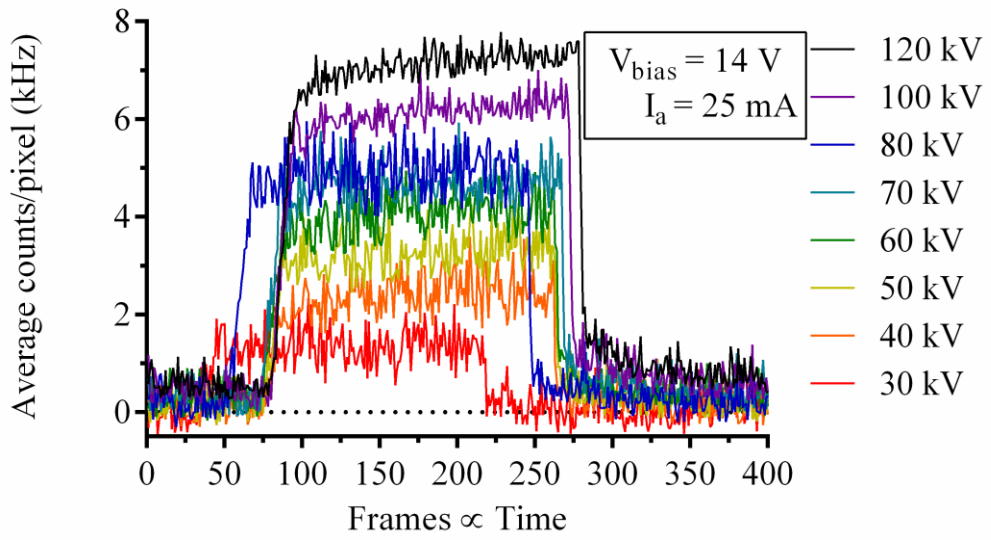

Figure 5.20. Normalised average counts/pixel at 14 V SPAD bias voltage over 400 frames for X-ray irradiation at peak photon energies from 30 and 120 keV. During each irradiation the X-ray tube is turned on for approximately 15 seconds.

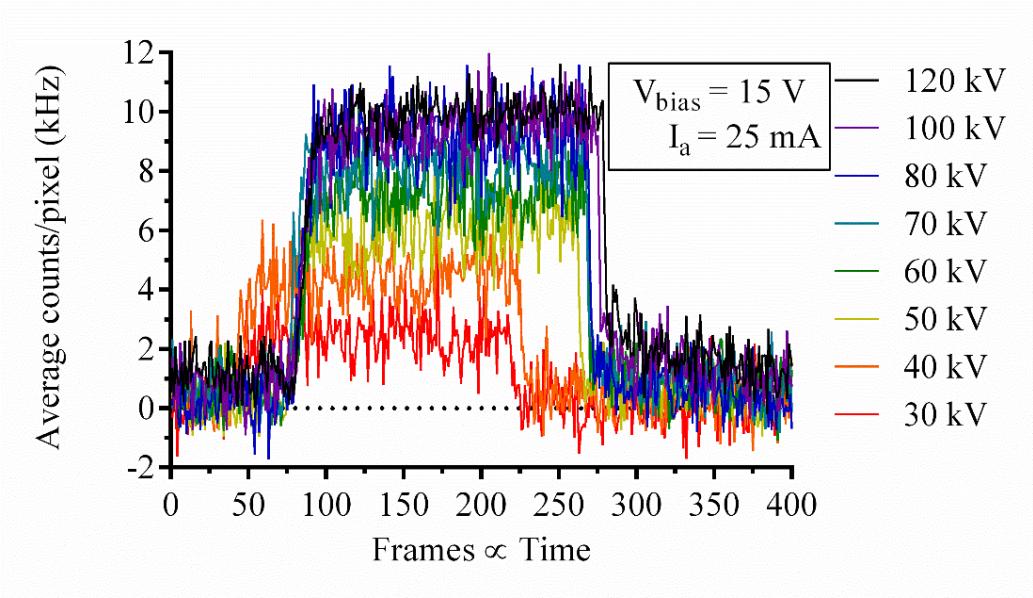

Figure 5.21. Normalised average counts/pixel at 13 V SPAD bias voltage over 400 frames for X-ray irradiation at peak photon energies from 30 and 120 keV. During each irradiation the X-ray tube is turned on for approximately 15 seconds.

5.4.2 X-ray Radiation Hardness Experiment A

After successful detection of X-rays, a radiation hardness experiment was conducted to investigate potential DCR degradation [195]. For hybrid pixel detectors the required X-ray TID tolerance is 50 Mrad, the total expected amount over a 10 year period of

constant radiation at the LHC at CERN, e.g., the ATLAS experiment inner tracker detector [28]. For the Precision X-ray IR-160 biological irradiator, the dose rate calibration of the X-ray tube has already been calculated and the maximum absorbed dose at output voltage of 160 kV and beam current of 18.75 mA is as follows,

$$D = \frac{375}{x^2} \tag{5.4}$$

where D is the TID in Mrad/h and x the distance of the sample from the source in cm [196]. Therefore, with a known SPAD placement distance of 10 cm from the source, a nonirradiated SPAD was irradiated for 1 hour, a calculated TID of approximately 3.75 Mrad or 37.5 kGy. The SPAD DCR was measured before and after irradiation for comparison, where 10 000 frames were taken for each SPAD bias voltage, 12.5 to 15 V. The initial HDCR pixels were removed and the statistical results are presented in Table 5.3, furthermore, DCR distributions for each SPAD bias voltage are shown in Figure 5.22 to Figure 5.25 with bin centres in average counts/frame.

Table 5.3. Statistical results for SPAD DCR before and after 3.75 Mrad TID.

	SPAD Bias Voltage 12.5 V		**SPAD Bias Voltage 13 V**		**SPAD Bias Voltage 14 V**		**SPAD Bias Voltage 15 V**	
	Before	**After**	**Before**	**After**	**Before**	**After**	**Before**	**After**
Frames	10000	10000	10000	10000	10000	10000	10000	10000
	Units: Average Counts per Pixel (kHz)							
Minimum	0.1253	0.0647	0.5190	0.3572	3.5600	2.7060	19.510	15.110
25% Percentile	0.1448	0.0794	0.5553	0.3865	3.9810	3.3150	21.440	17.100
Median	0.1502	0.0835	0.5661	0.3951	4.1600	3.5320	21.980	17.580
75% Percentile	0.1555	0.0876	0.5781	0.4029	4.3550	3.8350	22.530	18.090
Maximum	0.6461	0.2708	1.0760	0.7361	5.6240	5.4190	25.890	20.520
Mean	0.1544	0.0839	0.5920	0.3988	4.1900	3.5940	22.000	17.610
Std. Deviation	0.0288	0.0105	0.0710	0.0300	0.2988	0.3772	0.8059	0.7315
Lower 95% CI of mean	0.0968	0.0629	0.4500	0.3388	3.5924	2.8396	20.388	16.147
Upper 95% CI of mean	0.2120	0.1048	0.7340	0.4588	4.7876	4.3484	23.611	19.073

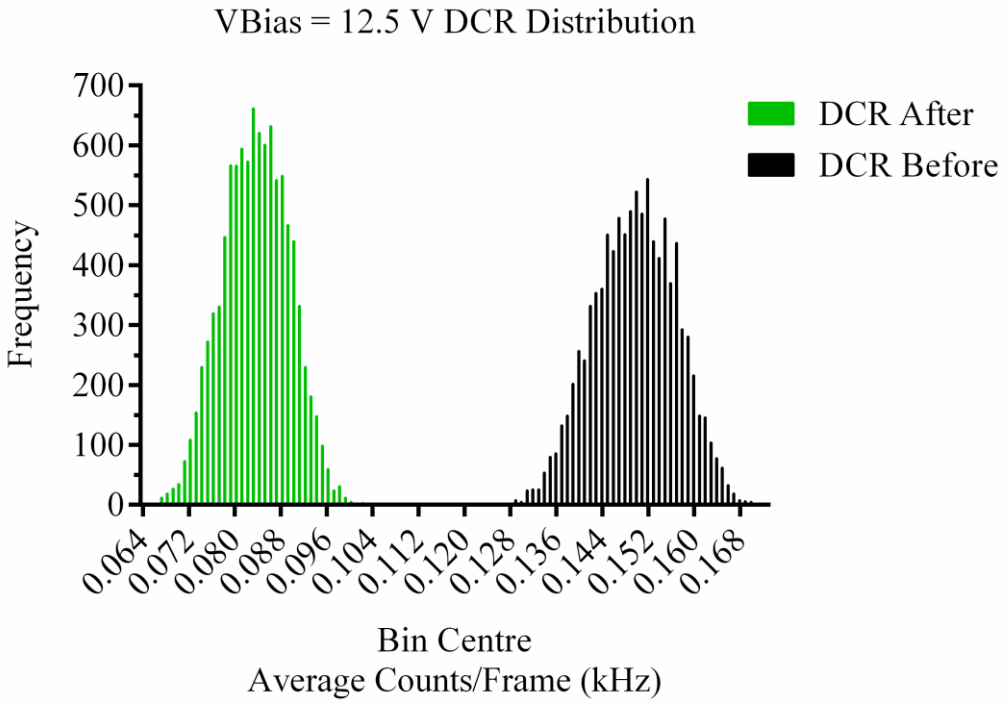

Figure 5.22. DCR Distributions of average counts/frame for MINI3D CMOS SPAD image sensor for before and after 3.75 Mrad TID using Tungsten X-ray tube at SPAD bias voltage of 12.5 V.

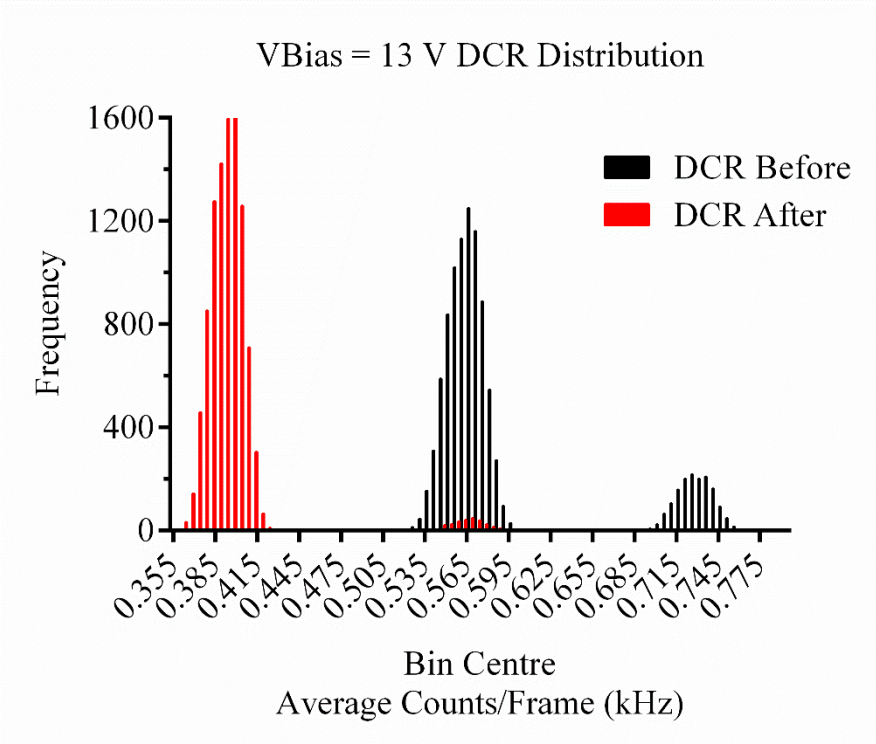

Figure 5.23. DCR Distributions of average counts/frame for MINI3D CMOS SPAD image sensor for before and after 3.75 Mrad TID using Tungsten X-ray tube at SPAD bias voltage of 13 V.

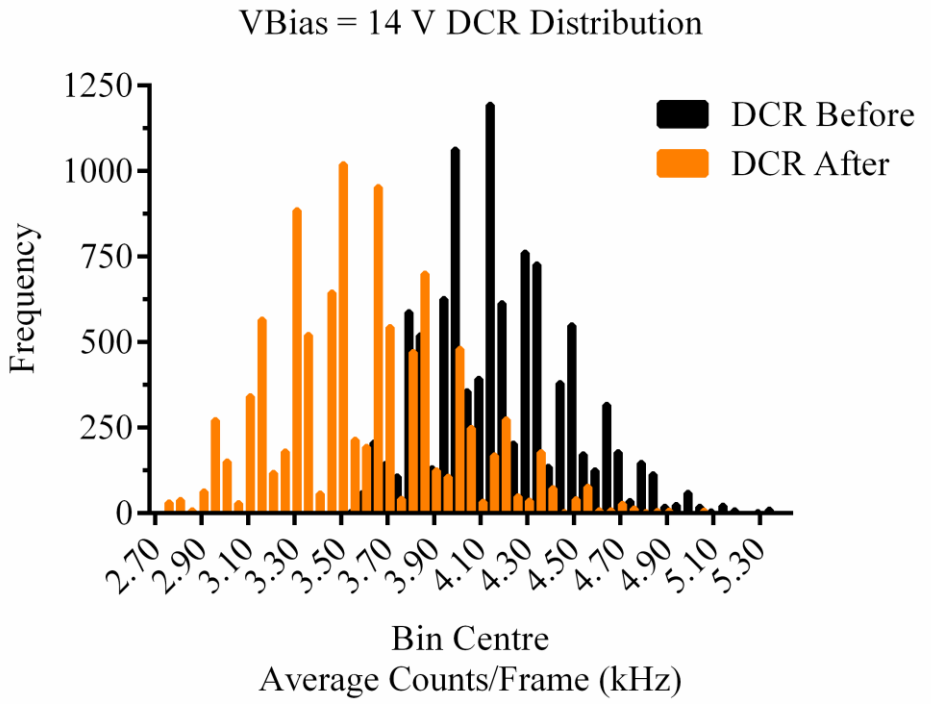

Figure 5.24. DCR Distributions of average counts/frame for MINI3D CMOS SPAD image sensor for before and after 3.75 Mrad TID using Tungsten X-ray tube at SPAD bias voltage of 14 V.

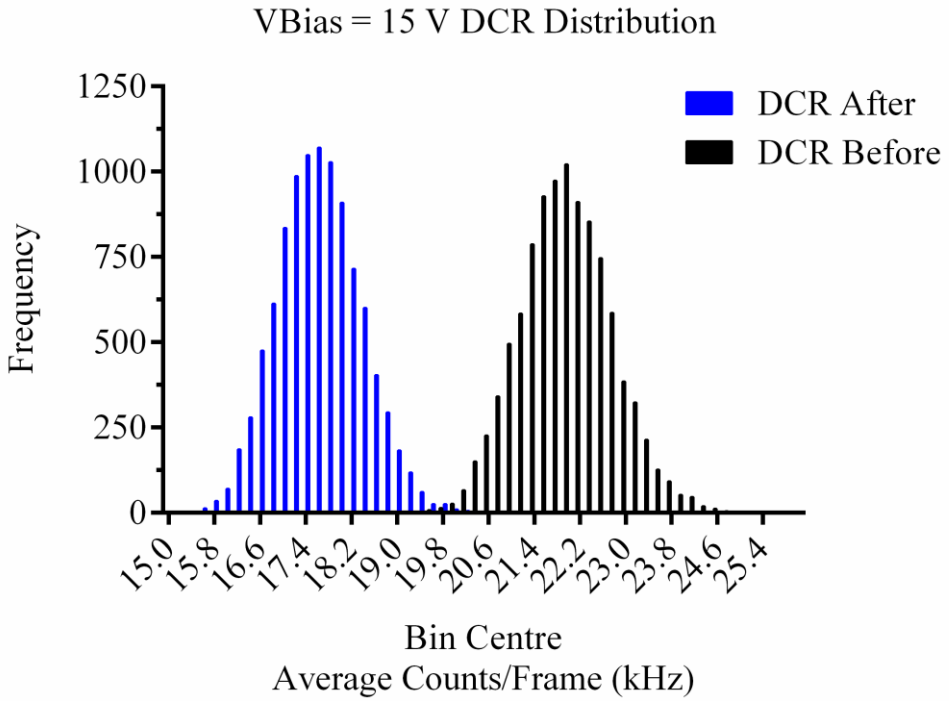

Figure 5.25. DCR Distributions of average counts/frame for MINI3D CMOS SPAD image sensor for before and after 3.75 Mrad TID using Tungsten X-ray tube at SPAD bias voltage of 15 V.

From Table 5.3 and DCR distributions shown in Figure 5.22 to Figure 5.25, the DCR decreases for all SPAD bias voltages after a TID of 3.75 Mrad or 37.5 kGy. This decrease in DCR was also observed in the pion experimental results in section 4.5 in Figure 4.13, where after pion experiment 3 the next set of control data taken before experiment 4 showed a lower DCR for all SPAD bias voltages. There is no significant increase in operational standard deviation and the SPAD image sensor continued to operate typically thereafter, therefore no observed SPAD DCR degradation.

Further radiation hardness experiments were scheduled, but the X-ray irradiator stage required maintenance, therefore experimentation was concluded.

5.4.3 X-ray Experiment B

For experiment B the X-ray tube has an operational output voltage range from 20 to 100 kV, and maximum beam current of 17 mA at 40 and 50 kV, and 9 mA at 100 kV. The initial experiment was to investigate the linear regression of the previous investigation in experiment A, as well as to investigate the distinct drop in average counts/pixel observed at 80 kV.

The SPAD image sensor was placed 10 cm from the source and irradiated with increasing energies from 20 to 100 kV, as well as sweeping the beam current from 3 to 17 mA to investigate the effect of X-ray tube intensity (proportional to input current) and peak photon energy on average counts per frame. Before irradiation a control set of data was taken and HDCR identified. Thereafter, 500 frames for each irradiation was measured. Figure 5.26 to Figure 5.29 show the measured normalised increase in average counts/pixel as a function of peak X-ray photon energy, for SPAD bias voltages 12.5 to 15 V respectively, with beam current sweep from 3 to 17 mA. Furthermore, for Figure 5.26 to Figure 5.29 a second order polynomial (quadratic) regression fitted curve is interpolated for each data set, except for measurements with beam current of 17 mA. From the figures it is evident that for all SPAD bias voltages an increase in both peak photon energy and/or beam intensity result in an increase in average counts. Moreover, the dip at 80 keV is not observed in these measured results, which indicates potential error with the measurement above 80 keV in experiment A, as a repeat measurement was not possible. The X-ray irradiator used in experiment A

did require maintenance on the stage, therefore it is hypothesised that during experimentation, the stage level may have lowered due to a technical fault, increasing the distance between source and detector, resulting in lower average counts/pixel.

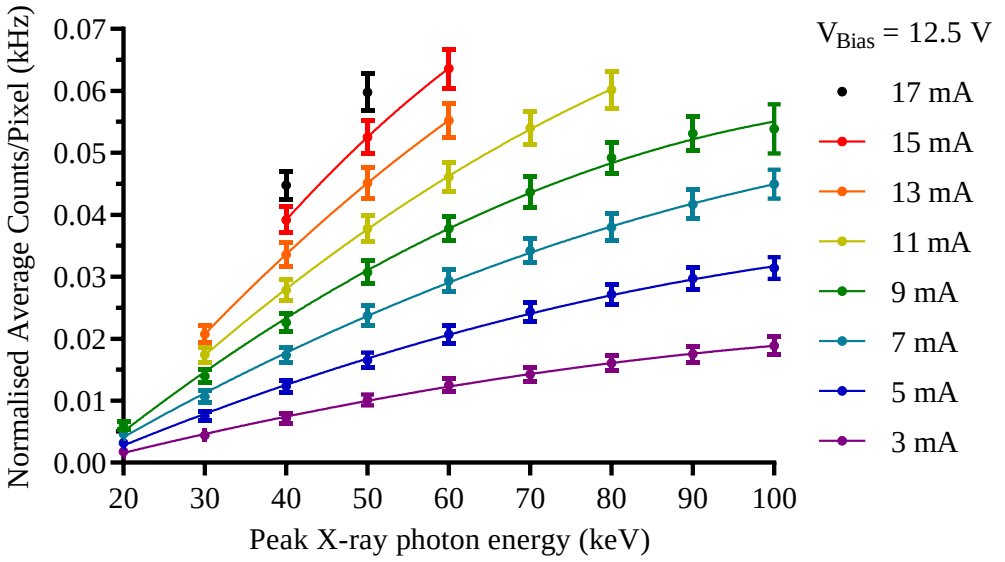

Figure 5.26. Normalised increase in average counts/pixel as a function of peak X-ray photon energy (keV) for SPAD bias voltage of 12.5 V with beam current sweep from 3 mA to 17 mA. Including standard deviation of the sample mean. A second order polynomial (quadratic) regression fitted curve is interpolated for each data set, except for measurements with beam current of 17 mA.

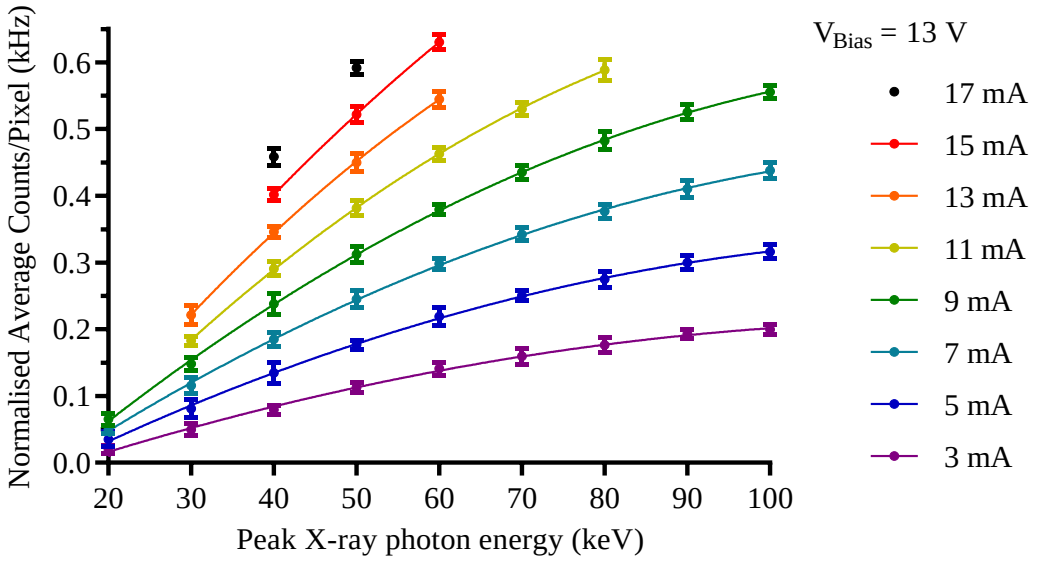

Figure 5.27. Normalised increase in average counts/pixel as a function of peak X-ray photon energy (keV) for SPAD bias voltage of 13 V with beam current sweep from 3 mA to 17 mA. Including standard deviation of the sample mean. A second order polynomial (quadratic) regression fitted curve is interpolated for each data set, except for measurements with beam current of 17 mA.

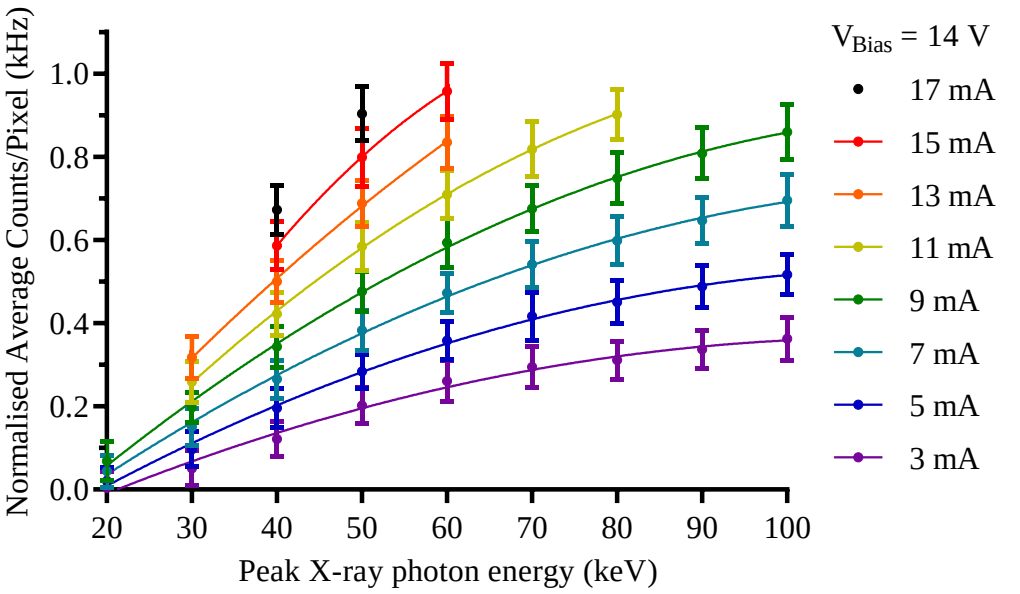

Figure 5.28. Normalised increase in average counts/pixel as a function of peak X-ray photon energy (keV) for SPAD bias voltage of 14 V with beam current sweep from 3 mA to 17 mA. Including standard deviation of the sample mean. A second order polynomial (quadratic) regression fitted curve is interpolated for each data set, except for measurements with beam current of 17 mA.

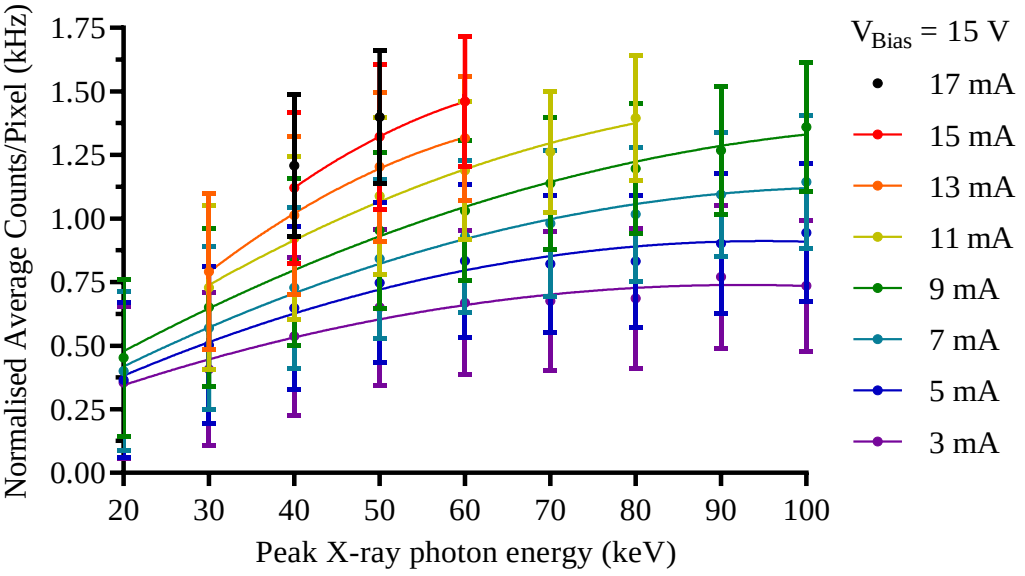

Figure 5.29. Normalised increase in average counts/pixel as a function of peak X-ray photon energy (keV) for SPAD bias voltage of 15 V with beam current sweep from 3 mA to 17 mA. Including standard deviation of the sample mean. A second order polynomial (quadratic) regression fitted curve is interpolated for each data set, except for measurements with beam current of 17 mA.

For comparison of the effect of increasing SPAD bias voltage on average counts, Figure 5.30 shows the normalised increase in average counts/pixel as a function of peak X-ray photon energy for SPAD bias voltages 12.5 to 15 V with a constant beam current of 9 mA. Furthermore, a second order polynomial (quadratic) regression fitted curve is interpolated for each data set. From the figure it is evident that an increase in SPAD bias voltage results in an increase in average counts, as well as an increase in standard deviation of the sample means.

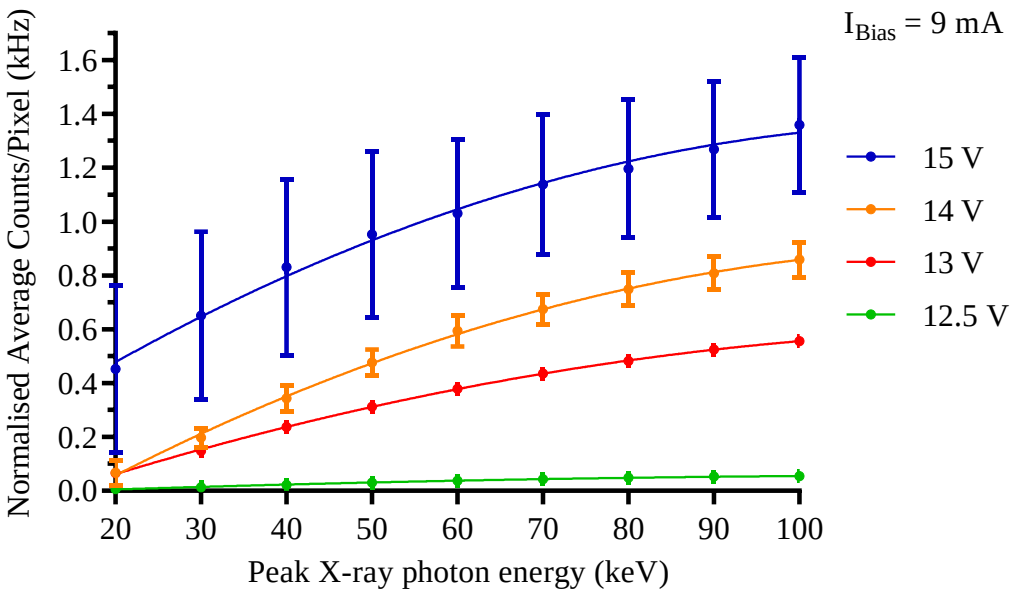

Figure 5.30. Normalised increase in average counts/pixel as a function of peak X-ray photon energy for SPAD bias voltages from 12.5 to 15 V with fixed beam current of 9mA. Including standard deviation of the sample mean. A second order polynomial (quadratic) regression fitted curve is interpolated for each data set.

5.4.4 X-ray Radiation Hardness Experiment B

The following experiment is further investigation of the radiation hardness of the MINI3D CMOS SPAD image sensor. For the experiment, the SPAD was exposed to four consecutive sets of X-ray irradiations for 1 hour respectively, at an X-ray output voltage of 100 kV and beam current of 9 mA. The SPAD was biased at a constant 13 V and placed 10 cm from the X-ray source. From Figure 5.9 the known TID is approximately 1.2 Mrad/h, therefore after four hours of irradiation, the calculated TID is 4.8 Mrad or 48 kGy. A control measurement was taken before irradiation, named C1. After each hour irradiation a control measurement was taken directly after

exposure (C2, C4 and C6), and an additional control measurement taken 10 min later (C3, C5 and C7) for comparison. After the last irradiation a control measurement is taken directly after (C8), but instead of a control set of data taken 10 min later, a final control measurement was taken 24 hours later (C9) for comparison. Table 5.4 provides the experimental statistical results for each control measurement taken after a cumulative TID of 4.8 Mrad. The average counts/frame vs each measured frame for each control measurement is shown collectively in Figure 5.31.

Table 5.4. Statistical results for SPAD DCR before, during and after cumulative 4.8 Mrad TID.

	C1	**C2**	**C3**	**C4**	**C5**	**C6**	**C7**	**C8**	**C9**
Frames	1000	1000	1000	1000	1000	1000	1000	1000	2000
Function	Control Before Irr.	Control After Irr. 1	Control 10 Min after Irr. 1	Control After Irr. 2	Control 10 Min after Irr. 2	Control After Irr. 3	Control 10 Min after Irr. 3	Control After Irr. 4	Control 24 Hrs after Irr. 4
Cumulative TID (Mrad)	0	1.2	1.2	2.4	2.4	3.6	3.6	4.8	4.8
Mean	0.2116	0.2331	0.3168	0.3694	0.2684	0.3457	0.2824	0.4029	0.2164
Std. Deviation	0.0061	0.0078	0.0098	0.0141	0.0081	0.0116	0.0084	0.0374	0.0100
Lower 95% CI of mean	0.1994	0.2175	0.2972	0.3413	0.2523	0.3226	0.2657	0.3281	0.1964
Upper 95% CI of mean	0.2237	0.2488	0.3364	0.3975	0.2845	0.3689	0.2991	0.4778	0.2363

From the results it is evident that after irradiation the DCR of the SPAD increases. However, it can be observed in C4, C6 and C8 that the DCR is decreasing for each following measured frame, and with a complimentary measurement 10 min later as seen in C5 and C7, the DCR has significantly decreased, although higher than the initial control measurement in C1. The results would initially indicate that the SPAD DCR has degraded resulting in permanent increased DCR, but control measurement C9 shows that eventually, in this case a measurement taken 24 hours later, the DCR had returned to within its original state, with a slight increase in standard deviation of the sample mean. Therefore, indicating that DCR degradation in this case has not noticeably occurred. Further investigation is required.

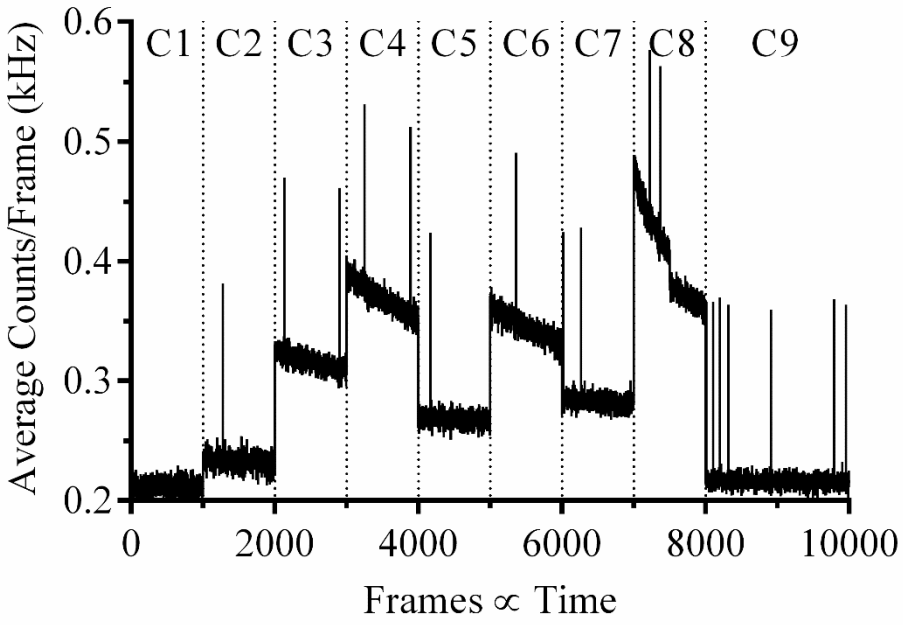

Figure 5.31. DCR for each measured frame during control measurements C1 to C9 during SPAD radiation hardness experiment after a cumulative 4.8 Mrad TID, at SPAD bias of 13 V.

5.4.5 X-ray Experiment B with Added Aluminium Filter

The following experiment resulted by chance, in which a measurement was taken with the MINI3D CMOS SPAD image sensor, where the plastic protective lid of the die package was not removed. The measurements were analysed, and the results showed a significant increase in average counts when compared to previous measurements taken without the lid. The subsequent experiment investigated this effect with the addition of a 150 µm thick aluminium filter between the source and SPAD image sensor. First the X-ray spectrum was measured with a 150 and 300 µm thick aluminium filter added, and the respective spectrums for comparison are shown in Figure 5.32.

From Figure 5.32 it is evident that the addition of an aluminium filter results in X-ray attenuation, especially lower energy photons. From the previous results it was assumed that the added filters would result in a decrease in X-ray intensity and therefore a decrease in average counts. Figure 5.33 to Figure 5.36 show the measured average counts/pixels for the SPAD image sensor as a result of the added 150 µm thick aluminium filter for SPAD bias voltages 12.5 V to 15 V respectively. Furthermore, for Figure 5.33 to Figure 5.36 a second order polynomial (quadratic) regression fitted curve is interpolated for each data set.

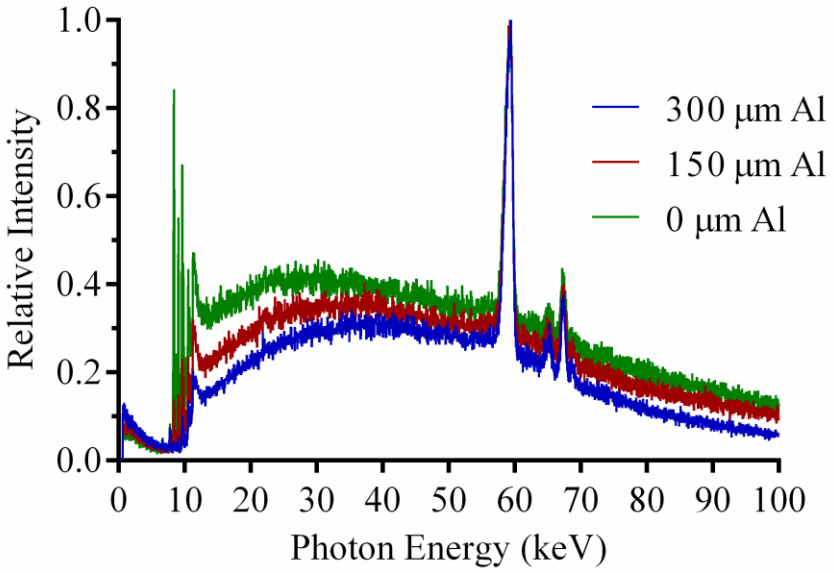

Figure 5.32. Measured X-ray spectrum for GLADD X-ray source at 100 kV output voltage, with tungsten target and added aluminium filters of 150 and 300 µm thickness respectively.

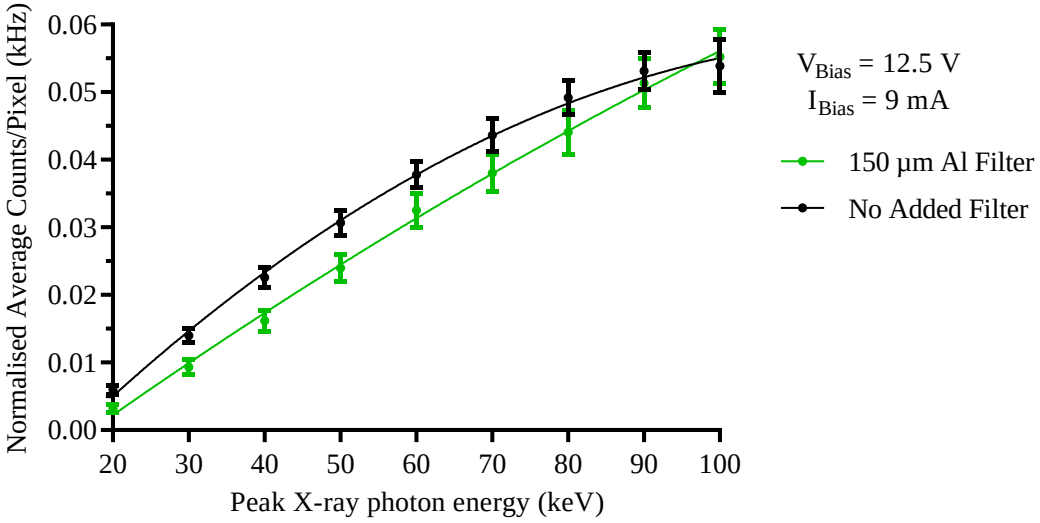

Figure 5.33. Comparison of measured average counts/pixel as a function of peak X-ray photon energy with and without 150 µm thick aluminium filter added between X-ray tube at constant beam current of 9mA and SPAD image sensor biased at 12.5 V. Including standard deviation of the sample mean. A second order polynomial (quadratic) regression fitted curve is interpolated for each data set.

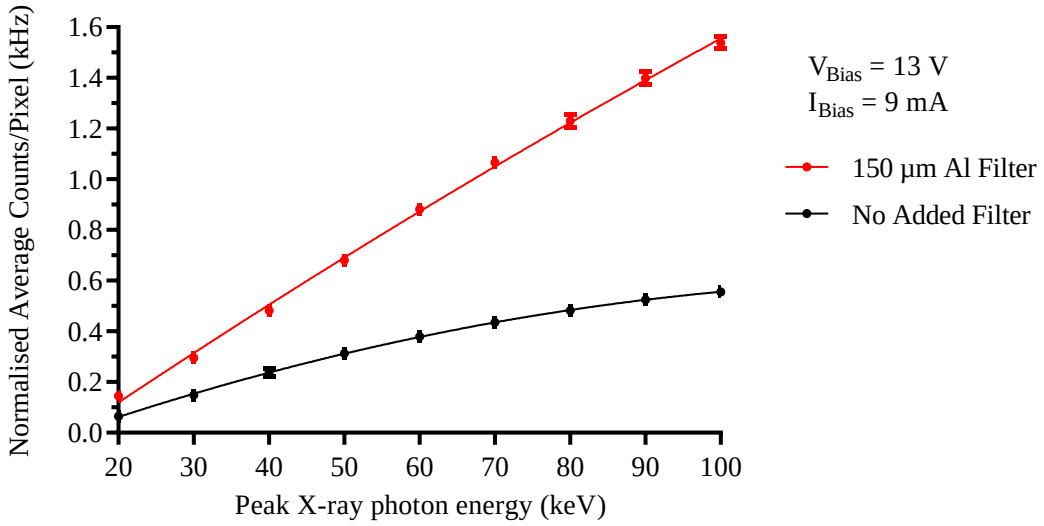

Figure 5.34. Comparison of measured average counts/pixel as a function of peak X-ray photon energy with and without 150 µm thick aluminium filter added between X-ray tube at constant beam current of 9mA and SPAD image sensor biased at 13 V. Including standard deviation of the sample mean. A second order polynomial (quadratic) regression fitted curve is interpolated for each data set.

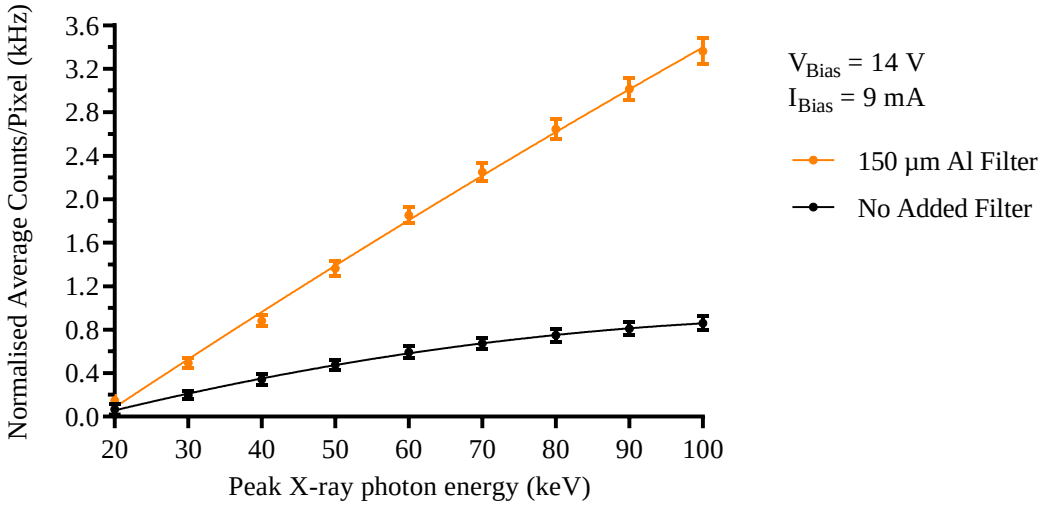

Figure 5.35. Comparison of measured average counts/pixel as a function of peak X-ray photon energy with and without 150 µm thick aluminium filter added between X-ray tube at constant beam current of 9mA and SPAD image sensor biased at 14 V. Including standard deviation of the sample mean. A second order polynomial (quadratic) regression fitted curve is interpolated for each data set.

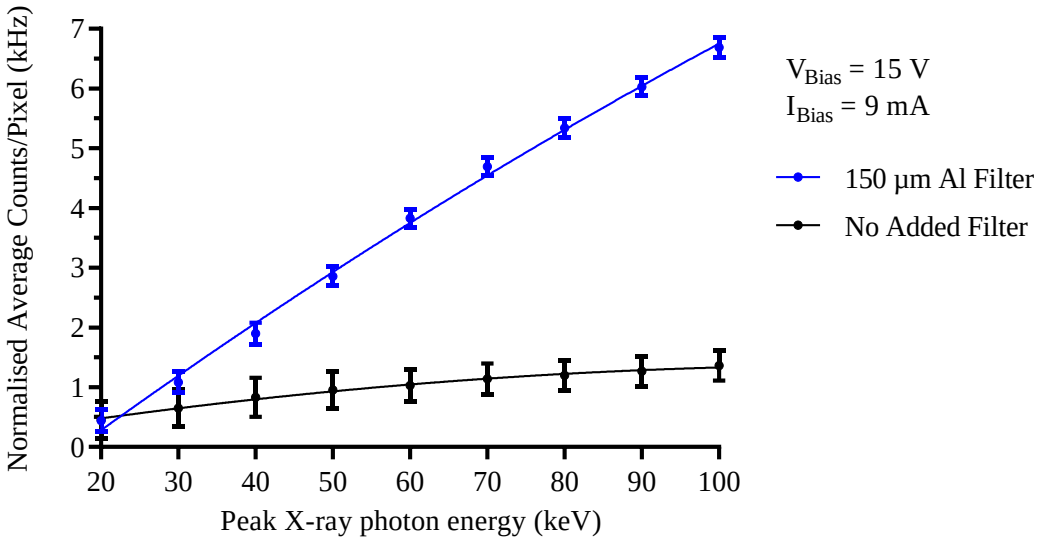

Figure 5.36. Comparison of measured average counts/pixel as a function of peak X-ray photon energy with and without 150 µm thick aluminium filter added between X-ray tube at constant beam current of 9mA and SPAD image sensor biased at 15 V. Including standard deviation of the sample mean. A second order polynomial (quadratic) regression fitted curve is interpolated for each data set.

From Figure 5.33 to Figure 5.36, it is evident for SPAD bias voltages 13 to 15 V that the addition of the 150 µm thick aluminium filter results in a significant increase in average counts/pixel, even though the intensity of the initial X-ray spectrum is attenuated. This response is unshared at SPAD bias voltage of 12.5 V. The factor change in average counts is tabulated in Table 5.5 to Table 5.8 for SPAD bias voltages 12.5 to 15 V respectively

Table 5.5. Factor decrease in average counts with added 150 µm thick Al filter at SPAD bias voltage of 12.5 V for varying X-ray peak photon energies and beam currents.

	X-ray Beam current							
X-ray peak photon Energy	**3 mA**	**5 mA**	**7 mA**	**9 mA**	**11 mA**	**13 mA**	**15 mA**	**17 mA**
20 keV	0.458	0.496	0.515	0.536				
30 keV	0.618	0.638	0.652	0.665	0.677	0.689		
40 keV	0.725	0.725	0.726	0.717	0.733	0.726	0.725	0.734
50 keV	0.823	0.804	0.781	0.781	0.779	0.776	0.778	0.791
60 keV	0.964	0.891	0.868	0.861	0.855	0.838	0.832	
70 keV	1.005	0.912	0.864	0.872	0.860			
80 keV	1.015	0.937	0.909	0.896	0.894			
90 keV	1.057	0.967	0.956	0.966				
100 keV	1.101	1.009	0.981	1.025				
Average factor decrease in measured average counts with added filter							0.812	-18.8 %

Table 5.6. Factor increase in average counts with added 150 µm thick Al filter at SPAD bias voltage of 13 V for varying X-ray peak photon energies and beam currents.

	X-ray Beam current							
X-ray peak photon Energy	**3 mA**	**5 mA**	**7 mA**	**9 mA**	**11 mA**	**13 mA**	**15 mA**	**17 mA**
20 keV	4.723	3.075	2.531	2.226				
30 keV	2.658	2.267	2.041	1.991	1.938	1.885		
40 keV	2.662	2.159	2.081	2.025	2.005	2.009	1.995	1.992
50 keV	2.838	2.378	2.227	2.179	2.150	2.160	2.159	2.160
60 keV	3.021	2.504	2.382	2.324	2.298	2.298	2.307	
70 keV	3.216	2.656	2.501	2.450	2.433			
80 keV	3.069	2.719	2.602	2.551	2.540			
90 keV	3.204	2.823	2.726	2.664				
100 keV	3.353	2.907	2.808	2.768				
Average factor increase in measured average counts with added filter							2.503	150 %

Table 5.7. Factor change in average counts with added 150 µm thick Al filter at SPAD bias voltage of 14 V for varying X-ray peak photon energies and beam currents.

	X-ray Beam current							
X-ray peak photon Energy	**3 mA**	**5 mA**	**7 mA**	**9 mA**	**11 mA**	**13 mA**	**15 mA**	**17 mA**
20 keV	7.92	3.25	2.41	2.20				
30 keV	2.54	2.46	2.39	2.49	2.44	2.41		
40 keV	2.54	2.41	2.52	2.57	2.63	2.68	2.72	2.75
50 keV	2.86	2.84	2.80	2.87	2.89	2.94	2.97	3.02
60 keV	3.38	3.16	3.13	3.12	3.17	3.22	3.26	
70 keV	3.58	3.21	3.27	3.33	3.35			
80 keV	3.68	3.44	3.47	3.53	3.57			
90 keV	3.82	3.65	3.68	3.73				
100 keV	3.86	3.80	3.82	3.91				
Average factor increase in measured average counts with added filter							3.170	217 %

Table 5.8. Factor change in average counts with added 150 µm thick Al filter at SPAD bias voltage of 15 V for varying X-ray peak photon energies and beam currents.

	X-ray Beam current							
X-ray peak photon Energy	**3 mA**	**5 mA**	**7 mA**	**9 mA**	**11 mA**	**13 mA**	**15 mA**	**17 mA**
20 keV	0.42	0.65	0.83	0.97				
30 keV	1.05	1.20	1.45	1.67	1.88	2.02		
40 keV	1.53	1.76	2.05	2.29	2.50	2.73	2.89	3.10
50 keV	2.21	2.42	2.73	3.00	3.17	3.41	3.62	3.92
60 keV	2.99	2.93	3.30	3.72	3.86	4.11	4.29	
70 keV	3.66	3.63	3.87	4.12	4.47			

80 keV	3.76	4.00	4.19	4.46	4.64			
90 keV	3.76	4.16	4.51	4.75				
100 keV	4.11	4.29	4.72	4.92				
Average factor increase in measured average counts with added filter							3.07	207 %

From the results shown in Table 5.5 to Table 5.8, the average counts/pixel increased on average by a factor of 2.5, 3.17 and 3.07 at SPAD bias voltage 13, 14 and 15 V respectively. This equates to an average increase of 150 %, 217 % and 207 % respectively as a result of the added 150 μm thick aluminium filter, a substantial increase. However, for SPAD bias voltage of 12.5 V the average counts/pixel decreased on average by 19 %. This phenomenon is discussed further in the following section.

5.5 Summary and Conclusion

The chapter begins with a brief history on X-rays and an overview of their interaction with matter including the generation of continuous and characteristic X-rays and their combined spectrums, with the use an accelerated electron beam incident upon a fixed target in an X-ray tube.

The chapter reports the detection of ionising photons, specifically X-rays with X-ray tube sources. The investigation was split between two different X-ray tube sources as a result of required maintenance on the initial source. Both X-ray tubes use a tungsten target to generate X-rays, but their maximum achievable peak photon energies were dissimilar, with 160 keV and 100 keV respectively. The initial X-ray experiment, experiment A, investigates the detection of X-rays, where a distinct increase in average counts is observed for X-ray peak photon energies from 15 to 160 keV, which confirms that SPADs can be used to detect X-rays. Furthermore, it was observed that an increase in SPAD bias voltage results in higher relative average counts/pixel.

An additional test was conducted to test the radiation hardness of the MINI3D CMOS SPAD image sensor. The SPAD was irradiated for an hour at 160 keV with a calculated TID of approximately 3.75 Mrad or 37.5 kGy. For all SPAD bias voltages the DCR decreased, and the SPAD did not demonstrate DCR degradation. Moreover, no significant change in standard deviation was observed in the DCR distributions. The SPAD image sensor continued to operate normally.

The second X-ray experiment, termed experiment B, was conducted to investigate the effect of X-ray tube intensity (proportional to input current) and peak photon energy on average counts per frame. It was observed that an increase in both beam intensity (3 to 17 mA) and peak photon energy (20 to 100 keV) results in an increase in average counts, as well as an increase in standard deviation of the sample means.

A second radiation hardness experiment was conducted and the SPAD was exposed to a cumulative TID of 4.8 Mrad or 48 kGy. The experiment was conducted in intervals, where between X-ray irradiation the DCR was measured. It was observed that directly after each irradiation the DCR had increased, but gradually decreases with each subsequent measured frame. A complimentary control measurement is taken 10 min later which shows that the DCR significantly decreases, although still higher in comparison to the initial control measurement. The results would initially indicate that the SPAD DCR has degraded resulting in permanent increased DCR, but after the final irradiation a DCR measurement is taken 24 hours later and shows the DCR had returned to within its original state. Therefore, indicating that DCR degradation in this case has not noticeably occurred. Further investigation into radiation hardness is required.

An ancillary experiment during experiment B was conducted where an additional filter of 150 µm thick aluminium was placed between the SPAD image sensor and X-ray source to further attenuate lower energy photons to observe its effect. It was observed that the average counts per pixel did not decrease with decreasing X-ray intensity, but increased for SPAD bias voltages of 13 to 15 V with an average increase in average counts of approximately 200 %. The added filter attenuates lower energy photons incident upon the SPAD. Therefore, it is hypothesised that the abundance of lower energy photons incident upon the SPAD image sensor result in the limitation of electromagnetic cascade, afterpulsing and crosstalk combined (spurious counts), as the probability of a lower energy photon to interact and cause avalanche detection, is larger than higher energy photons. Therefore, with the attenuation of lower energy photons, the SPAD image sensor is detecting less photons, but experiencing more interactions with higher energy photons, which transfer higher energies, and in turn result in significantly more spurious counts. Furthermore, with regard to lower average counts

detected at SPAD bias voltage of 12.5 V, with the added filter, the SPAD image sensor is biased at the avalanche breakdown threshold. Therefore, it is hypothesised that the potential for significant spurious counts to occur is limited. However, further investigation into this phenomenon is required.

The following chapter is the final chapter of the thesis, and summarises all the research covered in this thesis including conclusions, future work and outlook.

6. Summary, Conclusions, Outlook and Future Work

This is the final chapter of the thesis and provides a summary of all the research and results conducted throughout, as well as conclusions reached. Thereafter, future work and an outlook on the detection of ionising radiation using SPADs is presented.

6.1 Summary, Conclusions and Outlook

The thesis begins with a literature review on ionising radiation and the process thereof, where the interaction between atomic electrons and incident ionising radiation results in electron emission, thus ionising the atom. There are two types of ionising radiation, namely ionising photons, such as X- and gamma-rays, and high energy charged particles. The literature review continues with an overview of ionising radiation detector types, with emphasis on the mechanism for detection being the generation of electron-hole pairs in mediums sensitive to propagating ionising radiation. Furthermore, a literature review on silicon radiation damage as a result of incident ionising radiation and NIEL is presented, with emphasis on surface and bulk damage defects and the measure of TID.

Current state-of-the-art silicon-based hybrid pixel detectors are the preferred detector type used in HEP as a result of their size, pixel resolution, radiation hardness and timing capabilities. However, they are fabricated using multiple processes requiring bump bonding, which affects expediency, integrity and overall expenditure. Therefore, the HEP community are considering CMOS pixel detectors as a favourable future alternative with the associated benefits of lower costs, integrated circuitry and mass manufacture without the need for post processing. Furthermore, the successful development of hybrid pixel detectors has resulted in the commercial application of these detectors in SPC, medical imaging, space dosimetry and material analyses under the Medipix collaboration [21], [30], [32].

Hybrid pixel detectors use a depleted pn-junction, creating an ionisation chamber, to detect traversing ionising radiation. Hybrid pixel detectors operate similarly to APDs with limited gain to ensure adequate signal-to-noise-ratio (SNR) and require a preamplifier for detection. The incident radiation produces electron-hole pairs which under an induced electric field generate a current through the junction. This form of

detection is referred to as charge collection and allows for calculation of the incident radiation energy loss.

Following the literature review on ionising radiation and current detectors, an overview of SPADs is presented. SPADs operate similarly to hybrid pixel detectors with a reverse biased pn-junction, however distinctly SPADs operate in Geiger mode, where the junction is reverse biased beyond its planar breakdown voltage, wherein impact ionisation results in runaway avalanche breakdown and allows rapid detection of incident single photons.

Geiger operation makes SPADs highly sensitive to incident photons (visible spectrum) as a result of excess bias and large inherent gain resulting in avalanche breakdown, with picosecond temporal resolution. The fundamental mechanism for detection is the transfer of energy from an incident photon to an atomic electron, generating an electron-hole pair, which is accelerated under a large induced electric field, which causes impact ionisation and ultimately results in avalanche breakdown and a detected pulse.

Therefore, it was hypothesised that incident ionising radiation will result in electron-hole pair generation incident upon a SPAD depletion region, and coupled with Geiger operation, the induced electric field and large inherent gain, will generate impact ionisation and subsequent avalanche breakdown. Thus, resulting in the detection of incident ionising radiation using SPADs.

Moreover, SPADs have already been integrated into CMOS technologies and with their mature development and performance capabilities, are used in multiple applications, most notably biomedical FLIM, LiDAR, ToF imaging, SPC, high speed imaging etc. [3]–[10]. Although, all current applications are constrained to the visible and near infrared spectrums (NIR). The advances and broad applications of CMOS SPADs has led to increased R&D and financial backing as a commercially viable technology. The motivation is towards further miniaturisation, performance improvements, 3D-stacking and developing highly integrated intelligent sensors with abounding built-in capabilities.

SPADs operate similarly to silicon-based ionising radiation detectors, therefore it is believed that with SPAD advancement and maturity in CMOS, this parallel and rapidly developing technology may lend itself favourably towards progress and application in the detection of ionising radiation. Limited not only in high energy particle physics, but every day commercial applications, such as X-ray imaging, beam therapy and electron microscopy, which would greatly reduce cost and help advance miniaturisation of current technology, improving both availability and mobility. Furthermore, the development of highly integrated ionising radiation detectors will allow for the ministration and development of intelligent lab on-chip applications, as well as facilitate the development of table-top particle accelerators for both research and potential medical therapy [41], [42].

The investigation of the application of SPADs in the detection of ionising radiation has significant commercial potential as an alternative technology to current detectors. Therefore, the aim of this research was to investigate the direct detection of ionising radiation using a CMOS SPAD.

The subsequent chapter presents a literature review on SPADs beginning with an overview of their history and eventual inception into CMOS. Subsequently, a review on SPAD operation is presented, including a review on SPAD biasing, quenching, guard ring structures and performance parameters. Thereafter, the MINI3D 3D-stacked BSI CMOS SPAD image sensor used throughout this thesis is presented, including operation, architecture, layout and performance. The SPAD was selected as the structure resembles a hybrid pixel detector, therefore it was predicted to have improved radiation hardness capabilities.

The first type of ionising radiation to be investigated was accelerated electrons using a SEM with a range of electron energies from 5 to 30 keV. First a literature review on electron interaction with matter is presented, where electron energy loss and total stopping powers are discussed. Additionally, an overview on electron acceleration and its application in electron microscopy is presented. For accelerated electrons with kinetic energies in the keV range, collisional energy loss dominates as a result of inelastic scattering.

The SPAD image sensor is placed within the vacuum chamber of an SEM and irradiated with the electron beam at incremental kinetic energies from 5 to 30 keV. The SEM beam follows a raster scan pattern, and the first experiment confirms the detection of incident accelerated electrons, therefore confirming the initial hypothesis of this thesis. Furthermore, the results present the first time-resolved imaging of the electron beam raster scanning pattern using a SPAD.

Further experimentation was conducted, and a technique for the removal of HDCR pixels is presented. The results confirm that incident accelerated electrons with energies in the range 5 to 30 keV are detectable using a CMOS SPAD. Furthermore, statistical analysis shows that a change in SPAD excess bias voltage and/or change in electron kinetic energy results in a statistically significant output in counts but does not show linear regression. The analytical results are shown in Figure 3.32 and 3.33, where it is revealed that a SPAD bias voltage of 13 V, compared to 12.5, 14 and 15 V, results in the largest average counts per pixel during irradiation. An investigation into the non-linear regression is required.

During accelerated electron irradiation it was observed that pixels display hysteresis, especially after higher electron kinetic energy exposure, with previously irradiated pixels exhibiting increased DCR. The effect is not permanent and after a period of non-exposure the DCR returns to normal. A control data set taken approximately 9 minutes after the final irradiation at 30 keV, showed no hysteresis. Therefore, it is hypothesised that the cause for the pixel hysteresis or “after-glow” is primarily the result of phonon generation. However, long term exposure may lead to permanent radiation damage, as discussed in section 3.2.3.

Figure 3.30 presents the average counts per pixel for each operating bias voltage as a function of incident electron kinetic energy, where it is observed that there is a surge in counts between 10 and 15 keV. It was concluded that the difference in counts is a result of the incident electrons reaching the depletion area of the SPAD, as the approximate linear stopping length of electrons increases with increasing kinetic energy. Therefore, this technique could be used to determine the depth of a SPADs depletion region.

With the discovery that SPADs can detect ionising radiation, it was decided to investigate the detection of higher energy electrons as well as heavy charged particles. Chapter 4 reports the detection of 120 GeV pions, and 2.5 GeV electrons, using synchrotron particle accelerators at CERN and ELSA respectively. Before the experimental results are presented, an overview of the standard model of particle physics is given, followed by a literature review on the passage of heavy charged particles in matter. Thereafter, an overview of particle accelerators used are presented including the pion production, which is a hadron with mass approximately 270 times larger than the mass of an electron.

For the investigation of the detection of pions, the MINI3D CMOS SPAD image sensor is fixed to a beam telescope and aligned to the incident pion beam. Beam availability allows for 4 irradiation experiments to be taken over a period of 14 days. The measured results confirm the detection of 120 GeV incident pions, as the average counts per pixel distinctly increase during irradiation. The measured average counts per frame are significantly larger than the calculated range of approximately 75 Hz to 1.55 MHz, with a minimum measured value of approximately 8.3 MHz at a bias voltage of 12.5 V and maximum of 432.1 MHz at 15 V. When comparing the measured values presented in Figure 4.22, there is a positive linear correlation between the average counts per frame and increasing SPAD bias voltage.

For SPADs an increase in reverse bias voltage results in a proportional increase in detection probability, therefore the increase in detected counts during pion irradiation may be attributed to increased impact ionisation, electromagnetic cascade, afterpulsing and crosstalk. Additionally, electron-hole pair generation in the silicon bulk around the depletion region may occur, causing secondary free carriers to drift into the depletion region resulting in additional spurious counts. Regardless, the exact intensity and total quantity of incident pions per frame is unknown, therefore further examination is required to investigate the particle detection efficiency of the device as well as calculation of the TID. Furthermore, after pion irradiation, the SPAD image sensor DCR was permanently altered as a result of ionising radiation damage, thus further investigation into the radiation hardness of the SPAD image sensor is required.

For the investigation of detection of 2.5 GeV electrons, one set of irradiation measurements were taken due to limited beam availability, and no discernible detection was observed. However, due to beam technical difficulties the intensity of the incident electron beam was approximately 50 kHz spread over a relatively large area, approximately 100 mm^2. The calculated electron intensity upon the SPAD was calculated to be 470 Hz or 0.47 electrons per frame. Therefore, over the measured DCR of the SPAD the result is inconclusive and further investigation is required.

The final experimental chapter of the thesis reports the detection of ionising photons, specifically X-rays with X-ray tube sources. The investigation was split between two different X-ray tube sources as a result of required maintenance on the initial source. Both X-ray tubes use a tungsten target to generate X-rays, but their maximum achievable peak photon energies were dissimilar, with 160 keV and 100 keV respectively. A literature review on X-rays and their interaction with matter is presented including an overview on the generation of continuous and characteristic X-rays and their combined spectrums. The initial X-ray experiment reports the detection of X-rays, where a distinct increase in average counts is observed for X-ray peak photon energies from 15 to 160 keV, which confirms that SPADs can be used to detect X-rays. Furthermore, it was observed that an increase in SPAD bias voltage results in higher relative average counts per pixel. An additional test was conducted to test the radiation hardness of the MINI3D CMOS SPAD image sensor. The SPAD was irradiated for an hour at 160 keV with a calculated TID of approximately 3.75 Mrad or 37.5 kGy. For all SPAD bias voltages the DCR did not increase, but decrease, and the SPAD did not demonstrate DCR degradation. Moreover, no significant change in standard deviation was observed in the DCR distributions. The SPAD image sensor continued to operate normally.

The second X-ray experiment was conducted to investigate the effect of X-ray tube intensity (proportional to input current) and peak photon energy on average counts per frame. It was observed that an increase in both beam intensity (3 to 17 mA) and peak photon energy (20 to 100 keV) results in an increase in average counts, as well as an increase in standard deviation of the sample means.

A second radiation hardness experiment was conducted and the SPAD was exposed to a cumulative TID of 4.8 Mrad or 48 kGy, approximately 10 % of the tested radiation hardness of Medipix hybrid pixel detectors used in X-ray imaging [28]. The experiment was conducted in intervals, where between X-ray irradiation the DCR was measured. It was observed that directly after each irradiation the DCR had increased, but gradually decreases with each subsequent measured frame. A complimentary control measurement was taken 10 min later which shows that the DCR significantly decreases, although still higher in comparison to the initial control measurement. The results initially indicate that the SPAD DCR has degraded resulting in permanent increased DCR, but after the final irradiation a DCR measurement is taken 24 hours later and shows the DCR had returned to within its original state. Therefore, indicating that DCR degradation in this case has not noticeably occurred. Further investigation into radiation hardness is required, however, initial results are encouraging and advocate the application of CMOS SPAD image sensors in X-ray imaging.

An ancillary experiment was conducted where an additional filter of 150 µm thick aluminium was placed between the SPAD image sensor and X-ray source to further attenuate lower energy photons to observe its effect. It was observed that the average counts per pixel did not decrease as expected with decreasing X-ray intensity but increased. For SPAD bias voltages of 13 to 15 V an average increase in average counts of approximately 200 % was measured. The added filter attenuates lower energy photons incident upon the SPAD. Therefore, it is hypothesised that the abundance of lower energy photons incident upon the SPAD image sensor result in the limitation of electromagnetic cascade, afterpulsing and crosstalk combined (spurious counts) effects to occur, as the probability of a lower energy photon to interact and cause avalanche detection, is larger than higher energy photons. Therefore, with the attenuation of lower energy photons, the SPAD image sensor is detecting less photons, but experiencing more interactions with higher energy photons, which transfer higher energies, and in turn result in significantly more spurious counts. Furthermore, with regard to lower average counts detected at SPAD bias voltage of 12.5 V, with the added filter, the SPAD image sensor is biased at the avalanche breakdown threshold. Therefore, it is hypothesised that the potential for significant spurious counts to occur is limited. However, further investigation into this phenomenon is required.

SPADs operate beyond premature avalanche breakdown and have been robustly designed to ensure a uniformly distributed electric field along the junction interface by employing guard rings. The use of guard ring structures significantly reduces surface noise effects caused by lattice imperfections, as the resulting breakdown area is shifted. This key design advantage lends itself favourably towards SPAD radiation tolerance, as incident radiation results in increased lattice deformation, which SPADs have been inherently optimised for. Furthermore, the operation of SPADs as a "counter" detector, and applied pixel discrimination for DCR detection, provides SPADs with an increased radiation tolerance longevity in repeated radiation environments, as shown by the HDCR pixel discrimination method presented in chapter 3.

The MINI3D CMOS SPAD image sensor radiation tolerance benefits from a hybrid pixel design, which separates the integrated circuitry from pixel array, shown in Figure 2.5. The wafer to wafer hybrid bonding combines a substrate, double layer of oxide and associated metal and via interconnects, for added protection and improved radiation tolerance of the integrated circuitry. Furthermore, with BSI, the incident medium is the substrate, which mitigates the generation of charge traps at the oxide interface, which in turn reduces performance degradation and results in improved radiation tolerance. This configurations radiation tolerance is easily improved, by reducing wafer etching and increasing the incident substrate thickness, thereby increasing shielding, and reducing radiation damage at the detection medium. However, the trade-off for increased thickness, is the limitation in the detection of lower energy ionising radiation.

To conclude, the research covered in this thesis focuses on the detection of ionising radiation using a 3D-stacked BSI CMOS SPAD, where it is confirmed that SPADs can be used to detect ionising radiation, both ionising photons and high energy charged particles. SPADs operate well in environments where the type of radiation source is already known and abundant, unlike pixel detectors which can determine the total energy loss by incident ionising radiation. Therefore, it is proposed that SPADs are suitable for the application in environments with, and the detection of, ionising radiation. Combined with CMOS compatibility, mature development, performance capabilities (timing and image resolution), commercial viability and the drive towards

miniaturisation, 3D-stacking and performance advancements; SPADs are exceedingly versatile and highly integrated intelligent optical sensors that will dominate the optical sensor market for decades to come.

The ability to detect ionising radiation and demonstrate radiation hardness capabilities unveils novel areas of application. With cost-effective CMOS compatibility, SPADs are highly recommended for the application in X-ray detection, e.g., medical and biomedical imaging; electronic and material inspection; and most excitingly the development of cost-effective lab on chip or hand-held devices, for the use in the field, research and outpatient areas. However, as SPADs cannot precisely measure the total energy loss by incident ionising radiation, there recommendation in dose measurement applications is not recommended.

The ability to detect accelerated electrons and high energy charged particles, coupled with their abundant advantages, makes SPADs an attractive option for the application in astrionics; HEP imaging, detection, tracking; and electron microscopy. SPAD timing and imaging capabilities, could be applied in time-resolved imaging and improve visual perception of nano structures in motion with high refresh rates. As SPADs can detect high energy charged particles, it is recommended to investigate the use of SPADs in the detection of cosmic ray muons and in the development of table-top particle accelerator detectors.

With the shown technique to measure the depth of the SPADs depletion region, discussed in chapter 3, specific materials can be placed in front of the SPAD image sensor to determine the range of incident energy. Furthermore, depending on the application, individual pixel passivation layers can be etched at varying depths to provide an array of detectors sensitive at varying energies, extending SPAD application in X-ray fluorescence.

6.2 Future Work

Succeeding the research covered in this thesis certain areas necessitate further experimental investigation and unveil novel areas of future work, which are summarised as follows.

1. For SPADs an extensive investigation into the radiation hardness of the sensor is required to ensure adequate operation during ionising radiation exposure. This includes various SPADs developed in multiple CMOS processes. The initial finding in this thesis on BSI CMOS SPAD radiation hardness may be limited but their initial capability is encouraging.
2. For the detection of accelerated electrons, future work is required to determine the electron detection efficiency of SPADs. Additionally, an investigation of the nonlinear regression on SPAD output counts as a function of reverse bias voltage is also required. Furthermore, future work includes investigation on temporary pixel hysteresis as a function of TID and the application of SPAD image sensors in electron microscopy, including the use of thermal annealing to reduce long term radiation damage.
3. For the application of SPADs in HEP, future work includes the investigation of SPADs in particle tracking, detection and imaging, as well as an investigation into the detection of other charged particles e.g., cosmic ray muons.
4. With the ability to detect X-rays using a BSI illuminated SPAD image sensor future work includes investigating the application of SPAD image sensors for X-ray and medical imaging, and comparison thereof with existing detectors. Furthermore, an investigation into the phenomenon that results in increased SPAD counts as a result of lower photon energy spectrum attenuation.
5. Future work may investigate improved SPAD designs for improved radiation tolerance. Possible design improvements may include 3D-stacking, optimal metal shielding and alternative guard ring configurations for improved DCR suppression as a result of increased lattice deformation and charge trapping.

7. Appendices

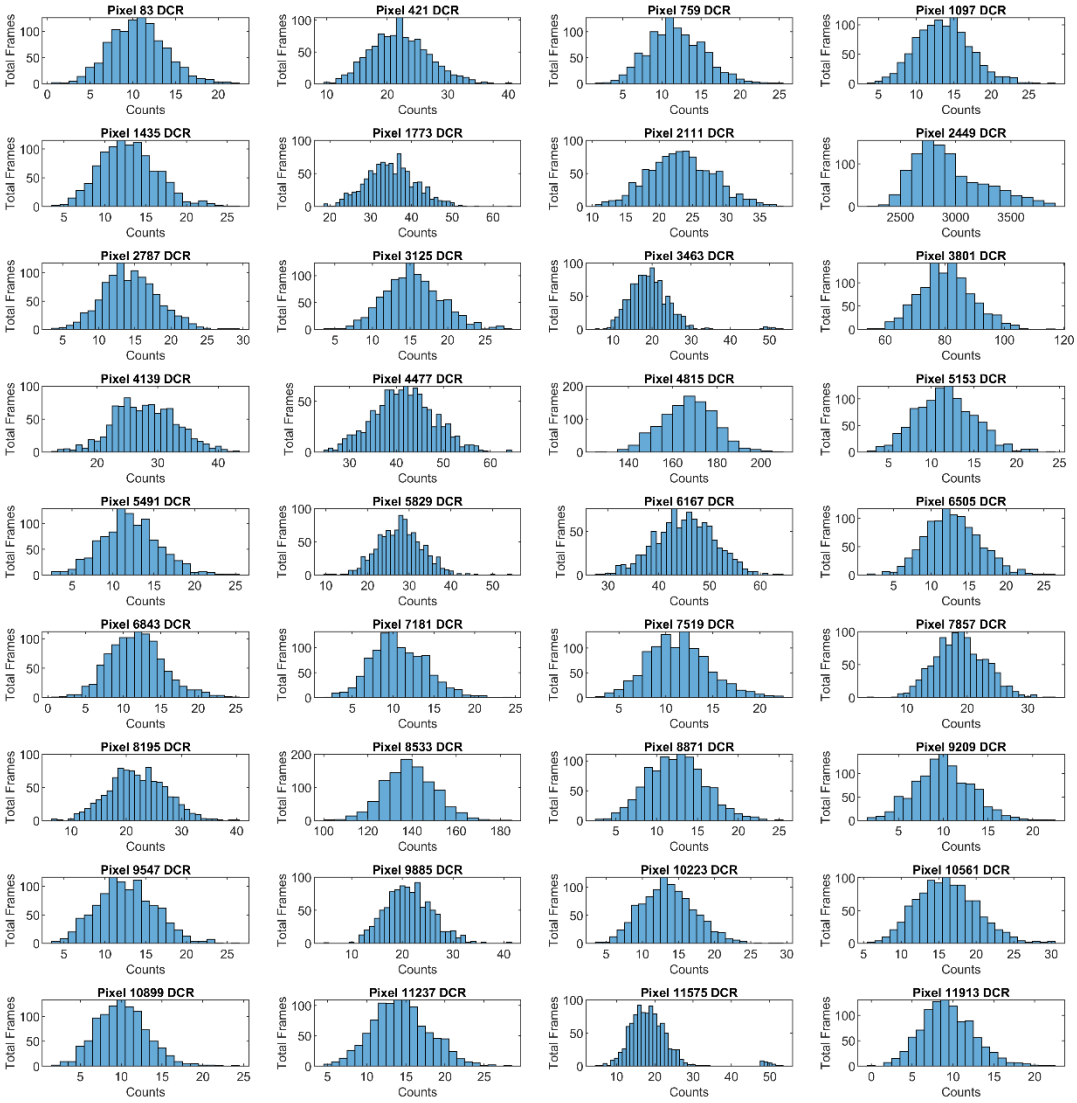

Figure 7.1. DCR distribution for a sample of pixels from the MINI3D SPAD image sensor at a SPAD bias voltage of 15 V over 1000 frames at a set exposure time of 1 ms.

Table 7.1. Tabulated statistical results for pion beam irradiation experiment 1 at SPAD bias voltages 12.5, 13, 14 and 15 V respectively.

120 GeV Pion Beam Irradiation Experiment 1

Bias Voltage	12.5 V			13V			14 V			15 V		
Sequence	**Control Before**	**Irradiation**	**Control After**	**Control Before**	**Irradiation**	**Control After**	**Control Before**	**Irradiation**	**Control After**	**Control Before**	**Irradiation**	**Control After**
Frames Measured	1500	52500	13000	1500	52500	13000	1500	52500	13000	1500	47500	13000
Pixels Measured	12468	12468	12468	12468	12468	12468	12468	12468	12468	12468	12468	12468
HDCR Pixels	2892	2892	2892	2892	2892	2892	2892	2892	2892	2892	2892	2892
Average Counts/Pixel (kHz)	1.515	2.178	2.843	2.812	4.406	5.443	6.963	9.306	10.877	21.107	24.305	26.145
Std Dev Counts/Pixel (kHz)	0.084	0.185	0.071	0.362	0.324	0.067	0.399	0.700	0.130	0.372	1.112	0.167
Maximum Counts/Pixel (kHz)	1.711	2.802	3.058	3.363	5.926	5.733	7.675	11.812	11.321	21.939	29.133	26.666
Average Counts/Frame (kHz)	18886	27149	35447	35061	54931	67861	86815	116031	135618	263157	303031	325973
Average Pion Counts/Pixel (kHz)	**0**	**0.663**		**0**	**1.594**		**0**	**2.343**		**0**	**3.198**	
Std Dev Pion Counts/Pixel (kHz)		0.185			0.324			0.700			1.112	
Maximum Pion Counts/Pixel (kHz)		1.287			3.114			4.849			8.026	
Average Pion Counts/Frame (kHz)	**0**	**8263**		**0**	**19869**		**0**	**29217**		**0**	**39874**	
Total Pion Counts in Billions		**0.4338157**			**1.0431465**			**1.5338693**			**1.8940208**	

Table 7.2. Tabulated statistical results for pion beam irradiation experiment 3 at SPAD bias voltages 12.5, 13, 14 and 15 V respectively.

120 GeV Pion Beam Irradiation Experiment 3

Bias Voltage	12.5 V			13V			14 V			15 V		
Sequence	**Control Before**	**Irradiation**	**Control After**	**Control Before**	**Irradiation**	**Control After**	**Control Before**	**Irradiation**	**Control After**	**Control Before**	**Irradiation**	**Control After**
Frames Measured	10000	207000	10000	10000	207000	10000	10000	196000	10000	10000	196000	10000
Pixels Measured	12468	12468	12468	12468	12468	12468	12468	12468	12468	12468	12468	12468
HDCR Pixels	2892	2892	2892	2892	2892	2892	2892	2892	2892	2892	2892	2892
Average Counts/Pixel (kHz)	1.606	2.702	1.673	3.090	5.728	3.167	7.156	13.759	7.282	21.059	34.643	21.430
Std Dev Counts/Pixel (kHz)	0.034	0.098	0.031	0.036	0.140	0.049	0.048	0.216	0.164	0.127	0.422	0.280
Maximum Counts/Pixel (kHz)	1.703	2.964	1.764	3.233	6.164	3.371	7.533	14.661	7.615	21.594	29.133	22.060
Average Counts/Frame (kHz)	20024	33682	20859	38523	71421	39486	89215	171546	90792	262568	431931	267189
Average Pion Counts/Pixel (kHz)	**0**	**1.095**		**0**	**2.639**		**0**	**6.603**		**0**	**13.584**	
Std Dev Pion Counts/Pixel (kHz)		0.098			0.140			0.216			0.422	
Maximum Pion Counts/Pixel (kHz)		1.358			3.074			7.505			14.951	
Average Pion Counts/Frame (kHz)	**0**	**13658**		**0**	**32898**		**0**	**82331**		**0**	**169364**	
Total Pion Counts in Billions		**2.8272464**			**6.8099768**			**16.13684**			**33.195357**	

Table 7.3. Tabulated statistical results for pion beam irradiation experiment 4 at SPAD bias voltages 12.5, 13, 14 and 15 V respectively.

120 GeV Pion Beam Irradiation Experiment 4

Bias Voltage	12.5 V			13V			14 V			15 V		
Sequence	**Control Before**	**Irradiation**	**Control After**	**Control Before**	**Irradiation**	**Control After**	**Control Before**	**Irradiation**	**Control After**	**Control Before**	**Irradiation**	**Control After**
Frames Measured	12000	102000	10000	12000	102000	10000	12000	102000	10000	12000	102000	10000
Pixels Measured	12468	12468	12468	12468	12468	12468	12468	12468	12468	12468	12468	12468
HDCR Pixels	2892	2892	2892	2892	2892	2892	2892	2892	2892	2892	2892	2892
Average Counts/Pixel (kHz)	0.864	7.975	0.834	1.978	15.678	2.004	5.564	28.796	6.975	19.188	53.844	26.529
Std Dev Counts/Pixel (kHz)	0.045	3.070	0.144	0.073	5.679	0.164	0.107	8.062	0.445	0.187	10.945	0.848
Maximum Counts/Pixel (kHz)	0.960	12.532	1.411	2.111	22.895	2.814	5.985	39.658	9.360	19.836	69.517	30.393
Average Counts/Frame (kHz)	10771	99433	10398	24666	195471	24983	69374	359034	86967	239234	671325	330761
Average Pion Counts/Pixel (kHz)	**0**	**7.111**		**0**	**13.700**		**0**	**23.232**		**0**	**34.656**	
Std Dev Pion Counts/Pixel (kHz)		3.070			5.679			8.062			10.945	
Maximum Pion Counts/Pixel (kHz)		11.668			20.917			34.094			50.329	
Average Pion Counts/Frame (kHz)	**0**	**88661**		**0**	**170805**		**0**	**289660**		**0**	**432091**	
Total Pion Counts in Billions		**9.0434546**			**17.422147**			**29.545352**			**44.073283**	

Table 7.4. Statistical data for average counts/pixel and standard deviation at SPAD bias voltage of 12.5, 13, 14 and 15 V as a function of peak X-ray photon energies from 0 to 120 keV.

	SPAD Bias Voltage 12.5 V			**SPAD Bias Voltage 13 V**		
Peak X-ray photon energy (keV)	**Mean (counts/ pixel)**	**Std. dev (counts/ pixel)**	**Frames**	**Mean (counts/ pixel)**	**Std. dev (counts/ pixel)**	**Frames**
0	0.1544	0.0288	10000	0.5920	0.0710	10000
15	0.2017	0.0235	400	0.7065	0.0809	400
30	0.5445	0.0467	400	1.2509	0.0984	400
40	0.9961	0.0715	400	1.9248	0.1160	400
50	1.3165	0.0895	400	2.3999	0.1672	400
60	1.6443	0.1119	400	2.9866	0.2458	400
70	1.9829	0.1461	400	3.5643	0.2638	400
80	1.7698	0.1383	400	3.4834	0.3200	400
100	2.7610	0.2168	400	4.7975	0.4123	400
120	3.2753	0.2397	400	5.5363	0.4198	400
	SPAD Bias Voltage 14 V			**SPAD Bias Voltage 15 V**		
Peak X-ray photon energy (keV)	**Mean (counts/ pixel)**	**Std. dev (counts/ pixel)**	**Frames**	**Mean (counts/ pixel)**	**Std. dev (counts/ pixel)**	**Frames**
0	4.1900	0.2988	10000	18.1625	0.8288	10000
15	4.5496	0.2330	400	22.9032	0.5131	400
30	5.5258	0.3660	400	24.4421	0.7346	400
40	6.5817	0.4160	400	26.3229	0.9056	400
50	7.4156	0.4471	400	28.0086	1.0415	400
60	8.2087	0.4691	400	29.1824	1.0263	400
70	8.8091	0.4756	400	30.1398	0.9281	400
80	9.0462	0.5372	400	31.0715	1.2924	400
100	10.2353	0.5008	400	31.2768	0.9525	400
120	11.2298	0.4778	400	31.8290	0.7812	400

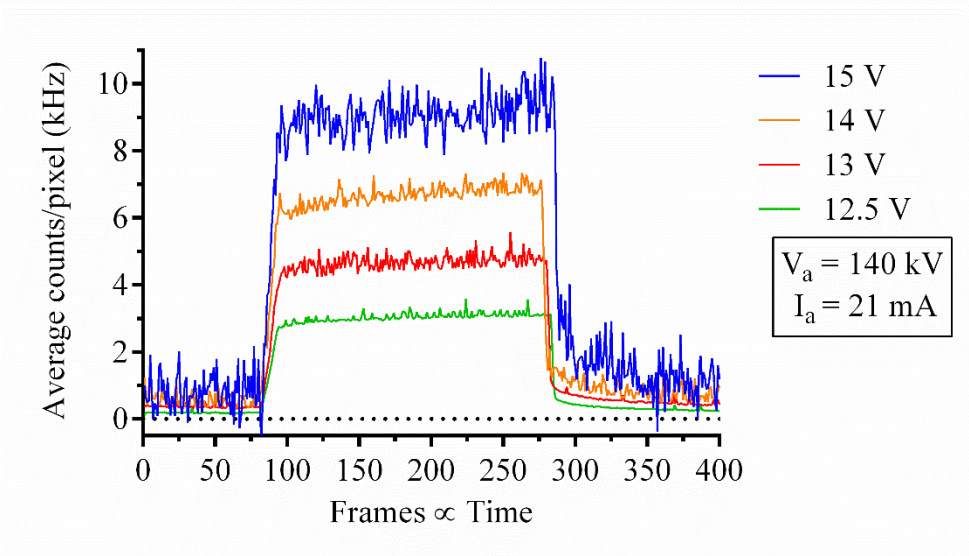

Figure 7.2. Normalised average counts/pixel at SPAD bias voltages 12.5 to 15 V over 400 frames for X-ray irradiation at peak photon energy of 140 keV and beam current of 21 mA. During each irradiation the X-ray tube is turned on for approximately 15 seconds.

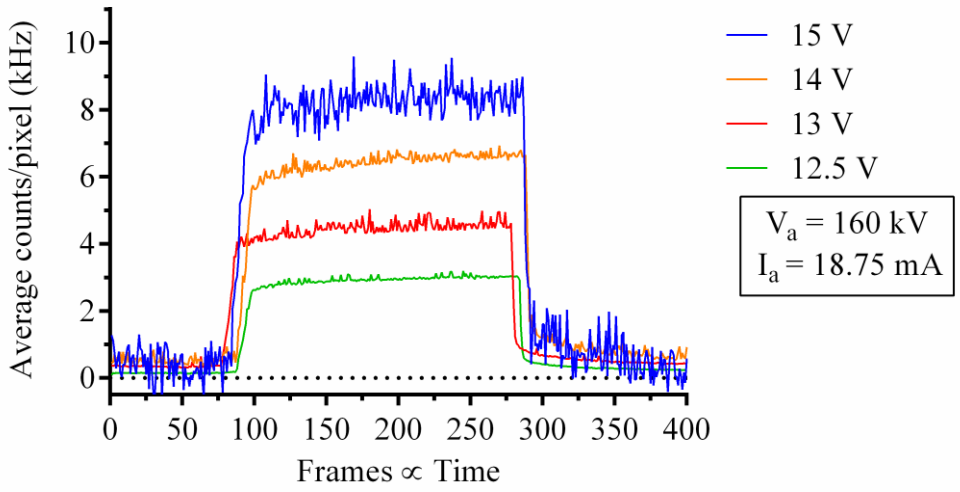

Figure 7.3. Normalised average counts/pixel at SPAD bias voltages 12.5 to 15 V over 400 frames for X-ray irradiation at peak photon energy of 160 keV and beam current of 18.75 mA. During each irradiation the X-ray tube is turned on for approximately 15 seconds.

References

[1] T. Al Abbas, “Miniature high dynamic range time-resolved CMOS SPAD image sensors,” The University of Edinburgh, 2019.

[2] E. A. G. Webster, “Single-Photon Avalanche Diode theory, simulation, and high performance CMOS integration,” The University of Edinburgh, 2013.

[3] E. Williams, G. O. S. Williams, A. T. Erdogan, N. Finlayson, R. K. Henderson, and J. M. Girkin, “High speed spectral fluorescence lifetime imaging for life science applications,” in *High-Speed Biomedical Imaging and Spectroscopy IV*, Mar. 2019, vol. 10889, p. 25, doi: 10.1117/12.2509466.

[4] I. Gyongy *et al.*, “Fluorescence lifetime imaging of high-speed particles with single-photon image sensors,” in *High-Speed Biomedical Imaging and Spectroscopy IV*, Mar. 2019, vol. 10889, p. 24, doi: 10.1117/12.2510773.

[5] C. Zhang, S. Lindner, I. Antolovic, M. Wolf, and E. Charbon, “A CMOS SPAD Imager with Collision Detection and 128 Dynamically Reallocating TDCs for Single-Photon Counting and 3D Time-of-Flight Imaging,” *Sensors*, vol. 18, no. 11, p. 4016, Nov. 2018, doi: 10.3390/s18114016.

[6] A. R. Ximenes, P. Padmanabhan, M.-J. Lee, Y. Yamashita, D. N. Yaung, and E. Charbon, “A 256×256 45/65nm 3D-stacked SPAD-based direct TOF image sensor for LiDAR applications with optical polar modulation for up to 18.6dB interference suppression,” in *2018 IEEE International Solid - State Circuits Conference - (ISSCC)*, Feb. 2018, pp. 96–98, doi: 10.1109/ISSCC.2018.8310201.

[7] T. Al Abbas, N. A. W. Dutton, O. Almer, S. Pellegrini, Y. Henrion, and R. K. Henderson, “Backside illuminated SPAD image sensor with 7.83μm pitch in 3D-stacked CMOS technology,” *Tech. Dig. - Int. Electron Devices Meet. IEDM*, pp. 8.1.1-8.1.4, 2017, doi: 10.1109/IEDM.2016.7838372.

[8] M. Ghioni, A. Gulinatti, I. Rech, P. Maccagnani, and S. Cova, “Large-area low-jitter silicon single photon avalanche diodes,” Feb. 2008, vol. 6900, p. 69001D, doi: 10.1117/12.761578.

[9] E. Sarbazi, M. Safari, and H. Haas, “Statistical Modeling of Single-Photon Avalanche Diode Receivers for Optical Wireless Communications,” *IEEE Trans. Commun.*, vol. 66, no. 9, pp. 4043–4058, Sep. 2018, doi: 10.1109/TCOMM.2018.2822815.

[10] J. Kosman *et al.*, “29.7 A 500Mb/s -46.1dBm CMOS SPAD Receiver for Laser Diode Visible-Light Communications,” in *Digest of Technical Papers - IEEE International Solid-State Circuits Conference*, Feb. 2019, pp. 468–470, doi: 10.1109/ISSCC.2019.8662427.

[11] “World record for compact ‘tabletop’ particle accelerator.”

https://phys.org/news/2014-12-world-compact-tabletop-particle.html (accessed Nov. 21, 2019).

[12] E. A. Peralta *et al.*, "Demonstration of electron acceleration in a laser-driven dielectric microstructure," *Nature*, vol. 503, no. 7474, pp. 91–94, Nov. 2013, doi: 10.1038/nature12664.

[13] R. Schlaf, "Tutorial on Work Function."

[14] N. J. Carron, *An Introduction to the Passage of Energetic Particles through Matter*. Boca Raton: CRC Press, 2007.

[15] M. D. R. Silva, "Ionizing Radiation Detectors," in *Evolution of Ionizing Radiation Research*, InTech, 2015.

[16] N. Tsoulfanidis and S. Landsberger, *Measurement & detection of radiation.* .

[17] L. Meng, "Development of CMOS Sensors for High-Luminosity ATLAS Detectors." .

[18] G. Knoll, *Radiation detection and measurement*. Hoboken, NJ: John Wiley & Sons, 2010.

[19] M. S. Alam *et al.*, "ATLAS silicon pixel sensors," *Nucl. Instruments Methods Phys. Res. Sect. A Accel. Spectrometers, Detect. Assoc. Equip.*, vol. 456, no. 3, pp. 217–232, Jan. 2001, doi: 10.1016/S0168-9002(00)00574-X.

[20] J. Albert *et al.*, "Prototype ATLAS IBL modules using the FE-I4A front-end readout chip," *J. Instrum.*, vol. 7, no. 11, Nov. 2012, doi: 10.1088/1748-0221/7/11/P11010.

[21] G. Aad *et al.*, "The ATLAS experiment at the CERN large hadron collider," *J. Instrum.*, vol. 3, no. 8, 2008, doi: 10.1088/1748-0221/3/08/S08003.

[22] J. Grosse-Knetter, "The ATLAS pixel detector," *Nucl. Instruments Methods Phys. Res. Sect. A Accel. Spectrometers, Detect. Assoc. Equip.*, vol. 568, no. 1, pp. 252–257, Nov. 2006, doi: 10.1016/j.nima.2006.05.240.

[23] S. Chatrchyan *et al.*, "Observation of a new boson at a mass of 125 GeV with the CMS experiment at the LHC," *Phys. Lett. B*, vol. 716, no. 1, pp. 30–61, Sep. 2012, doi: 10.1016/J.PHYSLETB.2012.08.021.

[24] G. Aad *et al.*, "Observation of a new particle in the search for the Standard Model Higgs boson with the ATLAS detector at the LHC," *Phys. Lett. B*, vol. 716, no. 1, pp. 1–29, Sep. 2012, doi: 10.1016/J.PHYSLETB.2012.08.020.

[25] "ATLAS Experiment at CERN | Exploring the secrets of our universe." https://atlas.cern/ (accessed Nov. 06, 2019).

[26] H. Pernegger *et al.*, "First tests of a novel radiation hard CMOS sensor process

for Depleted Monolithic Active Pixel Sensors," *J. Instrum.*, vol. 12, no. 6, Jun. 2017, doi: 10.1088/1748-0221/12/06/P06008.

[27] G. Aad *et al.*, "ATLAS pixel detector electronics and sensors," *J. Instrum.*, vol. 3, no. 7, 2008, doi: 10.1088/1748-0221/3/07/P07007.

[28] S. Procz, C. Avila, J. Fey, G. Roque, M. Schuetz, and E. Hamann, "X-ray and gamma imaging with Medipix and Timepix detectors in medical research," *Radiat. Meas.*, vol. 127, p. 106104, Aug. 2019, doi: 10.1016/j.radmeas.2019.04.007.

[29] "Flip chip technology | X-RAY.camera." http://x-ray.camera/technology/flip-chip-bonding/ (accessed Nov. 07, 2019).

[30] M. Campbell *et al.*, "Charge collection from proton and alpha particle tracks in silicon pixel detector devices," in *IEEE Nuclear Science Symposium Conference Record*, 2007, vol. 2, pp. 1047–1050, doi: 10.1109/NSSMIC.2007.4437190.

[31] N. Wermes, "Trends in pixel detectors: Tracking and imaging," in *IEEE Transactions on Nuclear Science*, Jun. 2004, vol. 51, no. 3 III, pp. 1006–1015, doi: 10.1109/TNS.2004.829438.

[32] "Medipix." https://medipix.web.cern.ch/ (accessed Nov. 07, 2019).

[33] M. Garcia-Sciveres and N. Wermes, "A review of advances in pixel detectors for experiments with high rate and radiation," *Reports on Progress in Physics*, vol. 81, no. 6. Institute of Physics Publishing, May 29, 2018, doi: 10.1088/1361-6633/aab064.

[34] T. Wang *et al.*, "Depleted fully monolithic CMOS pixel detectors using a column based readout architecture for the ATLAS Inner Tracker upgrade," in *Journal of Instrumentation*, Mar. 2018, vol. 13, no. 3, doi: 10.1088/1748-0221/13/03/C03039.

[35] R. Cardella *et al.*, "MALTA: an asynchronous readout CMOS monolithic pixel detector for the ATLAS High-Luminosity upgrade," *J. Instrum.*, vol. 14, no. 06, pp. C06019–C06019, 2019, doi: 10.1088/1748-0221/14/06/c06019.

[36] M. Moll, "Radiation damage in silicon particle detectors: Microscopic defects and macroscopic properties." 1999, Accessed: Oct. 23, 2019. [Online]. Available: http://bib-pubdb1.desy.de/record/300958.

[37] M. Huhtinen, "Simulation of non-ionising energy loss and defect formation in silicon," *Nucl. Instruments Methods Phys. Res. Sect. A Accel. Spectrometers, Detect. Assoc. Equip.*, vol. 491, no. 1–2, pp. 194–215, Sep. 2002, doi: 10.1016/S0168-9002(02)01227-5.

[38] G. Lindström *et al.*, "Developments for radiation hard silicon detectors by defect engineering - Results by the CERN RD48 (ROSE) Collaboration," *Nucl.*

Instruments Methods Phys. Res. Sect. A Accel. Spectrometers, Detect. Assoc. Equip., vol. 465, no. 1, pp. 60–69, Jun. 2001, doi: 10.1016/S0168-9002(01)00347-3.

[39] K. Dette, "Total Ionising Dose effects in the FE-I4 front-end chip of the ATLAS Pixel IBL detector," *J. Instrum.*, vol. 11, no. 11, Nov. 2016, doi: 10.1088/1748-0221/11/11/C11028.

[40] F. Faccio and C. Giovanni, "Radiation-induced edge effects in deep submicron CMOS transistors," in *IEEE Transactions on Nuclear Science*, Dec. 2005, vol. 52, no. 6, pp. 2413–2420, doi: 10.1109/TNS.2005.860698.

[41] F. Faccio *et al.*, "Total ionizing dose effects in shallow trench isolation oxides," *Microelectron. Reliab.*, vol. 48, no. 7, pp. 1000–1007, Jul. 2008, doi: 10.1016/j.microrel.2008.04.004.

[42] M. R. Shaneyfelt *et al.*, "Interface-trap buildup rates in wet and dry oxides," *IEEE Trans. Nucl. Sci.*, vol. 39, no. 6, pp. 2244–2251, 1992, doi: 10.1109/23.211427.

[43] G. Lindström, "Radiation damage in silicon detectors," in *Nuclear Instruments and Methods in Physics Research, Section A: Accelerators, Spectrometers, Detectors and Associated Equipment*, Oct. 2003, vol. 512, no. 1–2, pp. 30–43, doi: 10.1016/S0168-9002(03)01874-6.

[44] G. Pearson and B. Sawyer, "Silicon P-N Junction Alloy Diodes," *Proc. IRE*, vol. 40, no. 11, pp. 1348–1351, Nov. 1952, doi: 10.1109/JRPROC.1952.273960.

[45] A. G. Chynoweth and K. G. McKay, "Photon Emission from Avalanche Breakdown in Silicon," *Phys. Rev.*, vol. 102, no. 2, pp. 369–376, Apr. 1956, doi: 10.1103/PhysRev.102.369.

[46] K. G. McKay and K. B. McAfee, "Electron Multiplication in Silicon and Germanium," *Phys. Rev.*, vol. 91, no. 5, pp. 1079–1084, Sep. 1953, doi: 10.1103/PhysRev.91.1079.

[47] K. G. McKay, "Avalanche Breakdown in Silicon," *Phys. Rev.*, vol. 94, no. 4, pp. 877–884, May 1954, doi: 10.1103/PhysRev.94.877.

[48] P. A. Wolff, "Theory of Electron Multiplication in Silicon and Germanium," *Phys. Rev.*, vol. 95, no. 6, pp. 1415–1420, Sep. 1954, doi: 10.1103/PhysRev.95.1415.

[49] B. Senitzky and J. L. Moll, "Breakdown in Silicon," *Phys. Rev.*, vol. 110, no. 3, pp. 612–620, May 1958, doi: 10.1103/PhysRev.110.612.

[50] R. H. Haitz, A. Goetzberger, R. M. Scarlett, and W. Shockley, "Avalanche Effects in Silicon p-n Junctions. I. Localized Photomultiplication Studies on Microplasmas," *J. Appl. Phys.*, vol. 34, no. 6, pp. 1581–1590, Jun. 1963, doi:

10.1063/1.1702639.

[51] A. Goetzberger, B. McDonald, R. H. Haitz, and R. M. Scarlett, "Avalanche Effects in Silicon p-n Junctions. II. Structurally Perfect Junctions," *J. Appl. Phys.*, vol. 34, no. 6, pp. 1591–1600, Jun. 1963, doi: 10.1063/1.1702640.

[52] S. M. Sze and K. K. Ng, *Physics of semiconductor devices*, 3rd ed. Wiley-Interscience, 2007.

[53] R. H. Haitz, "Mechanisms Contributing to the Noise Pulse Rate of Avalanche Diodes," *J. Appl. Phys.*, vol. 36, no. 10, pp. 3123–3131, Oct. 1965, doi: 10.1063/1.1702936.

[54] R. H. Haitz, "Studies on optical coupling between silicon p−n junctions," *Solid. State. Electron.*, vol. 8, no. 4, pp. 417–425, Apr. 1965, doi: 10.1016/0038-1101(65)90119-X.

[55] R. J. McIntyre, "The distribution of gains in uniformly multiplying avalanche photodiodes: Theory," *IEEE Trans. Electron Devices*, vol. 19, no. 6, pp. 703–713, Jun. 1972, doi: 10.1109/T-ED.1972.17485.

[56] R. J. McIntyre, "Recent developments in silicon avalanche photodiodes," *Measurement*, vol. 3, no. 4, pp. 146–152, Oct. 1985, doi: 10.1016/0263-2241(85)90024-7.

[57] S. Cova, A. Longoni, and A. Andreoni, "Towards picosecond resolution with single-photon avalanche diodes," *Rev. Sci. Instrum.*, vol. 52, no. 3, pp. 408–412, Mar. 1981, doi: 10.1063/1.1136594.

[58] S. Cova, A. Longoni, A. Andreoni, and R. Cubeddu, "A semiconductor detector for measuring ultraweak fluorescence decays with 70 ps FWHM resolution," *IEEE J. Quantum Electron.*, vol. 19, no. 4, pp. 630–634, Apr. 1983, doi: 10.1109/JQE.1983.1071905.

[59] M. Ghioni, S. Cova, A. Lacaita, and G. Ripamonti, "New silicon epitaxial avalanche diode for single-photon timing at room temperature," *Electron. Lett.*, vol. 24, no. 24, p. 1476, 1988, doi: 10.1049/el:19881007.

[60] A. Lacaita, M. Ghioni, and S. Cova, "Double epitaxy improves single-photon avalanche diode performance," *Electron. Lett.*, vol. 25, no. 13, p. 841, 1989, doi: 10.1049/el:19890567.

[61] A. Lacaita, S. Cova, M. Ghioni, and F. Zappa, "Single-photon avalanche diode with ultrafast pulse response free from slow tails," *IEEE Electron Device Lett.*, vol. 14, no. 7, pp. 360–362, Jul. 1993, doi: 10.1109/55.225573.

[62] A. Gulinatti, F. Panzeri, I. Rech, P. Maccagnani, M. Ghioni, and S. D. Cova, "Planar silicon SPADs with improved photon detection efficiency," Apr. 2010, vol. 7681, p. 76810M, doi: 10.1117/12.849664.

[63] A. Gulinatti, I. Rech, P. Maccagnani, M. Ghioni, and S. Cova, "Improving the performance of silicon single-photon avalanche diodes," May 2011, vol. 8033, p. 803302, doi: 10.1117/12.883863.

[64] S. Cova, M. Ghioni, F. Zappa, I. Rech, and A. Gulinatti, "A view on progress of silicon single-photon avalanche diodes and quenching circuits," Oct. 2006, vol. 6372, p. 63720I, doi: 10.1117/12.685963.

[65] M. Ghioni, A. Gulinatti, I. Rech, F. Zappa, and S. Cova, "Progress in Silicon Single-Photon Avalanche Diodes," *IEEE J. Sel. Top. Quantum Electron.*, vol. 13, no. 4, pp. 852–862, 2007, doi: 10.1109/JSTQE.2007.902088.

[66] A. Rochas *et al.*, "Single photon detector fabricated in a complementary metal–oxide–semiconductor high-voltage technology," *Rev. Sci. Instrum.*, vol. 74, no. 7, pp. 3263–3270, Jul. 2003, doi: 10.1063/1.1584083.

[67] A. Rochas, "Single photon avalanche diodes in CMOS technology," 2003, doi: 10.5075/EPFL-THESIS-2814.

[68] E. Charbon, "Single-photon imaging in complementary metal oxide semiconductor processes.," *Philos. Trans. A. Math. Phys. Eng. Sci.*, vol. 372, no. 2012, p. 20130100, Mar. 2014, doi: 10.1098/rsta.2013.0100.

[69] T. Kunikiyo *et al.*, "A Monte Carlo simulation of anisotropic electron transport in silicon including full band structure and anisotropic impact-ionization model," *J. Appl. Phys.*, vol. 75, no. 1, pp. 297–312, Jan. 1994, doi: 10.1063/1.355849.

[70] T. Kunikiyo, M. Takenaka, M. Morifuji, K. Taniguchi, and C. Hamaguchi, "A model of impact ionization due to the primary hole in silicon for a full band Monte Carlo simulation," *J. Appl. Phys.*, vol. 79, no. 10, pp. 7718–7725, May 1996, doi: 10.1063/1.362375.

[71] S. Cova, M. Ghioni, A. Lacaita, C. Samori, and F. Zappa, "Avalanche photodiodes and quenching circuits for single-photon detection," *Appl. Opt.*, vol. 35, no. 12, p. 1956, Apr. 1996, doi: 10.1364/AO.35.001956.

[72] A. Gallivanoni, I. Rech, and M. Ghioni, "Progress in Quenching Circuits for Single Photon Avalanche Diodes," *IEEE Trans. Nucl. Sci.*, Dec. 2010, doi: 10.1109/TNS.2010.2074213.

[73] H. Finkelstein, M. J. Hsu, S. Zlatanovic, and S. Esener, "Performance trade-offs in single-photon avalanche diode miniaturization," *Rev. Sci. Instrum.*, vol. 78, no. 10, p. 103103, Oct. 2007, doi: 10.1063/1.2796146.

[74] J. Richardson, R. K. Henderson, and D. Renshaw, "Dynamic Quenching for Single Photon Avalanche Diode Arrays." 2007, Accessed: Sep. 16, 2019. [Online]. Available: https://www.semanticscholar.org/paper/Dynamic-Quenching-for-Single-Photon-Avalanche-Diode-Richardson-Henderson/9ed55b2819f7bd7e6457f90290c8c9ce33e36b5e.

[75] A. Eisele *et al.*, "185 MHz count rate, 139 dB dynamic range single-photon avalanche diode with active quenching circuit in 130 nm CMOS technology," *Pap. Present. Int. Image Sens. Work. (IISW'11), Hokkaido, Japan, June 08-11, 2011*, p. 43, 2011, Accessed: Sep. 16, 2019. [Online]. Available: https://publikationen.bibliothek.kit.edu/1000032077.

[76] F. Villa *et al.*, "CMOS SPADs with up to 500 μm diameter and 55% detection efficiency at 420 nm," *J. Mod. Opt.*, vol. 61, no. 2, pp. 102–115, Jan. 2014, doi: 10.1080/09500340.2013.864425.

[77] J. A. Richardson, E. A. G. Webster, L. A. Grant, and R. K. Henderson, "Scaleable Single-Photon Avalanche Diode Structures in Nanometer CMOS Technology," *IEEE Trans. Electron Devices*, vol. 58, no. 7, pp. 2028–2035, Jul. 2011, doi: 10.1109/TED.2011.2141138.

[78] M. Ghioni, G. Armellini, P. Maccagnani, I. Rech, M. K. Emsley, and M. S. Unlu, "Resonant-Cavity-Enhanced Single-Photon Avalanche Diodes on Reflecting Silicon Substrates," *IEEE Photonics Technol. Lett.*, vol. 20, no. 6, pp. 413–415, Mar. 2008, doi: 10.1109/LPT.2008.916926.

[79] H. Finkelstein, M. J. Hsu, and S. C. Esener, "STI-Bounded Single-Photon Avalanche Diode in a Deep-Submicrometer CMOS Technology," *IEEE Electron Device Lett.*, vol. 27, no. 11, pp. 887–889, Nov. 2006, doi: 10.1109/LED.2006.883560.

[80] M. J. Hsu, S. C. Esener, and H. Finkelstein, "A CMOS STI-Bound Single-Photon Avalanche Diode With 27-ps Timing Resolution and a Reduced Diffusion Tail," *IEEE Electron Device Lett.*, vol. 30, no. 6, pp. 641–643, Jun. 2009, doi: 10.1109/LED.2009.2019974.

[81] R. C. Jaeger and T. N. Blalock, *Microelectronic circuit design*, 4th ed. New York: McGraw-Hill, 2011.

[82] M. A. Marwick and A. G. Andreou, "Fabrication and Testing of Single Photon Avalanche Detectors in the TSMC 0.18μm CMOS Technology," in *2007 41st Annual Conference on Information Sciences and Systems*, Mar. 2007, pp. 741–744, doi: 10.1109/CISS.2007.4298405.

[83] L. Pancheri and D. Stoppa, "Low-Noise CMOS single-photon avalanche diodes with 32 ns dead time," in *ESSDERC 2007 - 37th European Solid State Device Research Conference*, 2007, pp. 362–365, doi: 10.1109/ESSDERC.2007.4430953.

[84] C. Niclass, M. Gersbach, R. Henderson, L. Grant, and E. Charbon, "A Single Photon Avalanche Diode Implemented in 130-nm CMOS Technology," *IEEE J. Sel. Top. Quantum Electron.*, vol. 13, no. 4, pp. 863–869, 2007, doi: 10.1109/JSTQE.2007.903854.

[85] R. M. Field, J. Lary, J. Cohn, L. Paninski, and K. L. Shepard, "A low-noise,

single-photon avalanche diode in standard 0.13 μm complementary metal-oxide-semiconductor process," *Appl. Phys. Lett.*, vol. 97, no. 21, p. 211111, Nov. 2010, doi: 10.1063/1.3518473.

[86] C. Veerappan and E. Charbon, "A Substrate Isolated CMOS SPAD Enabling Wide Spectral Response and Low Electrical Crosstalk," *IEEE J. Sel. Top. Quantum Electron.*, vol. 20, no. 6, pp. 299–305, Nov. 2014, doi: 10.1109/JSTQE.2014.2318436.

[87] C. Veerappan and E. Charbon, "CMOS SPAD Based on Photo-Carrier Diffusion Achieving PDP >40% From 440 to 580 nm at 4 V Excess Bias," *IEEE Photonics Technol. Lett.*, vol. 27, no. 23, pp. 2445–2448, Dec. 2015, doi: 10.1109/LPT.2015.2468067.

[88] C. Niclass, M. Gersbach, R. Henderson, L. Grant, and E. Charbon, "A 130-nm CMOS single-photon avalanche diode," Sep. 2007, vol. 6766, p. 676606, doi: 10.1117/12.728878.

[89] R. K. Henderson, J. Richardson, and L. A. Grant, "Reduction of band-to-band tunneling in deep-submicron CMOS single photon avalanche photodiodes," 2009, Accessed: Sep. 27, 2019. [Online]. Available: https://www.researchgate.net/publication/229022021_Reduction_of_band-to-band_tunneling_in_deep-submicron_CMOS_single_photon_avalanche_photodiodes.

[90] E. O. Kane, "Theory of Tunneling," *J. Appl. Phys.*, vol. 32, no. 1, pp. 83–91, Jan. 1961, doi: 10.1063/1.1735965.

[91] M. A. Karami, M. Gersbach, H.-J. Yoon, and E. Charbon, "A new single-photon avalanche diode in 90nm standard CMOS technology," *Opt. Express*, vol. 18, no. 21, p. 22158, Oct. 2010, doi: 10.1364/OE.18.022158.

[92] M. A. Karami, H. J. Yoon, and E. Charbon, "Single-photon Avalanche Diodes in sub-100nm Standard CMOS Technologies," *Proc. Intl. Image Sens. Work.*, 2011, Accessed: Sep. 27, 2019. [Online]. Available: https://infoscience.epfl.ch/record/178147.

[93] H. Finkelstein, M. J. Hsu, and S. Esener, "An ultrafast Geiger-mode single-photon avalanche diode in 0.18-μm CMOS technology," Oct. 2006, vol. 6372, p. 63720W, doi: 10.1117/12.705259.

[94] M. Gersbach, C. Niclass, E. Charbon, J. Richardson, R. Henderson, and L. Grant, "A single photon detector implemented in a 130nm CMOS imaging process," in *ESSDERC 2008 - 38th European Solid-State Device Research Conference*, 2008, pp. 270–273, doi: 10.1109/ESSDERC.2008.4681750.

[95] M. A. Marwick and A. G. Andreou, "Single photon avalanche photodetector with integrated quenching fabricated in TSMC 0.18 [micro sign]m 1.8 V CMOS process," *Electron. Lett.*, vol. 44, no. 10, p. 643, 2008, doi:

10.1049/el:20080673.

[96] L. Pancheri, G.-F. Dalla Betta, L. H. Campos Braga, H. Xu, and D. Stoppa, "A single-photon avalanche diode test chip in 150nm CMOS technology," in *2014 International Conference on Microelectronic Test Structures (ICMTS)*, Mar. 2014, pp. 161–164, doi: 10.1109/ICMTS.2014.6841486.

[97] J. A. Richardson, L. A. Grant, and R. K. Henderson, "A Low Dark Count Single Photon Avalanche Diode Structure Compatible with Standard Nanometer Scale CMOS Technology," 2009, Accessed: Sep. 27, 2019. [Online]. Available: http://www.imagesensors.org/Past Workshops/2009 Workshop/2009 Papers/063_paper_richardson_spad.pdf.

[98] J. A. Richardson, L. A. Grant, and R. K. Henderson, "Low Dark Count Single-Photon Avalanche Diode Structure Compatible With Standard Nanometer Scale CMOS Technology," *IEEE Photonics Technol. Lett.*, vol. 21, no. 14, pp. 1020–1022, Jul. 2009, doi: 10.1109/LPT.2009.2022059.

[99] R. Henderson, E. A. G. Webster, J. A. Richardson, and L. A. Grant, "Single Photon Avalanche Diodes in 90nm CMOS Technology with sub-1Hz Median Dark Count Rate." 2011, Accessed: Sep. 30, 2019. [Online]. Available: https://www.research.ed.ac.uk/portal/en/publications/single-photon-avalanche-diodes-in-90nm-cmos-technology-with-sub1hz-median-dark-count-rate(e03b35ac-2592-4d3f-b630-e49039d01541)/export.html.

[100] S. Pellegrini and B. Rae, "Fully industrialised single photon avalanche diodes," in *Advanced Photon Counting Techniques XI*, May 2017, vol. 10212, doi: 10.1117/12.2264364.

[101] S. Pellegrini *et al.*, "Industrialised SPAD in 40 nm technology," in *2017 IEEE International Electron Devices Meeting (IEDM)*, Dec. 2017, pp. 16.5.1-16.5.4, doi: 10.1109/IEDM.2017.8268404.

[102] T. Al abbas *et al.*, "8.25µm Pitch 66% Fill Factor Global Shared Well SPAD Image Sensor in 40nm CMOS FSI Technology," Jun. 2017, Accessed: Sep. 30, 2019. [Online]. Available: https://www.research.ed.ac.uk/portal/en/publications/825m-pitch-66-fill-factor-global-shared-well-spad-image-sensor-in-40nm-cmos-fsi-technology(880e484a-6adf-4d90-8e16-9a927a1a1bde).html.

[103] E. A. G. Webster, J. A. Richardson, L. Grant, and R. K. Henderson, "An Infra-Red Sensitive, Low Noise, Single-Photon Avalanche Diode in 90nm CMOS," 2011, Accessed: Sep. 30, 2019. [Online]. Available: https://www.semanticscholar.org/paper/An-Infra-Red-Sensitive%2C-Low-Noise%2C-Single-Photon-in-Webster-Richardson/31e9fe425fd65d596fc58e3b332bde98bc1da756.

[104] E. A. G. Webster, R. J. Walker, R. K. Henderson, and L. A. Grant, "A silicon photomultiplier with >30% detection efficiency from 450–750nm and

11.6μm pitch NMOS-only pixel with 21.6% fill factor in 130nm CMOS," in *2012 Proceedings of the European Solid-State Device Research Conference (ESSDERC)*, Sep. 2012, pp. 238–241, doi: 10.1109/ESSDERC.2012.6343377.

[105] R. K. Henderson *et al.*, "A 192×128 Time Correlated Single Photon Counting Imager in 40nm CMOS Technology," in *ESSCIRC 2018 - IEEE 44th European Solid State Circuits Conference (ESSCIRC)*, Sep. 2018, pp. 54–57, doi: 10.1109/ESSCIRC.2018.8494330.

[106] M.-J. Lee *et al.*, "A back-illuminated 3D-stacked single-photon avalanche diode in 45nm CMOS technology," in *2017 IEEE International Electron Devices Meeting (IEDM)*, Dec. 2017, pp. 16.6.1-16.6.4, doi: 10.1109/IEDM.2017.8268405.

[107] M.-J. Lee *et al.*, "High-Performance Back-Illuminated Three-Dimensional Stacked Single-Photon Avalanche Diode Implemented in 45-nm CMOS Technology," *IEEE J. Sel. Top. Quantum Electron.*, vol. 24, no. 6, pp. 1–9, Nov. 2018, doi: 10.1109/JSTQE.2018.2827669.

[108] E. Charbon, H.-J. Yoon, and Y. Maruyama, "A Geiger mode APD fabricated in standard 65nm CMOS technology," in *2013 IEEE International Electron Devices Meeting*, Dec. 2013, pp. 27.5.1-27.5.4, doi: 10.1109/IEDM.2013.6724705.

[109] S. Lindner, S. Pellegrini, Y. Henrion, B. Rae, M. Wolf, and E. Charbon, "A High-PDE, Backside-Illuminated SPAD in 65/40-nm 3D IC CMOS Pixel With Cascoded Passive Quenching and Active Recharge," *IEEE Electron Device Lett.*, vol. 38, no. 11, pp. 1547–1550, Nov. 2017, doi: 10.1109/LED.2017.2755989.

[110] E. A. G. Webster, J. A. Richardson, L. A. Grant, D. Renshaw, and R. K. Henderson, "A Single-Photon Avalanche Diode in 90-nm CMOS Imaging Technology With 44% Photon Detection Efficiency at 690 nm," *IEEE Electron Device Lett.*, vol. 33, no. 5, pp. 694–696, May 2012, doi: 10.1109/LED.2012.2187420.

[111] E. A. G. Webster, L. A. Grant, and R. K. Henderson, "A High-Performance Single-Photon Avalanche Diode in 130-nm CMOS Imaging Technology," *IEEE Electron Device Lett.*, vol. 33, no. 11, pp. 1589–1591, Nov. 2012, doi: 10.1109/LED.2012.2214760.

[112] R. K. Henderson, E. A. G. Webster, R. Walker, J. A. Richardson, and L. A. Grant, "A 3×3, 5μm pitch, 3-transistor single photon avalanche diode array with integrated 11V bias generation in 90nm CMOS technology," in *2010 International Electron Devices Meeting*, Dec. 2010, pp. 14.2.1-14.2.4, doi: 10.1109/IEDM.2010.5703359.

[113] J. A. Richardson, L. A. Grant, E. A. G. Webster, and R. K. Henderson, "A 2um diameter, 9hz dark count, single photon avalanche diode in 130nm cmos

technology," in *2010 Proceedings of the European Solid State Device Research Conference*, Sep. 2010, pp. 257–260, doi: 10.1109/ESSDERC.2010.5618371.

[114] Z. You, L. Parmesan, S. Pellegrini, and R. K. Henderson, "3um Pitch, 1um Active Diameter SPAD Arrays in 130nm CMOS Imaging Technology," 2017, Accessed: Sep. 30, 2019. [Online]. Available: https://www.semanticscholar.org/paper/3um-Pitch%2C-1um-Active-Diameter-SPAD-Arrays-in-130nm-You-Parmesan/638f19960d510cdc57a339febd02f4439070155e.

[115] A. Eisele *et al.*, "185 MHz count rate, 139 dB dynamic range single-photon avalanche diode with active quenching circuit in 130 nm CMOS technology," *Int. Image Sens. Work.*, p. 43, 2011, Accessed: Sep. 30, 2019. [Online]. Available: https://publikationen.bibliothek.kit.edu/1000032077.

[116] W. G. Oldham, R. R. Samuelson, and P. Antognetti, "Triggering phenomena in avalanche diodes," *IEEE Trans. Electron Devices*, vol. 19, no. 9, pp. 1056–1060, Sep. 1972, doi: 10.1109/T-ED.1972.17544.

[117] S. Gnecchi *et al.*, "Analysis of Photon Detection Efficiency and Dynamic Range in SPAD-Based Visible Light Receivers," *J. Light. Technol.*, vol. 34, no. 11, pp. 2774–2781, Jun. 2016, doi: 10.1109/JLT.2016.2550497.

[118] R. N. Hall, "Electron-Hole Recombination in Germanium," *Phys. Rev.*, vol. 87, no. 2, pp. 387–387, Jul. 1952, doi: 10.1103/PhysRev.87.387.

[119] W. Shockley and W. T. Read, "Statistics of the Recombinations of Holes and Electrons," *Phys. Rev.*, vol. 87, no. 5, pp. 835–842, Sep. 1952, doi: 10.1103/PhysRev.87.835.

[120] E. A. G. Webster and R. K. Henderson, "A TCAD and Spectroscopy Study of Dark Count Mechanisms in Single-Photon Avalanche Diodes," *IEEE Trans. Electron Devices*, vol. 60, no. 12, pp. 4014–4019, Dec. 2013, doi: 10.1109/TED.2013.2285163.

[121] H. Xu, L. Pancheri, G.-F. D. Betta, and D. Stoppa, "Design and characterization of a p+/n-well SPAD array in 150nm CMOS process," *Opt. Express*, vol. 25, no. 11, p. 12765, May 2017, doi: 10.1364/OE.25.012765.

[122] F. Di Capua *et al.*, "Random Telegraph Signal in Proton Irradiated Single-Photon Avalanche Diodes," *IEEE Trans. Nucl. Sci.*, vol. 65, no. 8, pp. 1654–1660, Aug. 2018, doi: 10.1109/TNS.2018.2814823.

[123] M. A. Karami, L. Carrara, C. Niclass, M. Fishburn, and E. Charbon, "RTS Noise Characterization in Single-Photon Avalanche Diodes," *IEEE Electron Device Lett.*, vol. 31, no. 7, pp. 692–694, Jul. 2010, doi: 10.1109/LED.2010.2047234.

[124] A. Lacaita, M. Mastrapasqua, M. Ghioni, and S. Vanoli, "Observation of avalanche propagation by multiplication assisted diffusion in *p - n* junctions," *Appl. Phys. Lett.*, vol. 57, no. 5, pp. 489–491, Jul. 1990, doi: 10.1063/1.103629.

[125] D. Dolgos, H. Meier, A. Schenk, and B. Witzigmann, “Full-band Monte Carlo simulation of high-energy carrier transport in single photon avalanche diodes: Computation of breakdown probability, time to avalanche breakdown, and jitter,” *J. Appl. Phys.*, vol. 110, no. 8, p. 084507, Oct. 2011, doi: 10.1063/1.3652844.

[126] S. L. Tan, D. S. Ong, and H. K. Yow, “Theoretical analysis of breakdown probabilities and jitter in single-photon avalanche diodes,” *J. Appl. Phys.*, vol. 102, no. 4, p. 044506, Aug. 2007, doi: 10.1063/1.2772531.

[127] A. W. Ziarkash, S. K. Joshi, M. Stipčević, and R. Ursin, “Comparative study of afterpulsing behavior and models in single photon counting avalanche photo diode detectors,” *Sci. Rep.*, vol. 8, no. 1, p. 5076, Dec. 2018, doi: 10.1038/s41598-018-23398-z.

[128] S. Bellisai, “SPAD lab - Device - Crosstalk in SPAD devices.” http://www.everyphotoncounts.com/device-crosstalk.php (accessed Oct. 01, 2019).

[129] S. Jahromi and J. Kostamovaara, “Timing and probability of crosstalk in a dense CMOS SPAD array in pulsed TOF applications,” *Opt. Express*, vol. 26, no. 16, p. 20622, Aug. 2018, doi: 10.1364/OE.26.020622.

[130] R. Newman, “Visible Light from a Silicon p − n Junction,” *Phys. Rev.*, vol. 100, no. 2, pp. 700–703, Oct. 1955, doi: 10.1103/PhysRev.100.700.

[131] A. G. Chynoweth and K. G. McKay, “Photon Emission from Avalanche Breakdown in Silicon,” *Phys. Rev.*, vol. 102, no. 2, pp. 369–376, Apr. 1956, doi: 10.1103/PhysRev.102.369.

[132] J. Shewchun and L. Y. Wei, “Mechanism for reverse-biased breakdown radiation in p-n junctions,” *Solid. State. Electron.*, vol. 8, no. 5, pp. 485–493, May 1965, doi: 10.1016/0038-1101(65)90024-9.

[133] J. Bude, N. Sano, and A. Yoshii, “Hot-carrier luminescence in Si,” *Phys. Rev. B*, vol. 45, no. 11, pp. 5848–5856, Mar. 1992, doi: 10.1103/PhysRevB.45.5848.

[134] M. Lahbabi *et al.*, “Analyses of electroluminescence spectra of silicon junctions in avalanche breakdown using an indirect interband recombination model,” *Appl. Phys. Lett.*, vol. 77, no. 20, pp. 3182–3184, Nov. 2000, doi: 10.1063/1.1326038.

[135] M. Lahbabi *et al.*, “Analysis of electroluminescence spectra of silicon and gallium arsenide p–n junctions in avalanche breakdown,” *J. Appl. Phys.*, vol. 95, no. 4, pp. 1822–1828, Feb. 2004, doi: 10.1063/1.1643188.

[136] J. Michailos *et al.*, “New challenges and opportunities for 3D integrations,” in *Technical Digest - International Electron Devices Meeting, IEDM*, Feb. 2015, vol. 2016-February, pp. 8.5.1-8.5.4, doi: 10.1109/IEDM.2015.7409655.

[137] W. W. Shen *et al.*, "3-D Stacked Technology of DRAM-Logic Controller Using Through-Silicon Via (TSV)," *IEEE J. Electron Devices Soc.*, vol. 6, no. 1, pp. 396–402, Mar. 2018, doi: 10.1109/JEDS.2018.2815344.

[138] S. Lhostis *et al.*, "Reliable 300 mm Wafer Level Hybrid Bonding for 3D Stacked CMOS Image Sensors," *Proc. - Electron. Components Technol. Conf.*, pp. 869–876, 2016, doi: 10.1109/ECTC.2016.202.

[139] "Structure of atom: Discovery of electrons, protons and neutrons – Open Teaching Project." http://padakshep.org/otp/subjects/chemistry/physical-chemistry/discovery-of-electrons-protons-and-neutrons/ (accessed Nov. 29, 2019).

[140] The Editors of Encyclopaedia Britannica, "Thermionic emission," *Britannica*. Encyclopædia Britannica, inc., 2009, [Online]. Available: https://www.britannica.com/science/thermionic-emission.

[141] D. B. Williams and C. B. Carter, *Transmission electron microscopy: A textbook for materials science*. Boston, MA: Springer US, 2009.

[142] E. Segrè, *Nuclei and Particles : an Introduction to Nuclear and Subnuclear Physics*, 2nd ed. London: Reading, Mass., 1977.

[143] W. Loveland, D. Morrissey, and T. Seaborg, Glenn, *Modern Nuclear Chemistry*, Second. Hoboken, New Jersey: John Wiley & Sons Inc., 2017.

[144] D. E. Groom, N. V. Mokhov, and S. I. Striganov, "Muon stopping power and range tables 10 MeV-100 TeV," *At. Data Nucl. Data Tables*, vol. 78, no. 2, pp. 183–356, 2001, doi: 10.1006/adnd.2001.0861.

[145] D. E. Groom, "Atomic Nuclear Properties of Materials for more than 300 materials," 2019. http://pdg.lbl.gov/2019/AtomicNuclearProperties/ (accessed Jun. 06, 2019).

[146] M. Tanabashi *et al.*, "Review of Particle Physics," *Phys. Rev. D*, vol. 98, no. 3, p. 030001, Aug. 2018, doi: 10.1103/PhysRevD.98.030001.

[147] M. Tanabashi *et al.*, "Review of Particle Physics," *Phys. Rev. D*, vol. 98, no. 3, p. 030001, Aug. 2018, doi: 10.1103/PhysRevD.98.030001.

[148] "National Institute of Standards and Technology - Stopping-power and range tables for electrons." https://physics.nist.gov/PhysRefData/Star/Text/ESTAR.html (accessed May 29, 2019).

[149] M. J. Berger, J. S. Coursey, M. A. Zucker, and J. Chang, "Stopping-Power and Range Tables for Electrons, Protons, and Helium Ions," *ESTAR, PSTAR, and ASTAR: Computer Programs for Calculating Stopping-Power and Range Tables for Electrons, Protons, and Helium Ions (version 2.0.1)*, 2017. https://www.nist.gov/pml/stopping-power-range-tables-electrons-protons-and-

helium-ions (accessed Jun. 12, 2019).

[150] T. J. Booth and M. A. B. Baker, "Nanotechnology," in *Pharmacognosy*, Elsevier, 2017, pp. 633–643.

[151] G. D. Najafpour, "Sterilisation," in *Biochemical Engineering and Biotechnology*, Elsevier, 2007, pp. 342–350.

[152] S. Dieterich, E. Ford, D. Pavord, and J. Zeng, "The Use of Electrons for External Beam Radiotherapy," in *Practical Radiation Oncology Physics*, Elsevier, 2016, pp. 207–220.

[153] M. Knoll and E. Ruska, "Das Elektronenmikroskop," *Zeitschrift für Phys.*, vol. 79, no. 9–10, pp. 699–699, Sep. 1932, doi: 10.1007/BF01330526.

[154] "Scottish Microelectronics Centre (SMC) | School of Engineering." https://www.eng.ed.ac.uk/research/facilities-and-resources/resources/scottish-microelectronics-centre (accessed Jul. 11, 2019).

[155] D. Kalpić, N. Hlupić, and M. Lovrić, "Student's t-Tests," in *International Encyclopedia of Statistical Science*, Springer Berlin Heidelberg, 2011, pp. 1559–1563.

[156] Student, "The Probable Error of a Mean," *Biometrika*, vol. 6, no. 1, p. 1, Mar. 1908, doi: 10.2307/2331554.

[157] I. Miller and M. Miller, *John E. Freund's Mathematical Statistics with Applications (Classic Version), 8th Edition*. Pearson, 2019.

[158] B. J. Winer, *Statistical principles in experimental design.* McGraw-Hill Book Company, 2009.

[159] R. A. Johnson, I. Miller, and J. E. Freund, *Miller & Freund's Probability and Statistics for Engineers, Global Edition*. Pearson, 2017.

[160] A. F. Bulling and I. Underwood, "Accelerated Electron Detection Using Single Photon Avalanche Diodes," in *2018 IEEE SENSORS*, Oct. 2018, pp. 1–4, doi: 10.1109/ICSENS.2018.8589781.

[161] "The Standard Model and beyond | The United States at the LHC." http://united-states.cern/physics/standard-model-and-beyond (accessed Oct. 10, 2019).

[162] M. J. Berger *et al.*, "Report 49," *J. Int. Comm. Radiat. Units Meas.*, vol. os25, no. 2, p. NP-NP, May 1993, doi: 10.1093/jicru/os25.2.Report49.

[163] J. F. Gibbons, "Ion implantation in semiconductors—Part II: Damage production and annealing," *Proc. IEEE*, vol. 60, no. 9, pp. 1062–1096, 1972, doi: 10.1109/PROC.1972.8854.

[164] "Taking a closer look at LHC - Home." https://www.lhc-

closer.es/taking_a_closer_look_at_lhc/1.home (accessed Oct. 16, 2019).

[165] O. Mohamad *et al.*, "Carbon Ion Radiotherapy: A Review of Clinical Experiences and Preclinical Research, with an Emphasis on DNA Damage/Repair.," *Cancers (Basel).*, vol. 9, no. 6, Jun. 2017, doi: 10.3390/cancers9060066.

[166] G. Kasprowicz, "Determination of beam intensity and position in a particle accelerator," Warsaw U. of Tech., 2011.

[167] "The Large Hadron Collider | CERN." https://home.cern/science/accelerators/large-hadron-collider (accessed Oct. 16, 2019).

[168] E. Mobs, "The CERN accelerator complex," Jul. 08, 2016. https://cds.cern.ch/record/2197559 (accessed Oct. 16, 2019).

[169] "Linear accelerator 2 | CERN." https://home.cern/science/accelerators/linear-accelerator-2 (accessed Oct. 16, 2019).

[170] "The Proton Synchrotron Booster | CERN." https://home.cern/science/accelerators/proton-synchrotron-booster (accessed Oct. 16, 2019).

[171] "The Proton Synchrotron | CERN." https://home.cern/science/accelerators/proton-synchrotron (accessed Oct. 16, 2019).

[172] "The Super Proton Synchrotron | CERN." https://home.cern/science/accelerators/super-proton-synchrotron (accessed Oct. 16, 2019).

[173] "NA61/SHINE | CERN." https://home.cern/science/experiments/na61shine (accessed Oct. 16, 2019).

[174] H. W. Atherton *et al.*, "Precise measurements of particle production by 400 GeV/c protons on beryllium targets," 1980, doi: 10.5170/CERN-1980-007.

[175] G. Fidecaro, "The Discoveries of Rare Pion Decays at the CERN Synchrocyclotron," in *Adv. Ser. Dir. High Energy Phys.*, vol. 23, 2015, pp. 397–414.

[176] "ELSA - electron stretcher system ELSA." https://www-elsa.physik.uni-bonn.de/index.html (accessed Oct. 17, 2019).

[177] "How to control the north area beam lines." https://sba.web.cern.ch/sba/Documentations/How2controlNAbeams.htm (accessed Oct. 18, 2019).

[178] J. Bernhard, D. Bannerjee, E. Montbardon, and L. Gatignon, "Future of the M2

beam at CERN in the Physics Beyond Colliders Context," 2018, Accessed: Oct. 18, 2019. [Online]. Available: https://indico.cern.ch/event/658983/timetable/#all.detailed.

[179] M. Backhaus, "Characterization of the FE-I4B pixel readout chip production run for the ATLAS Insertable B-layer upgrade," *J. Instrum.*, vol. 8, no. 03, pp. C03013–C03013, Mar. 2013, doi: 10.1088/1748-0221/8/03/C03013.

[180] B. Beckhoff, habil. B. Kanngießer, N. Langhoff, R. Wedell, and H. Wolff, Eds., *Handbook of Practical X-Ray Fluorescence Analysis*. Berlin, Heidelberg: Springer Berlin Heidelberg, 2006.

[181] "Physiology or Medicine 1979 - Press release." https://www.nobelprize.org/prizes/medicine/1979/press-release/ (accessed Nov. 14, 2019).

[182] "The Nobel Prize in Physiology or Medicine 1962 - Speed read: Deciphering Life´s Enigma Code - NobelPrize.org." https://www.nobelprize.org/prizes/medicine/1962/speedread/ (accessed Nov. 14, 2019).

[183] E. Segrè and D. Frisch, "FromX - Rays to Quarks : Modern Physicists and Their Discoveries by Emilio Segré ," *Am. J. Phys.*, vol. 49, no. 3, pp. 285–286, Mar. 1981, doi: 10.1119/1.12629.

[184] R. F. (Richard F. Mould, *A century of x-rays and radioactivity in medicine : with emphasis on photographic records of the early years*. Institute of Physics Pub, 1993.

[185] F. Hippert, E. Geissler, J. L. Hodeau, E. Lelièvre-Berna, and J.-R. Regnard, Eds., *Neutron and X-ray Spectroscopy*. Dordrecht: Springer Netherlands, 2006.

[186] "Electromagnetic Spectrum - Introduction." https://imagine.gsfc.nasa.gov/science/toolbox/emspectrum1.html (accessed Oct. 24, 2019).

[187] J. H. Hubbell and S. M. Seltzer, "Tables of X-Ray Mass Attenuation Coefficients and Mass Energy-Absorption Coefficients (version 1.4)," *National Institute of Standards and Technology, Gaithersburg, MD.*, 2004. https://www.nist.gov/pml/x-ray-mass-attenuation-coefficients (accessed Jun. 06, 2019).

[188] "Characteristic X-rays | MyScope." https://myscope.training/legacy/analysis/eds/xraygeneration/characteristic/ (accessed Nov. 16, 2019).

[189] M. Haschke, *Laboratory Micro-X-Ray Fluorescence Spectroscopy*, vol. 55. Cham: Springer International Publishing, 2014.

[190] O. Renner and F. B. Rosmej, "Challenges of x-ray spectroscopy in

investigations of matter under extreme conditions," *Matter and Radiation at Extremes*, vol. 4, no. 2. American Institute of Physics Inc., Mar. 01, 2019, doi: 10.1063/1.5086344.

[191] A. Thompson *et al., Center for X-ray Optics and Advanced Light Source X-Ray Data Booklet*. Berkley: Lawrence Berkeley National Laboratory, 2009.

[192] "Precision X-Ray | X-RAD160 - Accurate, Reliable, Repeatable : Precision." https://precisionxray.com/x-rad-range/x-rad160/ (accessed Nov. 17, 2019).

[193] "University of Glasgow - Schools - School of Physics & Astronomy - Research - Research Groups - Particle Physics Experiment - Research Overview - GLADD - Infrastructure." https://www.gla.ac.uk/schools/physics/research/groups/particlephysicsexperiment/research/gladd/infrastructure/ (accessed Nov. 17, 2019).

[194] "University of Glasgow - Schools - School of Physics & Astronomy - Our staff - Dr Dima Maneuski." https://www.gla.ac.uk/schools/physics/staff/dimamaneuski/ (accessed Nov. 28, 2019).

[195] L. Ratti *et al.*, "Dark Count Rate Degradation in CMOS SPADs Exposed to X-Rays and Neutrons," *IEEE Trans. Nucl. Sci.*, vol. 66, no. 2, pp. 567–574, Feb. 2019, doi: 10.1109/TNS.2019.2893233.

[196] F. Haslbeck, A. Sharma, and C. Solans, "Dose calibration of the IR-160 x-ray machine," 2018. Accessed: Jun. 17, 2019. [Online]. Available: https://ade-pixel-group.web.cern.ch/ade-pixel-group/xray/xraycalibration.pdf.